THÈSE

Pour obtenir le grade de

DOCTEUR DE L'UNIVERSITÉ GRENOBLE ALPES

École doctorale : STEP - Sciences de la Terre de l'Environnement et des Planètes
Spécialité : Sciences de la Terre et de l'Environnement
Unité de recherche : Institut des Sciences de la Terre

Diversité spatiale et temporelle des ruptures et impact sur la prédiction du mouvement du sol pour les séquences de séismes

Spatial and temporal diversity of rupture characteristics and impact on ground-motion prediction for earthquake sequences

Présentée par :

Jafar KARASHI

Direction de thèse :

Mathieu CAUSSE — Directeur de thèse
CHARGE DE RECHERCHE, Université Gustave Eiffel

Sreeram KOTHA — Co-encadrant de thèse
Universite Gustave Eiffel

Rapporteurs :

P. Martin MAI
FULL PROFESSOR, King Abdullah University of Science and Technology (KAUST), Saudi Arabia

Frantisek GALLOVIC
FULL PROFESSOR, Charles University, Prague, Czech Republic

Thèse soutenue publiquement le **17 juin 2026**, devant le jury composé de :

Mathieu CAUSSE, CHARGEE DE RECHERCHE HDR, Université Grenoble Alpes	Directeur de thèse
P. Martin MAI, FULL PROFESSOR, King Abdullah University of Science and Technology (KAUST), Saudi Arabia	Rapporteur
Frantisek GALLOVIC, FULL PROFESSOR, Charles University, Prague, Czech Republic	Rapporteur
Anne SOCQUET, PHYSICIENNE, CNRS Délégation Alpes	Présidente
Giovanna CALDERONI, SENIOR SCIENTIST, Istitute Nazionale di Geofisica Vulcanologia (INGV), Rome, Italy	Examinatrice
Paola TRAVERSA, INGENIEURE DE RECHERCHE, Électricité de France (EDF)	Examinatrice

Invités :

Sreeram KOTHA
CR2, Université Gustave Elffel

© 2026

Jafar Karashi

All Rights Reserved

Spatial and Temporal Diversity of Rupture Characteristics and Impact on Ground-Motion Prediction for Earthquake Sequences

Jury composed of:

Jury President:

Anne Socquet, *Professor, Université Grenoble Alpes, France*

Reviewers:

Paul Martin Mai, *Professor, King Abdullah University of Science and Technology (KAUST), Saudi Arabia*

František Gallovič, *Professor, Charles University, Czech Republic*

Examinators:

Anne Socquet, *Professor, Université Grenoble Alpes, France*

Giovanna Calderoni, *Senior Researcher, National Institute of Geophysics and Volcanology (INGV), Italy*

Paola Traversa, *Engineer Seismologist, Électricité de France (EDF), France*

Director of the thesis:

Mathieu Causse, *Directeur de Recherche*, *Université Gustave Eiffel, Université Grenoble Alpes, France*

Co-director of the thesis:

Sreeram Reddy Kotha, *Chargé de recherche*, *Université Gustave Eiffel, Université Grenoble Alpes, France*

Acknowledgments

Finalizing this thesis would have been impossible without the support of my family: my parents, my brothers, my sister-in-law, and my little nephew (who is now 3.5 years old, and by the time he can read his uncle's thesis, I am sure he will be a true gentleman). I can say with confidence and without any uncertainty ($\sigma_{family} = 0$) that they sacrificed their own needs to provide me with the conditions to study abroad, without ever feeling far from home. Therefore, if the results of this thesis somehow lead to another Big Bang, please blame them. Conversely, if my thesis wins a Nobel Prize, kindly award it to them. Thanks!

My supervisor, Mathieu; I could easily write pages about him, but he always encouraged me to keep my papers and thesis concise, which I did not appreciate much at the time. Now I should finally listen to him and write just a short paragraph about him. I thank him immensely for the opportunity he gave me to start my Ph.D. journey and for his endless patience during our countless meetings. I see him not only as a supervisor, but also as a friend who has supported me in science, and, just as importantly, in life beyond it. I am also grateful for the many great moments we shared, whether in academia or on climbing, skiing, and occasionally pretending to rest. Many thanks, as well, to his family for warmly welcoming me. Merci Beaucoup!

My co-advisor, Sreeram; a huge thank you, perhaps as large as the number of coffees he drinks per day (countless, believe me), for his patience during our scientific discussions and for helping me adapt to life in France almost as quickly as he finishes his coffee. It has been a great pleasure working with him, and I feel very lucky to have had him not only as a co-advisor but also as a friend. Thanks!

I would like to sincerely thank the jury members, Martin Mai, František Gallovič, Anne Socquest, Giovanna Calderoni, and Paola Traversa, for agreeing to be part of my thesis committee and for their time and effort in evaluating this work.

A special thanks to my dear friend Rebin Shirkhani, who was the first to encourage me to apply abroad and supported me for years in achieving this goal.

Many thanks as well to my closest friends and mountain partners back home, Abu, Inti, Awat, and many others, for their support and kindness.

Robin; a huge thank you, perhaps as large as the number of steps we took in the mountains. I was truly lucky to find such a friend early in my Ph.D., someone who shared my interests and was just as passionate about climbing, skiing, and hiking. I know it does not always "make sense to you", but thank you for always listening and for your kindness. Danke!

Carlos; it has been said that "most people never meet their heroes", but he met me when I recommended that he "trust his shoes" during a climbing session. Shortly afterward, he found himself in the hospital with some fancy fractures along the strike of his arm, exhibiting both strike-slip and normal mechanisms. This accident did not end our newborn friendship; instead, it marked the beginning of an era of making fun of other friends. Thanks for the ~~questionable~~ jokes, making me laugh, and for always listening to me. Gracias!

A very special thanks to Roland Hellmann for his efforts to teach me how to ski, for taking us hiking and skiing to beautiful places in his three legendary Volkswagens, and, most importantly, for inviting us to his lovely home for drinks and dinner after skiing. Many thanks as well to his family for always welcoming us so warmly.

I send a big thank you and a warm hug to all my friends and colleagues during my time in Grenoble, in alphabetical order: Aline, Alireza, Arpad, Binh, Diksha, Eirini, Eliane, Houssam, Juliette, Laura, Malaury, Navid, Nicko, Paola, Saeid, Yikai, GRE team members, and many others.

Abstract

Large earthquakes can cause significant damage to structures, particularly within a few kilometers of the fault. They are generally followed by sequences of aftershocks. Although smaller, aftershocks can further damage structures already weakened by the mainshock and are often overlooked in seismic hazard analyses. Predicting ground motion during earthquake sequences, including both mainshocks and aftershocks, is therefore critical.

In near-fault regions, earthquake ground motions exhibit strong variability. This variability is primarily driven by heterogeneities in rupture processes combined with the complexity of geological structures, making ground-motion prediction particularly challenging. In addition, large earthquakes can alter the physical properties of the Earth's crust by damaging the fault zone and temporarily modifying its mechanical behavior. As a result, aftershock ground motions may vary significantly depending on both their location and origin time. In this thesis, we rely on an extensive dataset of ground motions from the 2016–2017 Central Italy seismic sequence to quantify and investigate the origins of spatial and temporal variability.

First, we build a catalog of moment magnitude ($\boldsymbol{M}$) and stress drop ($\Delta\sigma$) for 2,503 earthquakes. To capture temporal variations in path effects and reduce biases in $\boldsymbol{M}$ and $\Delta\sigma$, event-specific quality factors are used as proxies for frequency-dependent attenuation. Ground motions are then analyzed through event-specific residuals relative to non-parametric models based on magnitude, distance, and, in some cases, earthquake location and origin time. Our results show that a model including event location reduces variability by up to 80% compared to models based only on magnitude and distance, highlighting the dominant role of spatial variations in source properties and attenuation. These effects are frequency dependent: high-frequency variability is mainly controlled by stress-drop, whereas low-frequency variability is dominated by attenuation. In addition, ground motions decrease sharply immediately after the mainshocks. Part of this decrease is due to seismicity migrating

to shallower depths, which typically generates weaker shaking. However, a significant portion is related to short-term changes in stress-drop and attenuation, likely caused by increased fluid pore pressure and/or damage-induced weakening of the fault zone.

Second, we investigate the rupture process of the ***M***6.5 Norcia mainshock using near-fault ground-motion records. We develop a Bayesian source inversion framework based on a Parallel Tempering Markov Chain Monte Carlo sampler. Rather than discretizing the fault into a dense grid of subfaults, we introduce a control-point representation, in which a limited number of points constrain the spatial and temporal evolution of the rupture. This approach significantly reduces model dimensionality while preserving the ability to capture key features of the rupture process. To model wave propagation, two approaches are considered. The first relies on numerical Green's functions computed using a 1D velocity model, a common assumption that may introduce bias in the inferred rupture process. To better account for propagation complexity, we implement a modified Empirical Green's Function (EGF) approach based on the previously analyzed catalog of small earthquakes. The EGF approach also enables the investigation of rupture evolution up to frequencies of about 1 Hz.

KeyWords: Seismic sequence, Aftershocks, Ground Motion Model, Ground-motion variability, Earthquake source rupture, Seismic Hazard

Résume

Les grands séismes peuvent causer des dommages importants aux structures, en particulier à quelques kilomètres de la faille. Ils sont généralement suivis de séquences de répliques. Bien que de plus faible magnitude, ces répliques peuvent aggraver les dommages subis par des structures déjà fragilisées par le séisme principal et sont souvent négligées dans les analyses d'aléa sismique. La prédiction des mouvements du sol au cours des séquences sismiques, incluant les chocs principaux et les répliques, est donc essentielle.

Dans les zones proches de la faille, les mouvements du sol présentent une forte variabilité. Cette variabilité est principalement due à l'hétérogénéité du processus de rupture combinée à la complexité des structures géologiques, rendant leur prédiction particulièrement difficile. De plus, les grands séismes peuvent modifier les propriétés physiques de la croûte terrestre en endommageant la zone de faille et en altérant temporairement son comportement mécanique. En conséquence, les mouvements du sol associés aux répliques varient fortement en fonction de leur localisation et de leur date. Dans cette thèse, nous utilisons un grand jeu de données de mouvements du sol issus de la séquence sismique d'Italie centrale de 2016–2017 afin de quantifier et d'analyser l'origine de la variabilité spatiale et temporelle.

Dans un premier temps, nous avons construit un catalogue de magnitudes de moment ($\boldsymbol{M}$) et de chutes de contrainte ($\Delta\sigma$) pour 2503 séismes. Pour prendre en compte les variations temporelles de l'atténuation des ondes et de limiter les biais, nous avons estimé pour chaque événement un facteur de qualité spécifique. Les mouvements du sol ont été calculés comme les résidus spécifiques à chaque événement par rapport à des modèles non paramétriques fondés sur la magnitude, la distance et, dans certains cas, la localisation et la date du séisme. Nos résultats montrent qu'un modèle intégrant la localisation des événements réduit la variabilité jusqu'à 80 % par rapport aux modèles reposant uniquement sur la magnitude et la distance, mettant en évidence le rôle dominant des variations spatiales des propriétés

de source et de l'atténuation. Ces effets dépendent de la fréquence : à haute fréquence, la variabilité est principalement contrôlée par la chute de contrainte, tandis qu'aux basses fréquences elle est dominée par l'atténuation. De plus, les mouvements du sol diminuent fortement après les chocs principaux. Une partie de cette diminution est liée à une migration de la sismicité vers la surface, produisant généralement des mouvements plus faibles. Cependant, une part significative est associée à des variations à court terme de la chute de contrainte et de l'atténuation, probablement dues à une augmentation de la pression des fluides et/ou à un endommagement de la zone de faille.

Dans un second temps, nous avons étudié le processus de rupture du séisme de Norcia ($\boldsymbol{M}$6.5) à l'aide d'enregistrements du mouvement fort en champ proche. Nous avons développé une méthode d'inversion bayésienne (Parallel Tempering Markov Chain Monte Carlo). Plutôt que de discrétiser la faille en un maillage dense de sous-failles, nous avons introduit une représentation par points de contrôle, ce qui réduit significativement la dimension du modèle tout en conservant sa capacité à reproduire les caractéristiques essentielles du processus de rupture. Pour modéliser la propagation des ondes, deux approches ont été considérées : une méthode numérique basée sur un modèle de vitesse 1D et une approche empirique, utilisant les enregistrements de petits séismes. Leur comparaison permet d'évaluer l'influence de la propagation des ondes sur les modèles de rupture. L'approche empirique permet également d'imager la rupture jusqu'à environ 1 Hz.

Mots-clés : Séquence sismique, Répliques, Modèle de mouvement du sol, Variabilité du mouvement du sol, Processus de rupture sismique, Aléa sismique

Table of Contents

General Introduction xvi

1. Earthquake Ground Motion Models and Earthquake Source Imaging 1

1.1. Introduction 1

1.2. Ground Motion Models (GMMs) and Ground Motion Variability 4

1.2.1. Parametric and Non-Parametric GMMs 4
1.2.2. Variability of Ground-Motions 7
1.2.3. Stress-Drop 10

1.3. Source Rupture Imaging Using Inversion Techniques 15

1.3.1. Seismological Data 17
1.3.2. Representation Theorem and Green's Functions 17
1.3.3. Inversion 20
1.3.4. The Bayesian Framework 28

2. Ground-Motion Analysis and Spatial Variability of Event Characteristics 31

2.1. Introduction 33

2.2. Dataset 37

2.3. Methods 41

2.3.1. Parametric Linear Mixed-Effects GMMs 42
2.3.2. Non-parametric Random Forest Mixed-Effects GMMs 46
2.3.3. Estimation of Seismological Parameters 50

2.4. Results 53

2.4.1. Seismological Parameters 53
2.4.2. GMM Fixed-effects 56
2.4.3. GMM Random-Effects and Residuals 64
2.4.3.1. Between-Event Random-Effects 65
2.4.3.2. Between-Site Random-Effects 73
2.4.3.3. Residuals 75

2.5. Discussion 77

2.6. Conclusion....86

Appendix 2....91

Text A2.1. Comparison of Moment Magnitude and Stress-Drop from the Three Catalogs...91

3. Temporal and Transient Changes in Ground-Motion 95

3.1. Introduction....97

3.2. Dataset....101

3.2.1. Source and attenuation parameters....101

3.2.2. Ground-motion parameters....104

3.3. Results....105

3.3.1. Comparison of Between-Event Variabilities of GMMs....105

3.3.2. Temporal Variability of $\Delta B(PGA)$, $\Delta\sigma_N$, and $Q_{0,e}$....106

3.3.2.1. Phases 1 & 2: Between the Amatrice and Visso Mainshocks....111

3.3.2.2. Phase 3: Between the Visso and Norcia Mainshocks....112

3.3.2.3. Phases 4 & 5: Between the Norcia and Campotosto Mainshocks....112

3.3.2.4. Phases 6 & 7: After Campotosto Mainshocks....113

3.3.3. Correlation Between $\delta B_e(PGA)$ and $\Delta\sigma_N$....114

3.3.4. Isolating the Contribution of Transient Changes to the Temporal Variability of $\delta B_e(PGA)$....117

3.3.5. Cluster Analysis....119

3.4. Discussion....122

3.4.1. Relationship Between $\Delta\sigma_N$ and $\delta B_e(PGA)$....122

3.4.2. Depth Dependency of $\Delta\sigma_N$ and δB_e....125

3.4.3. Spatial and Temporal Evolution of Stress-Drop, Attenuation, and Ground-motion....128

3.4.3.1. Migration of Seismicity....128

3.4.3.2. Temporal Variability of $\Delta\sigma_N$, $\delta B_e(PGA)$, and $Q_{0,e}$....131

3.4.3.3. Impact of Potential Changes of Shallow Subsurface on $\delta B_e(PGA)$....133

3.5. Conclusion....134

Appendix 3....138

Text A3.1. Comparison of Moment Magnitude and Stress-Drop from the Three Catalogs.138

Text A3.2. Comparison of the Standard Deviation of δB_e for FAS and PGA from the Three Catalogs 140

Text A3.3. Smoothing 141

Text A3.4. Comparison of Temporal Variability of δB_e(PGA) and $\Delta\sigma_N$ for the Three Catalogs 141

4. Kinematic Source Rupture Modeling of the 2016 Norcia Earthquake 153

4.1. Introduction 153

4.2. Strong Motion Waveforms Processing and Fault Geometry 158

4.3. Kinematic Source Inversion Methodology 158

4.3.1. Bayesian Inversion 158
4.3.2. Parallel Tempering 161
4.3.3. Random Walk to Draw Samples from PDF 163
4.3.4. Rupture Model Parametrization 164
4.4. Results 168

4.4.1. Inversion Synthetic Test 168
4.4.1.1 Inversion Results of the Synthetic Test 169
4.4.2. Primary Results for Inversion of the Norica Mainshock 173
4.5. Conclusion and Discussion 177

5. Improving Wave Propagation Models for Finite-Fault Inversion 181

5.1. Introduction 181

5.2. Waveforms Processing 186

5.3. Methodology 187

5.4. Results 191

5.4.1. Waveforms Similarity and Focal Mechanisms 191
5.4.2. Comparison of Computed Green's Functions with Reference EGFs 194
5.4.2.1. Comparison Between the CEGF Approach and Reference EGFs 194
5.4.2.2. Comparison Between the 1DGF approach and Reference EGFs 199

5.4.3. Impact of Uncertainty in Source Parameters on Deconvolved EGFs 203
5.5. Conclusion and Discussion 206
Appendix 5 209
Conclusion 210
Perspectives 213
Bibliography 217

List of Figures

Figure 1.2. Schematic illustration of the Random Forest regression algorithm. 7

Figure 1.3. A schematic showing the definition of the between-event residual (δB_e). 10

Figure 1.4. Spatial global stress-drop variations 15

Figure 1.5. A schematic representing the evolution of misfit as a function of parameter space exploration. 24

Figure 1.6. Schematic illustration of various tempered-based algorithms. 27

Figure 2.1. Overview of the study area, catalogue, and recording characteristics for the 2016–2017 Central Italy seismic sequence. 39

Figure 2.2. Schematic illustration of the definition of variables X and Y, used in the Random Forest Ground Motion Models (GMMs). 48

Figure 2.3. Distributions and scaling relations of the estimated seismological parameters for the analysed events. 55

Figure 2.4. Comparison of fixed-effect (median) predictions from the three GMMs.....58

Figure 2.5. Spatial distribution of fixed-effects predictions obtained from RF(***MRXYZ***) for an ***M***2.5 earthquake under different frequency and distance scenarios 61

Figure 2.6. Along strike cross-sectional view of the spatial distribution of fixed-effects prediction obtained from RF(***MRXYZ***) for an ***M***2.5 earthquake under different frequency and distance scenarios.....63

Figure 2.7. Comparison of between-event random-effects derived from the three mixed-effects ground-motion models.....67

Figure 2.8. Spatial distribution of between-event residuals for FAS obtained from RF(***M***) and RF(***MXYZ***) at different frequencies.....69

Figure 2.9. Along strike cross-sectional view of the spatial distribution of between-event residuals for FAS obtained from RF(***M***) and RF(***MXYZ***).....71

Figure 2.10. Comparison of between-site random-effects derived from the three mixed-effects ground-motion models....74

Figure 2.11. Comparison of residual distributions derived from the three mixed-effects ground-motion models....76

Figure 2.12. Spatial distribution of between-event residuals ($\delta B_e(PGA)$), normalized stress-drop ($\Delta\sigma_N$), and frequency-independent quality factor ($Q_{0,e}$)....80

Figure 2.13. Correlation between normalized stress-drop ($\Delta\sigma_N$) and between-event residuals ($\delta B_e(f)$) at different frequencies for two ground-motion models....83

Figure 2.14. Correlation between frequency-dependent quality factor ($Q_e(f)$) and between-event residuals ($\delta B_e(f)$) at different frequencies for two ground-motion models....85

Figure A2.1. Comparison of source parameters estimated using two different geometrical spreading models....93

Figure 3.1. Examples illustrating how deviations in $Q_e(f)$ affect the estimation of the source parameters $\boldsymbol{M}$, f_c, and $\Delta\sigma$....103

Figure 3.2. Distribution and variability of between-event residuals derived from three ground-motion models....106

Figure 3.3. Along strike cross-sectional distribution of aftershocks during the different phases of the 2016–2018 Central Italy seismic sequence....108

Figure 3.4. Temporal evolution of between-event residuals, stress-drop, depth, and frequency-independent term of quality factor during the 2016–2018 Central Italy seismic sequence....110

Figure 3.5. Temporal evolution of correlations between between-event residuals and stress-drop, frequency-independent term of quality factor, and magnitude ratios during the seismic sequence....116

Figure 3.6. Comparison of the temporal evolution of $\delta B_e(PGA)$ obtained from RF($\boldsymbol{M}$), RF($\boldsymbol{MXYZ}$), and RF($\boldsymbol{MXYZT}$)....118

Figure 3.7. Transient changes of $\delta B_e(PGA)$, $\Delta\sigma_N$, and $Q_{0,e}$ for the selected clusters....120

Figure 3.8. Comparison of the temporal evolution of $\delta B_e(PGA)$ obtained from RF(***M***) for real data (blue curve), simulation 1 (SIM1) (red curve), and simulation 2 (SIM2) (orange curve) 124

Figure 3.9. Schematic illustration of the spatial and temporal migration of seismicity during the 2016–2017 Central Italy sequence.....130

Figure A3.1. Map of the epicentral area of the 2016-2017 Central Italy seismic sequence. 143

Figure A3.2. Comparison of moment magnitude and stress-drop across the three catalogs. 144

Figure A3.3. Comparison of the standard deviation of δBe for PGA and FAS computed using the defined Random Forest GMMs across the three catalogs 145

Figure A3.4. Same as Figure A3.3, but for the spatial distribution of $\delta B_e(PGA)$ based on our catalog.....146

Figure A3.5. Same as Figure A3.3, but for the spatial distribution of $\Delta\sigma_N$ based on our catalog.....147

Figure A3.6. Same as Figure A3.3, but for the spatial distribution of $Q_{0,e}$ based on our catalog.....148

Figure A3.7. Temporal evolution of between-event residuals and normalized stress-drop derived from three earthquake catalogs. 149

Figure A3.8. Temporal evolution of cross-correlations between between-event residuals and stress-drop derived from simulations and real data.....150

Figure A3.9. Depth dependency of normalized stress-drop and PGA between-event residuals.....151

Figure A3.10. Comparison of the temporal evolution of $\delta B_e(PGA)$ obtained from model RF(***MXYZ***) for the full dataset and the dataset to test site effect variability 152

Figure 4.1. Map of the epicentral area showing the distribution strong-motion stations and the geometry of fault planes used in the inversion.....157

Figure 4.2. Schematic illustration of parameterizing space-time rupture evolution using control points. 167

Figure 4.3. Configuration of the reference SIV model for the Inv1 benchmark. 169

Figure 4.4. Comparison of the rupture model obtained in this study with the reference SIV model. 171

Figure 4.5. Comparison of displacement waveforms from the reference SIV model (black) and the synthetics (red) obtained from the rupture model of this study 172

Figure 4.6. Results of the Kinematic source rupture inversion for the Norcia Mainshock. 174

Figure 4.7. Comparison of velocity waveforms observed data (black) and the synthetics (red) obtained from the rupture model of this study 176

Figure 5.1. Map of the epicentral area showing the distribution of small events and near-field strong motion stations 185

Figure 5.2. Schematic illustration of the CEGFs methodology used to compute Green's functions. 190

Figure 5.3. Focal mechanism and waveform similarity of events within clusters. (a) Variability of Kagan angles for small events within the 13 selected clusters. 193

Figure 5.4. Comparison of CEGFs with reference EGFs for seven cases at two stations. .195

Figure 5.5. Investigation of potential nonlinear site effects beneath the stations. 198

Figure 5.6. Comparison of Green's functions obtained from 1DGF (red) with the reference EGFs (black) for the seven cases 201

Figure 5.7. Comparison of cross-correlation and peak ratio of C EGFs, Green's functions obtained from 1DGF, and reference EGFs across all possible reference events and stations. 202

Figure 5.8. Comparison of cluster-derived EGFs (CEGFs) deconvolved using seismic moment estimates from this study (black), K21 (red), and B24 (blue). 205

Figure P1. Reproducing the EGF of a reference event (black) using an ML technique (red). 215

List of Tables

Table 2.1. Selected Random Forest Parameters along with the metrics used to assess the overfitting ……..…..50

Table A4.1. A guideline for calibrating the proposal acceptance rate ……180

Table A4.2. A guideline for calibrating the swap acceptance rate ……..……180

Table A5.1. List of stations used in computing the Empirical Green's Functions ……..209

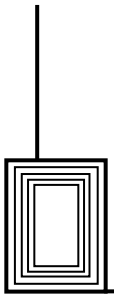

General Introduction

Earthquakes are among the most complex natural disasters, and unlike many other natural phenomena, neither the timing of their occurrence nor their rupture characteristics can be reliably predicted. Nevertheless, historical records indicate a significant decline in earthquake-related fatalities and building damage over time. This improvement is primarily due to our ability to record seismic waves at the Earth's surface, which carry crucial information about the rupture process on the causative fault, the propagation of energy along the wave path, and the near-surface geological conditions beneath recording stations. Additionally, seismic recordings are utilized to develop Probabilistic Seismic Hazard Assessments (PSHA) for target regions, which serve as the basis for building codes and facilitate the design of earthquake-resistant structures. The backbone of PSHA is Ground Motion Models (GMMs), which are empirical relationships that statistically model the intensity of recorded ground-motions as a function of earthquake magnitude, source-to-site distance, and site parameters.

GMMs are calibrated using datasets that include a combination of mainshock and aftershock ground-motion recordings. Aftershocks may accumulate damage to structures that have already been weakened by the mainshock. It is well known that the characteristics of aftershocks following a mainshock exhibit significant spatial and temporal variability, which is typically not explicitly accounted for in GMMs.

Because seismic sources in PSHA generally account only for mainshocks, the spatiotemporal variability associated with aftershocks can strongly influence hazard estimates. Therefore, to reduce the effect of these variabilities on hazard estimates and risk assessment, it is crucial to address the following questions: What are the origins of the observed variability in ground-motions during a seismic sequence? How can we reduce the imprint of these variabilities on GMMs and, consequently, seismic hazard? These questions are investigated in detail in Chapters 2 and 3.

The study of a seismic sequence provides a unique opportunity to examine the extent to which ground-motions vary both spatially and temporally, particularly in the near-field regions where earthquake source complexity exerts strong control. Therefore, constraining source rupture models for moderate-to-large earthquakes, particularly using near-field data, can significantly improve our understanding of the physical processes that govern rupture. Furthermore, reliable source models can be utilized in physics-based simulation methods to generate near-filed ground-motions and thereby improve the calibration of GMMs, which currently struggle to predict near-field ground-motion levels due to the limited availability of recordings. Source inversion techniques are powerful tools for reconstructing key properties of the rupture process, including the spatial and temporal evolution of slip and rupture velocity, from recorded data. However, the retrieved rupture model can be biased by inaccuracies in the Green's Functions (representing the wave path propagation model) and by simplified fault plane representations, particularly in cases with complex fault systems.

This thesis focuses on the 2016-2017 Central Italy seismic sequences. This sequence provides a unique dataset of mainshocks and aftershocks, allowing us to investigate in detail the spatiotemporal variability in ground-motions, the physical phenomena governing these variabilities, and the source rupture process of the largest mainshock in the sequence. The structure of this thesis is as follows:

Chapter 1 provides the theoretical background and fundamental concepts used in Chapters 2, 3, and 4. It begins with an introduction outlining the key questions

addressed in this thesis. Because both parametric and nonparametric GMMs are exploited in this study to assess ground-motion variability, the first part of this chapter describes the structure of the GMMs, including their fixed-effect and random-effect components. Previous studies indicate that ground-motion variability is strongly controlled by earthquake stress-drop; therefore, this chapter also presents a detailed discussion of stress-drop, including its meaning and the challenges scientists face in estimating it. The second part of this chapter is dedicated to the concept of source rupture imaging using inversion techniques and describes its key components, including the representation theorem, different types of Green's Functions, and commonly used inversion techniques. Finally, the algorithms for solving high-dimensional inversion problems and the Bayesian framework are introduced.

Chapter 2 provides a detailed description of the GMMs and the spatial variability of ground-motions observed during the 2016-2017 central Italy sequence. First, the dataset used in this study and the data-processing workflow are introduced. Second, key seismological parameters, including seismic moment, moment magnitude, stress-drop, and anelastic attenuation factor (Q factor), are estimated for each event in the dataset. Then, a parametric GMM and two nonparametric machine-learning GMMs based on the Random Forest algorithm are developed to compute the fixed-effects and random-effects terms. Also, a comparison among the three GMMs is performed to determine which model most effectively minimizes ground-motion variability at different frequencies. Because the ground-motion variability is expected to be primarily controlled by stress-drop, the spatial variability of stress-drop is compared with that of between-event residuals (a component of the random-effect term), while accounting for the potential influence of Q factor variability on their relationship.

Chapter 3 builds on the results of Chapter 2 to investigate the temporal variability of between-event, stress-drop, and Q factor, with a focus on Peak Ground Acceleration (PGA). This chapter demonstrates that variability in between-event residuals can be influenced by both stress-drop and Q factor, particularly during the

short time period following mainshocks. To support this conclusion, several tests are designed. Three small-sized clusters of events are selected to assess how their corresponding between-event residuals, stress-drop, and Q factor vary over time. Also, the entire catalog is simulated using the point source stochastic method, both with and without accounting for Q factor variability, and the same analyses performed on the real catalog are repeated for the simulated dataset. In addition, the role of near-surface geological conditions beneath recording stations is examined to evaluate whether temporal changes in site characteristics affect the between-event variability. Finally, another nonparametric GMM is introduced that effectively captures both spatial and temporal variability in ground-motions.

Chapter 4 discusses the developed Bayesian source inversion framework based on the Parallel Tempering Markov Chain Monte Carlo sampler. As a first step, the reliability and performance of the inversion method are evaluated through the recovery of a benchmark rupture model. The framework is then applied to retrieve the source rupture process of the Norcia mainshock, the M6.5 event of the 2016-2017 Central Italy seismic sequence, at the frequency band of 0.02-0.5 Hz. The resulting rupture models are subsequently compared with previously published studies.

Chapter 5 presents the methodology developed to compute empirical Green's functions (EGFs) in the frequency band 0.3–1.0 Hz using the dataset of small events analyzed in Chapter 2. First, the method describes how EGFs are obtained by grouping events with similar waveforms into clusters. Second, the cluster-derived EGFs are evaluated by comparison with reference EGFs to assess their reliability. Finally, Green's functions computed using a numerical method based on the discrete wavenumber technique are compared with the reference EGFs to examine the reliability of theoretical approaches for generating Green's functions within the considered frequency range. The ultimate objective is to use these EGFs to resolve the source rupture process at frequencies larger than 1 Hz, which remains ongoing work at the time of writing this thesis.

Conclusion and Perspective summarize the main findings of this thesis by highlighting the key results. It also outlines directions for future research based on the insights and developments achieved during this work.

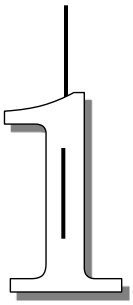

Earthquake Ground Motion Models and Earthquake Source Imaging

1.1. Introduction

Earthquake ruptures result from the relative motion of crustal blocks along fault surfaces within the shallow, brittle lithosphere. The faulting process is governed by a complex partitioning of energy among dissipation within the fault zone and surrounding medium, energy concentrated near the propagating rupture tip, and energy radiated away from the source in the form of seismic waves (Aki, 1980; Andrews, 2005; Rice et al., 2005). These seismic waves are recorded at Earth's surface and carry information about the rupture process, wave propagation characteristics, and local recording-site conditions. Analysis of such recordings enables investigation of the space-time evolution of earthquake rupture properties, including fault slip, rupture velocity, and stress release. Moreover, these observations provide the empirical and theoretical basis for developing and calibrating Ground Motion Models (GMMs), which are essential for quantifying seismic hazard and assessing earthquake risk.

Large earthquakes (mainshocks) are commonly followed by smaller earthquakes known as aftershocks. In some cases, a mainshock is succeeded by numerous aftershocks that persist for months or even years, forming what are commonly

referred to as “seismic sequences”. For example, the most recent famous seismic sequences are the 2016 Kumamoto (Japan), the 2016 Central Italy, and the 2019 Ridgecrest (California). Mainshocks induce significant damage within the fault zone and surrounding crust, accompanied by a sudden redistribution of stress that triggers aftershocks on the main fault and adjacent fault structures (Steacy et al., 2005). The occurrence and evolution of aftershocks reflect the progressive mechanical adjustment and healing of the damaged fault zone in response to the altered stress field (Marone, 1998; Ben-Zion & Sammis, 2003; Vidale & Li, 2003; Schaff & Beroza, 2004). Consequently, the spatial and temporal patterns of aftershocks provide important constraints on stress transfer, fault-zone properties, and postseismic deformation processes, offering valuable insights into the mechanics of earthquake rupture and fault-system interactions. Beyond their seismotectonic significance, aftershocks play an important role in source studies as Empirical Green’s Functions (EGFs) (S. H. Hartzell, 1978; Hough, 1997). By exploiting the similarity in wave-propagation paths and site effects between closely located aftershocks and the mainshock, EGF techniques allow effective removal of path and site contributions from seismic recordings. This approach isolates the source effects and enables more reliable analysis of rupture characteristics.

Engineered structures are primarily damaged or weakened by seismic waves generated during mainshocks, and such damage generally cannot be repaired immediately after the main event. As a result, subsequent aftershocks may enhance damage or even trigger collapse (Figure 1.1), despite receiving comparatively less attention within conventional performance-based earthquake engineering frameworks (Iervolino et al., 2020). PSHA commonly incorporates GMMs, which are calibrated using datasets that include a combination of mainshock and aftershock ground-motion recordings. However, this practice introduces an inconsistency, since the seismic sources represented in PSHA forecasts generally account only for mainshocks. Moreover, GMMs inherently capture the spatiotemporal variability of ground motions associated with aftershock sequences, which can strongly influence

hazard estimates, particularly at low probabilities of exceedance that are critical for engineering design and risk assessment (Bommer & Abrahamson, 2006; Cotton et al., 2013). Therefore, understanding the origin of spatiotemporal variability in ground motion in a seismic sequence is of significant interest for seismic hazard and structural design.

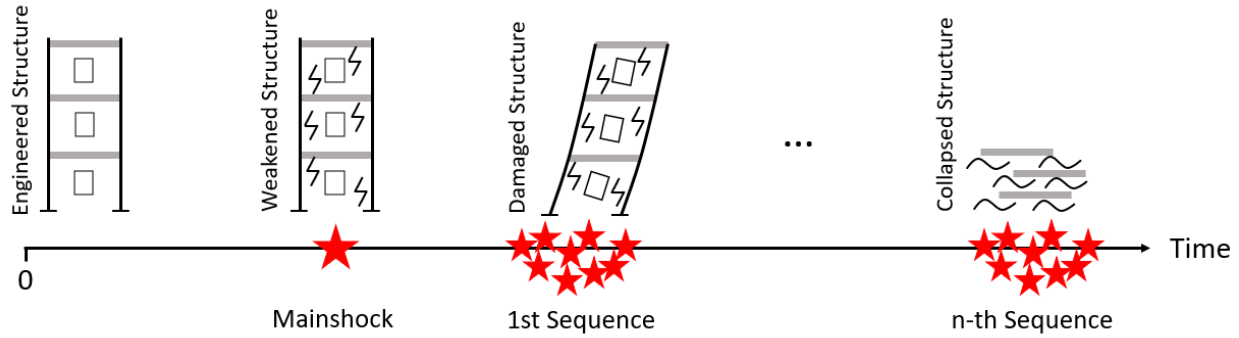

Figure 1.1. Damage accumulation for an engineered structure subjected to a mainshock and aftershock sequences.

GMMs are generally unable to reliably predict ground-motion levels in the near field (e.g., at distances shorter than 10 km) (Lanzano et al., 2019), primarily because available strong-motion datasets contain insufficient observations at such close distances to calibrate these models adequately (Chiou et al., 2008; Francesca Pacor et al., 2018). One way to fill this gap is to use physics-based simulation methods to generate ground-motion amplitudes in the near field. These approaches require a reliable description of the earthquake source, which can be obtained through high-quality and sufficiently dense observations using so-called inversion techniques. Inversion methods allow us to reconstruct key properties of the rupture process, including the spatial and temporal evolution of slip and rupture velocity, from seismic and geodetic data. By doing so, they provide insight into the complexity of rupture dynamics during individual earthquakes and help identify the physical mechanisms

that control rupture propagation and the resulting slip distribution on the fault plane (Boatwright & Cocco, 1996; Johnson, 2006; Kaneko et al., 2010). When combined with physics-based wave-propagation models, these source characterizations enable more realistic simulations of near-field ground motions, offering a pathway to improve hazard assessments in regions where empirical GMMs are poorly constrained (Goulet et al., 2015; Causse et al., 2021).

1.2. Ground Motion Models (GMMs) and Ground Motion Variability

1.2.1. Parametric and Non-Parametric GMMs

Parametric GMMs (PR-GMMs) are empirical relationships that statistically model observed ground-motion amplitude (GMA) as a function of earthquake magnitude (M), source-to-site distance (R), and site parameters (V_{S30} or site classification). GMA typically includes Peak Ground Acceleration (PGA), Peak Ground Velocity (PGV), Pseudo-Spectral Acceleration (PSA), or acceleration Fourier Amplitude Spectral (FAS). In a simplified form, the mathematical form of PR-GMMs can be expressed as:

$$G(\boldsymbol{M}, R, \Theta) = G_e(\boldsymbol{M}) + G_p(R) + G_s(\Theta) + \Delta B + \Delta S2S + E, \quad (1.1)$$

where $G(\boldsymbol{M}, R, \Theta) = ln\,(GMA)$ and $G_e(\boldsymbol{M})$ is the source term and can be expressed as:

$$G_e(\boldsymbol{M}) = c_1 + c_2.\boldsymbol{M} + c_3.\boldsymbol{M^2}, \quad (1.2)$$

$G_p(R)$ as the path and attenuation term is written as:

$$G_p(R) = c_4.ln(R) + c_5.R, \quad (1.3)$$

and $G_s(\Theta)$ describes the site term and can be expressed using soil class or average shear-wave velocity at 30 m uppermost (V_{S30}):

$$G_s(\Theta) \propto (Soil\ class\ or\ V_{S30}), \quad (1.4)$$

$c_i (i = 1, \ldots, 5)$ are regression coefficients; ΔB and $\Delta S2S$ represent between-event (event-to-event) and site-to-site residuals, respectively, which are known as random-effect terms. E denotes the left-over record-to-record residuals of seismic processes not captured by the model. The terms associated with c_4 and c_5 account for geometrical spreading and anelastic attenuation, respectively. PR-GMMs are commonly calibrated using a linear mixed-effects regression approach (Bates et al., 2015). More complex PR-GMMs (e.g., Bommer & Abrahamson, 2006; Chiou et al., 2008; Boore et al., 2014; Campbell & Bozorgnia, 2014; N. A. Abrahamson et al., 2014; Abrahamson et al., 2016) incorporate additional predictive variables such as faulting mechanisms, tectonic regimes, regional attenuation characteristics, and basin effects. These models are calibrated against thousands of high-quality recordings from global strong-motion networks developed under, e.g., the NGA-West2 project. PR-GMMs rely on a relatively simple linear mixed-effects structure, which may produce systematic misfits as a function of the input variables when the interaction between variables is nonlinear (Bishop, 2006). This limitation highlights the need for more flexible modeling approaches that can capture nonlinear dependencies and interactions, ultimately improving predictive performance and reducing epistemic uncertainty in ground-motion estimates.

One solution for capturing nonlinear interactions is to use non-parametric machine learning methods. These approaches provide flexible, data-driven ways to model complex relationships without assuming a fixed functional form (such as Eq. 1.1) between predictor variables and GMA. Unlike PR-GMMs, non-parametric models allow the data itself to determine the model structure. This flexibility makes them powerful for capturing nonlinear patterns, variable interactions, and spatial and temporal dependencies, especially when the underlying process is difficult to express analytically. However, because they adapt closely to the training data, they often require larger datasets and careful hyperparameter tuning to avoid overfitting.

Among the available machine-learning approaches, the Random Forest Regression Algorithm (e.g., Breiman, 2001; Bishop, 2006; Hastie et al., 2009;

Fernandez-Delgado et al., 2014; Louppe, 2014) has shown strong performance, particularly because of its robustness, ability to model nonlinear dependencies, and built-in measures of variable importance. Random Forests have been successfully applied to earthquake ground-motion modeling in several recent studies (e.g., Trugman & Shearer, 2018; Khosravikia & Clayton, 2021; Alidadi & Pezeshk, 2024). Random Forest regression is a supervised learning algorithm that employs an ensemble learning approach, wherein multiple decision tree regressors (Figure 1.2) are trained independently on the same dataset. The outputs of these trees are then averaged to produce a more robust and accurate prediction of ground motion amplitude (Bishop, 2006; Hastie et al., 2009). A key feature of Random Forest is bootstrapping, whereby each decision tree is trained on a random subset of the training data, sampled with replacement. This process, which is repeated over a specified number of trees and a defined number of predictor variables (features), introduces diversity among the trees, reduces overfitting, and enhances the model's generalization performance (Breiman, 2001). One of the main challenges in using Random Forest regression is avoiding overfitting, which occurs when the model learns the training data, including noise and random fluctuations, too well. Overfitting reduces the model's ability to generalize to new, unseen data. It can result from excessive model complexity, poor-quality data, or suboptimal parameter choices.

Random Forest GMMs (RF-GMMs) model the observed ground motion amplitude (GMA) as a nonparametric function (G^{RF}) of input variables and random effect terms:

$$G(\boldsymbol{M}, R, \Theta) = \frac{1}{B}\sum_{b=1}^{B} G_b^{RF}\left[\boldsymbol{M} + ln(R) + \Theta + \cdots\right] + \Delta B + \Delta S2S + E, \tag{1.5}$$

where B denotes the number of randomized regression trees used in the ensemble.

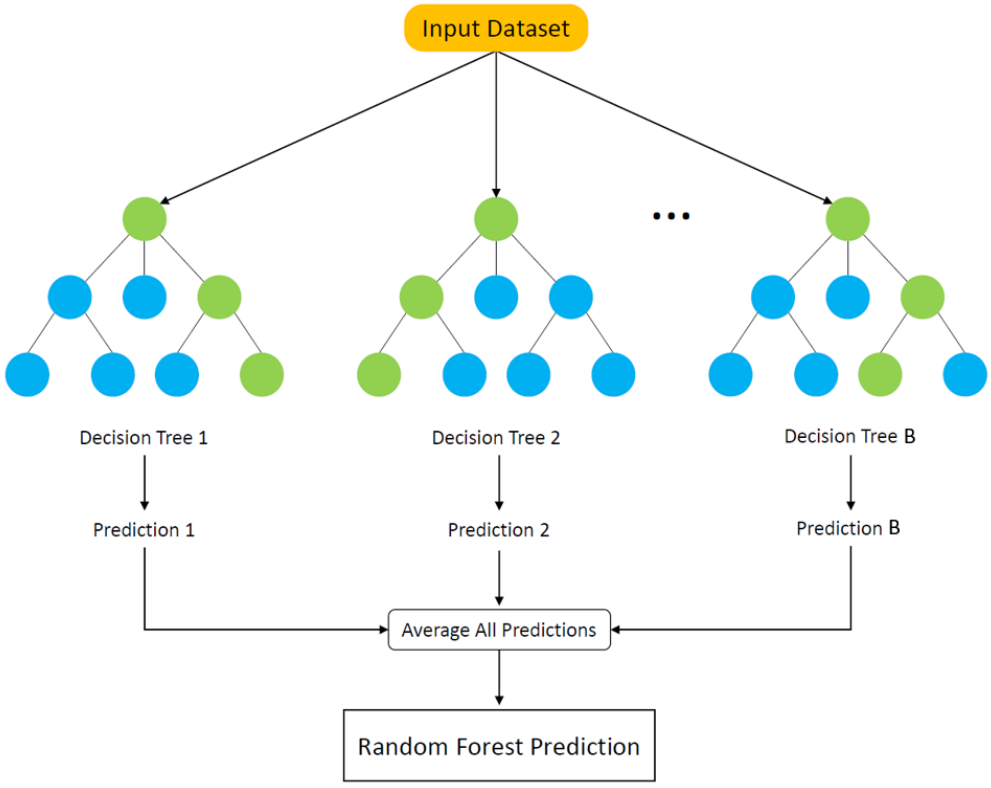

Figure 1.2. Schematic illustration of the Random Forest regression algorithm. The input dataset is used to train an ensemble of decision trees (1, …, B). Each tree produces an individual prediction of the ground-motion intensity measure, and the final Random Forest prediction is obtained by averaging the outputs of all trees.

1.2.2. Variability of Ground-Motions

Regardless of whether PR-GMMs or RF-GMMs are used, the performance of any ground-motion model is typically evaluated by examining its ability to reduce the total ground-motion variability referred to as the aleatory uncertainty (σ). GMMs are typically developed using records from multiple stations across different earthquakes, thereby combining various source, path, and site responses. In other words, the variability in ground motion due to differences in source, path, and site response is typically considered as aleatory. On the contrary, the epistemic uncertainty refers to the uncertainty in the model caused by limited data and

knowledge (e.g., uncertainty in magnitude estimates or site characterization), which can theoretically be reduced to zero. This simplifying assumption, which effectively substitutes spatial variability for temporal randomness, is commonly referred to as the *ergodic* model (Anderson & Brune, 1999). In other words, ergodic assumption treats the variability of ground motions across different locations as if it represents the variability of ground motions at a single location over time.

Following Eqs. 1.1 and 1.5, and under the ergodic assumption, the event-to-event variability of ground motions unexplained by the source term is quantified as the between-event random distribution $\Delta B = N(0, \tau^2)$, the site-to-site variability unexplained by path propagation effect and site condition terms as the between-site random effect distribution $\Delta S2S = N(0, \Phi_{S2S}^2)$, and the left-over record-to-record residual variabilities of seismic processes unexplained by $G(\boldsymbol{M}, R, \Theta)$ are quantified in the distribution $\mathrm{E} = N(0, \Phi^2)$. The aleatory variability is expressed as:

$$\sigma = \sqrt{\tau^2 + \Phi_{S2S}^2 + \Phi^2}, \tag{1.6}$$

In classical PSHA, the annual probability of exceedance of a ground-motion level ($Y > y$) is computed by integrating all possible earthquakes, distances, and magnitudes. The exceedance probability for a given earthquake is typically modeled as lognormally distributed $ln\, Y \sim N(\ln \hat{Y}, \sigma)$. $\hat{Y}$ is the median prediction from GMMs, and σ is the total aleatory uncertainty. At long return periods, hazard estimates are strongly influenced by σ; consequently, large values of σ can lead to extreme ground motions even for moderate-sized earthquakes. Removing the ergodic assumption in seismic hazard analysis results in a substantial reduction in aleatory variability. *Non-ergodic* GMMs (Caramenti et al., 2022; Lavrentiadis & Abrahamson, 2023) do not assume that spatial variability can substitute for temporal variability. Instead, they recognize that each site and each source-to-site path has unique and repeatable characteristics that systematically affect ground-motion. By explicitly accounting for site-specific and path-specific effects, non-ergodic models reduce the aleatory

uncertainty in seismic hazard analysis. However, implementing the fully non-ergodic assumption is more challenging, as it requires epistemic uncertainty to be explicitly modeled for each site–path combination, which demands dense datasets with repeated recordings from the same earthquakes and stations. Moreover, non-ergodic models can realistically reduce only the portion of aleatory variability associated with site and path effects (Al Atik et al., 2010). Source effects remain only partially predictable, such that the between-event variability (τ) cannot be fully eliminated. Consequently, understanding the physical origin and behavior of between-event variability is of fundamental importance for both seismic hazard assessment and structural design, which is the interest of this study. It will be investigated in detail in Chapters 2 and 3.

As illustrated in Figure 1.3, the between-event residual (δB_e) represents the average deviation of the observed ground motion for an individual earthquake from the population median predicted by the ground-motion model. Theoretically, the variability of ground-motion is described in terms of between-event variability, which reflects the variability in the rupture process (e.g., Atkinson, 1990; Al Atik et al., 2010; Baltay & Hanks, 2014; Causse & Song, 2015). Compared to low frequencies, the between-event variability is more pronounced at high frequencies (see Chapter 2 for more details). High-frequency ground-motion correlates well with the corner frequency, which can be directly linked to stress-drop (see Section 1.2.3). Consequently, the between-event variability of high-frequency ground motion is primarily governed by stress-drop variability (e.g., Hanks & McGuire, 1981; Cotton et al., 2013; Oth et al., 2017; Trugman & Shearer, 2018). For instance, Cotton et al. 2013 demonstrated a close relationship between the variability of PGA and dynamic stress-drop, expressed as $\sigma_{\ln(\Delta\tau)} = (6/5)\,\sigma_{\ln(\mathrm{PGA})}$. This naturally raises the question of whether incorporating event-specific stress-drop into GMMs could reduce ground-motion variability. While this is theoretically possible, stress-drop estimation remains highly challenging and subject to substantial uncertainty. Moreover, it is unclear whether stress-drop alone controls this variability or whether other physical

processes, such as attenuation, also play a significant role. Chapters 2 and 3 are devoted to addressing these questions.

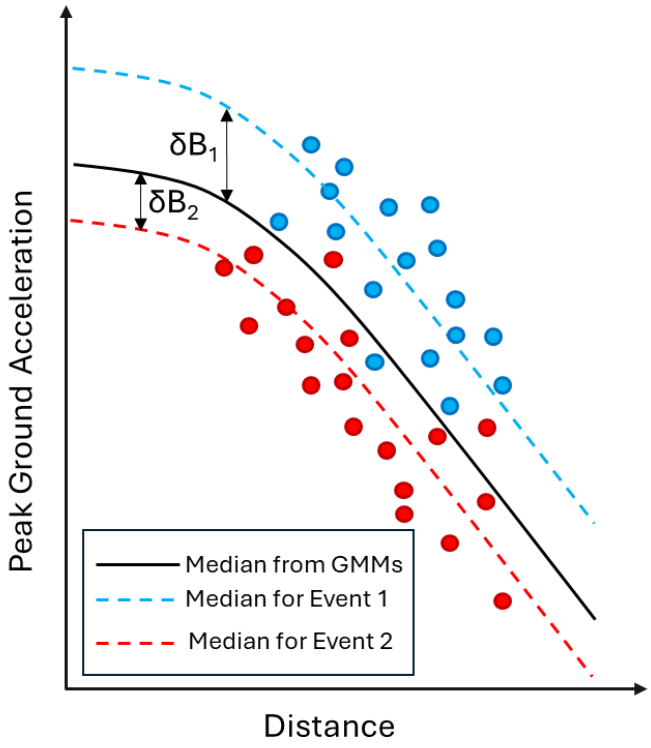

Figure 1.3. A schematic showing the definition of the between-event residual (δB_e). Blue and red dots represent the data for event 1 and event 2, respectively, with the same magnitude. The dashed blue and red curves show the model fitted to the data of event 1 and event 2, respectively. The black curve denotes the median predicted from GMMs.

1.2.3. Stress-Drop

Stress-drop is a fundamental parameter in earthquake source physics that quantifies the decrease in shear stress on a fault resulting from seismic rupture. In the simplest conceptual model of faulting, rupture initiates at a localized nucleation point and propagates across the fault surface as long as the available shear stress exceeds the frictional resistance. Rupture continues until the driving stress is

sufficiently reduced and the remaining unruptured fault area exhibits frictional resistance high enough to arrest further propagation. Therefore, it represents the difference between the average stress acting on the fault immediately before and after an earthquake, and provides a measure of the efficiency with which accumulated tectonic stress is released during slip (e.g., Aki, 1966; Kanamori & Anderson, 1975; McGuire, 2004). Because stress-drop cannot be observed or measured directly, it is typically inferred from recorded ground motion by combining estimates of seismic moment with characteristic source dimensions or spectral corner frequency, within the framework of simple rupture models, such as the circular crack model.

Observed ground-motion time series in the time domain *A(t)* can be described as a convolution of the slip process on the fault surface, referred to as the source time function *e(t)*, Green's functions of propagation media *p(t)*, local site response *s(t)*, and the instrumental response *I(t)*:

$$A(t) = e(t) * p(t) * s(t) * I(t), \tag{1.7}$$

In the frequency domain, the ground-motion Fourier amplitudes, used in the seismological models (e.g., Brune, 1970; Hanks & McGuire, 1981; Boore, 1983; Boore & Atkinson, 1987; Atkinson & Silva, 1997), can be expressed as a product of the mentioned parameters:

$$A(f) = e(f).p(f).s(f).I(f), \tag{1.8}$$

To compute stress-drop released during faulting, the observed time domain seismograms *A(t)* are first transformed into the frequency domain to obtain acceleration or displacement Fourier amplitude spectra *A(f)*. Then, the Fourier spectra are corrected for path propagation *p(f)* and site effects *s(f)*, to isolate the source amplitude spectrum *e(f)*. The source spectrum for displacement is subsequently modeled using the Brune source model (Brune, 1970), which is parameterized as a function of moment (M_0) and the spectral corner frequency (f_c):

$$e(f) = \frac{CM_0}{1 + (\frac{f}{f_c})^2}, \tag{1.9}$$

where C is a scaling factor, and f is the frequency. The corresponding Fourier amplitude spectrum for acceleration is represented accordingly by:

$$e(f) = \frac{CM_0(2\pi f_c)^2}{1 + (\frac{f_c}{f})^2}, \tag{1.10}$$

The seismic moment is often expressed in terms of the moment magnitude $\boldsymbol{M}$ (Hanks & Kanamori, 1979):

$$\boldsymbol{M} = \frac{2}{3} log M_0 - 10.7, \tag{1.11}$$

The source model described by Equations 1.9 and 1.10 is commonly referred to as the "ω^2 source model". The displacement amplitude is controlled by M_0 at low frequencies, and the acceleration amplitude is controlled by $M_0 f_c^2$ at high frequencies. The f_c is inversely proportional to the required time to rupture the fault, causing a permanent slip (Beresnev & Atkinson, 1997). Therefore, a short rupture duration leads to a higher f_c, which corresponds to higher frequency content in the resulting seismic shear waves. Also, the corner frequency can be computed from the rupture rise-time (T_{rise}) (Beresnev & Atkinson, 1997):

$$f_c = \frac{1}{2\pi\tau} = \frac{1.68}{2\pi T_{rise}} = \frac{0.27}{T_{rise}}, \tag{1.12}$$

where τ is the rise-time and $T_{rise} = 1.68\tau$ is the duration at which the fault slip is 50% of the final slip. Assuming that the rupture propagates radially from the center of a circular fault surface (circular crack model), with a uniform rupture velocity V_r, T_{rise} can be written as:

$$T_{rise} = \frac{\frac{r}{2}}{V_r}, \tag{1.13}$$

by substituting Eq. 1.13 into Eq. 1.12, the corner frequency can be approximated by the expression:

$$f_c = \frac{0.27V_r}{\frac{r}{2}}, \tag{1.14}$$

Brune (1970) suggests that the rupture velocity is equal to 0.69β, in which β is the shear wave velocity of the medium. Thus, Eq. 1.14 can be rewritten as:

$$f_c = \frac{0.27(0.69\beta)}{\frac{r}{2}} = 0.37\frac{\beta}{r}, \tag{1.15}$$

The seismic moment is related to the fault rupture area A by the following well-known expression:

$$M_0 = \mu AD, \tag{1.16}$$

where μ is the coefficient of rigidity, $A = \pi r^2$, and D is the total slip caused by the rupture. From the basic principles of mechanics, D is proportional to the stress-drop $\Delta\sigma$ and the fault dimension, and inversely proportional to the coefficient of rigidity. D for a circular crack model can be written as (Kanamori & Anderson, 1975):

$$D = \frac{\left(\frac{16}{7}\pi\right) r\Delta\sigma}{\mu}, \tag{1.17}$$

by putting Eq. 1.17 into Eq.1.16, the fault radius (r) can be expressed as a function of M_0 and $\Delta\sigma$:

$$r = \left(\frac{7M_0}{16\Delta\sigma}\right)^{1/3}, \tag{1.18}$$

by substituting Eq. 1.18 into Eq. 1.15, the corner frequency can be scaled by M_0 and $\Delta\sigma$:

$$f_c = 0.49\beta\left(\frac{\Delta\sigma}{M_0}\right)^{1/3}, \tag{1.19}$$

where β is in km/s, $\Delta\sigma$ is in MPa, and M_0 is in N.m.

Although the above equations suggest that stress-drop can be computed straightforwardly, its estimation is in practice highly challenging and subject to significant systematic uncertainties, particularly for small- to moderate-sized earthquakes (e.g., Abercrombie, 2021; Calderoni & Abercrombie, 2023; Abercrombie & Baltay, 2025). The primary difficulty lies in isolating the source contribution from observed seismograms, which requires the accurate removal of path-propagation effects and site response. Despite the application of advanced methodologies, such as the Generalized Inversion Technique (Adrien Oth, 2013; Dino Bindi et al., 2020), Empirical Green's Functions (Hartzell, 1978; Hough, 1997), and Cluster-Event-Methods (Ko et al., 2012), stress-drop estimates continue to carry substantial uncertainty (Abercrombie, 2021).

Many studies attempted to estimate stress-drop by exploring abundant and high-quality seismic data across a wide magnitude range of events with different faulting styles recorded in various tectonic regimes. However, the outcomes reveal that the scaling of stress-drop with these features is still under debate. For instance, some studies suggested that earthquakes are self-similar (e.g., Aki, 1967; Abercrombie, 1995; Prieto et al., 2004), implying that stress-drop is independent of earthquake moment, whereas others reported that stress-drop decreases with a reduction in earthquake size on both regional and global scales (e.g., Kanamori et al., 1993; Malagnini et al., 2014; Bindi et al., 2020). As illustrated in Figure 1.4, Allmann & Shearer (2009) compared stress-drop estimates for subduction-interface thrust faulting systems with those for normal and strike-slip faulting systems, revealing that the latter tend to exhibit higher stress-drop values. Additionally, some studies have identified a depth dependency of stress-drop (Hardebeck & Aron, 2009; Trugman & Shearer, 2018); however, Abercrombie et al. (2021) argued that this trend might be an artifact. Even applying the various methodologies to estimate stress-drop adds further complexity to the existing controversy (Abercrombie, 2021; Shearer et al., 2019). As noted above, stress-drop variability plays a critical role in ground-

motion prediction, and unresolved uncertainties in its estimation can lead to inflated variability in predicted high-frequency ground motions.

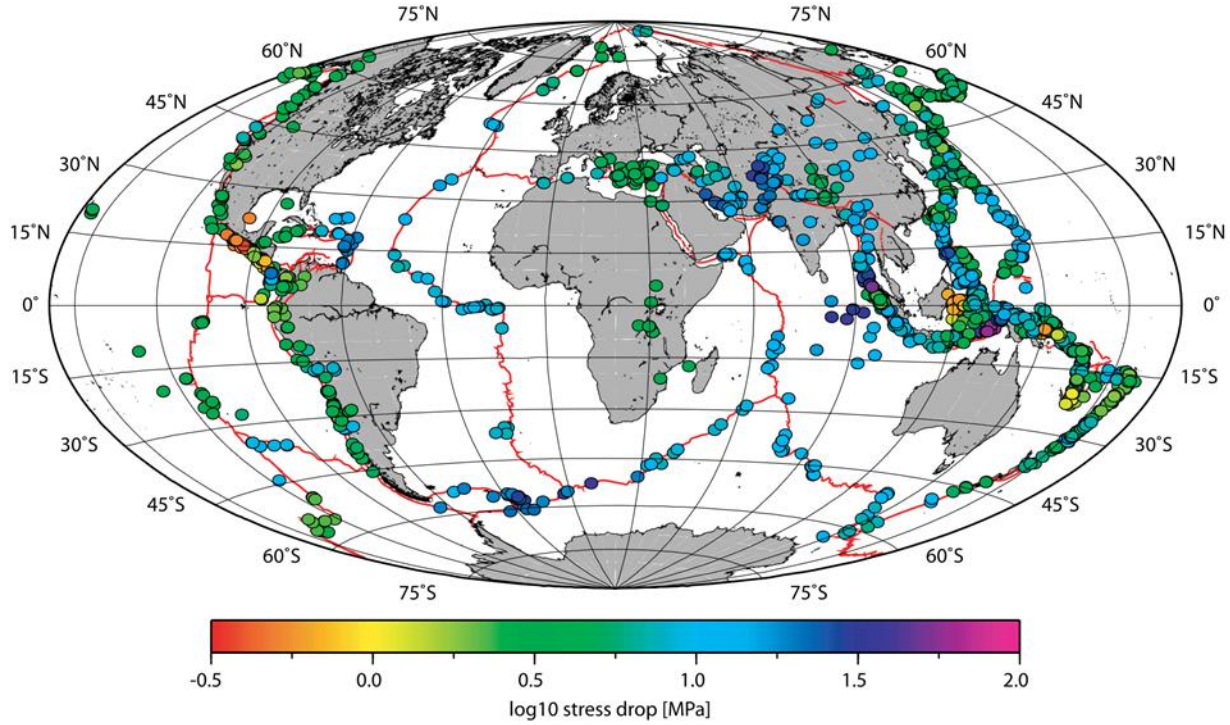

Figure 1.4. Spatial global stress-drop variations (Allmann & Shearer, 2009).

1.3. Source Rupture Imaging Using Inversion Techniques

Since direct observations of the rupture process are unavailable, we rely on seismic recordings at Earth's surface. These observations are used to construct physical and mathematical models, which enable us to infer rupture characteristics and extract information about the underlying source processes. Such modeling approaches are referred to as "source inversion techniques". Source inversion methods can be applied to different stages of the seismic cycle. During the *co-seismic* phase, inversions are used to image the spatial and temporal distribution of slip on the fault plane and to characterize rupture propagation. In the *post-seismic* phase,

inversion techniques help constrain fault relaxation processes, including afterslip and viscoelastic deformation. In the *pre-seismic* phase, similar approaches can be applied to model slow-slip events and other aseismic deformation that may precede large earthquakes. Together, these inversion-based analyses provide critical insights into earthquake mechanics and the complex interactions governing fault-system behavior.

In this study, we are exclusively interested in the co-seismic phase, for which a rich observational dataset is available. Constraining the earthquake rupture process through inversion typically involves five fundamental steps:

1. Collection of observations related to the seismic event, which may include seismological, geodetic, etc.
2. Discretization of the causative fault plane into smaller sub-faults.
3. Computation of Green's Functions ($\boldsymbol{g}$), which represents the impulse response of the medium.
4. Combining local source time function with Green's Functions based on the "representation theorem" (Aki & Richards, 2002).
5. Search for the model parameters ($\boldsymbol{m}$) that best explain the observed data ($\boldsymbol{d}$). This step constitutes the inversion problem. The parameter vector $\boldsymbol{m}$ typically includes the position of the rupture starting point (nucleation point), rise time, rupture velocity, and slip values on each sub-fault.

Given the Green's Function ($\boldsymbol{g}$), the objective is to determine the model parameter vector $\boldsymbol{m}$ that satisfies:

$$\boldsymbol{d} = \boldsymbol{g}\boldsymbol{m}, \tag{1.20}$$

A workflow combining the five steps above constitutes the "finite-fault inversion technique". Finite-fault inversion can be *static*, aiming to determine the spatial distribution of slip along the fault, or *kinematic*, in which both the spatial distribution

and the temporal evolution of the rupture process are determined. In the following sections, we briefly describe all the required steps to constrain a source rupture model, including seismological data, the representation theorem, Green's functions, and the inversion methodology.

1.3.1. Seismological Data

Earthquake-generated seismic waves are recorded by various instruments, including accelerometers, velocimeters, GPS stations, etc. In this study, only strong-motion accelerometer data are used; therefore, we provide a brief description of this type of data. Strong-motion data are beneficial for constraining high-frequency kinematic properties, even when stations are located close to the rupture fault, because their recordings do not saturate at high frequencies, even for very high-magnitude earthquakes. However, at very high frequencies (> 0.5 Hz), accelerograms become highly sensitive to the 3D complexity of the propagation medium, about which we have limited information. In the context of finite-fault inversion, analyses are typically restricted to frequencies below 0.5 Hz, where the medium's complexity plays a lesser role. In addition, accelerograms can be integrated once or twice to obtain velocity or displacement time series, which are more suitable for representing the low-frequency ground motions associated with earthquakes. But before their use in the inversion process, the data must be band-pass filtered within the frequency range of interest (e.g., 0.02–0.5 Hz).

1.3.2. Representation Theorem and Green's Functions

From the representation theorem, the displacement recorded at the Earth's surface can be expressed as the convolution of the slip-rate function with the Green's Functions:

$$u_n(\boldsymbol{r},t) = \int_S \dot{S}_i(\boldsymbol{\xi},t) * \left[c_{ijkl}(\boldsymbol{\xi}) v_j(\boldsymbol{\xi})\, G_{nk,l}(\boldsymbol{r},\boldsymbol{\xi};t)\right] dS(\boldsymbol{\xi}), \tag{1.21}$$

where u_n is the $n\text{-}th$ component of the displacement at the receiver located at position r and at time t. $\dot{S}$ and G denote the slip rate function and the Green's Functions, respectively. c is the elastic coefficient matrix and ν is the normal to the fault. The integration over S (fault surface) sums the contributions of all sub-faults. The symbol * denotes time convolution. The contribution of $c_{ijkl}.\nu_j.G_{n,k,l}$ is the $n\text{-}th$ component of the displacement produced by a unit slip in the $i\text{-}th$ direction, localized in space and time. $\dot{S}$ is the slip-rate function, which defines how slip evolves in time and is computed as the product of local slip at each sub-fault with a normalized slip velocity time function (known as the slip rate function). This slip-rate serves as the *source time function* in the convolution with the Green's functions to produce the observed displacement. Several functional forms have been proposed for it, such as boxcar (Haskell, 1964), triangle (Sato & Hirasawa, 1973), exponential (Cotton & Campillo, 1995), power law (Liu & Archuleta, 2004), and Yoffe (Nielsen & Madariaga, 2003; Piatanesi et al., 2004; Tinti et al., 2005) functions, among many others.

According to the representation theorem, reliable determination of source parameters from seismograms requires accurate modeling of wave propagation along the path in the frequency band used to resolve the rupture history. A complete description of the propagation medium involves knowledge of the spatial distribution of P- and S-wave velocities, density, and anelastic attenuation parameters for the target region. In most cases, the best available model of the propagation medium is one-dimensional (1D), which can satisfactorily represent the low-frequency propagation of seismic waves up to the Earth's surface. However, 1D models may be inadequate for describing wave propagation in regions dominated by three-dimensional (3D) effects, which perturb seismic-wave amplitudes and phases due to the presence of sedimentary basins, strong lateral heterogeneities, and steep topography (e.g., Hartzell, 1989; Graves & Wald, 2001; Gallovič et al., 2015). Because true velocity structures are not fully known, the velocity models used in wave-propagation modeling inevitably contain uncertainties, which strongly affect Green's function computations. Any inaccuracies in the Green's functions propagate into

uncertainties in the inferred rupture model and source parameter estimates (e.g., Graves & Wald, 2001; Liu & Archuleta, 2004; Razafindrakoto & Mai, 2014; Hallo & Gallovič, 2016; Spudich et al., 2019).

Several approaches are commonly used to compute Green's functions in axisymmetric media, providing the viscoelastic dynamic response of a one-dimensional Earth structure. For horizontally layered media, the reflectivity method (Kennett & Kerry, 1979; Muller, 1985) solves the wave equation in the frequency–wavenumber domain using propagator matrix techniques. This method can be combined with discrete wavenumber decomposition to compute Green's functions (Bouchon, 1981). This approach is implemented in AXITRA (Cotton & Coutant, 1997). A similar framework is employed in the frequency–wavenumber integration (FK) method developed by Zhu & Rivera (2002). For more complex geological settings, Green's functions can be computed using fully 3D velocity models. Such approaches include finite-difference methods (Graves, 1996; Moczo et al., 1999) and spectral-element methods (Komatitsch & Vilotte, 1998a; Chaljub et al., 2007).

Assuming linear wave propagation, the Green's Functions may be replaced by records of small earthquakes (foreshocks and aftershocks) occurring on the same fault with the same focal mechanism, commonly referred to as "Empirical Green's Functions" (EGFs) (Hartzell, 1978; Irikura, 1983; Hough, 1997). For a large earthquake, a database of EGFs could be represented by the records of the aftershocks following the main event. However, before using these small-event waveforms as Green's functions, it is necessary to correct them for source effects to isolate the effects of wave propagation and site response. Green's Functions are the impulse response of the medium to a point source dislocation with unit seismic moment. Also, their spectra are not flat at frequencies higher than their corner frequency, and they still have their own source signature. Therefore, they must be normalized for seismic moment and corner frequency using a source model, such as Brune's source model (Brune, 1970) as expressed in Eq. 1.5. This procedure effectively

removes the small-event source contribution, leaving an empirical approximation of the medium's Green's function.

Because EGFs accurately capture propagation effects, even at high frequencies, their use can, in principle, broaden the frequency band over which seismic source processes are investigated. However, several limitations restrict their applicability and must be carefully considered when EGFs are used in source inversion. In general, EGFs must be recorded at the same stations as the mainshock. Mainshocks are typically recorded by strong-motion (accelerometric) networks, which often lack the sensitivity to record small events with comparable accuracy. Ambient noise frequently contaminates the low-frequency band of small-event recordings due to limitations in instrumental sensitivity, instrumental noise, and dynamic range. Consequently, improving the quality of aftershock records requires strong-motion stations to be equipped with broadband sensors. Another limitation is that EGFs may not uniformly sample the fault plane. Aftershocks tend to occur in fault regions that did not experience significant slip during the mainshock. In areas of large coseismic slip, stress is typically reduced to dynamic levels during rupture, making repeated slip on the same patch unlikely (Day et al., 1998; Johnson & Nadeau, 2002; Toda et al., 2012). As a result, the number and spatial distribution of available EGFs may be suboptimal for accurately retrieving mainshock rupture details. Therefore, a specific interpolation algorithm is required to resample EGFs across the fault plane, which is discussed in Chapter 5.

1.3.3. Inversion

This section presents a summary of inverse problem theory based on Tarantola (2005). Eq. 1.20 formulates the inverse problem, in which the data $\boldsymbol{d}$ and the Green's functions $\boldsymbol{g}$ are known, whereas the parameter vector $\boldsymbol{m}$ is unknown. The goal is to solve this equation to estimate the rupture parameters encapsulated in $\boldsymbol{m}$. In practice, no predicted model $\boldsymbol{m}$ can perfectly reproduce the observed data $\boldsymbol{d}$ for two main reasons. First, the data are affected by measurement uncertainties and

limitations of the forward model. Second, although the inverse problem is often *overdetermined*, meaning the number of data points exceeds the number of unknowns. Furthermore, since the inverted seismological data exhibits a certain degree of spatial and temporal correlation, the effective rank of matrix **G** (**G** is a matrix form of $\boldsymbol{g}$) is generally smaller than the number of parameters, making the inverse problem *underdetermined*. Consequently, Eq. 1.20 typically does not admit a unique solution: multiple parameter vectors $\boldsymbol{m}$ can fit the data $\boldsymbol{d}$ within acceptable error bounds. Solving this inverse problem is therefore nontrivial, and a wide range of methods have been developed to address it.

In the case of static inversions, where the goal is to determine the spatial distribution of the co-seismic slip on the fault without considering its temporal complexity, Eq. 1.20 relates a data vector with a dimension of n_d (the number of observations) to a model vector with a dimension of n_m (the number of model parameters). When $n_d = n_m$, the matrix $\boldsymbol{G}$ has a square shape. If the rank of $\boldsymbol{G}$ is equal to n_m, $\boldsymbol{G}$ is invertible, and the solution of the problem becomes straightforward:

$$\boldsymbol{m} = \boldsymbol{G^{-1}d}, \tag{1.21}$$

Unfortunately, this ideal case never happens because, as mentioned earlier, both data and Green's Functions contain errors. In practice, $n_d \neq n_m$ (most of the time the problem is overdetermined $n_d > n_m$) and in some cases, size $\boldsymbol{G} < n_m$ (the problem is almost always underdetermined). Therefore, Eq. 1.21 is generally solved in the sense of least squares, where the goal is to determine the model $\boldsymbol{m}$ that minimizes the misfit between the observed and the synthetic data (ϕ^2) :

$$\phi^2 = \|\boldsymbol{d} - \boldsymbol{Gm}\| = \sum_{i=1}^{n_d} \left(\boldsymbol{d_i} - \sum_{j=1}^{n_m} \boldsymbol{G_{ij} m_j} \right)^2, \tag{1.22}$$

The simplest way to find the minimum of the misfit is to compute the derivative of the equation with respect to the model parameter $\boldsymbol{m}$ and then identify the model $\boldsymbol{m}$ for which the derivative equals zero:

$$\frac{\partial \phi^2}{\partial m_k} = 2\phi \frac{\partial \phi}{\partial m_k} = -2 \sum_{u=1}^{n_d} \left(\boldsymbol{d_i} - \sum_{j=1}^{n_m} \boldsymbol{G_{ij} m_j} \right) \boldsymbol{G_{ik}} = 0, \tag{1.23}$$

By re-arranging the terms, $\boldsymbol{m}$ is searched as follows:

$$\sum_{\boldsymbol{i=1}}^{\boldsymbol{n_d}} \boldsymbol{d_i G_{ik}} = \sum_{\boldsymbol{i=1}}^{\boldsymbol{n_d}} \left(\sum_{\boldsymbol{j=1}}^{\boldsymbol{n_m}} \boldsymbol{G_{ij} m_j} \right) \boldsymbol{G_{ik}}, \tag{1.24}$$

Eq. 1.24 can be written in the form of a matrix:

$$\boldsymbol{G^T d} = \boldsymbol{G^T G m}, \tag{1.25}$$

here, $\boldsymbol{G^T}$ is the transpose of the $\boldsymbol{G}$ matrix. Now, regardless of the dimensions of $\boldsymbol{G}$, $\boldsymbol{G^T G}$ is a symmetrical square matrix with dimensions of $n_m \times n_m$. In the case where the size of $\boldsymbol{G}$ is n_m, the rank of $\boldsymbol{G^T G}$ is also equal to n_m; therefore, $\boldsymbol{G^T G}$ is invertible. Finally, using Eq. 1.25, the model $\boldsymbol{m}$ can be computed as follows:

$$\boldsymbol{m} = (\boldsymbol{G^T G})^{-1} \boldsymbol{G^T d}, \tag{1.26}$$

where $\boldsymbol{(G^T G)^{-1} G^T}$ is commonly referred to as the "Generalized Inversion".

In the case of kinematic inversions, where the goal is to determine the spatial and temporal evolution of the slip distribution, parameter vector $\boldsymbol{m}$ contains extra parameters, such as the rupture initiation time of each sub-fault and the rupture velocity. The prediction of the data is no longer linearly related to the source parameters; therefore, the generalized inversion cannot be used. Consequently, it is essential to estimate the model $\boldsymbol{m}$ which minimizes the misfit, expressing the deviation of the prediction from the data in a nonlinear space:

$$\phi^2 = \|\boldsymbol{d} - \boldsymbol{g}(\boldsymbol{m})\|, \tag{1.27}$$

A first solution to Eq. 1.27 can be obtained by linearizing the equation around an initial model $\boldsymbol{m_0}$. Using Taylor expansion, $\boldsymbol{g}$ around $\boldsymbol{m_0}$ can be rewritten as follows:

$$\boldsymbol{g}(\boldsymbol{m}) = \boldsymbol{g}(\boldsymbol{m_0}) + \boldsymbol{G}(\boldsymbol{m} - \boldsymbol{m_0}), \tag{1.28}$$

here, the elements of the matrix $\boldsymbol{G}$ are the partial derivatives of the function $\boldsymbol{g}$ with respect to the source parameters, evaluated as the initial model $\boldsymbol{m_0}$:

$$\boldsymbol{G_{ij}} = \left(\frac{\partial \boldsymbol{g_i}}{\partial \boldsymbol{m_j}}\right)_{\boldsymbol{m=m_0}}, \tag{1.29}$$

By putting Eq. 1.28 into Eq. 1.27, and assuming $\boldsymbol{\Delta m = m - m_0}$, the corresponding linearized problem is expressed as:

$$\boldsymbol{G\Delta m = d - g(m_0)}, \tag{1.30}$$

the solution of Eq. 1.30 can be obtained using the generalized method:

$$\boldsymbol{\Delta m} = (\boldsymbol{G^T G})^{-1}\boldsymbol{G^T}\big(\boldsymbol{d - g(m_0)}\big), \tag{1.31}$$

The solution to this equation yields the evolution of the first perturbation, which corrects the initial model to $\boldsymbol{m_1 = m_0 + \Delta m}$ and reduces the data misfit. The model $\boldsymbol{m_1}$ is then treated as a new starting point, around which a new perturbation can be computed. This procedure is iterated until a model that satisfactorily explains the observations is obtained. However, a major limitation of this type of linearized solution is that the iterative process can become "trapped" in a local minimum (Figure 1.5), rather than converging to the global minimum, because the inverse problem is inherently nonlinear. A local minimum corresponds to a point where the objective function has a lower value than in its immediate neighborhood, even though other regions of the model space may contain points with lower misfit. In contrast, a global minimum represents the absolute lowest value of the objective function over the entire parameter space. To ensure convergence toward the global minimum of the misfit, "global optimization" and "global sampling" methods aim to explore the whole solution space, which is often nonlinear and high-dimensional.

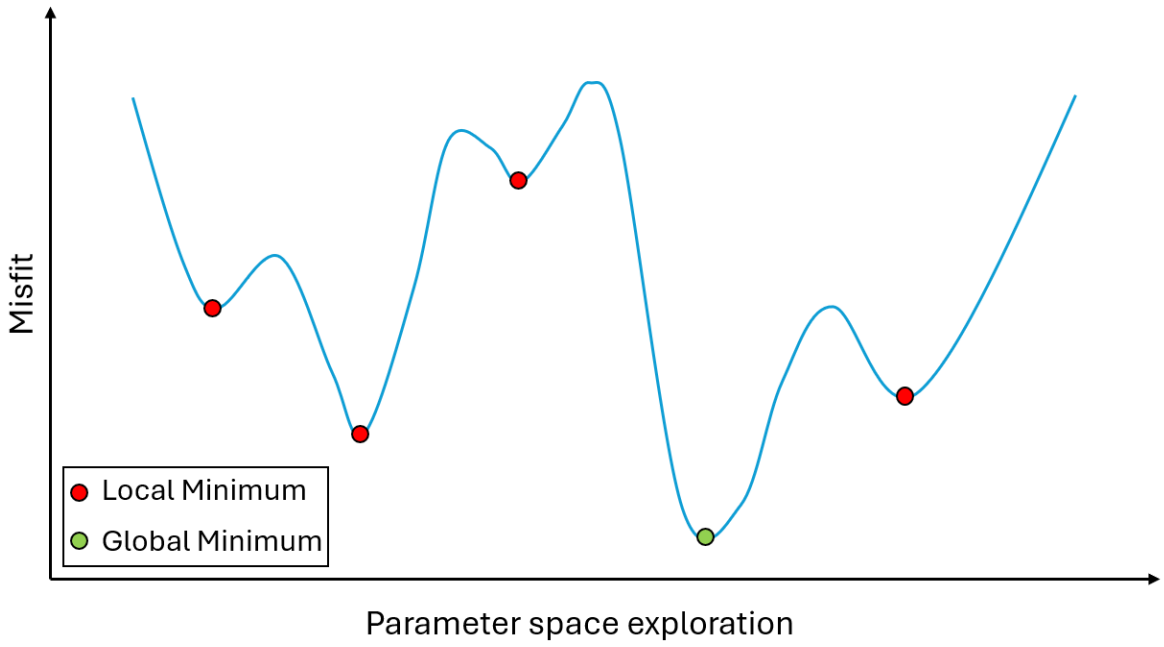

Figure 1.5. A schematic representing the evolution of misfit as a function of parameter space exploration. The red points indicate the local minima, and the green point denotes the solution, which corresponds to a global minimum.

These global optimization and sampling methods still aim to solve Eq. 1.27 by exploring a large number of candidate models $\boldsymbol{m}$, using stochastic sampling strategies that favor models with lower misfit. When the number of inverted parameters n_p is small, this can be achieved by evaluating the misfit over a large set of randomly drawn models. However, the computational complexity of such methods increases exponentially with the dimensionality of the parameter space. For instance, adding just one additional parameter (n_{p+1}) expands the search space by an extra dimension (n_p), requiring roughly an order-of-magnitude increase in computational effort to achieve comparable coverage. This rapid growth in complexity makes exhaustive exploration impractical for high-dimensional inverse problems. Instead, these algorithms are designed to efficiently explore complex misfit landscapes, allowing the identification of low-misfit (and potentially global minimum) models within a reasonable computational time, even for high-dimensional and strongly nonlinear

problems. Some of the most commonly used methods are Simulated Annealing (SA) (Kirkpatrick et al., 1983), Simulated Tempering (ST) (Marinari & Parisi, 1992; Geyer & Thompson, 1995), and Parallel Tempering (PT) (Geyer, 1991; Falcioni & Deem, 1998; Sambridge, 2014), which are shortly described in the following.

Simulated Annealing is a stochastic global optimization method inspired by the thermodynamic process in which a solid is heated and then slowly cooled, allowing its atoms to settle into a low-energy and stable configuration (Figure 1.6a). In the algorithm, this concept is translated into an iterative exploration of the model parameter space $\boldsymbol{m}$, implemented as a Markov Chain Monte Carlo (MCMC) (Metropolis & Ulam, 1949) random walker, where each proposed model update is evaluated based on the resulting change in the misfit function $\phi(\boldsymbol{m})$. Starting from an initial model $\boldsymbol{m_0}$, a new candidate model m_1 is generated through a random perturbation, and the misfit difference $\Delta\phi(\boldsymbol{m}) = \phi(\boldsymbol{m_1}) - \phi(\boldsymbol{m_0})$ is computed. If the new model reduces the misfit ($\Delta\phi < 0$), it is always accepted. If the misfit increases, the model is accepted with a probability:

$$\pi(\boldsymbol{m}, T) = \min\left(1, exp\left(-\frac{\Delta\phi}{T}\right)\right), \tag{1.32}$$

where T is the control parameter referred to as the temperature. The initial temperature, T_{max}, is chosen sufficiently high so that the tempered distribution $\pi(\boldsymbol{m}, T)$ is relatively flat, allowing frequent acceptance of higher-misfit solutions. This enables broad exploration of the parameter space, facilitates crossing of energy barriers, and helps escape local minima. As the temperature is progressively reduced according to a cooling schedule, such as $T_n = \alpha T_{n-1}$ with $\alpha < 1$, the acceptance of worse solutions becomes increasingly unlikely, and the search gradually focuses on regions of lower misfit. In the limit of sufficiently slow cooling, Simulated Annealing can theoretically converge to the global minimum; however, in practice, its performance strongly depends on the choice of the cooling schedule and the proposal step sizes.

Simulated Tempering is advised not as an optimization tool but rather for probabilistic sampling. This algorithm is similar to SA in that a temperature ladder is required, and an MCMC draws samples of m within the chain according to the conditional distribution $\pi(\boldsymbol{m}, T_i) = \exp(-\phi(\boldsymbol{m})/T_i)$. In ST, two new parameters are introduced: (1) the temperature level may either increase or decrease, (2) the decision to change the temperature level follows a stochastic scheme where proposals are made at random and accepted and rejected according to the Metropolis-Hastings rule used in an MCMC random walker (Sambridge, 2014), which is shown in Figure 1.6b. At points along the Markov chains, a jump is proposed between temperature T_i and T_j and accepted with probability:

$$\alpha(i,j) = min\left(1, \frac{p(\boldsymbol{m}|\boldsymbol{d})^{1/T_j}\, c(T_i)\, q(i|j)}{p(\boldsymbol{m}|\boldsymbol{d})^{1/T_i}\, c(T_j)\, q(j|i)}\right), \tag{1.33}$$

where $p(m|d)$ is the unnormalized a posteriori PDF in the concept of the Bayesian theorem (see section 1.3.4 for details); $c(T)$ is temperature weight controlling the frequency of visits to each temperature level. $q(i|j)$ is the probability of proposing a move from temperature level i to j. By intermittently visiting higher temperatures, the algorithm enables transitions across energy barriers and escape from local minima, while repeated returns to lower temperatures allow detailed sampling of high-probability regions.

Parallel Tempering extends ST by running multiple chains in parallel, each at a fixed temperature, rather than a single chain that moves through temperatures (Figures 1.6c and 1.6d). Chains periodically propose swaps of model states between temperatures, which are accepted using a Metropolis-Hastings criterion similar to ST. This structure allows high-temperature chains to explore broadly and cross energy barriers, while low-temperature chains refine promising solutions. Compared to ST, PT often achieves faster convergence and more efficient exploration of multimodal posteriors, making it particularly effective for complex, high-dimensional

inverse problems. Since in this study the Parallel Tempering algorithm is used, more details about this approach will be presented in Chapter 4.

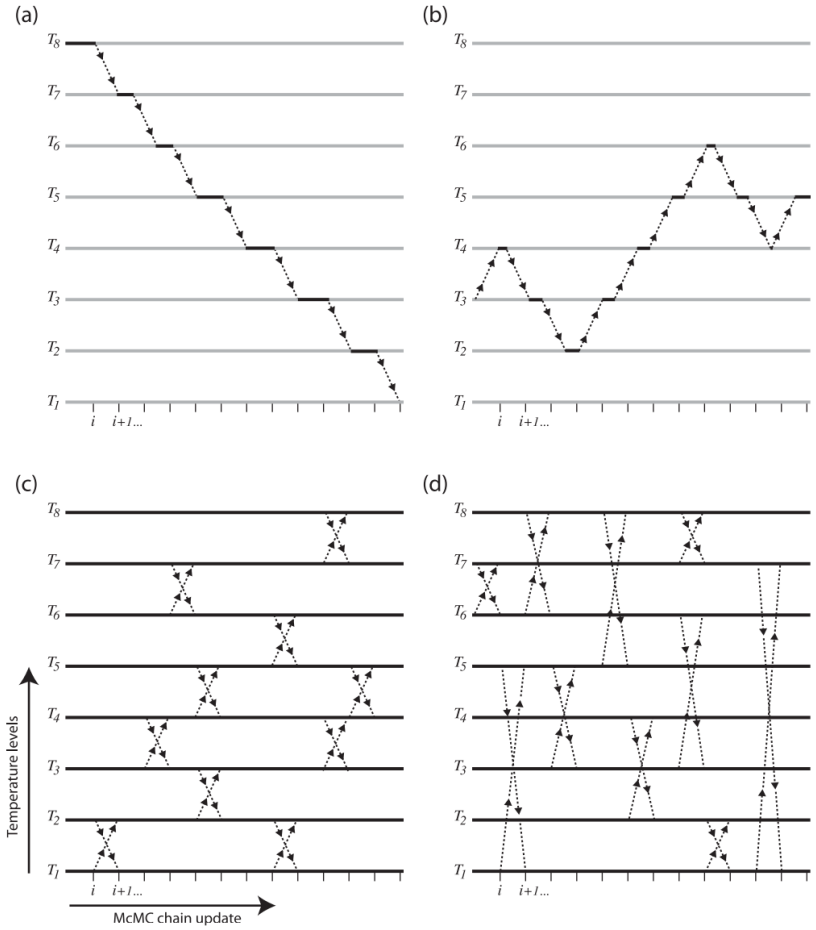

Figure 1.6. Schematic illustration of various tempered-based algorithms. Each horizontal line shows a Markov chain random walker at a different temperature ($T_1 < T_2 < \ldots < T_8$). A standard MCMC update of variables is shown as a horizontal step along a black line, whereas a temperature change is represented by a vertical jump between temperature levels, indicated by dashed lines. **(a)** Simulated Annealing algorithm, in which the temperature of a single walker is steadily reduced, **(b)** Simulated Tempering, where the temperature of a single walker can increase and decrease, **(c)** Standard Parallel Tempering algorithm applied to eight walkers (chains), with random swap between neighboring temperatures, **(d)** Parallel Tempering used in this study with randomized swap between any pairs of temperature levels (after Sambridge (2014)).

An important distinction between these approaches concerns the nature of their outputs. Simulated Annealing is fundamentally an optimization method and is therefore designed to identify a single best-fitting model, corresponding to the global minimum of the misfit (or equivalently, the maximum a posteriori estimate). In contrast, Simulated Tempering and Parallel Tempering are Bayesian sampling methods that aim to draw samples from tempered versions of the posterior probability distribution. As a result, ST and PT provide not only one optimal model but also an ensemble of acceptable solutions, allowing the exploration of model uncertainties, trade-offs, and potential multimodality in the posterior. This makes tempering-based methods particularly valuable for nonlinear and high-dimensional inverse problems, where multiple competing models may fit the data comparably well.

1.3.4. The Bayesian Framework

Bayes' theorem is straightforward to derive for discrete probabilities. In basic statistics, the probabilities of events A and B occurring are denoted by $P(A)$ and $P(B)$, respectively. The conditional probability that event A occurs given that event B has occurred is $P(A|B)$. The probability that both events occur simultaneously is $P(A \cap B)$, referred to as the joint probability of A and B. This joint probability can be expressed as the product of the probability of one event occurring and the conditional probability of the other event occurring given that the first event has occurred:

$$P(A \cap B) = P(A|B)P(B) = P(B|A)P(A), \tag{1.34}$$

therefore, the conditional probabilities can be expressed as follows:

$$P(A|B) = \frac{P(B|A)P(A)}{P(B)}, \tag{1.35}$$

For two continuous random variables X and Y, Bayes' theorem may be derived as:

$$P(x|Y = y) = \frac{P(y|X = x)P(x)}{\int P(y|X = x)P(x)dx}, \tag{1.36}$$

The denominator is known as the evidence, and it is not necessary and often impossible to compute. Therefore, Eq. 1.36 can be rewritten simply as:

$$P(x|y) \propto P(y|x)P(x), \tag{1.37}$$

Applied to the inverse problem, this equation is expressed as:

$$P(\boldsymbol{m}|\boldsymbol{d}) \propto P(\boldsymbol{d}|\boldsymbol{m})P(\boldsymbol{m}), \tag{1.38}$$

where $P(\boldsymbol{m}|\boldsymbol{d})$ is the posterior distribution, $P(\boldsymbol{d}|\boldsymbol{m})$ represents the likelihood, and $P(\boldsymbol{m})$ is prior distribution. This equation states that the probability density function (PDF) of a model $\boldsymbol{m}$ given the observation data $\boldsymbol{d}$ is proportional to how the model $\boldsymbol{m}$ explains the observation data $\boldsymbol{d}$ (likelihood term), and how plausible the model $\boldsymbol{m}$ was before observing the data (prior term).

The Bayesian framework is completely general: it does not specify the data, the model, or the form of the probability distributions. This flexibility is its strength. No simplifying assumptions are required; the model can be linear or nonlinear, smooth or rough, positive or negative, or take any form needed. Any prior knowledge about the physics of the problem can be included through the prior distribution. As a result, the problem can be solved in a way that reflects the true nature of the model, rather than forcing it into a simplified mathematical form (S. Minson, 2010).

The **Prior** is a probability distribution that represents our knowledge or assumptions about the model parameters $\boldsymbol{m}$ before observing the data. It encodes physical constraints, information from previous studies, or reasonable bounds on parameter values, thereby helping rule out implausible solutions. As such, it plays a crucial role in stabilizing the inversion and preventing non-physical or overfit models. For example, when estimating slip on a fault using seismic data, rock mechanics, and previous studies indicate that slip must be non-negative and unlikely to exceed a few meters. This information can be encoded through a prior distribution, such as a uniform prior slip ~u(0,5m), which excludes both unphysical negative slip values and unrealistically large slip amplitudes.

The **Likelihood** quantifies how well a given model explains the observed data and is therefore determined by the output of the forward model. In earthquake source modeling, the forward model generates synthetic data that are compared with the observations. Assuming Gaussian data errors, the likelihood is commonly expressed in terms of a misfit function, such as the L2 norm:

$$P(\boldsymbol{d}|\boldsymbol{m}) \propto exp\ (-\frac{1}{2}[\boldsymbol{d}-\boldsymbol{g}(\boldsymbol{m})]^T.C_d^{-1}.[\boldsymbol{d}-\boldsymbol{g}(\boldsymbol{m})], \tag{1.39}$$

where C_d is the data covariance matrix. The likelihood strongly depends on the assumed data errors: underestimating the errors leads to overfitting and an overly peaked posterior distribution, while overestimating them results in underfitting and an excessively broad posterior. In finite-fault earthquake source modeling, data errors may arise from inaccurate fault geometry, incorrect elastic structure used to compute Green's functions, and simplifications in the source parameterization that fail to fully represent the true rupture process (S. Minson, 2010).

The Bayesian approach offers several advantages over classical optimization techniques for inverse problems. Rather than producing a single best-fitting model, the Bayesian framework yields the full posterior probability distribution, allowing uncertainties, parameter trade-offs, and non-uniqueness to be explicitly quantified. Prior information and physical constraints are naturally incorporated through prior distributions, which improves the stability of ill-posed problems. In contrast to optimization methods that may converge to local minima, Bayesian sampling explores the entire parameter space, making it more robust for complex and highly nonlinear problems such as earthquake source inversion.

2 Ground-Motion Analysis and Spatial Variability of Event Characteristics

This chapter presents both parametric and non-parametric ground-motion models (GMMs) and provides a comparative analysis of their performance to analyze ground-motion variability. In addition, key seismological parameters, including moment magnitude, stress drop, and quality factor, are estimated. The spatial variability of ground motion throughout the sequence is investigated by examining between-event residuals derived from the GMMs and relating them to variations in stress drop and quality factor. This chapter was prepared in collaboration with **Mathieu Causse** and **Sreeram Reddy Kotha**, and has been submitted to the *Journal of Geophysical Research: Solid Earth* under the title "Ground-Motion Analysis of the 2016–2017 Central Italy Sequence: Spatial Variability of Event Characteristics."

Key Points:

- Parametric and non-parametric Random Forest Ground-Motion Model predictions and variances differ significantly depending on the parametric constraints.
- Random Forest models capture a Fourier frequency-dependent nonlinear interaction of moment magnitudes and locations of events relative to recording sites.
- Spatial variability of Random Forest predictions is consistent with the spatial variability of stress-drops and coseismic quality factor.

Abstract

One parametric (PR) and two non-parametric Random Forest (RF) mixed-effects Ground-Motion Models (GMMs) are developed using a dataset of 2503 events from the 2016-2017 Central Italy seismic sequences, comprising 106,336 Fourier amplitude spectra ($0.5 < f < 25$ Hz) recorded at $R_{hypo} < 120$ km. Moment magnitude ($2.35 \leq M \leq 4.62$), stress-drop $\Delta\sigma$, and frequency-dependent quality factor $Q(f)$ are estimated for all events. The PR(***M***)- and RF(***M***)-GMMs use moment magnitude (***M***) as their sole event parameter, whereas RF(***MXYZ***) additionally incorporates event location (*XYZ*). The PR-GMM is constrained as a linear combination of parametric source and attenuation functions, while the RF-GMMs capture nonlinear interactions inherent in the data. All three models predict similar Fourier spectra for well-sampled scenarios. Although between-site and residual variances of the three models are comparable, the between-event variability of RF(***MXYZ***) is up to 80% smaller than that of PR(***M***) and RF(***M***). At $f \geq 3$Hz, the fixed-effect predictions of RF(***MXYZ***) vary strongly with *XYZ* and resemble the *XYZ* trends of between-event random-effects of PR(***M***) and RF(***M***), both governed by the *XYZ* trends of $\Delta\sigma$. In contrast, at $f < 3$Hz, the fixed-effect predictions of RF(***MXYZ***) show negligible *XYZ* dependence, but the substantial between-event variabilities of PR(***M***) and RF(***M***) are primarily controlled by *XYZ* variability of $Q(f)$. However, neither $\Delta\sigma$ nor $Q(f)$ shows *XYZ* trends that can be parametrically modelled. Therefore, a mixture of PR(***M***) and RF(***MXYZ***) GMMs would be ideal in relaxing the linear-elastic assumption, reducing aleatory variability, and improving probabilistic seismic hazard and risk assessments.

Plain Language Summary

Ground-Motion Models (GMMs) are key tools used to estimate earthquake shaking in seismic hazard and risk assessments. Traditional parametric GMMs describe shaking as a combination of earthquake size, wave travel path, and local site conditions. They are mainly developed using recordings from stations located far from

the earthquake source. However, their basic assumptions may not hold close to the source, where shaking is strongest and most complex. This limits their reliability for critical hazard situations. Non-parametric models based on Random Forest methods are more flexible and can better capture complex patterns in the data. However, because they rely less on physical assumptions, they are less reliable when predicting shaking for situations that are not well represented in the data. In this study, we compiled a large dataset of earthquake recordings from small-to-moderate events observed at near-source distances during the 2016–2017 Central Italy seismic sequence. We developed both parametric and non-parametric mixed-effects GMMs. We found that spatial variations in earthquake stress-drop and crustal attenuation strongly influence ground-motion variability in a nonlinear manner. The non-parametric models captured these complex relationships and significantly reduced the unexplained variability, better describing the observed data, although they remain less suitable for extrapolation.

2.1. Introduction

In a seismic sequence, a mainshock is often followed by a significant multitude of aftershocks. Indeed, large mainshocks are likely to generate the largest ground-motions in a seismic sequence and cause extensive damage to engineered structures, but comparably large ground-motions from subsequent aftershocks can potentially cumulate structural damage and increase the risk of catastrophic structural failure (Iervolino et al., 2020). Probabilistic Seismic Hazard and Risk Assessments (PSHA and PSRA), however, estimate the hazard and risk to engineered structures exclusively from Poissonian mainshocks. This is because the hazard integral (e.g., Cornell, 1968; McGuire, 2008) is formulated exclusively for the average stationary rates of Poissonian events in a declustered seismic catalogue. Moreover, while the seismic sources in a PSHA are modelled to forecast only Poissonian mainshocks, the Ground Motion Prediction Models (GMPMs) used to predict their ground-motion distributions at a target site are calibrated using ground-motion datasets that contain both Poissonian mainshock and non-Poissonian aftershock ground-motions. In this

sense, there is an inconsistency in the PSHA workflow regarding the treatment of mainshocks and aftershocks; that is, while seismic sources in PSHA forecast only Poissonian mainshocks, the predictions of GMPMs also reflect spatiotemporal variability of non-Poissonian aftershock ground-motions. This study is a step towards resolving this inconsistency by investigating mainshock and aftershock ground-motions.

GMPMs are typically parametric models (PR), in the sense that they are statistical models that summarise the (dependent) observations using a set of (independent) predictor parameters. These parameters define the structure of GMPMs and constrain their behaviour when extrapolating and interpolating beyond their calibration dataset. PR-GMPMs predict ground-motions at a location as Gaussian distributions $N(\mu, \sigma^2)$; with μ as the median and σ^2 as the variance. While $\mu = G(M, R, \Theta)$ is a function of event moment-magnitude $\boldsymbol{M}$ (Hanks & Kanamori, 1979), event-to-site distance R, and site parameters Θ, the observed natural variability of ground-motions not modelled into μ is contained in the apparent aleatory variability σ. A critical aspect of PR-GMPMs is the assumptions underpinning the $G(M, R, \Theta)$ structure, and about the data distribution, which are derived from the classical theory of Elastodynamics.

The fundamental solutions (or Green's functions) for problems in Elastodynamics describe the displacements and stresses caused by transient and harmonic sources in solid elastic media. These functions are useful for numerical methods and applications to problems of wave propagation in elasticity, soil dynamics, earthquake engineering, mechanical vibration, or geophysics (Kausel, 2006). The separation of variables in 1D wave propagation in elastic half-space assumptions is thus more fundamental than just in the GMPM context, which is essentially: the observed ground-motion time-series at the surface is a *convolution* of a Source Time Function (temporal evolution of seismic moment release), the Green's functions of propagation media, and the impulse response of the receiving site. In the frequency domain, the ground-motion Fourier amplitudes are a *product* of event,

path, and site-response transfer functions (Aki & Richards, 2002). For the logarithm of ground-motions, the product translates into a *sum*. Therefore, $G(M,R,\Theta)$ for a typical PR-GMPM can be structured as $G_e(M) + G_p(R) + G_s(\Theta)$; a linear combination of (separated variables) event e, path p, and site s parametric functions. This assumption is fundamental to linear regression of GMPMs and even physics-based numerical simulations. As most PR-GMPMs are regressed from ground-motion observations at predominantly far-source distances, this *simplification* of earthquake physics is not severe. However, at near-source distances critical to hazard and risk assessments, it is arguable whether these assumptions on $G(M,R,\Theta)$ structure and data distribution can be justified. If the assumptions are violated, PR-GMMs may produce misleading results in situations where the physics of the underlying data is complex or unknown, leading to a loss of flexibility compared to non-parametric approaches (Bishop, 2006).

Non-parametric models, as opposed to PR models with specific functional forms, do not impose any restrictions, allowing a greater flexibility in modelling complex relationships. However, this flexibility often comes at the expense of computational efficiency, interpretability, and extrapolation beyond the regressed dataset, the basic requirements of a GMPM in PSHA. In this regard, non-parametric models do not have an obvious role as GMPMs in a PSHA, but are quite appealing as exploratory Ground Motion Models (GMMs). In this study, our choice of non-parametric regression algorithm is the Random Forests (Breiman, 2001). Random Forests (RF) is a supervised learning algorithm that employs an ensemble learning approach, wherein multiple decision tree regressors are trained independently on the same dataset. The outputs of these trees are then averaged to produce a more robust and accurate prediction of ground-motion amplitude (e.g., Trugman & Shearer, 2018; Khosravikia & Clayton, 2021; Alidadi & Pezeshk, 2024). Particularly relevant to this study is that of Trugman & Shearer (2018), wherein RF models were established to be quite effective in capturing the strong correlation between dynamic stress-drop $\Delta\sigma$ (Brune, 1970) and Peak Ground Accelerations (PGA) of $1 \leq \boldsymbol{M} \leq 4$ events recorded at

$R \leq 100$ km in the San Francisco Bay Area. Using [$\boldsymbol{M}$, R] as the independent parameters and PGA as the dependent parameter, Trugman & Shearer (2018) reported that RF models outperformed PR models in terms of total misfit. Noting its robustness, simplicity, and recognition in ground-motion analyses, our choice of non-parametric GMM regression in this study is the Random Forests.

Trugman & Shearer (2018) suggested localizing events to partially remove the spatial variability of event characteristics, thereby reducing the σ^2 of GMPMs (e.g., Atkinson & Boore, 2006; Lin et al., 2011; Kotha et al., 2020). PR-GMPMs are generally ergodic (stationary), meaning that $\mu = G(M, R, \Theta)$ does not vary with space [XYZ] and time (T), despite evidence suggesting that ground-motion characteristics vary over space and time due to processes affecting the fault zone and the propagation medium during an earthquake sequence. Partially ergodic (e.g., Kotha et al., 2020; Kuehn et al., 2023) and non-ergodic PR-GMPMs (Caramenti et al., 2022; Lavrentiadis & Abrahamson, 2023), whose predictions vary with event, path, and site locations (or regions), do exist in the literature. Still, these PR models are derived from predominantly far-source ground-motion data and do not attempt to model complex near-source phenomena. Moreover, it is not straightforward to incorporate [XYZ] and T in PR-GMMs (or GMPMs), as their interaction with the typical [$\boldsymbol{M}$, R] parameters is not fully understood. Therefore, non-parametric RF-GMMs could help better define the shortcomings or even complement the PR-GMMs (Trugman & Shearer, 2018).

To understand and isolate the origin of spatial and temporal variability of ground-motions during a seismic sequence, we derive multiple GMMs from PGA and Acceleration Fourier amplitude spectra (FAS) (0.5 to 25 Hz) datasets of the 2016-2017 Central Italy sequence. While similar studies on non-parametric GMMs (Trugman & Shearer, 2018; Khosravikia & Clayton, 2021) focused on PGA and PGV, this study analyzes broadband Fourier spectra to provide a more comprehensive understanding of the physics captured by the GMMs. In the same vein, while studies on the physics of the central Italy sequence (Bindi et al., 2018; Picozzi et al., 2024; Bindi et al., 2025) relied on PR-GMMs that can only be structured as

$G(\boldsymbol{M}, R, \Theta) = G_e(\boldsymbol{M}) + G_p(R) + G_s(\Theta)$, we can regress RF-GMMs with additional event localization, as in $G(\boldsymbol{M}XYZ, R, \Theta)$. Alongside, for the same dataset, we estimate seismological parameters, including the seismic moment (M_0), corner frequency (f_c), dynamic stress-drop ($\Delta\sigma$), and quality factor (Q). This allows consistency between the [$\boldsymbol{M}$, R] used in the PR- and RF-GMMs and the seismological parameters [$\Delta\sigma$, Q]. By studying the median and residual behaviours of the PR- and RF-GMMs at various Fourier frequencies and evaluating them against the seismological parameters, this study aims to provide a physical interpretation of non-parametric GMMs. The subsequent sections elaborate on the different datasets, methodological choices, and inferences drawn in this study.

2.2. Dataset

In this study, we examine the 2016-2017 seismic sequence in central Italy, where numerous earthquakes were recorded with dense seismic stations. This area, situated in the central and northern Apennines, features a complex system of thrust and normal faults (Figure 2.1a). The sequence triggered by the $\boldsymbol{M}$6.0 Amatrice earthquake on 24 August 2016 and activated an 80-km-long NNW-SSE trending system of normal faults. The $\boldsymbol{M}$6.0 led to a significant increase in seismicity, peaking after the $\boldsymbol{M}$5.9 Visso earthquake on 26 October and the $\boldsymbol{M}$6.5 Norcia earthquake on 30 October (Chiaraluce et al., 2017). The mainshocks ruptured two Normal fault segments of the Vettore-Bove fault system (VBFS) in the north and of the Laga fault system (LFS) in the south, with NNW-SSE trending and SW-dipping (Pizzi et al., 2017; Scognamiglio et al., 2018).

The seismic sequence triggered several efforts to compile a comprehensive catalogue of events (Chiaraluce et al., 2017; Improta et al., 2019; Michele et al., 2020). From the detected events, we systematically analyse a subset of 2,503 earthquakes occurring between 24 August 2016 and 15 January 2018, and recorded by at least 10 stations (Figure 2.1a). The origin times of the events are sufficiently spaced (within a 60-second interval) to ensure that the attribution of peak ground-motions to a

specific event remains unambiguous. The catalogue compiled by Michele et al. (2020) is chosen, as they utilized the double difference algorithm relocation technique pioneered by Waldhauser (2000). The selected events are situated in the region extending between 42.35°N and 43.22°N in latitude and 12.40°E and 13.60°E in longitude, with moment magnitudes ranging from $2.35 \leq \boldsymbol{M} \leq 4.62$ and hypocentral depths $0 \leq Z \leq 14$ km. From the selected events, we retrieve all two-component horizontal waveforms recorded at 290 broadband and strong-motion stations (Figure 2.1a), encompassing both permanent and temporary networks. The two permanent networks are the Italian Strong Motion Network (RAN) and the Italian National Seismic Network (INSN). The former is solely equipped with accelerographs, while the latter provides velocity waveforms at most stations and acceleration waveforms at some stations near the seismic sequence area. Additionally, the Amatrice Sequences International (ASI) network (Segou et al., 2016) is a rapid deployment of a broadband temporary network activated 10 days after the Amatrice mainshock. This network has supplied high-quality near-field waveforms, significantly aiding the objectives of this study. An additional temporary network, known as the 2016 Central Italy Seismic Sequence (CentroMz), used accelerographs placed within a limited area in the southern part of the sequence.

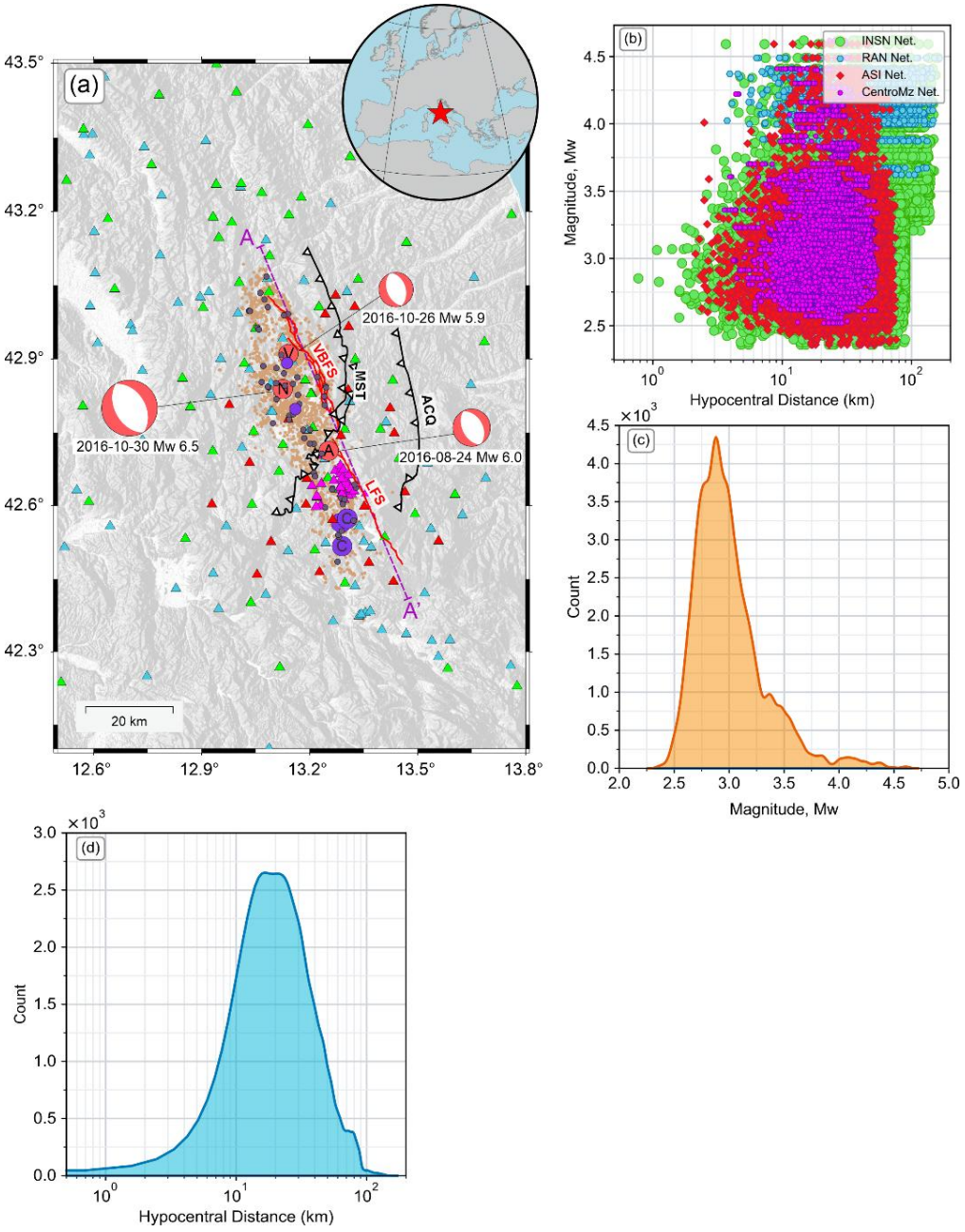

Figure 2.1. Overview of the study area, catalogue, and recording characteristics for the 2016–2017 Central Italy seismic sequence. **(a)** Map of the epicentral area. The red lines represent the two causative Normal faults of the Vettore-Bove (VBFS) and the Laga (LFS) regions. The black barbed lines indicate the thrust fronts of the Mount Sibilini Thrust (MST) and the Acquasanta Thrust (ACQ). The red circles labelled A, V, N, and C mark the epicenters of Amatrice, Visso, Norcia, and Compotosto mainshocks, respectively. The purple, dark grey, and brown circles denote the epicenters of events with ***M***5-6, ***M***4-5, and ***M*** < 4, respectively.

The triangles represent the locations of the recording stations, color-coded according to the network to which each station belongs. **(b)** The catalogue moment magnitude versus hypocentral distances: markers in different colours show recordings from stations associated with four different networks. **(c)** Histogram showing the distribution of the catalogue moment magnitudes. **(d)** Histogram illustrating the distribution of the recorded hypocentre distances.

We utilize an automated processing workflow that includes removing the instrumental response, applying a fourth-order Butterworth bandpass filter, applying a 5% Cosine taper to both sides of the signal, and adding zero padding. For the filtering step, we set the low-cut/high-pass frequency at 0.5 Hz and the high-cut/low-pass frequency at 25 Hz. Before filtering, we use the signal-to-noise ratio (SNR), defined as the root-mean-square ratio of the signal-smoothed and noise-smoothed spectra, to eliminate low-quality waveforms. SNR is calculated over 50 frequencies equally spaced on a logarithmic scale between 0.5 Hz and 25 Hz, which are the boundaries. Waveforms are included in the catalogue if their SNR within the target frequency range exceeded the set threshold. We set the SNR threshold to 3 for frequency intervals below 1 Hz and above 20 Hz, and to 6 for those between 1 and 20 Hz. The noise window for SNR calculation starts 20 seconds before the event origin time and extends up to it. We extract a 20-second window from all waveforms to estimate noise spectra. The spectra of the signal windows include the direct S-wave, with the window starting 1 second before the theoretical S-wave arrival time, calculated using the 1D velocity model for the Central Apennines by Herrmann et al. (2011). Following Pacor et al. (2016), the end of the signal window is based on a percentage of the cumulative energy (the squared velocity integral) as a function of source-to-site distance (R). Specifically, it is set at 90% for $R \leq 25$ km, 80% for 25 km $\leq R \leq 50$ km, and 70% for $R \geq 50$ km. Additionally, we impose a minimum window length of 5 seconds for shorter hypocentre distances and a maximum of 20 seconds.

Ultimately, 106,336 recordings, each comprising two horizontal components, with hypocentral distances ranging from 1 to 190 km, are retained for the analyses (Figure 2.1b). Events with $\boldsymbol{M} < 4$ were predominantly recorded at stations located within 75 km (with a median of 50 km), whereas larger $\boldsymbol{M} > 4$ events yielded data at stations with $R_{hypo} < 120$ km. About 90% of the events are $2.5 \leq \boldsymbol{M} \leq 3.5$ (Figure 2.1c). As shown in Figure 2.1d, approximately 70% of the dataset is recorded at the stations at $R_{hypo} \leq 40$ km, highlighting the abundance of near-field data. This configuration of data is significant for our analyses because the anelastic attenuation of high frequencies could have a stronger impact on recordings of smaller earthquakes, and their spectral energy is predominantly in the higher frequencies. To estimate the seismological parameters of moderate-to-small events, the observations must be at short distances (Trugman & Shearer, 2018; Baltay et al., 2019). Following data processing, we compute PGA and FAS for the direct S-wave window. Subsequently, the FAS for each waveform is smoothed by applying the (Konno & Ohmachi, 1998) method with a parameter value set to 40 for the target frequency range of 0.5 Hz to 25 Hz. Finally, the geometric mean of the two horizontal components is calculated.

Several studies have computed and analysed these seismological parameters [M_0, f_c, $\Delta\sigma$, Q] using various methodologies for small to large events in the sequence (Bindi et al., 2018, 2020, 2024; Kemna et al., 2021) Here, we use an approach specifically tailored for the study objectives, which is to investigate the physical processes that control ground-motion variability. The Methods sections and Appendix 2 elaborate on the approach.

2.3. Methods

At the time of this study, there were two datasets for seismological parameters available for this sequence: Kemna et al. (2021) (hereafter, K21) and Bindi et al. (2024) (hereafter, B24). K21 estimated the seismological parameters by adopting shear-wave velocity from a 1D velocity structure model and frequency-independent Q values, allowing Q to vary to account for potential spatial and temporal variations

during the fitting process. In contrast, B24 used a 3D shear-wave velocity model and a simplified non-parametric attenuation model, which depends on hypocentral distance and frequency. B24 study, extending from Central to Southern Italy, assumes constant attenuation parameters for our study region. The B24 approach assumes that ground-motion attenuation at a given distance is similar for two events with distinct locations and occurrence times, and hence, does not entirely capture the spatial and temporal variability of attenuation in the sequence. Compared to these approaches, our study employs a methodology that integrates a 3D shear-wave velocity model (similar to B24) with a frequency-dependent *Q(f)* model, and allows for spatial and temporal variability of attenuation. Our approach commences with regression of a mixed-effects linear parametric GMM and non-parametric GMMs, followed by estimation of seismological parameters.

2.3.1. Parametric Linear Mixed-Effects GMMs

In a customary linear mixed-effects regression (e.g., Bates et al., 2015) of a PR-GMM with fixed-effects structure $G(\boldsymbol{M}, R, \Theta) = G_e(\boldsymbol{M}) + G_p(R) + G_s(\Theta)$, the event-to-event variability of ground-motions unexplained by $G_e(\boldsymbol{M})$ is quantified as the between-event random-effect distribution $\Delta B = N(0, \tau^2)$, the site-to-site variability unexplained by $G_s(\Theta)$ as the between-site random-effect distribution $\Delta S2S = N(0, \Phi_{S2S}^2)$, and the left-over record-to-record residual variabilities of seismic processes unexplained by $G(\boldsymbol{M}, R, \Theta)$ are quantified in the distribution $E = N(0, \Phi^2)$. The total ground-motion variability is then $\sigma^2 = \tau^2 + \Phi_{S2S}^2 + \Phi^2$. Reducing any of these three variances will reduce the σ^2, indicating an improvement in the GMM mixed-effects structure in modelling ground-motion physics. Eq. 2.1 is the generic structure of our mixed-effects PR-GMM:

$$ln(FAS, f) = G_e(\boldsymbol{M}, f) + G_p\left(R_{hypo}, f\right) + \Delta B(f) + \Delta S2S(f) + E(f), \quad (2.1)$$

This model uses the event moment-magnitude $\boldsymbol{M}$ and hypocentral distance $R_{hypo} = \sqrt[2]{R_{epi}^2 + Z^2}$ as the predictor parameters, where R_{epi} is the epicentral

distance, and Z is the hypocentral depth of events in the dataset. The $ln\,(FAS, f)$ is the natural logarithm of the geometric mean of horizontal acceleration Fourier spectra with $f = 0.5 - 25$ Hz. As subsequent GMMs all have the [$\boldsymbol{M}$, R_{hypo} or R_{epi}, f] as common inputs or variables, for brevity, we refer to this parametric GMM as PR($\boldsymbol{M}$) from here on.

On the right-hand side of Eq. 2.1 are the fixed-effects parametric functions and the random-effect variables. $G_e(\boldsymbol{M}, f)$ takes the form of Eq. 2.2, with frequency-dependent regression coefficients $c_1(f)$, $c_2(f)$, $c_3(f)$ that scale $ln\,(FAS, f)$ with event $\boldsymbol{M}$. This is a rather common form among GMMs and GMPMs derived for small-to-moderate-sized earthquakes (Fukushima, 1996; Kotha et al., 2022).

$$G_e(\boldsymbol{M}, f) = c_1(f) + c_2(f)\boldsymbol{M} + c_3(f)\boldsymbol{M}^2, \tag{2.2}$$

Eq. 2.3 shows the parametric form of the distance scaling component of the PR($\boldsymbol{M}$):

$$G_p(R_{hypo}, f) = G_g(R_{hypo}) + c_4(f)R_{hypo}, \tag{2.3}$$

$G_p(R_{hypo}, f)$ is composed of two functions: $G_g(R_{hypo})$ describing the geometric spreading, and the $c_4(f)R_{hypo}$ describing the apparent anelastic attenuation of $ln\,(FAS, f)$. Note that the $G_g(R_{hypo})$ is frequency-independent, while the latter is frequency-dependent. Geometrical spreading and anelastic attenuation terms are known to trade off in a mixed-effects regression (e.g., Atkinson & Boore, 2006; Abrahamson et al., 2014; Yenier & Atkinson, 2015). To assess the impact of this trade-off, we test a two-segment model (Malagnini et al., 2011; Akinci et al., 2022) and a five-segment model (Gabrielli et al., 2025) geometrical spreading proposed for central Italy. We observe that both models yield practically identical regression coefficients. Eventually, in this study, we use the five-segment model for $G_g(R_{hypo})$:

$$G_g(R_{hypo}) = \begin{cases} -1.1.\ln(R_{hypo}), & R_{hypo} \le 10km \\ -1.0.\ln(R_{hypo}), & 10 < R_{hypo} \le 20km \\ -0.9.\ln(R_{hypo}), & 20 < R_{hypo} \le 30km \\ -0.7.\ln(R_{hypo}), & 30 < R_{hypo} \le 40km \\ -0.5.\ln(R_{hypo}), & R_{hypo} > 40km \end{cases}, \tag{2.4}$$

The apparent anelastic attenuation coefficient $c_4(f)$ theoretically equals zero for a perfectly elastic Earth. However, because the Earth's medium is not elastic, this coefficient takes non-zero values and generally increases with frequency. In most of the recent studies, regressed estimates of $c_4(f)$ are one of the following:

(1) ergodic: generic for all events, paths, and sites in the dataset (e.g., Trugman & Shearer, 2018),

(2) regional: specific to broad regions hosting the recording site (e.g., Kotha et al., 2020; Weatherill et al., 2020),

(3) spatially varying: with specific values for event or site geographical coordinates (e.g., Landwehr et al., 2016),

(4) path dependent: with specific values for each segment along a wave propagation path (e.g., Dawood & Rodriguez-Marek, 2013).

The progressively non-ergodic treatment of $c_4(f)$ across these approaches requires increasing (spatially) denser datasets. However, all these approaches model a spatially varying $c_4(f)$; they all assume a temporal invariability of apparent anelastic attenuation. It is worth noting that more complex formulations of $G_p(R_{hypo}, f)$ exist in literature. For example, certain GMPMs model $\boldsymbol{M}$ dependence of geometric spreading and anelastic attenuation, include additional distance metrics, and distinction based on focal depths and mechanisms (Bayless & Abrahamson, 2019; Kotha et al., 2022; Campbell & Bozorgnia, 2025). As we work with point-source approximant events and with Fourier amplitudes, a more sophisticated $G_p(R_{hypo}, f)$ is not necessary.

We recall that the frequency-dependent between-event random-effect distribution $\Delta B(f)$ quantifies the event-to-event variability of $ln\,(FAS, f)$. $\Delta B(f)$ is a Gaussian random variable composed of a unique $\delta B_e(f)$ value for each event e in the dataset (or sequence). Simply, for two events e_1 and e_2 of identical $\boldsymbol{M}$, $\delta B_{e1}(f) > \delta B_{e2}(f)$ implies that event e_1 has produced systematically higher $ln\,(FAS, f)$ than event e_2

(e.g., Strasser et al., 2009). For example, Trugman & Shearer (2018) estimated the *ΔB(PGA)* of Californian events and correlated them to their $\Delta\sigma$. Similarly, for the 2016-2017 sequence, Bindi et al. (2018) reported temporal variability of ground-motions, quantified in the event-to-event random-effect distribution *ΔB(f)* at f = 10 Hz of the sequence, and associated it with the temporal variability of event stress-drop.

It is well known that local site effects significantly influence ground-motions. Due to the lack of comprehensive site response information (Θ) for the stations in our catalogue, we do not include a fixed-effects component for site-response $G_s(\Theta)$ in Eq. 2.1. Instead, the random-effect *ΔS2S(f)* absorbs all the site-specific soil responses (e.g., Kotha et al., 2018). In this regard, our PR(***M***) is similar to those of Bindi et al. (2018) and Trugman & Shearer (2018).

The final component of the PR(***M***) shown in Eq. 2.1 is the frequency-dependent residual distribution *E(f)*. These distributions are composed of record-specific $\varepsilon_{e,s}(f)$ values for each combination of event e and site s. *E(f)* are called the *left-overs* (Sahakian et al., 2018) and are found to capture interesting, secondary earthquake processes, such as evidence of nonlinear soil responses (e.g., Loviknes et al., 2021), anisotropic shear-wave radiation patterns (e.g., Kotha et al., 2019), frequency-dependent directivity effects (e.g., Colavitti et al., 2022), etc. In this study, we are not particularly concerned with analyses of the residuals. Moreover, given that the events in the dataset are of small-to-moderate size and are recorded over a wide azimuthal range, the anisotropic features (e.g., directivity and shear-wave radiation), if any, would be absorbed into *E(f),* leaving the PR(***M***) and seismological parameters are unbiased and isotropic. Mixed-effect regression of PR(***M***) is then carried out for each of f = 0.5 – 25 Hz, independently as usual, without assuming any cross-frequency correlations. In summary, the fixed-effect coefficients estimated in the regression are $c_1(f)$, $c_2(f)$, $c_3(f)$, $c_4(f)$ (common for all events and stations), random-effect distributions $\Delta B(f) = N(0, \tau(f)^2)$ and $\Delta S2S(f) = N(0, \Phi(f)^2_{S2S})$, and the residual distribution $E(f) = N(0, \Phi(f)^2)$.

2.3.2. Non-parametric Random Forest Mixed-Effects GMMs

The PR(***M***)-GMM discussed above has a relatively simple linear mixed-effects structure and is suitable for our dataset. However, Figure 2.1d shows that approximately 70% of the dataset is recorded at the stations at $R_{hypo} \leq 40$ km. At such near-source distances, the linear combination $G_e(\boldsymbol{M}, f) + G_p(R, f)$ may produce misleading results in situations where the physics of the underlying data is complex or unknown, leading to a loss of flexibility compared to non-parametric approaches (Bishop, 2006). In addition, we aim to introduce additional predictors (or features) in the GMMs whose potential nonlinear interactions are yet to be understood and modelled analytically (e.g., Fernandez-Delgado et al., 2014; Louppe, 2014). Therefore, we develop non-parametric Random Forest mixed-effects GMMs, building upon those already used in ground-motion analyses (Trugman & Shearer, 2018; Khosravikia & Clayton, 2021; Alidadi & Pezeshk, 2024). We follow the model implemented by Trugman & Shearer (2018), resourced from Pedregosa et al. (2011), to define two Random Forest GMMs, which model the observed ground-motions values as interactions of input variables and random-effect terms:

$$ln(FAS, f) = \frac{1}{B}\sum_{b=1}^{B} G_b^{RF}[\boldsymbol{M}, ln(R_{hypo}), f] + \Delta B(f) + \Delta S2S(f) + E(f), \quad (2.5)$$

The first non-parametric model in Eq. 2.5 uses [***M***, R_{hypo}] as independent variables, and is hereafter referred to as RF(***M***). RF(***M***) is essentially the non-parametric counterpart of PR(***M***). It is interesting to note that, unlike the analytically structured PR(***M***), RF(***M***) requires only $ln\,(R_{hypo})$ as input and doesn't require additional R_{hypo} terms to explicitly model geometric spreading and anelastic attenuation. This allows the Random Forest algorithm to flexibly determine whether linear (geometric) and exponential (anelastic) distance-decays are relevant to the dataset, and if RF(***M***) should capture these effects rather than imposing both effects a priori and dealing with their potential trade-offs, as in PR(***M***).

Several studies reported that deeper events produce stronger high-frequency surface ground-motions than shallower events of similar $\boldsymbol{M}$, while this can be partially attributed to an increase in normal stresses and stress-drop with depth in the crust. Abercrombie et al. (2021) reported that the systematic increase in stress-drop (and rupture velocity) is observed only when depth-dependent attenuation (e.g., *Q(f)* increasing with depth) is ignored. With an empirical, depth-dependent attenuation correction, however, the depth dependence of stress-drop systematically decreases. Regardless of the depth dependence of normal stresses, stress-drop and attenuation are seldom isotropic. This means that the scaling of ground-motions (and seismological parameters) with Z could also depend on the horizontal location of the hypocenter [XY] (Figure 2.2) within the fault system. To allow such unconstrained interaction of $\boldsymbol{M}$ and hypocenter location [XYZ] in modelling ground-motions, we introduce a model with a higher complexity referred to as RF($\boldsymbol{MXYZ}$):

$$ln(FAS, f) = \frac{1}{B}\sum_{b=1}^{B} G_b^{RF}[(\boldsymbol{M}.X.Y.Z), ln(R_{epi}), f] + \Delta B(f) + \Delta S2S(f) + E(f), \quad (2.6)$$

The second non-parametric GMM in Eq. 2.6 uses the [$\boldsymbol{M}.X.Y.Z$, R_{epi}] as independent input variables. It is important to note that, unlike PR($\boldsymbol{M}$) and RF($\boldsymbol{M}$), which use R_{hypo} as the distance metric, RF($\boldsymbol{MXYZ}$) features R_{epi}. X and Y represent the spatial coordinates of each event in kilometres along and perpendicular to the strike of the Normal fault systems (average strike angle of 165°) relative to an arbitrary reference point, respectively (Figure 2.2). Z is the hypocentral depth of each event, which is considered an independent feature in the model. This choice allows the Random Forest algorithm the flexibility to determine whether the ground-motions should scale with Z without being constrained by $R_{hypo} = \sqrt[2]{R_{epi}^2 + Z^2}$ structure.

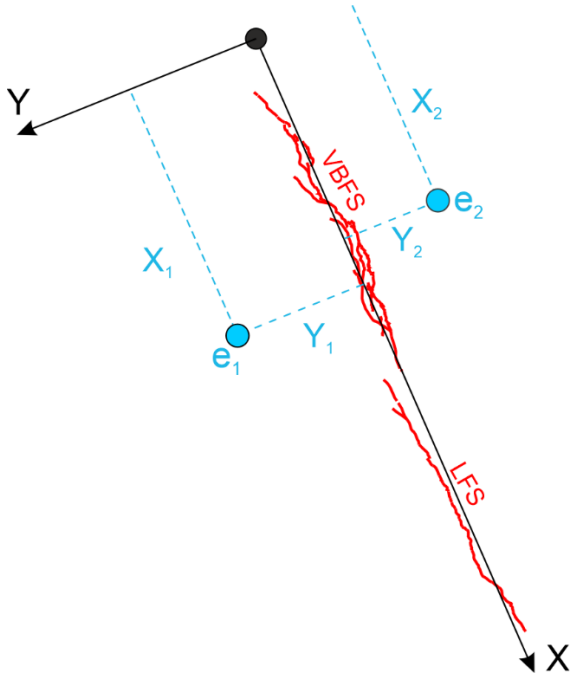

Figure 2.2. Schematic illustration of the definition of variables X and Y, used in the Random Forest Ground Motion Models (GMMs). *X* represents the distance of each event from the reference point (black circle) along the fault strike, while *Y* denotes the perpendicular distance of each event (e_1, e_2, …) from the fault strike.

A key feature of Random Forests is bootstrapping, whereby each decision tree is trained on a random subset of the training data, sampled with replacement. This process, repeated over a specified number of trees and a defined number of predictor variables (or features), introduces diversity among the trees, reduces overfitting, and enhances the generalization performance of the model (Breiman, 2001). One of the main challenges in using Random Forest regression is avoiding overfitting, which occurs when the model learns from the training data, including noise and random fluctuations, too well. Overfitting reduces the ability of the model to generalize to new, unseen data. It can result from excessive model complexity, poor-quality data, or suboptimal parameter choices. In our case, the models presented in Eq. 2.5 and Eq. 2.6 are not overly complex and are unlikely to be a direct source of overfitting. Moreover, the dataset used for training contains 106,336 data points, which provides

a sufficiently large and diverse sample to mitigate overfitting risks. To select optimal Random Forest parameters (Table 2.1) and assess overfitting, we use two complementary approaches, as described below:

- **Statistical Metrics (R^2 Scores)**: We evaluate model performance using two metrics: the prediction score (R^2) and the out-of-bag (OOB) score (OOB-R^2). Ideally, both scores should be high and closely matched, indicating strong predictive ability without overfitting. We tune the model to select parameters that maximize both metrics simultaneously. A small gap between the prediction and OOB scores signals a well-generalized model (Table 2.1).
- **Train/Test Split Validation**: We divide the dataset into training (80%) and test (20%) subsets. Using the parameters selected in the Statistical Metrics approach, we compute the prediction scores for both subsets. If overfitting were present, the training score would be significantly higher than the test score. However, our results show that the prediction scores are both high and comparable across subsets (Table 2.1), indicating no significant overfitting.

Based on these two validation steps, we confirm the reliability of the chosen Random Forest parameters and proceed with the final regression using these optimized settings.

Table 2.1. Selected Random Forest Parameters along with the metrics used to assess the overfitting.

Category	Parameter/Metric	RF(***M***)	RF(***MXYZ***)
Model Parameters	Number of trees	200	200
	Max. depth	20	36
	Max. features	2	8
	Min. samples split	2	4
	Min. samples leaf	1	1
Statistical Metrics	Prediction Score	0.87	0.95
	Out-of-bag Score	0.82	0.90
Train/Test split	Prediction Score – training subset	0.87	0.91
	Prediction Score – test subset	0.75	0.81

The two non-parametric models also estimate the random-effects $\Delta B(f)$ and $\Delta S2S(f)$, and the residual $E(f)$. Trugman & Shearer (2018) reported in their analyses of the PGA dataset that their RF(***M***) outperforms their PR(***M***) in terms of total misfit ($\sigma^2 = \tau^2 + \Phi_{S2S}^2 + \Phi^2$). In this study, we extend the investigation over Fourier amplitudes of f = 0.5-25 Hz. It is important to note that, unlike the parametric mixed-effect regressions, the Random Forest mixed-effects regression does not constrain the $\Delta B(f)$, $\Delta S2S(f)$, and $E(f)$ distributions to be Gaussian with zero mean. In the subsequent Results section, we will investigate the consistency of $\Delta B(f)$, $\Delta S2S(f)$, and $E(f)$ distributions between the RF(***M***), RF(***MXYZ***), and PR(***M***) to learn their compatibility and complementarity.

2.3.3. Estimation of Seismological Parameters

The Fourier spectra of recorded earthquake waveforms can be used to compute seismological parameters of [M_0, f_c, $\Delta\sigma$, $Q(f)$]. Single-spectra fitting based on Brune's source model is one of the most common methods for computing source parameters (Kemna et al., 2021; Zhang et al., 2022). In this method, correcting the displacement or the acceleration spectra for path attenuation and site effects to obtain source

spectra is the challenging aspect. Path attenuation is typically described as a combination of geometrical spreading and anelastic attenuation terms (Boore, 1983). Notably, an inherent trade-off exists between Q, M_0, and f_c during the fitting process (e.g., Allmann & Shearer, 2007; Sumy et al., 2017; Abercrombie, 2021; Calderoni & Abercrombie, 2023). In a seismic sequence, such as the 2016-2017 Central Italy, the attenuation may vary spatially due to changes in crustal shear-wave velocity with depth or lateral variations, and temporally due to changes in fluid pore pressure and the creation of damage around the mainshock area (e.g., Malagnini et al., 2022; Gabrielli et al., 2023). Di Luccio et al. (2010) investigated the events in the 2009 $\boldsymbol{M}$6 L'Aquila sequence in the central Apennines (Italy) between October 2008 and April 2009, and revealed a progressively increasing V_P/V_S because of increasing pore fluid pressure along the fault planes. The study concluded that deep fluids, more than tectonic stress, may control the seisomotectogenesis in the central Apennines. The temporal variability in V_P/V_S suggests that the $Q(f)$ of the surrounding medium may also be temporally variable. Therefore, assuming a time-stationary or 1D attenuation model likely biases the estimation of M_0, f_c, and subsequently $\Delta\sigma$.

First, to remove attenuation effects from the Fourier spectra, we compute the frequency-dependent quality factor $Q_{e,f}$ for each event e at each frequency, using the method introduced by Trifunac (1976) (e.g., Boore et al., 2009; Ghofrani & Atkinson, 2011). This approach requires computing the anelastic attenuation coefficient $c_4(f)$ separately for each event $c_{4,e}(f)$. Because our objective is to perform *PR-GMM* regression on an event-by-event basis, we modify Eq. 2.1 by removing the magnitude-dependent terms $c_2(f)$ and $c_3(f)$. This modification enables the estimation of attenuation parameters independently of magnitude-scaling effects, ensuring consistency with the single-event regression framework. The resulting event-specific apparent anelastic attenuation coefficients $c_{4,e}(f)$ are used to estimate $Q_{e,f}$ using:

$$Q_{e,f} = \frac{-\pi . f}{\beta . c_{4,e}(f)}, \tag{2.7}$$

where β is the shear-wave velocity in the event location taken from the 3D shear-wave velocity model used in B24, which was estimated with a trilinear interpolation of the tomographic model of Menichelli et al. (2023). Finally, the power-law model in the form of $Q_e(f) = Q_{0,e}.f^{n_e}$ (Aki & Chouet, 1975) is fitted to the estimated $Q_{e,f}$ values. The resulting fits yield coefficients of determination (R^2) exceeding 0.75 for all events. As mentioned earlier, trials with alternative multi-segment $G_g(R_{hypo})$ yield rather identical $c_{4,e}(f)$. It is important to note that, despite being event-specific, the $Q_e(f)$ should not be interpreted as the anelastic attenuation precisely at the earthquake location, but rather the *apparent* anelastic decay of the wave through varying geological structures along the event-to-site paths (Trifunac, 1976). However, since $Q_e(f)$ is computed for every single event, we expect them to have quantified any spatial and temporal variations of the anelastic properties of the medium.

Following the estimation of $Q_e(f)$ and the correction of Fourier spectra for path attenuation effects, the next step is to remove the site effects and obtain the source spectra for each event. It is well known that local site effects significantly influence ground-motion, and failing to remove or incorrectly removing site effects from the Fourier spectra can bias the estimation of M_0, f_c, and $\Delta\sigma$. Due to the lack of comprehensive site-response information for the stations in our catalogue, we adopt an empirical approach involving the non-parametric Random Forest PR($\boldsymbol{M}$) (Eq. 2.5). We regress the RF($\boldsymbol{M}$) using the $\boldsymbol{M}$ from the catalogue of K21 and treat the computed $\Delta S2S(f)$ as *station-correction*. The attenuation-corrected Fourier spectra are corrected for site effects by subtracting $\Delta S2S(f)$ from them to obtain the source spectra. In fact, our approach is similar to the Generalized Inversion Techniques or spectral decomposition approaches used by several authors to estimate attenuation characteristics, source spectra, and site-responses simultaneously (e.g., Drouet et al., 2008; Oth et al., 2011; Bindi & Kotha, 2020). With our approach, uncertainty in the estimated source parameters (particularly, $\boldsymbol{M}$) is substantially lower than that from alternative methods. One may even use the $\Delta S2S(f)$ of the $PR(\boldsymbol{M})$ in Eq. 2.4 or of the

RF(MXYZ) in Eq. 2.6 for the same purpose, because they are practically identical, which is shown in Section 2.4.3.2.

The FAS corresponding to the S-wave window for each event-station waveform is corrected for the path propagation effect (using the estimated $Q_e(f)$) and the site effect to isolate the source spectra. The corrected spectra are then fitted in a least-squares sense to an ω^2 spectral source model $S(f)$ as defined by Boore (2003), to estimate M_0 and f_c for each event-station individually:

$$S(f) = \frac{C.M_0.(2\pi.f_c)^2}{1+(\frac{f_c}{f})^2}, \tag{2.8}$$

where, $C = R_\varphi.F.V/4\pi.\rho.\beta^3.R_0$ with the radiation pattern coefficient R_φ = 0.55 (Boatwright & Boore, 1982), V = 0.71 for the partition of total shear-wave energy into two horizontal components, F = 2 to account for the free surface effect, ρ (in gr/cm^3) is the density, β (in km/s) is the shear-wave velocity from the same 3D velocity model used in estimating $Q_{e,f}$, and R_0 = 1 (in km) is the reference distance. Since M_0 and f_c are estimated for each event-station combination, we take the arithmetic mean to obtain a unique mean and variability per event. Next, assuming a circular rupture model (Eshelby, 1957), we estimate $\Delta\sigma = (7/16).(M_0/r^3)$, with $r = k\beta/f_c$, k = 0.37 (Brune, 1970), and β values are the same as earlier. Finally, we estimate $\boldsymbol{M} = (2/3).\log_{10}(M_0) - 10.7$ following Kanamori (1977).

2.4. Results

2.4.1. Seismological Parameters

We retrieve the quality factor (including $Q_{0,e}$ as the attenuation parameter and n_e as the frequency-dependent parameter), seismic moment, corner frequency, and stress-drop estimates for 2,503 earthquakes. $Q_{0,e}$ ranges from 15 to 140, with a mean value of 68 (Figure 2.3a), while n_e varies between 0.3 and 1.18, with a mean of 0.68 (Figure 2.3b). These mean values of $Q_{0,e}$ and n_e are consistent with those reported by Akinci et al. (2022) and Gabrielli et al. (2025) for the 2016-2017 Central Italy

sequence. Stress-drop estimates closely follow a lognormal distribution, ranging from 0.015 MPa to 7.4 MPa, with a median value of 0.37 MPa and a natural logarithm standard deviation of 1.1. The stress-drop variability in this study is notably higher than the standard deviations reported by K21 and B24 for similar events, which are 0.6 and 0.85, respectively. As illustrated in Figure 2.3c, the corner frequency estimates are well aligned with the theoretical corner frequency contours (dashed lines) corresponding to the constant stress-drop from 0.01 MPa to 10 MPa. One of the most debated topics in earthquake source physics is the scaling of stress-drop with earthquake magnitude. Figure 2.3d reveals a significant deviation from the self-similarity assumption, as the stress-drop increases with moment magnitude. Such a deviation is not unique to the 2016-2017 Central Italy sequence (e.g., Bindi et al., 2018; Kemna et al., 2021; Bindi et al., 2024), and indeed comparable deviations from self-similarity have also been observed in other regions around the world (e.g., Mayeda & Walter, 1996; Abercrombie et al., 2017; Trugman & Shearer, 2018; Trugman, 2020). As mentioned earlier, there is a strong trade-off between the geometrical spreading model and the Q factor. To evaluate the impact of the chosen geometrical spreading model on moment magnitude and stress-drop estimates, we compute them using the Q factor obtained from both models (Akinci et al., 2022; Gabrielli et al., 2025). The results, shown in Figure A2.1 in the Supporting Information, indicate that the differences in moment magnitude and stress-drop between the two models are negligible. A comparison of $\boldsymbol{M}$ and $\Delta\sigma$ estimates from this study, K21, and B24 is presented in Text A2.1 and Figure A2.2 in the Supporting Information. The discussion therein shows that, although the $\Delta\sigma$ estimates differ across three catalogues due to differences in the treatment of path and site effects, the $\boldsymbol{M}$ estimates from this study and K21 follow a linear trend with unit slope. This indicates that the mixed-effects GMMs are practically identical, regardless of the source of $\boldsymbol{M}$.

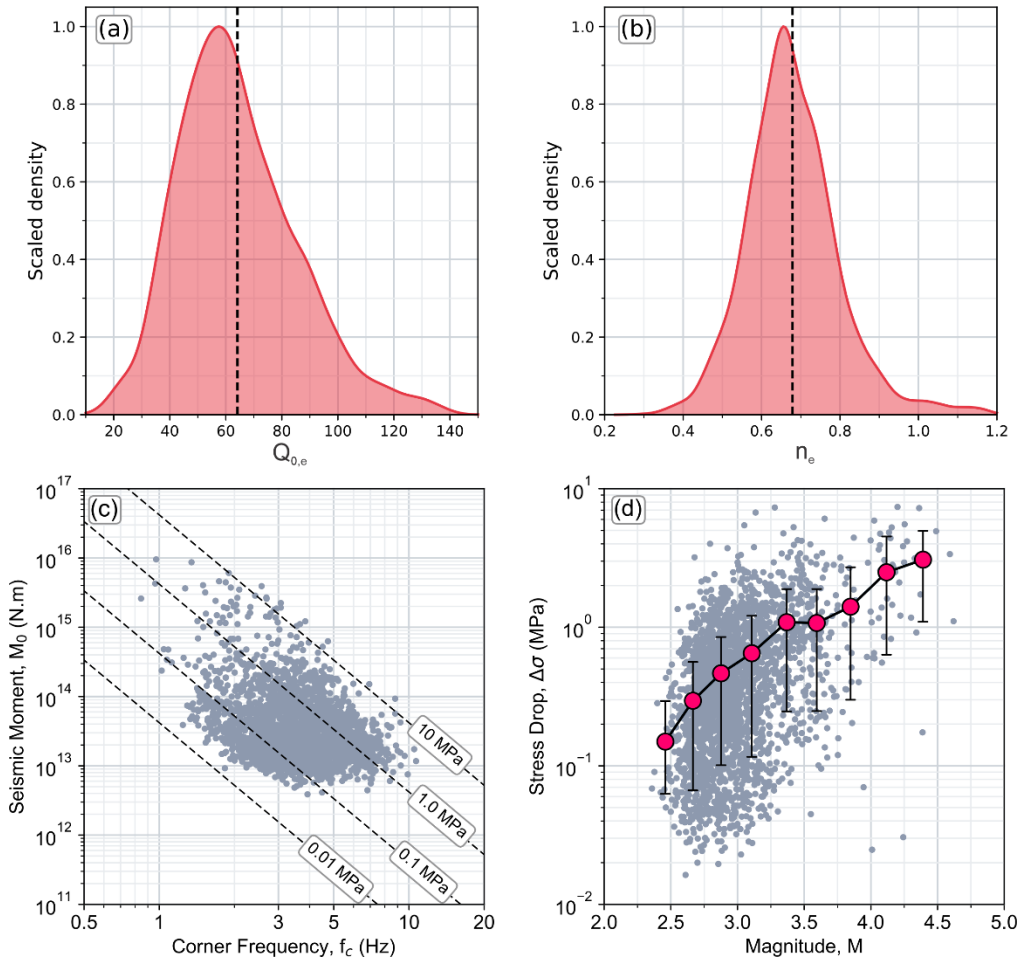

Figure 2.3. Distributions and scaling relations of the estimated seismological parameters for the analysed events. Histograms representing distributions of **(a)** $Q_{0,e}$ and **(b)** n_e. The vertical black dashed lines indicate the corresponding median of each parameter. **(c)** Estimated corner frequency versus seismic moment for all events from S-wave spectra. The dashed lines denote the corner frequencies corresponding to constant stress-drop values of 0.01 MPa, 0.1 MPa, 1.0 MPa, and 10 MPa, assuming an average shear-wave velocity of 3.3 km/s. (d) Estimated stress-drop versus moment magnitude for all events. Red circles indicate the mean values for each magnitude bin of 0.25. The vertical black error bars represent the 10% to 90% percentile intervals for each bin.

2.4.2. GMM Fixed-effects

Here, the fixed-effects predictions corresponding to the $e^{\ln(FAS,f)}$ estimates of the three GMMs, namely; $G_e(\boldsymbol{M},f) + G_p\left(R_{hypo},f\right)$ of PR($\boldsymbol{M}$) in Eq. 2.1, $\frac{1}{B}\sum_{b=1}^{B} G_b^{RF}[\boldsymbol{M}, ln\left(R_{hypo}\right), f]$ of RF($\boldsymbol{M}$) in Eq. 2.5, and $\frac{1}{B}\sum_{b=1}^{B} G_b^{RF}[(\boldsymbol{M}.X.Y.Z), ln\left(R_{epi}\right), f]$ of RF($\boldsymbol{MXYZ}$) in Eq. 2.6, are evaluated over the frequency range f = 0.5 – 25 Hz. It should be noted that, by construction, PR($\boldsymbol{M}$) can be extrapolated to [$\boldsymbol{M}$, R] scenarios beyond the regressed dataset, whereas RF($\boldsymbol{M}$) and RF($\boldsymbol{MXYZ}$) cannot.

Figure 2.4 shows the comparison of fixed-effects predictions for the three GMMs for six different scenarios. As already presented in Figure 2.1, $\boldsymbol{M}$2.8 and R = 10 km and R = 30 km are the best-sampled scenarios in the dataset, while $\boldsymbol{M}$3.5 and R = 80 km are at the dataset [$\boldsymbol{M}$, R] limits. Unlike the PR($\boldsymbol{M}$) and RF($\boldsymbol{M}$) predictions, the RF($\boldsymbol{MXYZ}$) predictions should vary with the XYZ of any event with $\boldsymbol{M}$. For illustrative purposes, Figure 2.4 shows RF($\boldsymbol{MXYZ}$) predictions obtained from 100 random samples of X, Y, and Z (X: 6 – 76 km, Y: -6 – 19 km, Z: 1 – 12 km). For the scenarios [$\boldsymbol{M}$2.8, R = 10 km] (Figure 2.4a), [$\boldsymbol{M}$2.8, R = 30 km] (Figure 2.4b), [$\boldsymbol{M}$3.5, R = 10 km] (Figure 2.4d), and [$\boldsymbol{M}$3.5, R = 30 km] (Figure 2.4e), the fixed-effect FAS predictions of the three models are generally very similar, with more pronounced differences appearing at $f \geq 3$ Hz. The RF($\boldsymbol{M}$) predictions appear rougher than those of PR($\boldsymbol{M}$) because the non-parametric models retrieve predictions directly from the dataset, whereas the parametric model interpolates between observations and therefore produces smoother predictions. It is not uncommon for PR($\boldsymbol{M}$) models yield rough response spectra when regressions are performed independently for each spectral period, thereby ignoring potential cross-spectral correlations (e.g., Kuehn & Scherbaum, 2015). To address this issue, some ground-motion modelers smooth the PR($\boldsymbol{M}$) fixed-effect coefficients during post-processing (e.g., Bayless & Abrahamson, 2019), others might choose not to (e.g., Kotha et al., 2022).

Nevertheless, the largest differences between PR(***M***) and RF(***M***) predictions appear at $f \geq 3$ Hz for the well-sampled scenarios. For the less well-sampled scenarios [***M***2.8, R = 80 km] (Figure 2.4c) and [***M***3.5, R = 80 km] (Figure 2.4f), the differences between PR(***M***) and its non-parametric counterparts are substantial, with the PR(***M***) predictions significantly lower in the $1 \leq f \leq 10$ Hz ranges. The origin of this discrepancy is relatively straightforward. In PR(***M***), Eq. 2.4 imposes a frequency-independent geometric-spreading $G_g(R_{hypo})$ on the fixed-effects predictions, whereas the non-parametric models are not constrained by such an assumption. Because the attenuation term $c_4(f)R_{hypo}$ in PR(***M***) is estimated relative to $G_g(R_{hypo})$ and is primarily controlled by the more abundant observations at $R \leq 40$ km, the predictions at R = 80 km are likely negatively biased. In contrast, the more flexible RF(***M***) and RF(***MXYZ***) are less constrained by the dominant data at $R \leq 40$ km and are therefore less prone to this bias. Such differences are not uncommon when comparing parametric and non-parametric ground-motion predictions. For example, the non-parametric spectral decomposition of the Engineering Strong Motion dataset (Lanzano et al., 2019; Bindi et al., 2019) by Bindi & Kotha (2020) (see their Figure 3) reported a strong frequency and regional dependence of geometric spreading, and a reduced attenuation in the $40 < R < 80$ km range compared to $R < 40$ km, but for a much larger region covering all of Italy. However, we adopt the more recent and region-specific geometric spreading model $G_g(R_{hypo})$ proposed by Gabrielli et al. (2025), shown in Eq. 2.4. Similarly large discrepancies between parametric and non-parametric geometric-spreading predictions were reported by Trugman & Shearer (2018) (see their Figure 6). A plausible physical explanation for the reduced attenuation in $40 < R < 80$ km is the generation of surface waves from shallower seismicity or from secondary arrivals from deeper seismicity. Both processes are strongly influenced by local geology and crustal structures, making them difficult to represent with simple parametric formulations. For this reason, we consider the RF(***M***) and RF(***MXYZ***) predictions to better represent the attenuation behavior of this

particular region and dataset, while also highlighting the limitations of the PR(***M***) formulation.

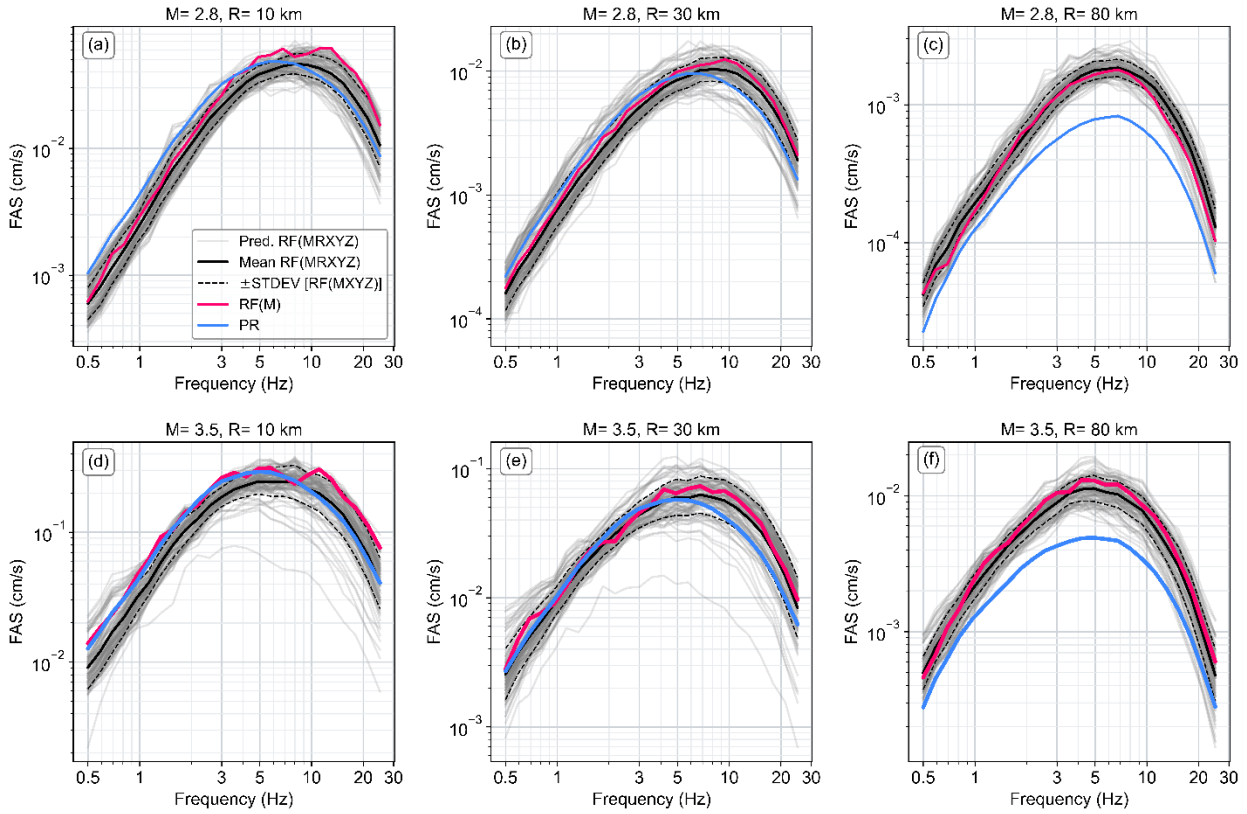

Figure 2.4. Comparison of fixed-effect (median) predictions from the three GMMs: PR(***M***) (blue curve), RF(***M***) (pink curve), and RF(***MXYZ***) (black curve), for six scenarios: **(a)** $\boldsymbol{M}$ = 2.8 and R = 10 km, **(b)** $\boldsymbol{M}$ = 2.8 and R = 30 km, **(c)** $\boldsymbol{M}$ = 2.8 and R = 80 km, **(d)** $\boldsymbol{M}$ = 3.5 and R = 10 km, **(e)** $\boldsymbol{M}$ = 3.5 and R = 30 km, and **(f)** $\boldsymbol{M}$ = 3.5 and R = 80 km. The median of RF(MXYZ) prediction is computed as the mean of predictions obtained from 100 random samples of X, Y, and Z, shown by thin grey curves. The dashed black curves represent the mean RF(***MXYZ***) prediction ± one standard deviation of the random samples.

We now investigate the more novel RF(***MXYZ***) model, whose randomly sampled fixed-effects predictions consistently encompass those of RF(***M***), as shown in Figure 2.4. Figures 2.5 and 2.6 present the RF(***MXYZ***) predictions for an ***M***2.8 earthquake

at frequencies f = 1, 3, 10 Hz, for sites located at R = 10, 30, 80 km from the hypocenter. The map views (Figure 2.5) present the RF(***M****XYZ*) predictions varying with X and Y, averaged over Z. The cross-section views (along cross-section A-A' in Figure 2.1a) in Figure 2.6 show the predictions varying with X and Z, averaged over Y. At first glance, the RF(***M****XYZ*) predictions exhibit substantial variability with respect to [R, XYZ, f] for the same ***M***:

- The f = 1 Hz predictions are presented in Figures 2.5a-2.5c. The mean and standard deviation of predictions for each R are included in the bottom-left. While R increases as 10, 30, and 80 km, the mean prediction decreases as 0.1, 0.03, and 0.006 cm/s^2, showing a typical attenuation with distance effect. Interestingly, the standard deviation of predictions also decreases, rather dramatically, to 0.04, 0.01, and 0.003, indicating an atypical, heteroskedastic variability. It appears that the importance of XYZ on RF(***M****XYZ*) predictions decreases as the receiving station moves further away from the earthquake. Essentially, the RF(***M****XYZ*) predictions in this case suggest that the hypocentral location [XYZ] becomes progressively irrelevant as R increases. At short distances [R = 10 km], however, the hypocentral location [XYZ] plays a rather significant role, as seen in both map and cross-sectional views, but this is better discussed for higher frequencies with higher prediction variabilities.

- The f = 3 Hz predictions are shown in Figures 2.5d-2.5f. The typical distance attenuation, i.e., decreasing mean predictions with distance, is similar to that observed for f = 1 Hz. However, the reduction in prediction standard deviation with increasing R is much more dramatic, dropping from 0.19 at R = 10 km to 0.005 at R = 80 km. While the XYZ-dependent variability at f = 1 Hz decreases by a factor of 10, at f = 3 Hz it decreases roughly by a factor of 40.

- The f = 10 Hz predictions are indicated in Figures 2.5g-2.5i. The decrease in standard deviation of predictions with distance is as pronounced as that observed for f = 3 Hz. The map view of the f = 10 Hz predictions exhibits a certain smoothness, without abrupt or noisy variabilities. Instead, RF(***M****XYZ*) appears to

predict weaker ground-motions for hypocentral locations in the northwest portion of the seismicity and stronger ground-motions for those in the southeast. In the central region, the model predicts stronger ground-motions for events originating in the northeast and weaker ground-motions for those in the southwest. However, these spatial patterns also vary with both frequency f and distance R.

- Across all frequencies and at sites located at R = 10 km and R = 30 km, we now investigate the cross-sectional plots showing the XZ dependencies in Figure 2.6. In general, RF(***M****XYZ*) predicts stronger ground-motions at deeper hypocentral locations, which is consistent with previous studies. However, there are a few very interesting deviations. For example, the shallow seismicity in the northwest of the Visso earthquake ($0 < Z < 5$ km and distance 0 – 15 km from A), the intermediate central seismicity between Visso and Norcia earthquakes ($4 < Z < 8$ km and distance 0 – 20 km from A), and the deeper seismicity in the southeast of Amatrice and close to Compotosto mainshocks ($Z > 8$ km and distance 47 – 80 km from A) are appear to produces stronger than average ground-motions, which also deviate from the otherwise gradual changes from northwest to southeast and shallow to deeper seismicity.

Several noteworthy features emerge from the RF(***M****XYZ*) predictions. However, these observations would have limited significance unless they can be linked to physically meaningful or parametrically interpretable processes. We attempt to address this in the subsequent Discussion section. Nonetheless, RF(***M****XYZ*) captures and predicts nonlinear interactions among its explanatory variables (features) that are not explicitly represented in the parametric PR(***M***) formulation. At the same time, such interactions may be dataset-specific and therefore not necessarily generalizable to other regions or earthquake sequences.

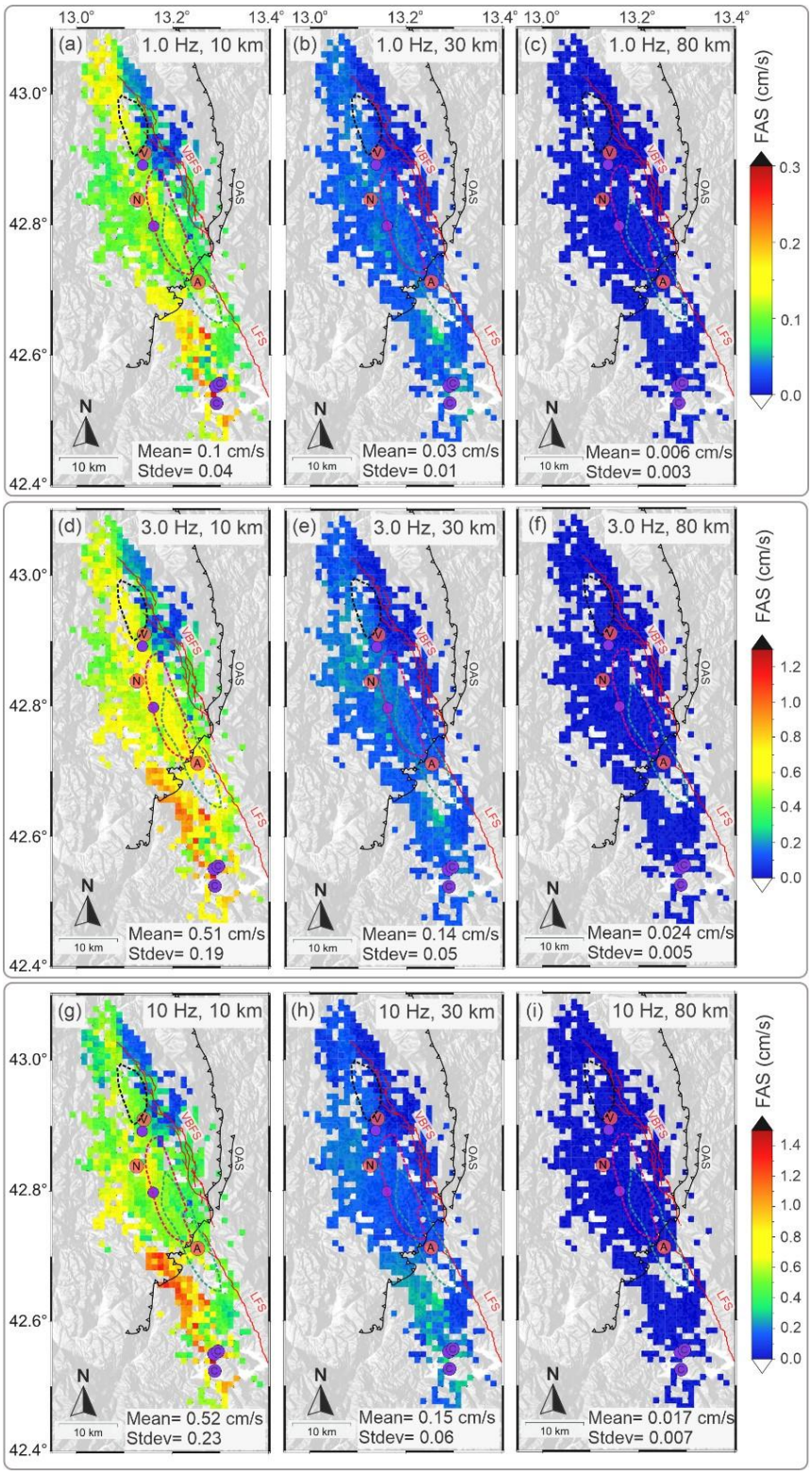

Figure 2.5. Spatial distribution of fixed-effects predictions obtained from RF(***MRXYZ***) for an ***M***2.5 earthquake under different frequency and distance scenarios: **(a)** f = 1 Hz, R = 10 km,

(b) f = 1 Hz, R = 30 km, **(c)** f = 1 Hz, R = 80 km, **(d)** f = 3 Hz, R = 10 km, **(e)** f = 3 Hz, R = 30 km, **(f)** f = 3 Hz, R = 80 km, **(g)** f = 10 Hz, R = 10 km, **(h)** f = 10 Hz, R = 30 km, and **(i)** f = 10 Hz and R = 80 km. The red lines in the subplots represent the two causative Normal faults of the Vettore-Bove Fault System (VBFS) and the Laga Fault System (LFS). The circles labelled A, V, N, and C mark the epicenters of Amatrice, Visso, Norcia, and Compotosto mainshocks, respectively. Each 1 km × 1 km square is colored according to the average values of FAS along Z for the events located within that cell. Green, black, and pink dashed circular shapes indicate the slip area (after Pizzi et al., 2017; Scognamiglio et al., 2018) corresponding to Amtarice (0.3 m), Visso (0.3 m), and Norcia (0.8 m) mainshocks, respectively. The black barbed lines indicate the thrust fault systems.

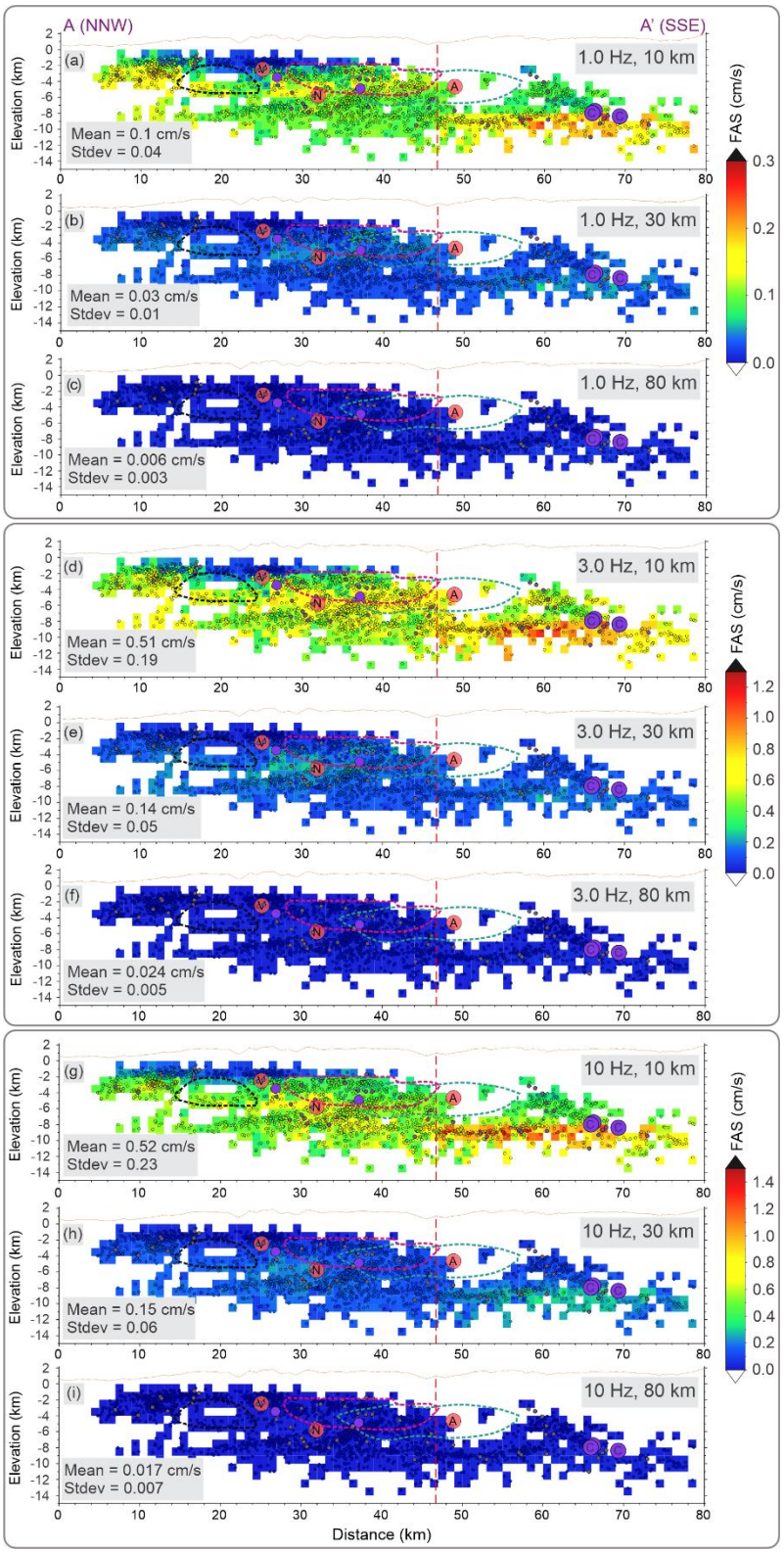

Figure 2.6. Along strike cross-sectional view of the spatial distribution of fixed-effects prediction obtained from RF(***MRXYZ***) for an ***M***2.5 earthquake under different frequency and

distance scenarios: **(a)** f = 1 Hz, R = 10 km, **(b)** f = 1 Hz, R = 30 km, **(c)** f = 1 Hz, R = 80 km, **(d)** f = 3 Hz, R = 10 km, **(e)** f = 3 Hz, R = 30 km, **(f)** f = 3 Hz, R = 80 km, **(g)** f = 10 Hz, R = 10 km, **(h)** f = 10 Hz, R = 30 km, and **(i)** f = 10 Hz and R = 80 km. The circles labelled A, V, N, and C mark the epicenters of Amatrice, Visso, Norcia, and Compotosto mainshocks, respectively. Each 1 km × 1 km square is colored according to the average values of FAS along Y for the events located within that cell. Green, black, and pink dashed circular shapes indicate the slip area (after Pizzi et al., 2017; Scognamiglio et al., 2018) corresponding to Amtarice (0.3 m), Visso (0.3 m), and Norcia (0.8 m) mainshocks, respectively. The black barbed lines indicate the thrust fault systems. The red vertical dashed lines in the subplots separate the earthquakes occurring along the strike of the VBFS (distance 0-47 km from A) and the LFS (distance 47-80 km from A).

2.4.3. GMM Random-Effects and Residuals

The random-effect terms and residuals of a mixed-effect GMM are as important as their fixed-effects. A mixed-effects GMM is composed of generic fixed-effect coefficients and specific adjustments to the generic coefficients for each level in the random-effect group. For instance, the between-site random-effect group $\Delta S2S(f)$ is composed of unique $\delta S2S_S(f)$ values for each site s in the dataset; here, the sites are the levels in the between-site group. $\delta S2S_S(f)$ can be used to adjust the generic coefficient $c_1(f)$ in Eq. 2.2 to produce site-specific predictions. $\Delta S2S(f)$ can also be used as a station correction to remove site effects from the observed Fourier spectra at the site, as described in our approach to estimate seismological parameters. However, the fixed-effects and random-effects must originate from the same mixed-effects GMM. This is because the random-effects are not supposed to show any biases or trends with respect to the explanatory variables [$\boldsymbol{M}$, R] used in the fixed-effects components.

In this study, we have three mixed-effects GMMs. The fixed-effects predictions of these three GMMs are similar and dissimilar in ways that are expected. In this section, we examine the random-effect estimates as a sanity check before investigating their physical meaning and relation to the estimated seismological

parameters. Our approach ensures that the [***M***, *R*] used in regressing the mixed-effects GMMs are fully consistent with the seismological parameters [M_0, f_c, $\Delta\sigma$, *Q(f)*].

2.4.3.1. Between-Event Random-Effects

First, we examine the *ΔB(f)* distributions of the three mixed-effect GMMs. In the case of the PR(***M***), the regression algorithm applies a constraint that *ΔB(f)* is (as closely as possible) to a symmetric Gaussian (Normal) distribution with zero-mean and standard deviation τ. This constraint is not applied in the non-parametric RF(***M***) and RF(***MXYZ***). However, the resulting empirical distributions of *ΔB(f)* are seldom Gaussian distributions and are often better characterised by a Student's t-distribution with heavier tails. To assess the normality of *ΔB(f)*, we perform Shapiro-Wilk tests (Massey, 1951) under the null hypothesis H_0: *ΔB(f)* follows a Gaussian distribution $N(0, \tau(f)^2)$. As expected, the test yields p-values << 0.05 at all frequencies for all three GMMs, strongly indicating that *ΔB(f)* does not follow a Gaussian distribution. In fact, the *ΔB(f)* is found to be skewed and to contain numerous outliers. Despite clear evidence that *ΔB(f)* is not a Gaussian, typical PSHA calculators treat it as such. Although challenging this assumption is not the primary objective of this study, it is worth noting that the parametric constraints, namely the Gaussian distribution of observations, also fail in this case. Therefore, as commonly recommended for skewed and heavy-tailed distributions, we estimate the mean (bias O_B) and robust median absolute deviation from the median (*MAD*, here τ) of *ΔB(f)* without the Gaussian assumption, rather than relying on the sample mean and standard deviation. For example, to use the *MAD* in PSHA calculations as a consistent estimator for the standard deviation of a Gaussian (Normal) distribution, it must be scaled by a factor of 1.46.

Figure 2.7a shows the $O_B(f)$ and $\tau(f)$ of the three GMMs. The $O_B(f)$ values of PR(***M***) and RF(***M***) are rather close to zero or contain zero at $f < 5$ Hz and lower than 10% of $\tau(f)$ at $f \geq 5$ Hz; while those of RF(***MXYZ***) are zero at all frequency ranges. The $\tau(f)$ of the PR(***M***) and RF(***M***) are rather close but distinct, with the latter having 5%

lower values at $f < 3$ Hz. The RF(***MXYZ***) has $\tau(f)$ 50% (on average across $0.5 \leq f \leq 25$ Hz) lower values than the other two. This is to be expected given the greater degree of freedom allowed for RF(***MXYZ***) through the hypocentral location [*XYZ*].

Figure 2.7b illustrates the similarity of event-specific terms $\delta B_e(f)$ obtained from the three GMMs. For this purpose, for each event *e*, we compute the Spearman correlation of its $\delta B_e(f)$ value estimated in the regression of the three GMMs. The histogram in Figure 2.7b shows the number of events as a function of their correlations: $\rho_{PR,RF}$, $\rho_{PR,RFXYZ}$, $\rho_{\mathrm{RF,RFXYZ}}$. The histogram of $\rho_{PR,RF}$ indicates that the $\delta B_e(f)$ estimates from PR(***M***) and RF(***M***) are almost perfectly correlated for almost all events. This implies that subsequent analyses of $\Delta B(f)$ can rely on the estimates from either PR(***M***) or RF(***M***). In contrast, the $\delta B_e(f)$ estimates from RF(***MXYZ***) are weakly correlated with those from the other two models, as reflected by most values of $\rho_{PR,RFXYZ}$, $\rho_{\mathrm{RF,RFXYZ}}$ being less than 0.5. In summary, the $\Delta B(f)$ terms of PR(***M***) and RF(***M***) are practically identical and can be considered interchangeable for further analyses.

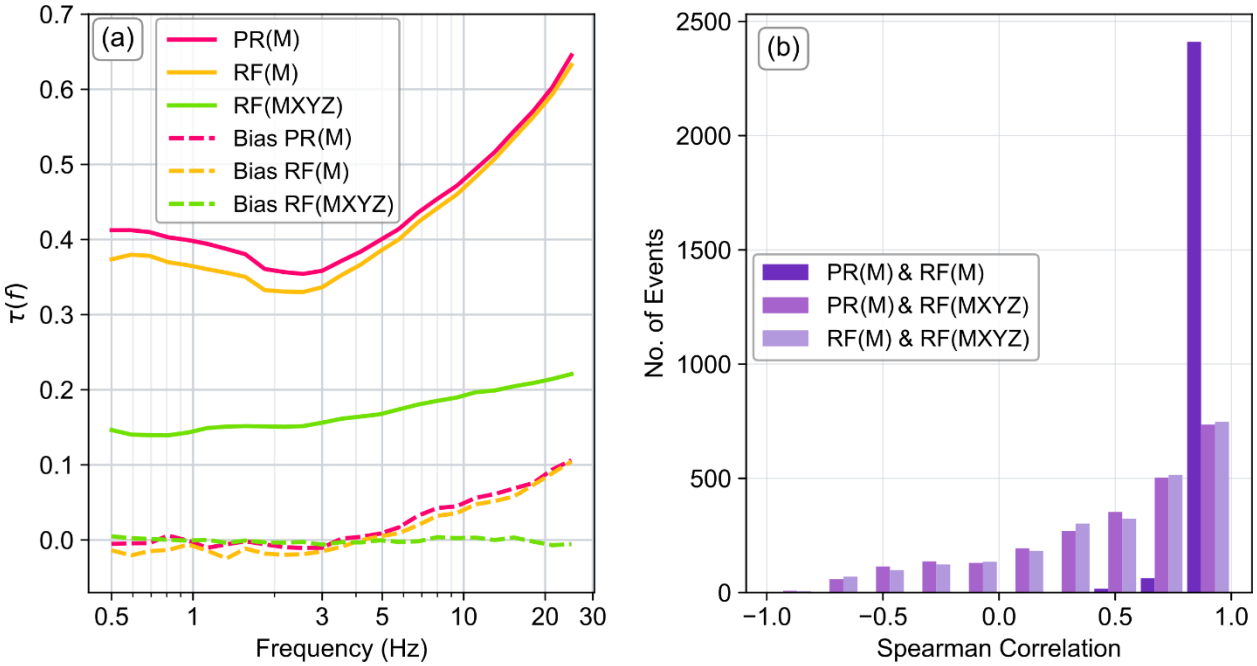

Figure 2.7. Comparison of between-event random-effects derived from the three mixed-effects ground-motion models: **(a)** The mean (bias O_B) and standard deviation (τ) of $\Delta B(f)$ from the three mixed-effect GMMs: PR(***M***) (pink curve), RF(***M***) (orange curve), and RF(***MXYZ***) (green curve). **(b)** Histogram of pair-wise Spearman correlation of $\delta B_e(f)$ from the three mixed-effect GMMs.

Figure 2.7a confirms that $\Delta B(f)$ derived from PR(***M***) and RF(***M***) are nearly perfectly correlated. Therefore, in the following analysis, we focus only on comparing $\Delta B(f)$ from RF(***M***) and RF(***MXYZ***). The map views in Figure 2.8 display XY distributions averaged along the Z direction. Accordingly, the average of $\Delta B(f)$ at a given [XY] location over Z is denoted as $\delta B_{XY}^{Z}(f)$. The cross-section views in Figure 2.9 show the predictions varying with X and Z (along the cross-section A-A' in Figure 2.1a), averaged over Y; thus, the average of $\Delta B(f)$ at a given [XZ] location over Y is denoted as $\delta B_{XZ}^{Y}(f)$. In Figures 2.8d-2.8f and Figures 2.9d-2.9f, corresponding to RF(***MXYZ***), no systematic spatial variability in $\Delta B(f)$ is observed. This indicates that the hypocentral dependence of $ln\,(FAS, f)$ at frequencies of 1, 3, and 10 Hz is effectively captured by the fixed-effects of RF(***MXYZ***), as previously illustrated in

Figure 2.5. In contrast, Figures 2.8a-2.8c and Figures 2.9a-2.9c, corresponding to RF(***M***), exhibit pronounced spatial variability in δB_{XY}^{Z} at frequencies of 1, 3, 10 Hz, revealing a clear dependence on [*XYZ*]. As a reminder, $\delta B_{XY}^{Z}(f) > 0$ indicates the events that generate systematically stronger $ln\,(FAS, f)$ than those with $\delta B_{XY}^{Z}(f) < 0$, despite having identical ***M***. Examination of the spatial patterns of $\delta B_{XY}^{Z}(f)$ and $\delta B_{XZ}^{Y}(f)$ for RF(***M***) reveals several notable features:

- At f = 1 Hz, the δB_{XY}^{Z} and δB_{XZ}^{Y} values for shallow events to the northwest of the Visso mainshock are systematically more positive than those for deeper events towards the southeast of the Amatrice and close to Compotosto mainshocks. However, the *RF(**M**XYZ)* fixed-effects predictions for f = 1 Hz at R = 10 km in Figure 2.5a, suggest nearly the opposite trend: shallow events in the northwest are predicted to generate stronger ground-motions than deeper events in the southeast. Moreover, the deepest events in the southeast exhibit mostly negative δB_{XY}^{Z} and δB_{XZ}^{Y} values, yet their RF(***M**XYZ*) predictions are among the largest. In robust mixed-effects regression using Huber's loss function (Huber, 1964), sample values exceeding ±1.35*MAD* from the center of a distribution are typically considered outliers. In this case, Figure 2.7a shows that although the *MAD* (τ) of the RF(***M***) at f = 1 Hz is approximately 0.4, the δB_{XY}^{Z} and δB_{XZ}^{Y} values at f = 1 Hz exceed 0.8 toward the northwest of the Visso, which is about 2τ away from the center of the distribution. From this perspective, events in this region may be regarded as outliers. At the same time, the standard deviation of the RF(***M**XYZ*) fixed-effects predictions in Figure 2.5a is less than 0.04. Taken together, these observations indicate that while the *RF(**M**XYZ)* fixed-effects predictions at f = 1 Hz exhibit only weak spatial variability, the ΔB of RF(***M***) at f = 1 Hz captures stronger spatial variability, including possible statistical outliers or physical anomalies.

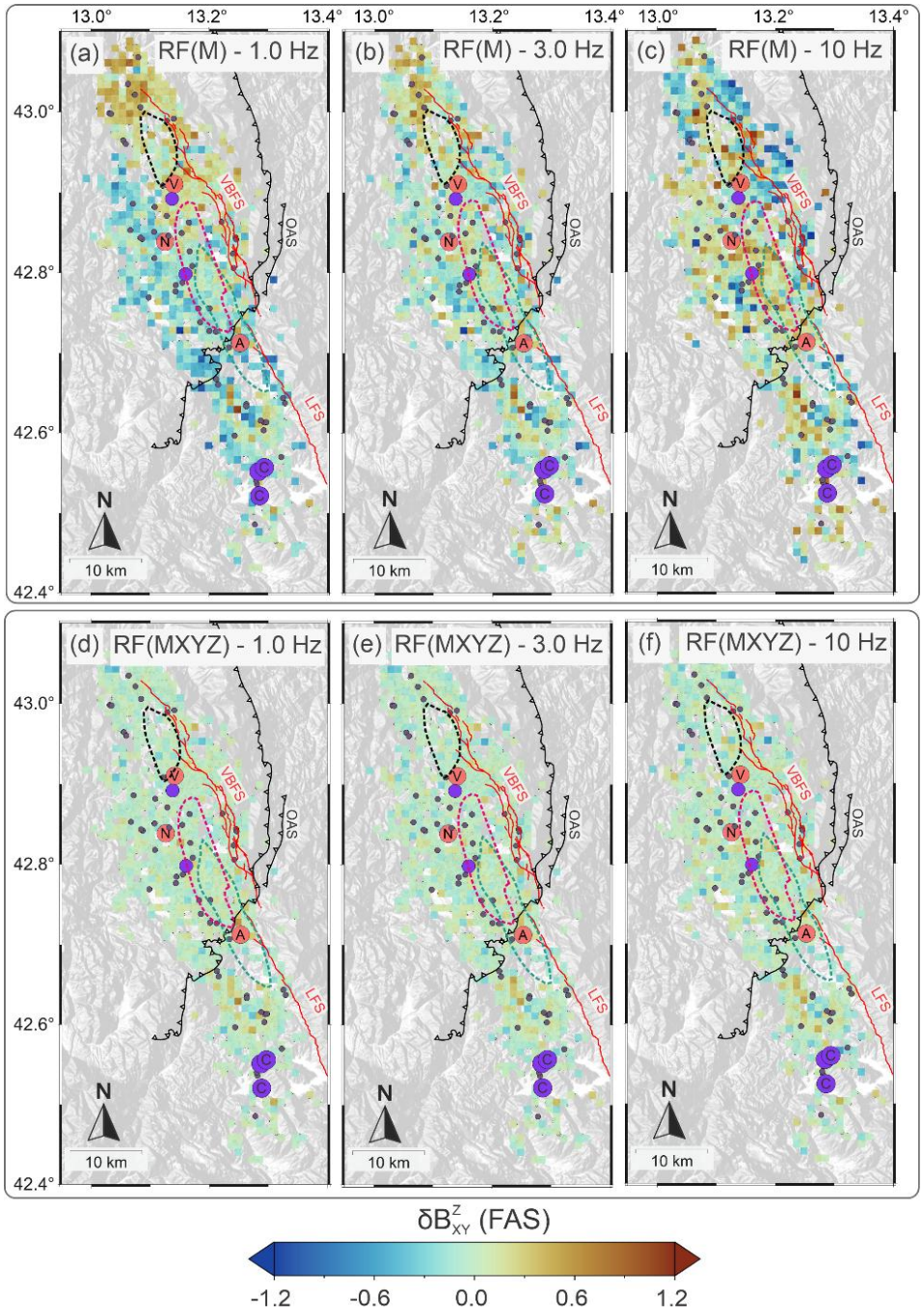

Figure 2.8. Spatial distribution of between-event residuals for FAS obtained from RF(***M***) and RF(***MXYZ***) at different frequencies. $\delta B_{XY}^{Z}(f)$ obtained from model RF(***M***) at **(a)** f = 1 Hz, **(b)** f = 3 Hz, **(c)** f = 10 Hz. $\delta B_{XY}^{Z}(f)$ obtained from model RF(***MXYZ***) at **(d)** f = 1 Hz, **(e)** f = 3 Hz, **(f)** f = 10 Hz. The red lines in the subplots represent the two causative Normal faults of the Vettore-Bove Fault System (VBFS) and the Laga Fault System (LFS). The circles labelled A, V, N, and C mark the epicenters of Amatrice, Visso, Norcia, and Compotosto mainshocks,

respectively. The purple and dark grey circles denote the epicenters of events with ***M***5-6 and ***M***4-5, respectively. Each 1 km × 1 km square is colored according to the average values of δB_e along Z for the events located within that cell. Green, black, and pink dashed circular shapes indicate the slip area (after Pizzi et al., 2017; Scognamiglio et al., 2018) corresponding to Amtarice (0.3 m), Visso (0.3 m), and Norcia (0.8 m) mainshocks, respectively. The black barbed lines indicate the thrust fault systems.

- The large cluster of positive δB_{XY}^{Z} and δB_{XZ}^{Y} values at f = 1 Hz for shallow events towards the northwest of the Visso earthquake are less pronounced at f = 3 Hz. At f = 3 Hz, the spatial patterns of positive δB_{XY}^{Z} and δB_{XZ}^{Y} values coincide with the larger Fourier ground-motions predicted by the RF(***MXYZ***) at R = 10 km in Figure 2.5d, and vice-versa. In addition, unlike the case for f = 1 Hz, the standard deviation (0.19) of RF(***MXYZ***) prediction at f = 3 Hz and R = 10 km is comparable to the difference (0.18) between τ at f = 3 Hz of the RF(***M***) and RF(***MXYZ***), as shown in Figure 2.7a. However, although the deeper seismicity south of the Amatrice rupture does not show any distinct δB_{XY}^{Z} and δB_{XZ}^{Y} trends at f = 3 Hz, the RF(***MXYZ***) predictions in that region are still the largest.
- The spatial trends of δB_{XY}^{Z} and δB_{XZ}^{Y} at f = 10 Hz are strikingly similar to the corresponding f = 10 Hz fixed-effects predictions of RF(***MXYZ***) at R = 10km shown in Figure 2.5f. Unlike the case for f = 1 and 3 Hz, the δB_{XY}^{Z} and δB_{XZ}^{Y} values at f = 10 Hz for the deeper seismicity south of Amatrice rupture are systematically more positive than elsewhere. This pattern is in closer agreement with the markedly larger-than-average Fourier amplitudes predicted by RF(***MXYZ***) at f = 10 Hz and R = 10 km.

We observe a strong frequency-dependent spatial variability of $\Delta B(f)$ random-effects of both PR(***M***) and RF(***M***) GMMs. This suggests that $\Delta B(f)$ is sensitive to the combination of different seismological properties at different frequencies (e.g., Bindi et al., 2020), and may reflect underlying physical anomalies or statistical outliers. These observations are discussed in the Discussion section subsequently.

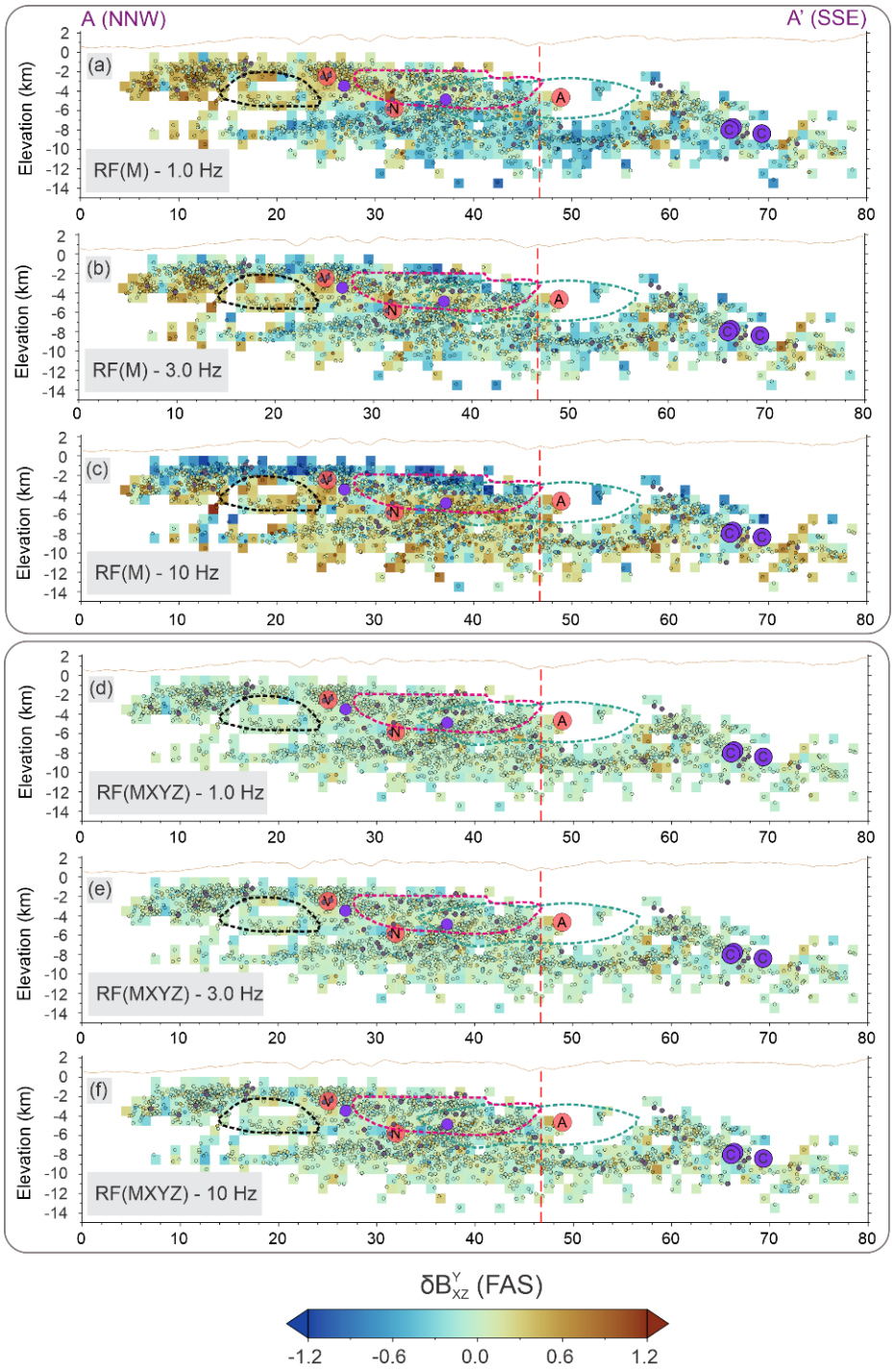

Figure 2.9. Along strike cross-sectional view of the spatial distribution of between-event residuals for FAS obtained from RF(***M***) and RF(***MXYZ***). $\delta B_{XZ}^{Y}(f)$ obtained from model RF(***M***) at **(a)** f = 1 Hz, **(b)** f = 3 Hz, **(c)** f = 10 Hz. $\delta B_{XZ}^{Y}(f)$ obtained from model RF(***MXYZ***) at **(d)** f = 1 Hz, **(e)** f = 3 Hz, **(f)** f = 10 Hz. The circles labelled A, V, N, and C mark the epicenters of Amatrice, Visso, Norcia, and Compotosto mainshocks, respectively. The purple and dark grey

circles denote the epicenters of events with $\boldsymbol{M}$5-6 and $\boldsymbol{M}$4-5, respectively. Each 1 km × 1 km square is colored according to the average values of δB_e along Y for the events located within that cell. Green, black, and pink dashed circular shapes indicate the slip area (after Pizzi et al., 2017; Scognamiglio et al., 2018) corresponding to Amtarice (0.3 m), Visso (0.3 m), and Norcia (0.8 m) mainshocks, respectively. The black barbed lines indicate the thrust fault systems. The red vertical dashed lines in the subplots separate the earthquakes occurring along the strike of the VBFS (distance 0-47 km from A) and the LFS (distance 47-80 km from A).

Although not shown here, the typical $\Delta B(f)$ versus $\boldsymbol{M}$ plots of all three GMMs show no biases or trends, confirming that the $\boldsymbol{M}$-scaling of $ln\,(FAS, f)$ is sufficiently captured by the fixed-effects. However, there is clear evidence of heteroskedasticity in the variability of $\Delta B(f)$ with respect to $\boldsymbol{M}$; specifically, $\tau(f)$ is larger for smaller magnitudes and decreases as $\boldsymbol{M}$ increases (Youngs et al., 1997). Typical GMPMs derived from datasets spanning $3 < \boldsymbol{M} < 8$ commonly show a larger dispersion in $\Delta B(f)$ for $\boldsymbol{M} < 5.5$ compared to $\boldsymbol{M} \geq 5.5$. To account for this behavior, GMPM developers fit a magnitude- and frequency-dependent $\tau(\boldsymbol{M}, f)$ to these trends and recommend its use in PSHA to avoid overestimating the probability of extreme ground-motions for relatively under-sampled $\boldsymbol{M} \geq 5.5$ events (Gregor et al., 2014; Weatherill et al., 2020). Interestingly, heteroskedasticity of $\tau(f)$ is also evident within the more limited $2.35 \leq \boldsymbol{M} \leq 4.62$ dataset used in this study.

Another notable feature is that the estimation and spatial variability of ΔB at f = 10 Hz in PR($\boldsymbol{M}$) regressions are (by construction, and as widely recognized) independent of distance (e.g., Strasser et al., 2009). In contrast, the spatial variability of the RF($\boldsymbol{MXYZ}$) fixed-effects predictions at f = 10 Hz (*Stdev* in Figure 2.5g-2.5i) rapidly diminishes with distance. This contrast suggests that τ at f = 10 Hz may be heteroskedastic with respect to R, contrary to the customary homoscedastic assumption adopted in PR($\boldsymbol{M}$) GMMs and in PSHA applications. If the ΔB of RF($\boldsymbol{M}$) and PR($\boldsymbol{M}$) GMMs at f = 10 Hz are indeed correlated with stress-drop (see

Discussions), then the long-standing question regarding τ and stress-drop variability, the so-called "sigma of stress-drop" (Cotton et al., 2013), may warrant reconsideration, as also suggested by Trugman & Shearer (2018).

2.4.3.2. Between-Site Random-Effects

As in the previous analysis, we first apply the Shapiro–Wilk and Two-sided Kolmogorov-Smirnov (Massey, 1951) tests with the null-hypothesis H_0: $\Delta S2S(f)$ follows a Gaussian distribution $N(0, \Phi_{S2S}(f)^2)$. The tests yield p-values << 0.05 at most frequencies for all three GMMs, suggesting that $\Delta S2S(f)$ does not consistently follow a Gaussian distribution. Similar to $\Delta B(f)$, $\Delta S2S(f)$ is found to be skewed and to contain a few outliers. Accordingly, we estimate the median (bias $O_S(f)$) and *MAD* ($\Phi_{S2S}(f)$) of $\Delta S2S(f)$ without the Gaussian assumption. Figure 2.10 presents the counterpart of Figure 2.7 for $\Delta S2S(f)$. In contrast to $\Delta B(f)$, for which the between-event variability $\tau(f)$ of PR(***M***) and RF(***M***) was substantially larger than that of RF(***MXYZ***), the single-station variability $\Phi_{S2S}(f)$ is nearly identical across the three GMMs (Figure 2.10a). The biases $O_S(f)$ are non-zero but small relative to their corresponding $\Phi_{S2S}(f)$ values. It is also noteworthy that the mean of $\Delta S2S(f)$ in the PR(***M***) is always zero, whereas the means of the non-parametric GMMs, without an imposed constraint on the $\Delta S2S(f)$ distribution, closely resemble $O_S(f)$ values shown here.

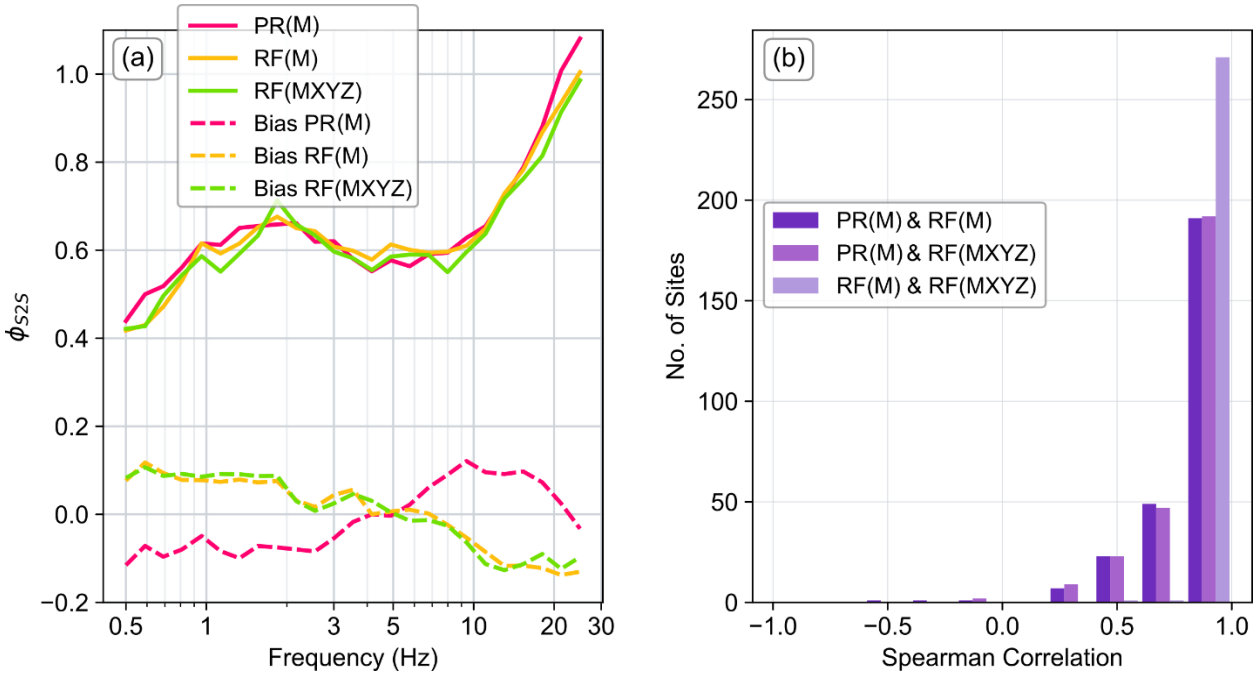

Figure 2.10. Comparison of between-site random-effects derived from the three mixed-effects ground-motion models: **(a)** The mean (bias O_B) and standard deviation (Φ_{S2S}) of $\Delta S2S(f)$ from the three mixed-effect GMMs: PR(***M***) (pink curve), RF(***M***) (orange curve), and RF(***MXYZ***) (green curve). **(b)** Histogram of pair-wise Spearman correlation of $\delta S2S_S(f)$ from the three mixed-effect GMMs.

Figure 2.10b shows the similarity of the site-specific $\delta S2S_S(f)$ estimated from the three GMMs. Following the approach used for Figure 2.7, we compute, for each site s, the Spearman correlation coefficient between $\delta S2S_S(f)$ obtained from the regressions of each pair of GMMs. The histogram illustrates the number of sites as a function of their correlations: $\rho_{PR,RF}$, $\rho_{PR,RFXYZ}$, $\rho_{RF,RFXYZ}$. The $\Delta S2S(f)$ term from RF(***M***) and RF(***MXYZ***) is nearly perfectly correlated. Moreover, the histograms of $\rho_{PR,RF} >$ 0.75 and $\rho_{PR,PFXYZ} >$ 0.75 indicate that $\delta S2S_S(f)$ of most sites are quite strongly correlated across models. Visual inspection of $\delta S2S_S(f)$ for 12 sites with $\rho_{PR,RF} <$ 0.5 reveals that $\delta S2S_S$ values at $f <$ 5 Hz obtained from RF(***M***) are consistently larger than those estimated using PR(***M***), and $\delta S2S_S$ values at $f >$ 5 Hz derived from RF(***M***) are consistently smaller than those estimated by PR(***M***) model. This is in complete

agreement with $O_S(f < 5\ \text{Hz}) > 0$ and $O_S(f > 5\ \text{Hz}) < 0$ of RF(***M***) and RF(***MXYZ***) shown in Figure 2.10a. Therefore, the non-zero $O_S(f)$ values of the two non-parametric models are driven by a small subset of sites and likely the asymmetric, non-Gaussian distributions of their $\Delta S2S(f)$.

It is important to recall that, in the estimation of seismological parameters, we used the $\Delta S2S(f)$ from RF(***M***) as a station correction to the Fourier spectra. Alternatively, the $\Delta S2S(f)$ terms from RF(***MXYZ***) could have been used without affecting the results, as they are nearly perfectly correlated with those from RF(***M***), as indicated by the high $\rho_{RF,RFXYZ}$ values in Figure 2.10a. Even if the slightly less correlated $\Delta S2S(f)$ terms from PR(***M***) were used instead, the estimated seismological parameters would remain largely unchanged. An additional observation is that all sites with $\rho_{PR,RF} < 0.5$ are aligned along the fault strike. However, the lack of detailed geological characterization at these sites precludes a critical evaluation of their $\delta S2S_s(f)$ behavior. We therefore conclude that $\Delta S2S(f)$ terms from any of the three GMMs can be used as site corrections in the estimation of seismological parameters. Nevertheless, $\Delta S2S(f)$ values derived from the non-parametric GMMs are preferable, similar to site terms obtained from non-parametric spectral decomposition approaches, because they are less likely to be biased by parametric constraints.

2.4.3.3. Residuals

Residuals, denoted as $E(f)$, are obtained from the three mixed-effects GMMs. Unlike the random-effects terms $\Delta B(f)$ and $\Delta S2S(f)$, which can be used as event-specific and site-specific adjustments to produce partially non-ergodic predictions, $E(f)$ cannot be applied in this manner. Nevertheless, these residuals can be analyzed to identify secondary phenomena that are not captured by the mixed-effects structure, such as shear-wave radiation anisotropy (e.g., Kotha et al., 2019), nonlinear soil response (e.g., Loviknes et al., 2021), path effects and crustal controls on ground-motions (e.g., Sahakian et al., 2018; Sahakian et al., 2019), and other forms of spatial variability (e.g., Brunelli et al., 2023). Despite their potential value for

improving ground-motion prediction models, such residuals remain underexplored. In this study, we therefore limit our analysis to demonstrating the statistical equivalence of *E(f)* derived from the three mixed-effects GMMs, as the event- and site-specific metadata required for a more detailed interpretation are not available in the dataset.

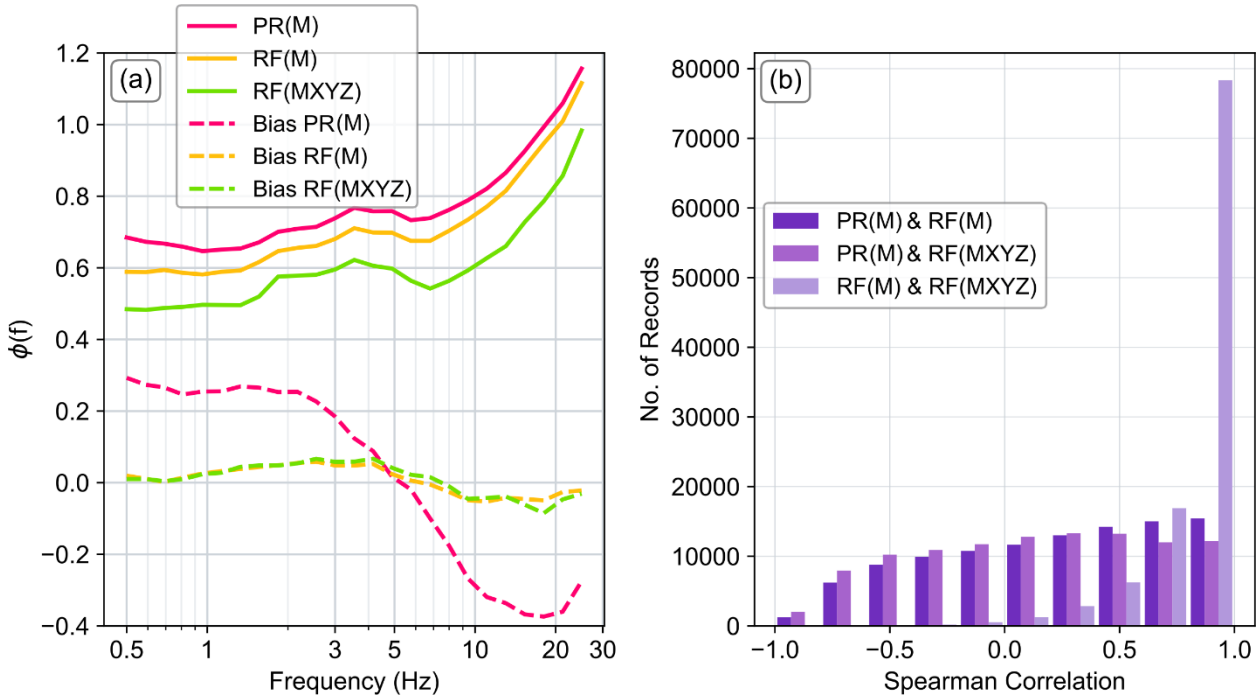

Figure 2.11. Comparison of residual distributions derived from the three mixed-effects ground-motion models: **(a)** The mean (bias O_B) and standard deviation (Φ) of *E(f)* from the three mixed-effect GMMs: PR(***M***) (pink curve), RF(***M***) (orange curve), and RF(***MXYZ***) (green curve). **(b)** Histogram of pair-wise Spearman correlation of $\varepsilon_{e,s}(f)$ from the three mixed-effect GMMs.

Figure 2.11 follows the same configuration as Figures 2.7 and 2.10, but for the residuals *E(f)*. We recall that *E(f)* represents frequency-dependent distributions composed of record-specific residual vectors $\varepsilon_{e,s}(f)$, indexed by event *e* and site *s*. Two-sided Kolmogorov-Smirnov Tests show that the *E(f)* do not consistently follow a

Gaussian distribution. As shown in Figure 2.11a, the *MAD Φ(f)* of *E(f)* is largest for the PR(***M***), and smallest for RF(***MXYZ***) due to its additional [*XYZ*] degrees of freedom. The median bias *O(f)* of PR(***M***) is often non-zero, representing a significant deviation from the assumed constraint $E(f) = N(0, \Phi(f)^2)$. This behavior, along with the comparatively large *Φ(f)*, is likely attributable to the parametric constraints imposed by the frequency-independent geometric spreading (Eq. 2.3) in the PR(***M***) model.

Figure 2.11b illustrates the record-to-record similarity of $\varepsilon_{e,s}(f)$ estimated from the three GMMs. As evidenced by the histograms of $\rho_{RF,RFXYZ} \geq 0.75$, the overwhelming majority of $\varepsilon_{e,s}(f)$ are strongly correlated across two non-parametric models. For example, although not shown here for brevity, nearly all events in the dataset are recorded with complete 360° azimuthal station coverage. Under such conditions, we observe strong and nearly identical spatial anisotropies in the event- and site-specific residuals $\varepsilon_{e,s}(f)$ of RF(***M***) and RF(***MXYZ***). The Spearman correlation of $\varepsilon_{e,s}(f)$ of the PR(**M**) is often very poor, as seen from the thousands of records with weak and negative correlations. The *E(f)* residual also shows strong anisotropies from both event and site perspectives, and is often different from those of the non-parametric counterparts. This anisotropy may be related to point-source shear-wave radiation patterns and/or directivity effects, as previously reported for the same region by Castro et al. (2006) and Pacor et al. (2016), and in other tectonic settings by Trugman et al. (2021). However, because centroid moment tensor solutions for the numerous small earthquakes in our catalog were not available at the time of this study, we do not pursue this analysis further.

2.5. Discussion

In summary, the Result section demonstrates that the three mixed-effects GMMs behave as expected. The fixed-effects predictions of the parametrically constrained PR(***M***) differ from those of RF(***M***) and RF(***MXYZ***) near the [***M***, *R*] boundaries of the dataset, whereas the non-parametric GMMs show close agreement with one another (Figure 2.4). The between-event random-effects and variances,

$\Delta B(f) = N(0, \tau(f)^2)$, of PR(***M***) and RF(***M***) are also in close agreement, while those of RF(***MXYZ***) differ significantly due to the inclusion of hypocentral location [*XYZ*] in its fixed-effects (Figure 2.7). The RF(***MXYZ***) fixed-effects exhibits coherent spatial variability (Figures 2.5 and 2.6), which is examined in detail subsequently. The between-site random-effects and variances, $\Delta S2S(f) = N(0, \Phi_{S2S}(f)^2)$, show strong agreement across all three GMMs (Figure 2.10). The *ΔS2S(f)* term from RF(***M***) was used as a site-correction in the estimation of seismological parameters because they are expected to be less biased by the parametric constraints of PR(***M***), similar to the use of site transfer functions obtained from non-parametric spectral decomposition. Nevertheless, *ΔS2S(f)* must be used strictly with the fixed-effects of its parent GMM when performing site-specific predictions in PSHA. The residuals and residual variances, $E(f) = N(0, \Phi(f)^2)$, from RF(***M***) and RF(***MXYZ***) are nearly perfectly correlated (Figure 2.11). Moreover, because almost all events are recorded by a network with near 360° azimuthal coverage, we infer that the estimated seismological parameters are largely unbiased by shear-wave radiation anisotropy, and that the RF(***MXYZ***) fixed-effects predictions are, as intended, isotropic. A more detailed investigation of *ΔS2S(f)* and *E(f)* would require additional site-characterization data and information on earthquake focal mechanisms, respectively.

The primary objective of this study is to investigate the physical meaning of *ΔB* from the three GMMs and the fixed-effects predictions of RF(***MXYZ***). This is accomplished by analyzing their correlations with consistently estimated seismological parameters. Given that both *ΔB* and *Q(f)* terms are magnitude-independent parameters, the stress-drop values are then normalized to remove the influence of magnitude scaling (Kemna et al., 2021). Hereafter, this is referred to as the normalized stress-drop $\Delta\sigma_N$, defined as the natural logarithm of the event-specific stress-drop $\Delta\sigma_i$ divided by the mean stress-drop of the corresponding magnitude-bin $\Delta\sigma_{bin}$, using a bin width of 0.5: $\Delta\sigma_N = \ln(\Delta\sigma_i / \Delta\sigma_{bin})$. Since the between-event residuals of PR(***M***) and RF(***M***) are nearly identical (Figure 2.7), we focus on the correlations between *ΔB* from RF(***M***) and RF(***MXYZ***) and the parameters of $\Delta\sigma_N$ and $Q_e(f)$.

Figure 2.12 presents the $\Delta B(PGA)$ from the RF($\boldsymbol{M}$), together with $\Delta\sigma_N$, and $Q_{0,e}$, in both *XY* map views and *XZ* cross-sectional views. We discuss $\Delta B(PGA)$ because it is frequency-independent, enabling direct comparison with the frequency-independent parameters of $\Delta\sigma_N$ and $Q_{0,e}$ ($Q_{0,e}$ represents the frequency-independent component of $Q_e(f)$). As in previous figures, the plotted values represent spatial averages rather than point estimates. The *XY* map views (Figures 2.12a-c) represent quantities averaged along the *Z* direction, whereas the *XZ* cross sections (Figures 2.12d-f) display quantities averaged along the *Y* direction. In the *XY* maps, the average of $\Delta B(PGA)$ at a given [*XY*] location over *Z* is denoted as $\delta B_{XY}^{Z}(PGA)$. The corresponding averaged normalized stress-drop and attenuation parameter are denoted as $\Delta\sigma_{N,XY}^{Z}$ and $Q_{0,XY}^{Z}$. In the *XZ* cross-sectional views, the analogous quantities averaged over *Y* are denoted as $\delta B_{XZ}^{Y}(PGA)$, $\Delta\sigma_{N,XZ}^{Y}$, and $Q_{0,XZ}^{Y}$.

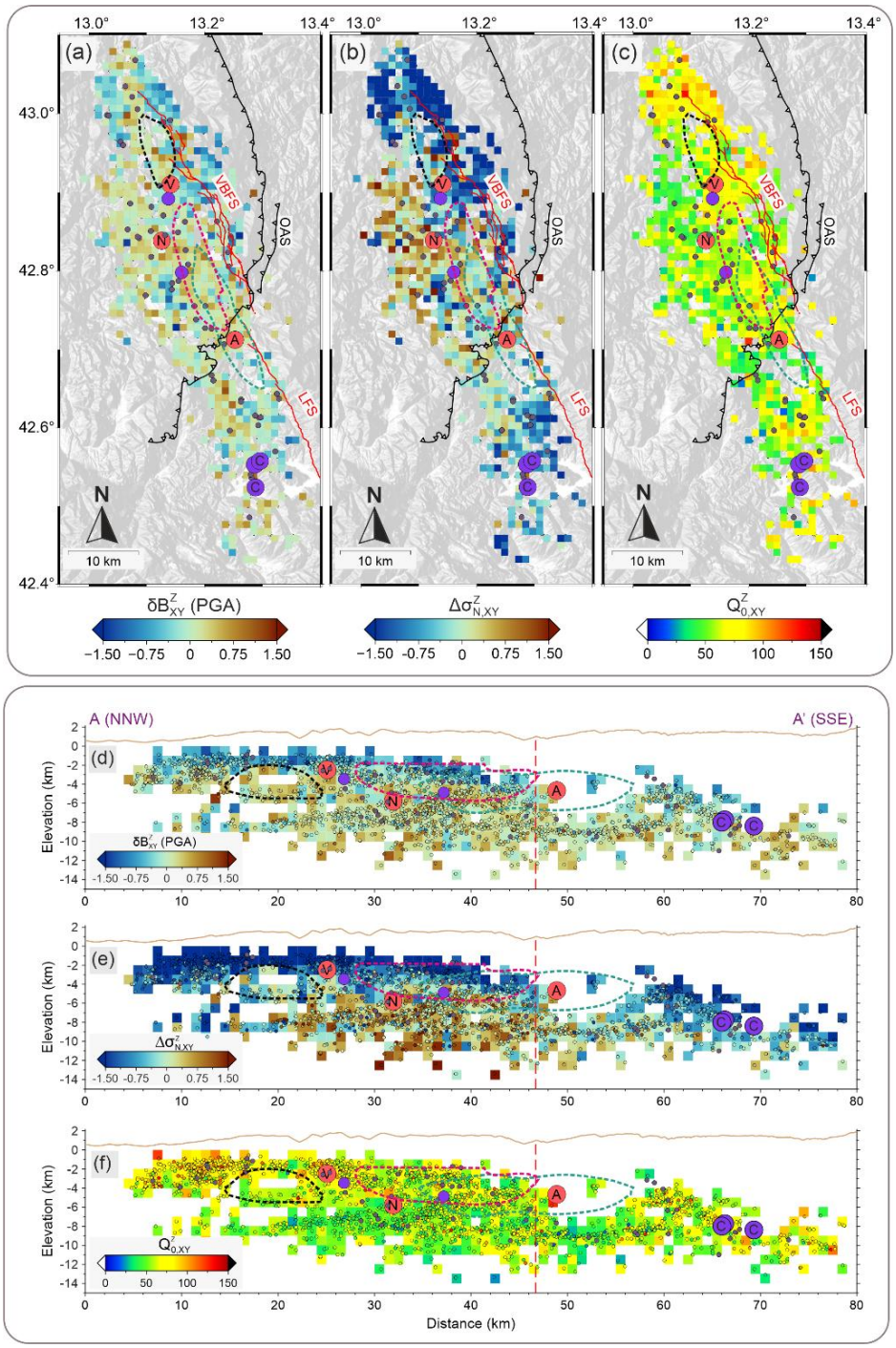

Figure 2.12. Spatial distribution of between-event residuals ($\delta B_e(PGA)$), normalized stress-drop ($\Delta\sigma_N$), and frequency-independent quality factor ($Q_{0,e}$). Map view of **(a)** spatial distribution of $\delta B_e(PGA)$ obtained from RF(***M***), **(b)** spatial distribution of ($\Delta\sigma_N$), and **(c)** spatial distribution of $Q_{0,e}$. Along strike cross-sectional view of the spatial distribution of **(d)** spatial distribution of $\delta B_e(PGA)$ obtained from RF(***M***), **(e)** spatial distribution of $\Delta\sigma_N$, and **(f)**

spatial distribution of $Q_{0,e}$. The red lines in subplots (a), (b), and (c) represent the two causative Normal faults of the Vettore-Bove Fault System (VBFS) and the Laga Fault System (LFS). The circles labelled A, V, N, and C mark the epicenters of Amatrice, Visso, Norcia, and Compotosto mainshocks, respectively. The purple and dark grey circles denote the epicenters of events with $\boldsymbol{M}$5-6 and $\boldsymbol{M}$4-5, respectively. Each 1 km × 1 km square is colored according to the mean values of $\delta B_e(PGA)$, $\Delta\sigma_N$, and Q_0 for the events located within it. Green, black, and pink dashed circular shapes indicate the slip area (after Pizzi et al., 2017; Scognamiglio et al., 2018) corresponding to Amtarice (0.3 m), Visso (0.3 m), and Norcia (0.8 m) mainshocks, respectively. The black barbed lines indicate the thrust fault systems. The red vertical dashed lines in subplots (d), (e), and (f) separate the earthquakes occurring along the strike of the VBFS (distance 0-47 km from A) and the LFS (distance 47-80 km from A).

At first glance, Figure 2.12 indicates that larger (more positive) values of $\delta B_{XY}^{Z}(PGA)$ and $\delta B_{XZ}^{Y}(PGA)$ tend to coincide with the above-average (more positive) values of $\Delta\sigma_{N,XY}^{Z}$ and $\Delta\sigma_{N,XZ}^{Y}$, as well as with lower values of $Q_{0,XY}^{Z}$ and $Q_{0,XZ}^{Y}$, and vice versa. In other words, earthquakes that generate stronger-than-average PGA are associated with more positive $\delta B_e(PGA)$. Intuitively, one might expect such events to originate in regions characterized by higher $Q_{0,e}$ (i.e., lower attenuation). However, the observed patterns suggest a more complex and somewhat counterintuitive relationship. For small earthquakes with f_c~5 Hz, PGA is primarily controlled by Fourier amplitudes around f_c. The spatial variability of $Q_{0,e}$ is smaller than $Q_e(f \sim 5$ Hz) because $Q_e(f) = Q_{0,e}.f^{n_e}$ with $n_e > 0$ (Figure 2.3). We therefore infer that, for smaller events, elevated PGA values are more sensitive to increased stress-drop than to variations in $Q_{0,e}$. For larger earthquakes with lower f_c, however, PGA may be influenced by both stress-drop and attenuation, particularly through $Q_e(f \sim fc) \geq Q_{0,e}$. Both $\delta B_e(PGA)$ and $\Delta\sigma_N$ vary along strike and with depth. At similar depths, VBFS earthquakes (distance 0 – 47 km from A in cross-section views) show higher $\Delta\sigma_N$ than LFS events (distance 47 – 80 km from A in cross-section views), likely due to geological contrasts along the entire normal fault systems created by the MST Fault (Chiaraluce et al., 2017; Barchi et al., 2021). Lower $\Delta\sigma_N$ in the LFS may reflect weaker

materials or elevated pore pressure reducing effective normal stress, while the higher $\Delta\sigma_N$ in the structurally complex VBFS is consistent with links between stress-drop and fault complexity (Goebel et al., 2015; Chu et al., 2021; Kemna et al., 2021). Despite this, $\delta B_e(PGA)$ is similar in both systems, suggesting lower attenuation in the LFS (Gabrielli et al., 2023). Lower $\Delta\sigma_N$ and $\delta B_e(PGA)$ at shallow depths likely result from weak materials, high pore pressure, increased attenuation, and lower normal stress.

We next examine the $\Delta B(f)$ terms of RF(***M***) and RF(***MXYZ***) and their correlations with $\Delta\sigma_N$ and $Q_e(f)$. This analysis complements the $\Delta B(PGA)$ investigation presented above (Figure 2.12) and, more importantly, helps clarify the differences in $\tau(f)$ (Figure 2.7) and in the spatial pattern of $\Delta B(f)$ between the two models (Figures 2.8 and 2.9). On average, $\tau(f)$ for RF(***MXYZ***) is approximately 50% lower than that of RF(***M***), and the spatial variability of its $\Delta B(f)$ is nearly negligible. This suggests that the spatially variable fixed-effects predictions of RF(***MXYZ***) (Figure 2.5) absorb a substantial portion of the spatial variability that appears as the $\Delta B(f)$ term in RF(M). Figures 2.13 and 2.14 are therefore designed to assess which components of the spatial variability in the seismological parameters [$\Delta\sigma_N$, $Q_e(f)$] contribute to the variability of $\Delta B(f)$ in the two GMMs.

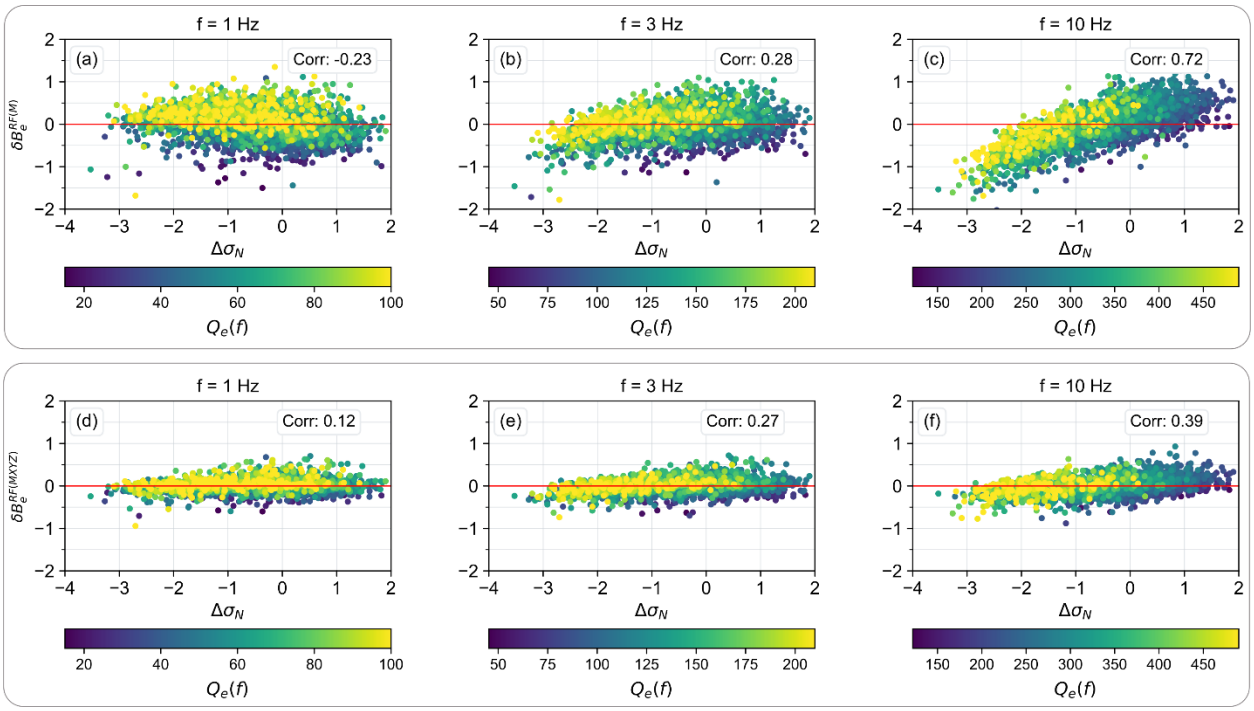

Figure 2.13. Correlation between normalized stress-drop ($\Delta\sigma_N$) and between-event residuals ($\delta B_e(f)$) at different frequencies for two ground-motion models. Subplots (a)-(c) show results obtained from RF(***M***) at f = 1, 3, and 10 Hz, respectively, while subplots (d)–(f) show results from RF(***MXYZ***) at the same frequencies. Each marker is colour-coded according to the corresponding $Q_e(f)$ value.

Figure 2.13 presents scatter plots of $\Delta B(f)$ of the two GMMs at f = 1, 3, and 10 Hz versus the frequency-independent $\Delta\sigma_N$. In these plots, the dispersion of $\Delta B(f)$ reflects its standard deviation $\tau(f)$. We denote the between-event distributions of RF(**M**) and RF(***MXYZ***) as $\Delta B^{RF(M)}(f)$ and $\Delta B^{RF(MXYZ)}(f)$, respectively. As expected, the dispersion of $\Delta B^{RF(MXYZ)}(f)$ is substantially smaller than that of $\Delta B^{RF(M)}(f)$. More importantly, $\Delta B^{RF(MXYZ)}(f)$ exhibits no frequency-dependent bias or systematic trend with $\Delta\sigma_N$, indicating that the stress-drop variability within the sequence is largely absorbed into the fixed-effects predictions of RF(***MXYZ***). In contrast, $\Delta B^{RF(M)}(f)$ at f = 1 and 3 Hz also shows no clear dependence on $\Delta\sigma_N$, suggesting that $\tau(f)$ at $f \leq 3$ Hz of RF(***M***) is not controlled by stress-drop variability. Consequently, the spatial variability of the RF(***MXYZ***) fixed-effects predictions at low frequencies does not

primarily reflect stress-drop variations within the sequence. However, at $f > 3$ Hz, where the largest reductions in $\tau(f)$ are observed, the fixed-effects predictions of RF(***MXYZ***) are expected to capture a significant portion of stress-drop variability that is otherwise contained in $\Delta B^{RF(M)}(f)$.

Figure 2.13 is also color-coded by the frequency-independent event-specific parameter $Q_e(f)$. We recall that these $Q_e(f)$ values were not intended to represent crustal properties strictly at the hypocenter, but rather effective averages over a volume surrounding each source. However, our analysis of $E(f)$ in Section 2.4.3.3 indicates that nearly all of the events are recorded with close to 360° azimuthal coverage and over a broad range of distances, yet the event-specific residuals still exhibit frequency-dependent anisotropy (not shown). Moreover, spatially separated events occurring at similar times and recorded by several common stations display distinct $Q_e(f)$ values. Taken together, these observations support treating $Q_e(f)$ as representative of a relatively small volume around each hypocenter, rather than of a large region extending tens of kilometers. In Figure 2.13, data markers are plotted so that extreme $Q_e(f)$ values appear above the larger population of moderate $Q_e(f)$ values. This visualization suggests that the scatter of $\Delta B^{RF(M)}$ at $f \leq 3$ Hz is not governed by the overall variability of $Q_e(f)$, but is instead amplified by its extreme values. For example, at $f = 1$ Hz, events with $Q_e(f) > 80$ tend to show more positive δB_e, whereas the influence of high $Q_e(f)$ diminishes at $f > 3$ Hz, where stress-drop variability becomes dominant. The sharp increase of $\tau(f)$ for RF(***M***) toward higher frequencies in Figure 2.7 is consistent with this interpretation. Finally, although $\Delta B^{RF(MXYZ)}(f)$ in Figure 2.13 indicates no systematic trend with $\Delta\sigma_N$, the color-coding suggests that higher and lower $Q_e(f)$ values broadly correspond to positive and negative $\delta B_e(f)$, respectively, across the full range of $\Delta\sigma_N$. This behavior is examined further in Figure 2.14.

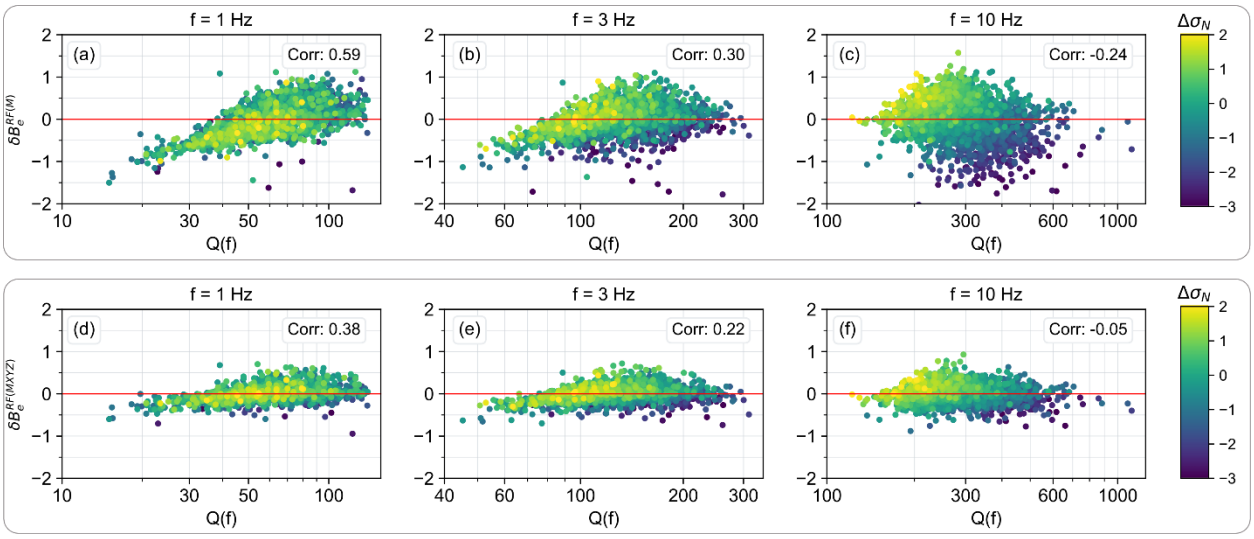

Figure 2.14. Correlation between frequency-dependent quality factor ($Q_e(f)$) and between-event residuals ($\delta B_e(f)$) at different frequencies for two ground-motion models. Subplots (a)-(c) show results obtained from RF(***M***) at f = 1, 3, and 10 Hz, respectively, while panels (d)-(f) show results from RF(***MXYZ***) at the same frequencies. Each marker is colour-coded according to the corresponding normalized stress-drop ($\Delta\sigma_N$) value.

Figure 2.14 presents scatter plots of $\Delta B^{RF(M)}(f)$ and $\Delta B^{RF(MXYZ)}(f)$ at f = 1, 3, and 10 Hz as a function of the frequency-dependent $Q_e(f)$, with markers color-coded by the frequency-independent normalized stress-drop $\Delta\sigma_N$. In contrast to Figure 2.13, where $\Delta B^{RF(M)}$ at f = 1 Hz shows no trend with $\Delta\sigma_N$, here $\Delta B^{RF(M)}$ exhibits a clear monotonic increase with $Q_e(f)$ at f = 1 Hz. This trend gradually weakens toward higher frequencies. Nevertheless, $\Delta B^{RF(M)}$ at f = 3 Hz for events with higher $\Delta\sigma_N$ still displays a strong dependence on $Q_e(f)$ at f = 3 Hz. Interestingly, the relationships between $\Delta B^{RF(M)}(f)$ and $Q_e(f)$ at f = 1 and 3 Hz appear inverted. Specifically, $\Delta B^{RF(M)}$ at f = 1 Hz for events with higher $\Delta\sigma_N$ tends to exhibit predominantly negative values, whereas the opposite is observed at f = 3 Hz. At f = 10 Hz, $\Delta B^{RF(M)}(f)$ for events with higher $\Delta\sigma_N$ are consistently positive, while those associated with the lowest $\Delta\sigma_N$ are consistently negative. These patterns suggest that the influence of $Q_e(f)$ on the event-specific term $\delta B_e^{RF(M)}(f)$ is modulated by the event stress-drop.

This behavior can be interpreted in the light of the relationship between f_c and $\Delta\sigma$ shown in Figure 2.3: for events with identical M_0, higher $\Delta\sigma$ corresponds to lower corner frequency f_c, whereas lower $\Delta\sigma$ implies higher f_c. We emphasize that $\Delta B^{RF(M)}(f)$ is free of explicit magnitude dependence because the GMM fixed-effects absorb the scaling of $ln\,(FAS, f)$ with $\boldsymbol{M}$. In contrast, although $\Delta\sigma$ itself is frequency-independent, it scales with M_0, and by extension with $\boldsymbol{M}$ (Figure 2.3). Moreover, M_0 and $\boldsymbol{M}$ are source parameters estimated primarily from low-frequency Fourier amplitudes, ideally at frequencies well below f_c for each event. Considering the observations from Figures 2.3, 2.13, and 2.14 jointly, we infer that, for this dataset of $2.35 \leq \boldsymbol{M} \leq 4.62$ earthquakes, $\Delta B^{RF(M)}$ at $f > 3$ Hz is predominantly controlled by variability in $\Delta\sigma$. In contrast, $\Delta B^{RF(M)}$ at $f \leq 3$ Hz is more likely influenced by variability in $Q_e(f)$ at $f \leq 3$ Hz, as well as by its strong effect on the estimation of $\boldsymbol{M}$.

2.6. Conclusion

Parametric GMMs are widely used as ground-motion prediction models (GMPMs) in PSHA because they are constrained to behave reasonably when extrapolated to unsampled combinations of $\boldsymbol{M}$ and R. These constraints, typically formulated as continuous functions of magnitude and distance, are based on the assumption that the propagation medium behaves in a linear elastic manner under infinitesimal strains. This assumption is generally appropriate for small magnitudes and large distances. However, hazard-critical scenarios often involve large earthquakes occurring at short distances. Under such conditions, the assumption of linear elasticity may no longer be valid. This raises important questions about the applicability of parametric GMMs in PSHA and whether ground-motion scaling can realistically be described by continuous linear functions of $\boldsymbol{M}$ and R across the full range of hazard-relevant scenarios. Non-parametric GMMs are inherently more flexible than parametric GMMs because they do not require the specification of continuous functional forms in $\boldsymbol{M}$ and R. Indeed, recent studies have demonstrated that, when applied to the same dataset, non-parametric models often exhibit greater

explanatory power than their parametric counterparts. However, non-parametric GMMs are generally not suitable for use in PSHA, as they cannot be reliably extrapolated or interpolated to unsampled scenarios.

In this study, we investigate the behavior of both parametric and non-parametric GMMs using a large dataset of small earthquakes from the 2016-2017 Central Italy seismic sequence. We regress one parametric linear mixed-effects GMM and two non-parametric Random Forest mixed-effects GMMs on the dataset. In addition, we consistently estimate several seismological parameters constituting the Fourier spectra. While our overarching objective is to better understand the spatial and temporal variability of ground-motion, our immediate goal is to leverage the flexibility of non-parametric GMMs to assess whether they capture aspects of earthquake physics that could eventually be incorporated into future parametric prediction models. In the following, we have identified several noteworthy findings:

- One of the key constraints of parametric linear mixed-effects GMMs is the assumption that the random-effect and residual distributions are Gaussian. However, our statistical tests indicate that these distributions are frequently skewed and heavy-tailed. This suggests that more robust estimates of ground-motion variability, capable of down-weighting the influence of outliers, may be necessary for PSHA applications.
- The non-parametric GMM using [$\boldsymbol{M}$, R, XYZ] (XYZ indicates the hypocentral location of the event as predictors) exhibits a substantial reduction in between-event random-effect variance across all frequencies and, consequently, in the aleatory variability used in PSHA. In investigating the reasons behind this markedly reduced variability, we observe that the fixed effects of this model appear to capture aspects of earthquake physics that are nonlinear in nature and deviate from the linear assumptions typically imposed in parametric GMMs.
- The fixed-effect predictions of high-frequency Fourier amplitudes exhibit a strong dependence on the hypocentral location of the event. In conventional Fourier-

based GMPMs, the between-event variability at high frequencies is often prohibitively large for practical use in PSHA. However, incorporating [$\boldsymbol{M}$, R, XYZ] as predictors leads to a substantial reduction in the between-event variability of high-frequency Fourier amplitudes. At high frequencies, the dependence on hypocentral location appears to be governed primarily by event-specific stress-drop. Furthermore, the influence of hypocentral location on the model fixed-effect predictions decreases rapidly with increasing distance R. This finding challenges the common assumption of distance-independent scaling of ground-motion with stress-drop and depth. For example, under the assumption that stress-drop increases with depth, most parametric GMPMs predict higher ground-motions for deeper earthquakes regardless of the source-to-site distance. Our results suggest that even if deeper earthquakes exhibit higher stress-drop values, and are therefore capable of generating stronger high-frequency ground-motions, the amplifying effect of depth or stress-drop diminishes rapidly with distance. This observation is consistent with earlier studies (Baltay et al., 2019; Bindi & Kotha, 2020), which showed that stress-drop estimates for small earthquakes are robust primarily when derived from short-distance recordings. We therefore propose revisiting the relationship between stress-drop and between-event ground-motion variability introduced by Cotton et al. (2013).

- The fixed-effect predictions of low-frequency Fourier amplitudes also exhibit dependence on the hypocentral location of the event; however, this dependence is substantially weaker than that observed for high-frequency ground-motions and similarly diminishes with increasing source-to-site distance. At lower frequencies, the spatial variability of the predictions appears to be primarily controlled by the event-specific quality factor. We emphasize that the quality factor values estimated in this study do not represent highly localized, point-specific properties at the hypocenter. Rather, they reflect a broader, volumetric property of the medium at the time of rupture. The influence of quality factor on high-frequency Fourier amplitudes is relatively limited; however, when combined with stress-drop variability, extreme quality factor values can increase high-frequency

ground-motion variability. An additional noteworthy implication is that recent studies (e.g., Di Luccio et al., 2010; Akinci et al., 2022; Malagnini et al., 2022; Gabrielli et al., 2025) have demonstrated that the quality factor in this region, characterized by extensive fluid migration, appears to be time-dependent. Specifically, pre- and post-mainshock quality factor values of the propagation medium are not identical and show evidence of temporal recovery following major events (Bindi et al., 2018). This finding challenges the common practice of estimating the moment magnitude of foreshocks and aftershocks using a single, time-invariant quality factor value. In our case, the temporal variability of the quality factor would directly translate into time-dependent low-frequency ground-motions. However, incorporating such time dependence into a parametric ground-motion model is not straightforward. As a result, the ground-motion variability adopted in Poissonian PSHA frameworks may be artificially inflated by an earthquake process that is known but not explicitly modeled. Although it remains debatable whether temporal variability should be treated as part of the aleatory variability in PSHA, these findings nonetheless raise important questions regarding the reliability of moment-magnitude estimates for foreshocks and aftershocks when time-dependent attenuation effects are ignored.

- Non-parametric Random Forest mixed-effects regressions are promising tools for exploring nonlinear earthquake processes in large ground-motion datasets generated by seismic sequences. Several studies have demonstrated their superior explanatory power, often reflected in substantially lower ground-motion variability compared to traditional parametric models. Nevertheless, we emphasize the importance of carefully examining their behavior when exploiting their flexibility. Among several additional model configurations not presented in this study, one that included event origin time as a predictor, together with hypocentral location, yielded up to an 80% reduction in ground-motion variability relative to a conventional parametric model; this configuration is investigated in detail in Chapter 3. While such a dramatic reduction may not directly translate to forecast-oriented PSHA applications, it can have significant implications for

seismic risk assessment within well-recorded earthquake sequences, such as the 2016-2017 Central Italy and the 2019 Ridgecrest.

Data and Resources

The catalog released by Kemna et al. (2021) is available for download at: https://zenodo.org/records/5196236 (last accessed March 2026). The catalog published by Bindi et al. (2020) is accessible at: https://zenodo.org/records/13313095 (last accessed March 2026). Random Forest regressions are performed using the publicly available scikit-learn Python programming package (Pedregosa et al., 2011). Several figures were plotted using GMT 6.6.0 (Wessel et al., 2019), available at: https://www.pygmt.org/v0.16.0/ (last accessed March 2026). Some figures were also generated using Matplotlib 3.10.0 (Hunter, 2007) available at: https://matplotlib.org/ (last accessed March 2026). R Statistical software (available at: https://www.r-project.org/, last accessed March 2026) was used to perform mixed-effect regression of the Parametric GMM.

Acknowledgments

This study benefited from funding from Ministère de la Transition Ecologique et de la Cohésion des Territoires, through Convention DGPR-Univ. Gustave Eiffel 2024. We would like to thank Dino Bindi for providing detailed information about the attenuation model they used in their study. We also thank Editor XXXX and XXXX reviewers for their valuable comments, which helped improve the quality of the manuscript.

Conflict of Interest

The authors declare there are no conflicts of interest for this manuscript.

Appendix 2

Text A2.1. Comparison of Moment Magnitude and Stress-Drop from the Three Catalogs

As illustrated in Figure A2.2, we compare the moment magnitude and stress-drop estimates from this study with those of Kemna et al. (2021) (K21) and Bindi et al. (2024) (B24). K21 estimated source parameters by adopting shear-wave velocity from a 1D velocity structure model and frequency-independent Q values, allowing Q to vary to account for potential spatial and temporal variations during the fitting process. In contrast, B24 used a 3D shear-wave velocity model and a simplified nonparametric attenuation model, which depends only on hypocentral distance and frequency. B24 study, extending from Central to Southern Italy, assumes constant attenuation parameters for the Amatrice-Norcia area. This approach implies that ground motion attenuation at a given distance is similar for two events with different locations and occurrence times; hence, it does not properly capture the spatial and temporal variability of attenuation in the sequence. Compared to these approaches, our study employs a methodology that integrates a 3D shear-wave velocity model (similar to B24) with a frequency-dependent Q model, and allows for spatial and temporal variability of attenuation. However, it is important to note that our Q estimates represent the effective, average attenuation between an event and a station network and are not expected to capture fine spatial variations of attenuation.

A comparison of moment magnitude estimates reveals that our $\boldsymbol{M}$ values have a mean slightly higher than $\boldsymbol{M}$(K21) (3.0 and 2.87, respectively, Figure A2.2a). This discrepancy may be attributed to differences in shear-wave velocity models and the fundamental distinction between using frequency-independent versus frequency-dependent attenuation models. Notably, several studies (e.g., Pisconti et al., 2015; Akinci et al., 2022; Castro et al., 2021) showed that the Q factor in Central Italy is

strongly frequency-dependent. Furthermore, (Supino et al., 2019) noted that when inverting source scaling parameters using a frequency-independent Q within an attenuation model with frequency-dependent Q, the estimated quality factor might not represent an averaged value for the quality factor. The influence of the attenuation model on magnitude bias becomes even more apparent when comparing our $\boldsymbol{M}$ estimates to $\boldsymbol{M}$(B24). Despite using the same 3D shear-wave velocity model, B24 reports systematically lower M values, with a mean of 2.61. This suggests that the simplified attenuation model employed by B24 may underestimate $\boldsymbol{M}$ relative to our study and K21 (Figures A2.2b and A2.2c).

As shown in Figure A2.2d, our $\Delta\sigma$ estimates exhibit lower values (median: 0.37 MPa) compared to $\Delta\sigma$(K21) (median: 2.61 MPa). Since our $\boldsymbol{M}$ is larger than $\boldsymbol{M}$(K21), the discrepancy in $\Delta\sigma$ estimations could be associated with the overestimation of the corner frequency by K21, in which stress-drop is controlled by the cube of corner frequency. Such overestimation of f_c can occur when the attenuation (expressed as the inverse of the Q factor) is lower than the assumed value. This suggests that the average attenuation model used by K21 during the fitting process is likely lower than the average attenuation represented in our model. On the other hand, $\Delta\sigma$(B24) estimates with a median of 0.076 MPa are notably lower than our estimates and those of K21 (Figures A2.2e and A2.2f). Given the identical shear-wave velocity model, discrepancies in stress-drop values are more likely driven by differences in the assumed attenuation model. It is plausible that the averaged attenuation employed by B24 is stronger than that used in our study. Despite these variations, our $\Delta\sigma$ estimates exhibit a stronger correlation with those of B24 (0.83) than with K21 (0.62). This suggests that although absolute stress-drop values differ across studies due to modeling assumptions, the relative trends in our estimates are more consistent with B24 than with K21.

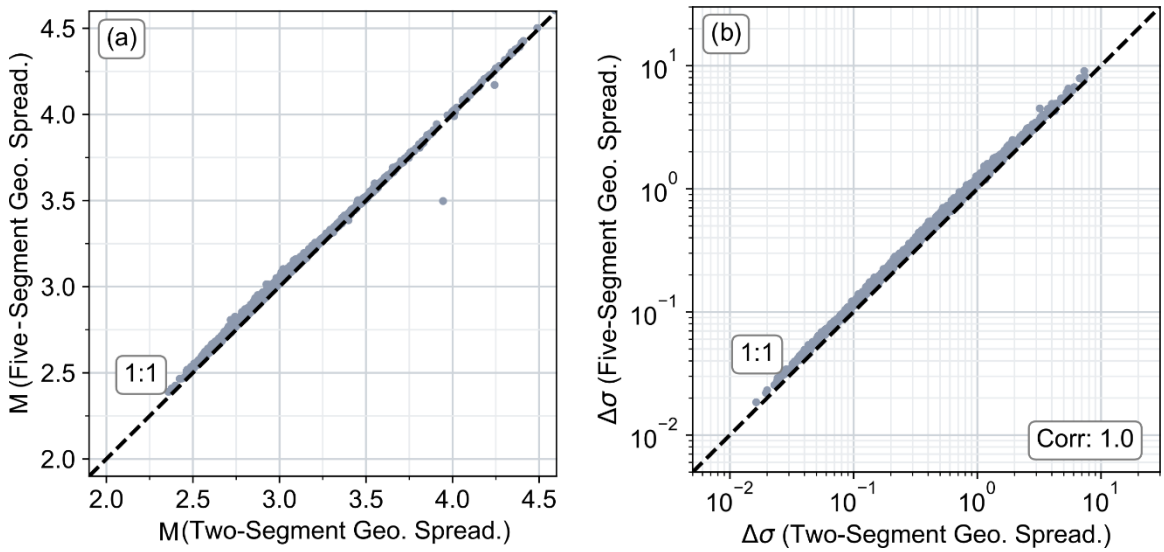

Figure A2.1. Comparison of source parameters estimated using a two-segment (Akinci et al., 2022; Malagnini et al., 2011) and a five-segment (Gabrielli et al., 2025) geometrical spreading models. **(a)** Comparison of moment magnitude computed using two different geometrical spreading models **(b)** Comparison of stress-drop calculated using two different geometrical spreading models.

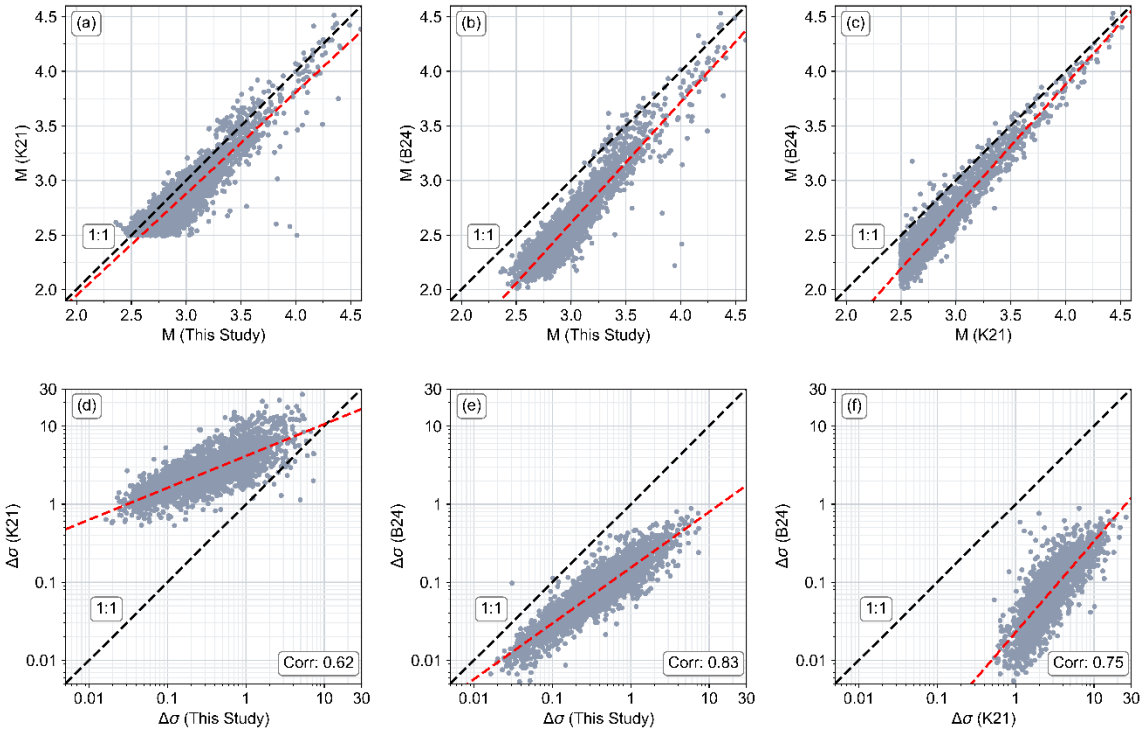

Figure A2.2. Comparison of moment magnitude and stress-drop across the three catalogs. **(a)** ***M*** from this study vs. K21, **(b)** ***M*** from this study vs. B24, **(c)** ***M*** from K21 vs. B24, (d) $\Delta\sigma$ from this study vs. K21, (e) $\Delta\sigma$ from this study vs. B24, (f) $\Delta\sigma$ from K21 vs. B24. The black dashed line depicts the 1:1 reference line, indicating perfect agreement, while the red dashed line represents the best-fitted line for each dataset, respectively.

3 Temporal and Transient Changes in Ground-Motion

This chapter builds upon the dataset and the non-parametric ground-motion models (GMMs) developed in Chapter 2 to investigate the origin of temporal and transient variations in ground motion throughout the seismic sequence. This is achieved through a direct comparison between the temporal variability of between-event residuals derived from the GMMs and corresponding variations in stress drop and quality factor. This chapter was prepared in collaboration with **Mathieu Causse** and **Sreeram Reddy Kotha**, and has been submitted to the *Journal of Geophysical Research: Solid Earth* under the title "Spatial Variability and Transient Changes in Stress Drop and Attenuation Control the Temporal Variability of Ground Motion during the 2016–2017 Central Italy Sequence."

Key Points:

- Residual Between-event variability of PGA shows strong temporal variability following mainshocks
- Temporal changes in source and medium properties significantly contribute to ground-motion variability
- Between-event variability of PGA is not a reliable proxy for stress-drop immediately after mainshocks due to rapid variations in frequency-dependent attenuation

Abstract

We investigate the origin of the spatiotemporal variability in high-frequency ground-motions during the 2016-2017 Central Italy seismic sequence. We rely on a dataset of moment-magnitude (***M***), stress-drop ($\Delta\sigma$), and between-event residuals of PGA ($\delta B_e(PGA)$) for 2,503 earthquakes, as computed in Chapter 2. To capture temporal variations in path-effect and reduce biases in $\Delta\sigma$ and ***M***, event-specific quality-factor $Q_e(f)$ is used as a proxy for frequency-dependent attenuation. $\delta B_e(PGA)s$ are calculated as the event-specific residuals relative to non-parametric ground-motion prediction models based on ***M***, distance, and possibly earthquake location and origin time (models RF(***M***), RF(***MXYZ***), and RF(***MXYZT***)). $\delta B_e(PGA)s$ from RF(***M***) vary significantly in the days immediately following the mainshocks (dropping 50% to 100%), driven by changes in $\Delta\sigma$ and $Q_e(f)$. The correlation between $\delta B_e(PGA)$ and $\Delta\sigma$ generally exceeds 0.80, except during these early periods, due to strong temporal variability in $Q_e(f)$. This suggests $\delta B_e(PGA)$ may be an unreliable proxy for stress-drop and fault frictional properties immediately after mainshocks. One notable case is a ~25% short-lived increase followed by a ~100% drop in $\delta B_e(PGA)$ within three days after the Amatrice event. Part of this decrease results from seismicity migrating towards shallower depths with typically lower $\delta B_e(PGA)$. However, RF(***MXYZ***) and cluster analysis reveal that transient changes in source and medium properties account for ~40%-50% of the variation. We attribute these to fault-strength modification induced by fluid-driven and/or damage-driven processes, observed only after the Amatrice earthquake. These findings may improve seismic hazard assessment by refining aftershock ground-motion predictions during earthquake sequences.

Plain Language Summary

A large earthquake is typically followed by numerous aftershocks, which can cumulatively damage buildings already weakened by the mainshock. However, seismic hazard and risk mitigation analyses often overlook aftershocks, neglecting their complexity, as aftershock ground motions can vary strongly depending on their location and origin time. In this study, we take advantage of the 2016-2017 Central Italy seismic sequence, characterized by four mainshocks, to investigate the origin of this variability. Our findings reveal that ground-motions decrease sharply immediately after the mainshocks, primarily due to changes in stress-drop and anelastic attenuation. Stress-drop refers to the amount of stored stress released in a specific region of the Earth's crust during an earthquake, while anelastic attenuation describes how seismic waves lose energy as they travel from the source to recording stations. Part of this drop is due to seismicity migrating to shallower depths, which typically generates weaker ground shaking. However, a significant portion arises from short-term changes in stress-drop and attenuation, likely caused by increased fluid pore pressure and/or damage-induced weakening of the fault zone. Understanding these transient behaviours can improve ground-motion predictions and enhance earthquake hazard assessments during seismic sequences.

3.1. Introduction

In a seismic sequence, a mainshock is typically followed by numerous aftershocks. Seismic hazard assessments mainly concentrate on mainshocks because they are expected to generate the strongest ground-motions and inflict the most severe structural damage. However, ground-motions produced by subsequent aftershocks can accumulate damage in structures and heighten the risk of catastrophic failure (Iervolino et al., 2020).

Seismic hazard analysis primarily relies on Ground Motion Prediction Models (GMPMs), which typically predict ground-motions at a location as Gaussian distributions $N(\mu, \sigma^2)$; with μ as the median and σ^2 as the variance. While

$\mu = f(M, R, \Theta)$ of a GMPM prediction is a function of earthquake moment-magnitude $\boldsymbol{M}$ (Hanks & Kanamori, 1979), source-to-site distance (R), and site parameters ($\boldsymbol{\Theta}$). The observed natural variability of ground-motions not modelled into μ is contained in the *apparent* aleatory variability σ. Most GMPMs are stationary, implying that $\mu = f(M, R, \Theta)$ does not vary across space (XYZ) or time (T), despite evidence indicating that ground-motion characteristics may indeed change spatially and temporally due to processes influencing the fault zone and the propagation medium during an earthquake sequence. For instance, aftershocks are expected to produce weaker ground-motions relative to similar-sized mainshocks (e.g., Boore & Atkinson, 1989; Baltay et al., 2013; Abrahamson et al., 2014). Thus, σ contains the variability of ground-motions of entire seismic sequences featured in the ground-motion datasets. In addition, a large σ inflated by spatial and temporal variability of ground-motions of an entire sequence, by design, inflates the probability of exceeding extreme ground-motions in Probabilistic Seismic Hazard Assessments (PSHA) (e.g., Bommer & Abrahamson, 2006; Cotton et al., 2013). Therefore, understanding and isolating the origin of the spatial and temporal variability of ground-motions in a seismic sequence from the σ of a GMPM is of critical interest in seismic hazard and risk assessments.

In a customary mixed-effects regression (Bates et al., 2015) of a GMPM, the event-to-event variability of ground-motions unexplained by $\boldsymbol{M}$ is quantified as the so-called between-event random-variance τ^2, which is a component of σ^2 along with path-to-path, site-to-site, and other random variabilities of seismic processes (e.g., Atkinson, 1990; Al Atik et al., 2010; A. S. Baltay & Hanks, 2014; Causse & Song, 2015). The spatial and temporal variabilities of earthquake (or event e) characteristics in a ground-motion dataset are captured by the $\Delta B = N(0, \tau^2)$; which is a Gaussian distribution composed of event-specific between-event δB_e values; i.e., a unique value for each event e in the dataset. Analyses of ΔB of earthquake sequences may reveal repeatable patterns that can be modelled into the $\mu = f(M, R, \Theta)$ of the GMPM; for example, by introducing a combination of T and XYZ as predictor

variables. In doing so, τ may be reduced, thereby reducing σ, and subsequently improving the accuracy of hazard and risk assessments. However, such statistically derived patterns must be substantiated by a robust physical interpretation.

Theoretically, high-frequency ground-motions, represented for instance by the Peak Ground Acceleration (PGA) values, correlate well with the corner-frequency, which can be directly linked to stress-drop. This explains why the τ of high-frequency ground-motion is primarily controlled by stress-drop variability (McGuire & Hanks, 1980; Bindi et al., 2007; Cotton et al., 2013; Adrien Oth et al., 2017; Trugman & Shearer, 2018). However, stress-drop measurements can be non-unique and contain systematic uncertainties, especially for small and moderate-sized earthquakes (e.g., Abercrombie, 2021; Abercrombie & Baltay, 2025, and references therein). Cotton et al. (2013) emphasized that stress-drop variability is a critical factor in ground-motion simulation and that uncertainties can lead to inaccurate predictions of high-frequency ground-motion variability. The complexity of stress-drop analyses becomes even more pronounced when attempting to estimate stress-drop in regions characterized by fault rheological and geometrical complexities, heterogeneous geological structures, or the presence of fluids. For example, it has been observed that stress-drop can vary spatially due to variations in fault frictional properties or high fault heterogeneity (e.g., Shearer et al., 2006; Goebel et al., 2015; Moyer et al., 2018; Trugman, 2020). In regions with high fluid pressure, stress-drop tends to be lower, likely due to reductions in effective normal stress (e.g., Chen & Shearer, 2011; Goertz-Allmann et al., 2011; Lengliné et al., 2014; Lin et al., 2016). Moreover, stress-drop can exhibit time dependency, influenced by temporal changes in pore fluid pressure as fluids migrate through the seismogenic zone (e.g., Chen & Shearer, 2013; Goertz-Allmann et al., 2011; Yoshida et al., 2017). Time-dependent variations may also result from modifications to the Earth's crust during mainshock rupture by creating cracks within the fault zone (e.g., Allmann & Shearer, 2007; Shaw et al., 2015; Bindi et al., 2018), perturbing the crustal medium during wave propagation (e.g., Gabrielli et al., 2022, 2023; Malagnini et al., 2022). In addition, mainshocks can modify shallow

surface properties beneath recording stations (e.g., Aguirre & Irikura, 1997; Vassallo et al., 2022; Esfahani et al., 2024; Hallo et al., 2025), which may introduce further bias in stress-drop estimates if site effects are not adequately corrected. These findings highlight the diversity of physical factors and uncertainties influencing stress-drop estimates that vary both spatially and temporally. This raises important questions for both earthquake source physics and engineering seismology communities: what physical processes control the spatial and temporal variability of ground-motion in a seismic sequence? Is the between-event variability of GMPMs solely driven by the variability of the stress-drop?

In this study, we analyze the 2016-2017 seismic sequence in Central Italy to uncover temporal patterns in their ground-motions and investigate their physical meaning. The sequence started with the ***M***6.0 Amatrice earthquake on 24 August 2016, which led to a significant increase in seismicity, peaking after the ***M***5.9 Visso earthquake on 26 October and the ***M***6.5 Norcia earthquake on 30 October (Chiaraluce et al., 2017). We use a high-resolution catalogue presented in Chapter 2 comprising 2,503 well-recorded earthquakes (Figure A3.1 in Appendix 2), for which we estimated event-specific between-event δB_e values for various ground-motion indicators (Fourier Amplitude Spectra and peak values) using non-parametric Random Forest GMMs. The catalogue also contains key source parameters, including ***M***, corner frequency (f_c), stress-drop ($\Delta\sigma$), and frequency-dependent quality factor ($Q(f)$) as a proxy for attenuation and path effects. For comparison purposes, we further expand our catalogue by incorporating source parameter estimates from Kemna et al. (2021) and Bindi et al. (2024) for events common to our catalogue, allowing for a direct comparison of the inferred values. Chapter 2 presents the methodology to build the catalogue and investigates the origin of the spatial ground-motion patterns. The present paper focuses on the temporal patterns and aims to identify the underlying physical processes. In the following, the term “transient changes” refers to short-term, often abrupt deviations from the background level, reflecting temporary modifications of medium or source properties in response to mainshocks. As shown

below, such changes may be associated with stress perturbations, fluid migration, or rupture-induced alterations of fault properties.

3.2. Dataset

Here, we present the key characteristics of the catalog of source and ground-motion parameters. The catalogue comprises a subset of 2,503 earthquakes that occurred between 24 August 2016 and 15 January 2018 and were recorded by at least 10 stations at hypocentral distances ranging from 1 to 190 km.

3.2.1. Source and attenuation parameters

First, we computed the seismological parameters [$\boldsymbol{M}$, f_c, $\Delta\sigma$, $Q(f)$]. The parameters $\boldsymbol{M}$, f_c, and $\Delta\sigma$ values were estimated by spectral-fitting of the displacement amplitude spectra of each event-station pair, assuming a Brune, (1970) source model, and subsequently averaged over all stations. To isolate source effects, spectra were first corrected for path attenuation and site effects. This step is critical, as inaccurate correction may lead to significant biases in estimates of $\boldsymbol{M}$ and $\Delta\sigma$ (e.g., Abercrombie et al., 2021). To account for attenuation effects, we computed the frequency-dependent quality factor for each event e, $Q_e(f) = Q_{0,e}.f^{n_e}$, using the method introduced by Trifunac (1976). Hereafter, $Q_{0,e}$ denotes the frequency-independent quality factor. Because $Q_e(f)$ is estimated independently for each event, it is expected to incorporate both spatial and temporal variations in the anelastic properties of the medium. This point is crucial, as attenuation may vary significantly in both space and time during the 2016-2017 central Italy sequence (e.g., Malagnini et al., 2022; Gabrielli et al., 2023). To estimate site amplification at each station and frequency, we interpret the $\Delta S2S$ term of the RF($\boldsymbol{M}$) model in Eq. 3.2 as a *station-correction*, assuming GMA = FAS(f). The attenuation-corrected Fourier spectra were then further corrected for site effects by subtracting $\Delta S2S(f)$, yielding the corresponding source spectra.

For comparison purposes, we further expand our catalog by incorporating $\boldsymbol{M}$ and $\Delta\sigma$ values from Kemna et al. (2021) (henceforth, K21) and Bindi et al. (2024) (henceforth,

B24). K21 estimated source parameters by fitting individual spectra for each event-station pair, assuming an event-specific, frequency-independent Q_e for path-propagation corrections, and did not account for site effects. In contrast, B24 employed a nonparametric spectral decomposition approach to isolate source parameters from propagation and site effects, assuming that $Q(f)$ is constant over the region considered in this study. Text A3.1 and Figure A3.2 in Appendix 3 examine the differences among the $\boldsymbol{M}$ and $\Delta\sigma$ estimates obtained in this study and those reported by K21 and B24, highlighting differences in attenuation modelling.

To illustrate how biases in $Q(f)$ affect source parameter estimates, we conduct synthetic tests (Figure 3.1). We generate synthetic displacement spectra at each station for two selected events from our catalog, characterized by different $\boldsymbol{M}_{(ref)}$, $f_{c(ref)}$, and $Q_e(f)_{ref}$ values. We assume a Brune's source model and no site amplification. To evaluate the impact of an incorrect quality-factor, we correct the displacement spectra from path-propagation using the $Q_e(f)_{test}$, corresponding to the mean value over the entire sequence. We then estimate $\boldsymbol{M}_{(test)}$ and $f_{c(test)}$ using the spectral-fitting procedure described above. In the first synthetic test (Figure 3.1a), $Q_e(f)_{ref}$ exceeds $Q_e(f)_{test}$ by ~45%, whereas in the second test, it is ~55% lower. In both cases, the inferred $\boldsymbol{M}$ varies by ±0.1 units and $\Delta\sigma$ by a factor of ~3. Underestimation of $Q_e(f)$ leads to overestimation of $\boldsymbol{M}$ and $\Delta\sigma$, and vice versa.

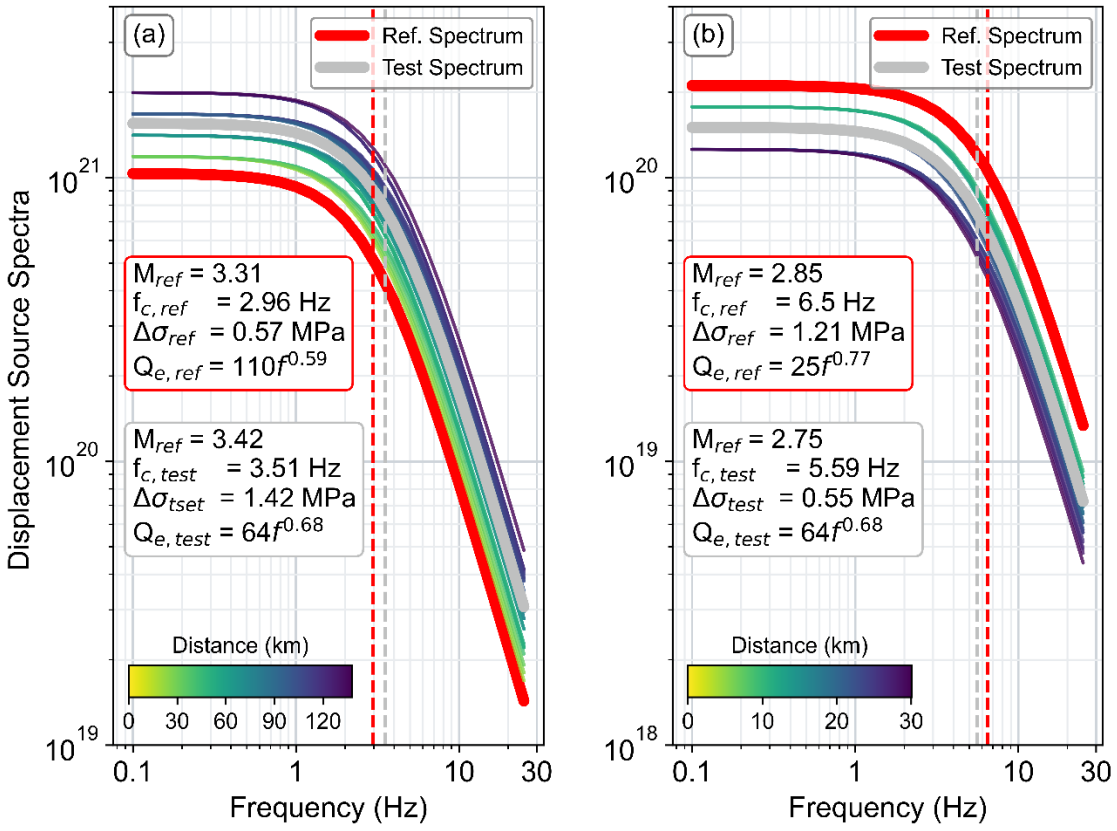

Figure 3.1. Examples illustrating how deviations in $Q_e(f)$ affect the estimation of the source parameters $\boldsymbol{M}$, f_c, and $\Delta\sigma$. **(a)** Reference source spectrum (red thick curve) is defined assuming a (Brune, 1970) source model with $\boldsymbol{M}_{ref}$ 3.31 and $f_{c,ref}$ = 2.96 Hz. The thin curves, color-coded according to the colorbar, show the source spectra for individual event-station recordings (where the number of stations and distances are selected based on the catalog), corrected for path-propagation by assuming $Q_{e,test} = 64.f^{0.68}$ instead of $Q_{e,ref} = 110.f^{0.5}$. The thick grey curve represents the mean spectra across all stations, referred to as the *test spectrum*. $Q_{e,ref}$ and $Q_{e,test}$ represent the event-specific estimate and the mean estimate over the entire sequence, respectively. The red and grey dashed lines show the reference corner frequency and the one inferred from the *test spectrum* **(b)** Same as (a) but assuming $\boldsymbol{M}_{ref}$ 2.85, $f_{c,ref}$ = 2.96 Hz, and $Q_{e,ref} = 25.f^{0.77}$.

Finally, because ΔB and $Q(f)$ are treated as magnitude-independent parameters, the stress-drop values are normalized to remove the influence of magnitude scaling

(e.g., Kemna et al., 2021). Hereafter, we refer to the normalized stress-drop, $\Delta\sigma_N$, defined as the natural logarithm of the event stress-drop ($\Delta\sigma_e$) divided by the mean stress-drop of the corresponding magnitude bin ($\overline{\Delta\sigma_m}$) using a bin width of 0.5:

$$\Delta\sigma_N = \ln\left(\frac{\Delta\sigma_e}{\overline{\Delta\sigma_m}}\right), \tag{3.1}$$

3.2.2. Ground-motion parameters

For each event *e*, we also determined the event-specific between-event ground-motion residuals, δB_e, computed using various Random Forest mixed-effects GMMs (Trugman & Shearer, 2018):

$$ln(GMA) = \frac{1}{B}\sum_{b=1}^{B} G_b^{RF}[\boldsymbol{M}, ln(R_{hypo})] + \Delta B + \Delta S2S + E, \tag{3.2}$$

where GMA (Ground-Motion Amplitude) refers to PGA, PGV, or acceleration Fourier amplitude spectrum, FAS(*f*), and R_{hypo} denotes the hypocentral distance. The between-event random-effect, $\Delta B = N(0, \tau^2)$, represents the distribution of the between-event residuals δB_e. The between-site random-effect, $\Delta S2S = N(0, \Phi_{S2S}^2)$, is defined by the between-site residuals. The remaining record-to-record residual variabilities are captured by the distribution E. To investigate the influence of earthquake location and origin time on the between-event residuals, we further considered two additional models:

$$ln(GMA) = \frac{1}{B}\sum_{b=1}^{B} G_b^{RF}[M.X.Y.Z, ln(R_{epi})] + \Delta B + \Delta S2S + E, \tag{3.3}$$

$$ln(GMA) = \frac{1}{B}\sum_{b=1}^{B} G_b^{RF}[M.X.Y.Z.T, ln(R_{epi})] + \Delta B + \Delta S2S + E, \tag{3.4}$$

where the variables *X, Y, Z* denote event location in km (see Figure 2.2 in Chapter 2), with *Z* representing depth in km, and *T* (in days) denotes the origin time of each event relative to the day of occurrence of the Amatrice mainshocks. The models defined by

Eqs. 3.2, 3.3, and 3.4 are hereafter referred to as RF(***M***), RF(***MXYZ***), and RF(***MXYZT***), respectively. We additionally use the ***M*** estimates reported in K21 and B24, and compute the corresponding δB_e values. In this study, we focus on PGA as a proxy for high-frequency ground-motion.

3.3. Results

3.3.1. Comparison of Between-Event Variabilities of GMMs

Figure 3.2a compares the ΔB distributions of the three *GMPMs* regressed on the PGA ground-motion dataset. By design, the medians of ΔB for all three models are close to zero. However, the ΔB of RF(***M***) exhibits a much wider dispersion. As illustrated in Figure 3.2b, the large τ at $f \geq 3$ Hz obtained from RF(***M***) may be partially attributed to variability in stress-drop and attenuation, which contribute more significantly to ground-motion variability at higher frequencies. However, by incorporating event location parameters, RF(***MXYZ***) reduces τ by ~60%. This substantial reduction highlights the influence of the spatial distribution of events on ground-motion variability within a seismic sequence as investigated in Chapter 2. Furthermore, RF(***MXYZT***), which further incorporates event origin time (T), decreases the standard deviation by an additional ~18%. Notably, RF(***MXYZT***) practically eliminates the frequency dependence of τ observed in RF(***M***). The standard deviation of δB_e derived from the three catalogs is similar for PGA. For FAS, the overall trends are also comparable, although notable differences are observed for RF(***M***) (Figure A3.3 and Text A3.2 in Appendix 3).

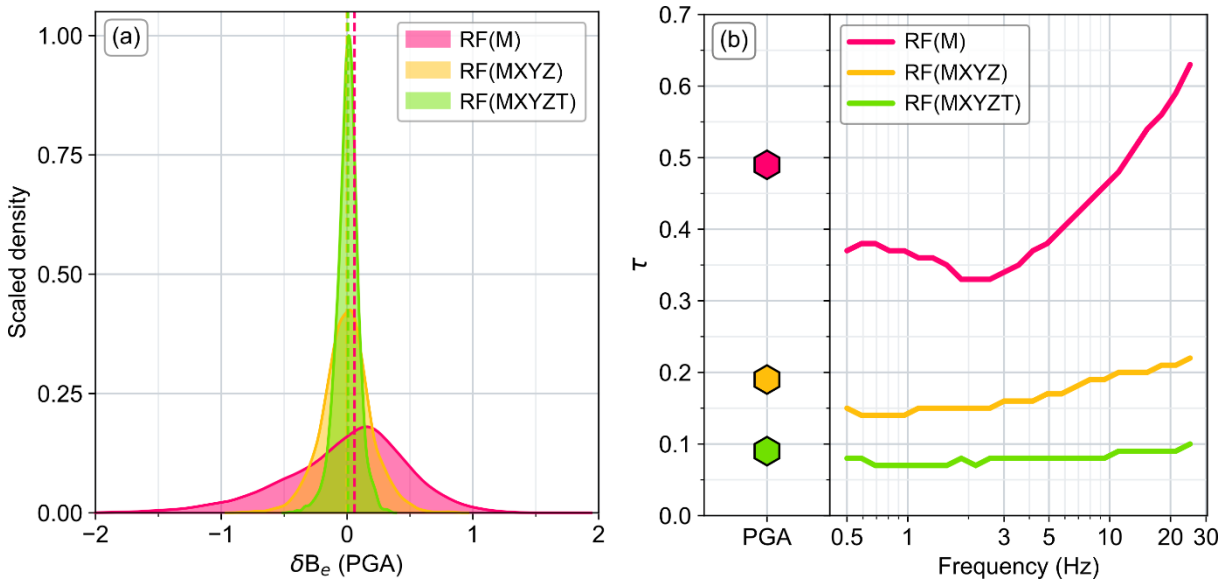

Figure 3.2. Distribution and variability of between-event residuals derived from three ground-motion models **(a)** Histograms representing distributions of $\delta B_e(PGA)$ derived from *GMMs*: RF(***M***) (shaded pink area), RF(***MXYZ***) (shaded orange area), and RF(***MXYZT***) (shaded green area). The dashed pink, orange, and green lines indicate the median δBe values for RF(***M***), RF(***MXYZ***), and RF(***MXYZT***), respectively. **(b)** Standard deviation of δB_e for PGA and FAS (f = 0.5 - 25 Hz). Pink, orange, and green markers/lines show the standard deviation estimates from RF(***M***), RF(***MXYZ***), and RF(***MXYZT***), respectively.

3.3.2. Temporal Variability of $\Delta B(PGA)$, $\Delta\sigma_N$, and $Q_{0,e}$

In the following, we describe the temporal variability of $\delta B_e(PGA)$ in relation to $Q_{0,e}$ and $\Delta\sigma_N$, after each mainshock and throughout the entire sequence, to examine how event characteristics evolve during the seismic sequence. Given the assumed strong correlation between $\delta B_e(PGA)$ variability and stress-drop (Bindi et al., 2007; Cotton et al., 2013; A. Baltay & Hanks, 2014; Oth et al., 2017), any notable deviation from this assumption may provide insight into additional physical processes, beyond stress-drop, that influence $\delta B_e(PGA)$ variability.

To analyze temporal variability, the entire sequence is segmented into seven distinct time phases, including four phases corresponding to the first week following

each mainshock. Figure 3.3 depicts the cross-sectional (cross-section A-A' in Figure A3.1 in Appendix 3) views of the mainshocks and aftershocks distributions for the selected phases, while the associated spatial patterns of $\delta B_e(PGA)$ obtained from $RF(\boldsymbol{M})$, $\Delta\sigma_N$, and $Q_{0,e}$ are presented in Figures A3.4-A3.6 in Appendix 3, respectively. Figure 3.4 illustrates the smoothed temporal evolution of $\delta B_e(PGA)$ computed using $RF(\boldsymbol{M})$, $\Delta\sigma_N$, $Q_{0,e}$, and depth across the entire sequence (Figures 3.4a and 3.4b), as well as within one week following the Amatrice (Figure 3.4c), four days after the Visso (Figure 3.4d), one week following the Norica (Figure 3.4e), and one week after the Campotosto (Figure 3.4f) mainshocks. The temporal smoothing is performed using the Moving Median approach (Text A3.3 in Appendix 3).

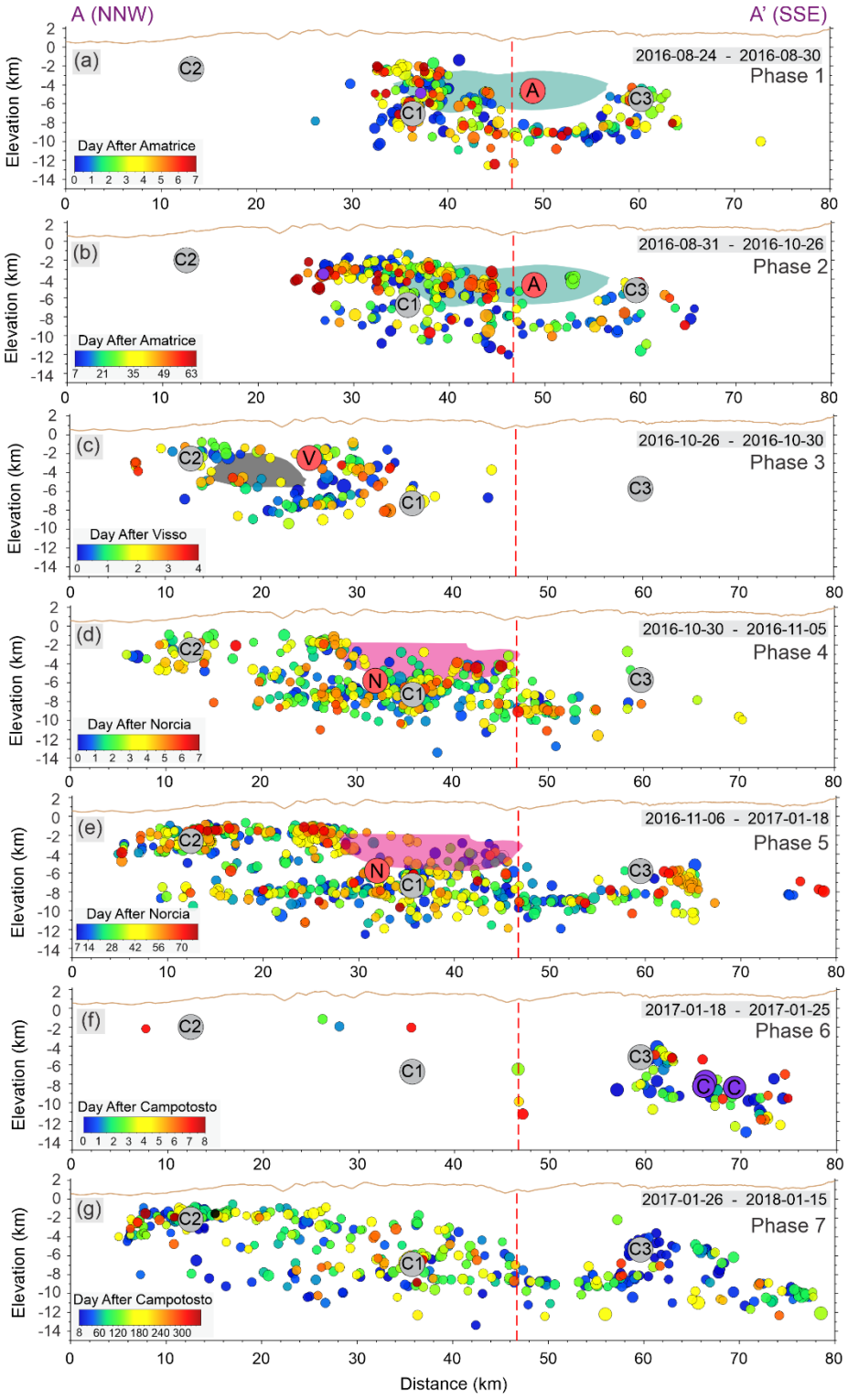

Figure 3.3. Along strike cross-sectional distribution of aftershocks during the different phases of the 2016–2018 Central Italy seismic sequence. Cross-sectional view along profile A-A' (Figure A3.1 in Appendix 3) of the spatial distribution of aftershocks (brown circles) for

each of the seven defined time phases: **(a)** Phase 1: the first week following the Amatrice mainshock from 2016-08-24 to 2016-08-30, **(b)** Phase 2: the period before the Visso mainshock between 2016-08-31 and 2016-10-26 **(c)** Phase 3: the four days following the Visso mainshock from 2016-10-26 to 2016-10-30 before the occurrence of the Norcia mainshock **(d)** Phase 4: the first week following the Norcia mainshock from 2016-10-30 to 2016-11-05 **(e)** Phase 5: the period between 2016-11-06 and 2017-01-18 before the occurrence of the Campotosto mainshocks **(f)** Phase 6: the one week following the three Campotosto mainshocks between 2017-01-18 and 2017-01-25 **(g)** Phase 7: the period from 2017-01-26 to 2018-01-15. The circles labelled A, V, N, and C mark the epicenters of Amatrice, Visso, Norcia, and Campotosto mainshocks, respectively. The grey circles labelled C1, C2, and C3 depict the location of the clusters presented in Section 3.5. The dark grey circles denote the epicenters of events $\boldsymbol{M}$4-5. Each maker is color-coded by the day after each mainshock. Green, black, and pink circular shapes indicate the slip area (after Pizzi et al., 2017; Scognamiglio et al., 2018) corresponding to Amtarice (0.3 m), Visso (0.3 m), and Norcia (0.8 m) mainshocks, respectively. The red vertical dashed line separates the earthquakes occurring along the strike of the VBFS (distance 0-47 km from A) and the LFS (distance 47-80 km from A).

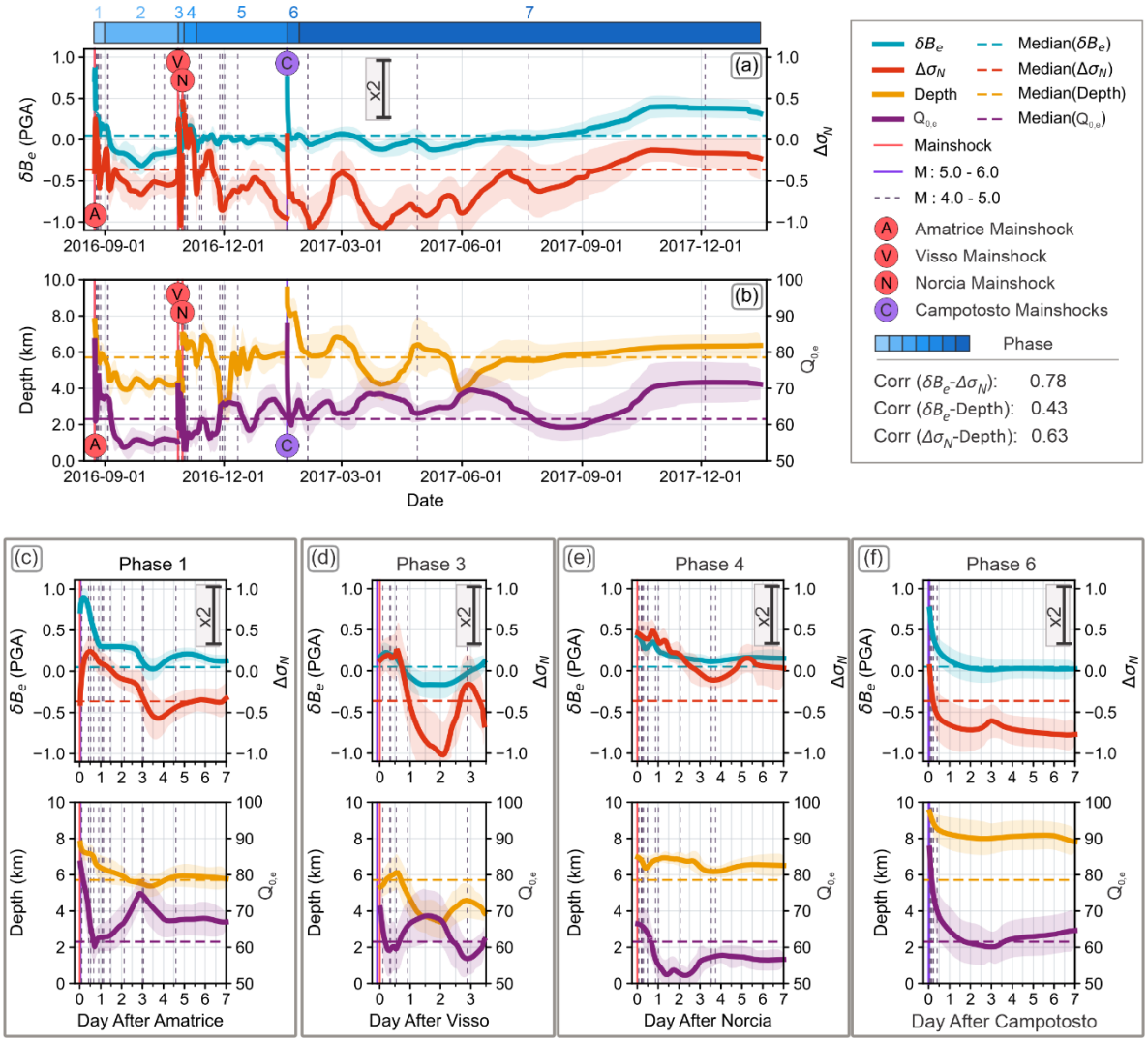

Figure 3.4. Temporal evolution of between-event residuals, stress-drop, depth, and frequency-independent term of quality factor during the 2016–2018 Central Italy seismic sequence. **(a)** Temporal evolution of $\delta B_e(PGA)$ computed using RF($\boldsymbol{M}$) and $\Delta\sigma_N$ for the entire sequence, **(b)** Temporal evolution of depth and $Q_{0,e}$ for the entire sequence. Zoom-in temporal evolution of $\delta B_e(PGA)$, $\Delta\sigma_N$, depth, and $Q_{0,e}$ corresponding to **(c)** Phase 1: the first week following the Amatrice mainshock, **(d)** Phase 3: the four days after the Visso mainshock, **(e)** Phase 4: the first week following the Norcia mainshock, **(f)** Phase 6: the first week post the three Campotosto mainshocks. The cyan, red, orange, and purple curves represent $\delta B_e(PGA)$, $\Delta\sigma_N$, depth, and $Q_{0,e}$, respectively. The blue color bar indicates the period corresponding to each phase. Horizontal dashed lines and shaded areas in matching colors illustrate the median values and ±1 standard deviation of $\delta B_e(PGA)$, $\Delta\sigma_N$, depth, and $Q_{0,e}$, respectively. Circles labelled A, V, N, and C denote the occurrence times of the Amatrice, Visso, Norcia,

and Campotosto mainshocks, respectively. The vertical red, purple, and dashed grey lines demonstrate the occurrence times of the mainshocks, events with ***M***5.0-6.0, and events with ***M***4.0-5.0, respectively. The scale line labeled "x2" represents two units on a linear scale.

3.3.2.1. Phases 1 & 2: Between the Amatrice and Visso Mainshocks

During Phases 1 and 2, aftershocks are distributed along both the VBFS and LFS segments (Figures 3.3a and 3.3b), consistent with the bilateral rupture inferred by Lavecchia et al. (2016). In Phase 1 (2016-08-24 to 2016-08-30), aftershocks mainly occur at depth near the maximum slip patch (as defined by Pizzi et al. (2017)), with an additional shallow cluster around an ***M***5.2 event (Figure 3.3a). Within the first day, $\delta B_e(PGA)$ increases slightly (+18%) before dropping sharply (−80%), while $\Delta\sigma_N$ rises rapidly (+91%) and then gradually decreases. During this period, aftershock depths remain stable, $Q_{0,e}$ decreases sharply, and then recovers. From day 3 onward, all parameters converge toward their median values. Spatially, events in the LFS section are characterized by high $Q_{0,e}$ and low $\Delta\sigma_N$, whereas events in the VBFS section exhibit high $\Delta\sigma_N$ and low $Q_{0,e}$, both leading to elevated $\delta B_e(PGA)$ (Figures A3.4a-A3.6a in Appendix 3). This indicates that during Phase 1, $\delta B_e(PGA)$ is controlled by both stress-drop and attenuation, particularly within the first three days.

In Phase 2 (2016-08-31 to 2016-10-26), most aftershocks migrate to shallow depths within the VBFS segment toward the Visso hypocenter (Figure 3.3b). At the phase onset, $\delta B_e(PGA)$, $\Delta\sigma_N$, and $Q_{0,e}$ decrease rapidly below their median values, coincident with a sudden decrease of aftershock depths, and then remain stable (Figures 3.4a and 3.4b). In contrast to Phase 1, $Q_{0,e}$ is spatially uniform, resulting in a strong spatial correlation between $\delta B_e(PGA)$ and $\Delta\sigma_N$, with higher stress-drop corresponding to higher $\delta B_e(PGA)$.

3.3.2.2. Phase 3: Between the Visso and Norcia Mainshocks

During Phase 3 (2016-10-26 to 2016-10-30), aftershocks are mainly concentrated around the Visso slip area, extending northward at shallow depths, with a narrower, deeper cluster toward the Norcia hypocenter (Figure 3.3c). Within the first 12 hours after the Visso mainshock, $\delta B_e(PGA)$ and $\Delta\sigma_N$ remain stable, coinciding with a slight deepening of seismicity and a rapid 17% decrease in $Q_{0,e}$ (Figure 3.4d). By day 2, $\delta B_e(PGA)$ decreases by 40%, and $\Delta\sigma_N$ drops sharply (−220%), as seismicity migrates to shallower depths and $Q_{0,e}$ increases by 17%. This combination of low $\Delta\sigma_N$ and high $Q_{0,e}$ results in $\delta B_e(PGA)$ values close to the median. From day 2 onward, $\delta B_e(PGA)$ gradually increases (+32%), while $\Delta\sigma_N$ rises markedly (+130%) before declining again. During this interval, $\Delta\sigma_N$ varies in phase with depth, whereas $Q_{0,e}$ shows the opposite trend. Overall, temporal variations in $\Delta\sigma_N$, $Q_{0,e}$, and depth are more pronounced than those in $\delta B_e(PGA)$. Spatially, deeper events (5–8 km) exhibit low $Q_{0,e}$, high $\Delta\sigma_N$, and elevated $\delta B_e(PGA)$, while shallower events show the opposite behavior (Figures A3.4c-A3.6c in Appendix 3).

3.3.2.3. Phases 4 & 5: Between the Norcia and Campotosto Mainshocks

During Phase 4 (2016-10-30 to 2016-11-05), the aftershocks predominantly occur at greater depths and adjacent to the main slip patch of the Norcia mainshock (as defined by Scognamiglio et al. (2018)), and gradually migrate southward toward the LFS segment (Figure 3.3d). $\delta B_e(PGA)$ and $\Delta\sigma_N$ reveal relatively limited temporal variability compared to Phases 1 and 3 (Figure 3.4e). $\Delta\sigma_N$ exhibits a stronger depth dependence than $\delta B_e(PGA)$, with higher values for events deeper than 5 km (Figures A3.4d-A3.6d in Appendix 3). Conversely, $Q_{0,e}$ decreases with depth, showing lower values at greater depths and higher values above 5 km. As a result, the opposing effects of stress-drop and attenuation lead to relatively stable $\delta B_e(PGA)$ values close to the median.

In Phase 5 (2016-11-05 to 2017-01-18), aftershocks persist at depth near the Norcia main slip patch, while shallow seismicity increases to the north and continues

its gradual southward migration toward the LFS segment (Figure 3.3e). During this period, $\delta B_e(PGA)$ shows negligible variation (Figures 3.4a and 3.4b), whereas $\Delta\sigma_N$ varies markedly in tandem with depth. Two major (~100%) drops in $\Delta\sigma_N$ coincide with the abrupt shallowing of seismicity in the northern VBFS, where $Q_{0,e}$ increases. As in previous phases, the inverse relationship between $\Delta\sigma_N$ and $Q_{0,e}$ results in only modest changes in $\delta B_e(PGA)$.

3.3.2.4. Phases 6 & 7: After Campotosto Mainshocks

The occurrence of three $\boldsymbol{M}$5.1, $\boldsymbol{M}$5.5, and $\boldsymbol{M}$5.3 Campotosto mainshocks at the onset of Phase 6 may result from seismicity migration during Phases 4 and 5 (Michele et al., 2020). During Phase 6 (2017-01-15 to 2017-01-25), aftershocks are sparsely distributed around the mainshocks within the LFS segment (Figure 3.3f). All parameters decrease sharply within the first 1.5 days and then stabilize (Figure 3.4f). Unlike earlier phases, $\Delta\sigma_N$ and $Q_{0,e}$ decrease simultaneously at the phase onset, while stress-drop remains below its median, in contrast to $\delta B_e(PGA)$. $Q_{0,e}$ values are higher than in previous phases, possibly indicating changes in fluid pore pressure near the mainshock area (Malagnini et al., 2022).

During Phase 7 (2017-01-25 to 2018-01-15), aftershock activity is distributed across the entire fault system (Figure 3.3g). Strong variations are observed in $\Delta\sigma_N$, $Q_{0,e}$, and depth, while $\delta B_e(PGA)$ shows only modest changes (Figures 3.4a and 3.4b). These variations may reflect the migration of seismicity from deeper to shallower levels, either along or perpendicular to the fault strike. The spatial distributions of $\delta B_e(PGA)$, $\Delta\sigma_N$, and $Q_{0,e}$ are consistent with patterns observed in earlier phases: events within the VBFS segment typically exhibit higher $\delta B_e(PGA)$ and $\Delta\sigma_N$ values than those in the LFS segment at similar depths, while $Q_{0,e}$ maintains a comparable spatial distribution across both segments (Figures A3.4g-A3.6g in Appendix 3).

Furthermore, we provide a direct comparison between $\delta B_e(PGA)$ and $\Delta\sigma_N$ from the three catalogs as described in detail in Text A3.4 and Figure A3.7 in Appendix 3. Notably, $\delta B_e(PGA)$ exhibits highly consistent patterns and amplitudes across all

phases for the three catalogs, except at the onset of Phases 1 and 6, where our model produces systematically higher values. These differences are likely related to magnitude discrepancies resulting from the use of spatiotemporally variable $Q(f)$ and a three-dimensional velocity model.

3.3.3. Correlation Between $\delta B_e(PGA)$ and $\Delta\sigma_N$

As previously noted, $\delta B_e(PGA)$ variability is generally assumed to reflect variability in stress-drop. Therefore, a similar trend is expected between the two parameters, suggesting a high degree of cross-correlation (e.g., Oth et al., 2017; Trugman & Shearer, 2018). However, our results indicate that the variability in $\delta B_e(PGA)$ can diverge from stress-drop variability due to other physical processes, such as changes in attenuation and/or shear-wave velocity. To investigate how this relationship evolves over time and whether discrepancies occur only during specific periods or persist throughout the sequence, we analyze the temporal variation in the cross-correlation between $\delta B_e(PGA)$ and $\Delta\sigma_N$ (Figure 3.5) using a moving window median. The window length is set to 5% of each sub-dataset, with a 50% overlap. The entire dataset is divided into four sub-datasets from the Amatrice to Visso mainshocks, from Visso to Norcia, from Norcia to Campotosto, and after the Campotosto mainshocks. The three catalogs yield different overall cross-correlation levels: B24 (Figure 3.5c) shows the highest value of 0.96 compared to our study (Figure 3.5a) and K21(Figure 3.5b) with values of 0.78 and 0.59, respectively. Despite these differences in overall values, all catalogs reveal a consistent temporal pattern, namely, a pronounced drop in cross-correlation immediately after each mainshock (Phases 1, 3, 4, and 6), followed by a rebound to higher values. A direct comparison with the temporal variation of $Q_{0,e}$ (Figure 3.5d) indicates that these drops in the cross-correlations coincide with significant changes in $Q_{0,e}$ following each mainshock. Conversely, during phases when $Q_{0,e}$ remains stable (such as Phase 2), the cross-correlation tends to remain steady at elevated levels. Notably, periods with significant changes of $Q_{0,e}$ coincide with discrepancies between $\boldsymbol{M}$ estimates from K21, B21, and our study. The $\boldsymbol{M}$ ratios, calculated as $\boldsymbol{M}$(This Study)/$\boldsymbol{M}$(K21) and $\boldsymbol{M}$(This

Study)/***M***(B24), demonstrate large variations during the phases following the mainshocks (Figure 3.5e). Since $\delta B_e(PGA)$ depends on ***M*** (Eq. 3.2), this results in discrepancies in the correlation between stress-drop and $\delta B_e(PGA)$ computed from the three catalogs.

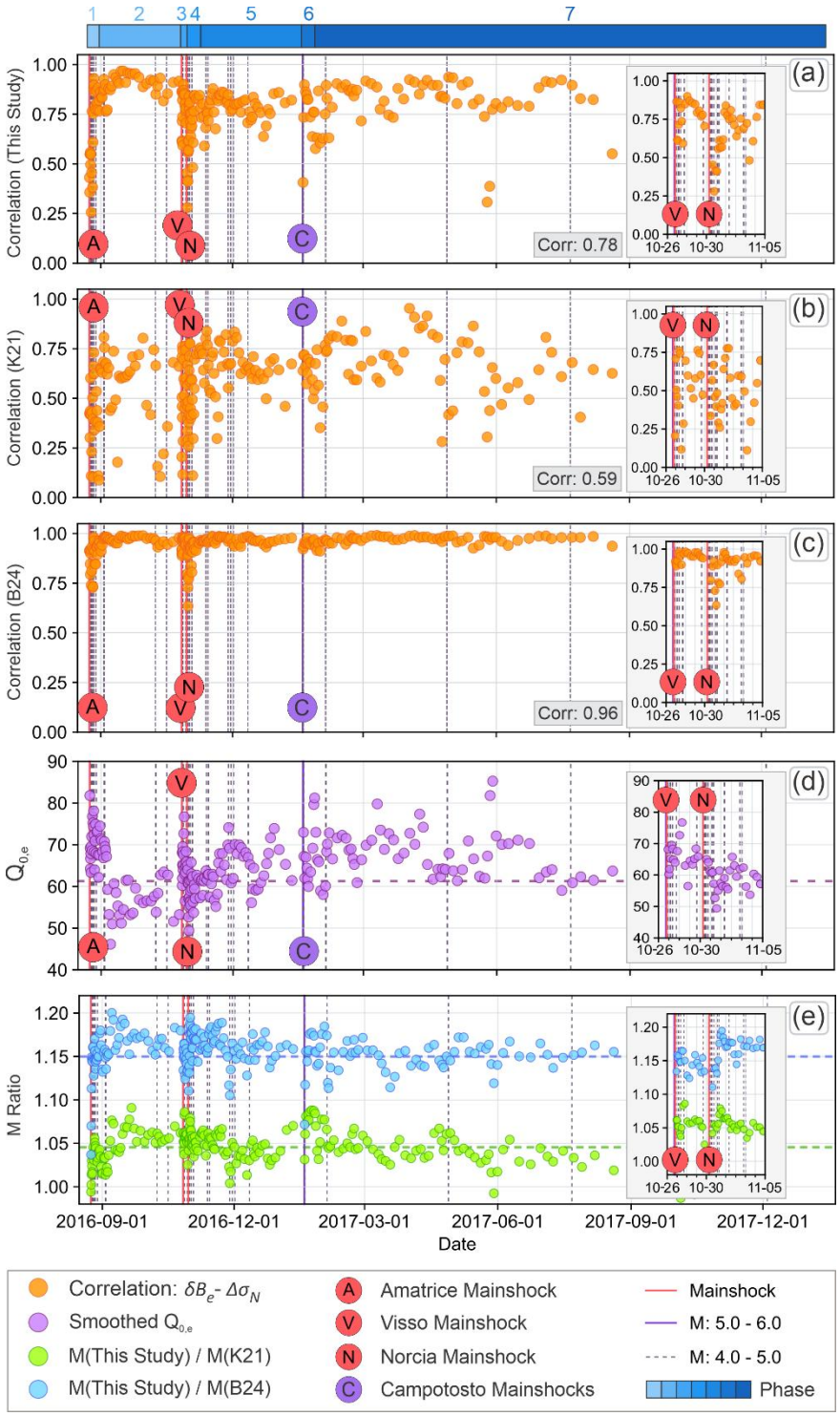

Figure 3.5. Temporal evolution of correlations between between-event residuals and stress-drop, frequency-independent term of quality factor, and magnitude ratios during the seismic sequence. Temporal evolution of **(a)** cross-correlation between $\delta B_e(PGA)$ and $\Delta\sigma_N$ from this study, **(b)** cross-correlation between $\delta B_e(PGA)$ and $\Delta\sigma_N$ from *K21*, **(c)** cross-correlation

between $\delta B_e(PGA)$ and $\Delta\sigma_N$ from *B24*, **(d)** $Q_{0,e}$ from this study, and **(e)** ratio of ***M***(this study) to ***M***(K21) shown in green circles and ratio of ***M***(this study) to ***M***(B24) shown in blues circles. The inset in each subplot provides a zoomed-in view for the period from 2016-10-26 to 2016-11-05 (Phases 3 and 4). The blue color bar indicates the period corresponding to each phase. Horizontal dashed lines in matching colors indicate the median values of $Q_{0,e}$, and ***M*** ratios over the entire sequence. Circles labelled A, V, N, and C denote the occurrence times of the Amatrice, Visso, Norcia, and Campotosto mainshocks, respectively. The vertical red, purple, and dashed grey lines demonstrate the occurrence times of the mainshocks, events with ***M***5.0-6.0, and events with ***M***4.0-5.0, respectively.

3.3.4. Isolating the Contribution of Transient Changes to the Temporal Variability of $\delta B_e(PGA)$

In the previous sections, we demonstrated that $\delta B_e(PGA)$ obtained from RF(***M***) exhibits both spatial and temporal variability. To separate these two components, we compare the $\delta B_e(PGA)$ values from RF(***M***) with those computed using RF(***MXYZ***) and RF(***MXYZT***) (Figure 3.6). As previously discussed, RF(***MXYZ***) and RF(***MXYZT***) significantly reduce the overall variability across all phases, particularly in Phases 1, 3, 4, and 6, which follow the mainshocks and display the largest variability in RF(***M***). By design, RF(***MXYZ***) eliminates spatial variability in *δBe(PGA)* associated with aftershock location, thereby isolating its temporal variability, which may reflect transient changes in the medium or source properties. RF(***MXYZ***) and RF(***MXYZT***) yield nearly identical results, with *δBe(PGA)* remaining close to zero across phases, except for Phase 1 following the Amatrice mainshock. During Phase 1, RF(***MXYZ***) indicates a positive variation in *δBe(PGA)* (+25%), followed by a decrease of 50% lasting for three days after the mainshock. These changes are almost fully absorbed by RF(***MXYZT***), suggesting that they are associated with local changes in source characteristics or path propagation effects. These transient changes contribute to 40%-50% of the total changes of $\delta B_e(PGA)$ obtained from RF(***M***). It is important to point out that such transient changes are not observed after the other mainshocks of

the sequence, even after the Norcia event, which is the largest of the sequence. Given that *δBe(PGA)* is influenced by stress-drop and attenuation, it remains unclear whether the observed transient changes result primarily from transient changes in stress-drop, attenuation, or a combination of both. To understand the cause, we first attempt to analyze the residuals from predictions of $\Delta\sigma$ and $Q_{0,e}$ using a Random Forest Regression approach, with input variables of ***M*** (for stress-drop only), *X*, *Y*, and *Z*. Since both $\Delta\sigma$ and $Q_{0,e}$ are earthquake-specific parameters, the dataset consists of only 2,503 data, which was not sufficient to robustly train the Random Forest models and avoid overfitting issues. As an alternative, we implement a cluster analysis, as described in Section 3.3.5.

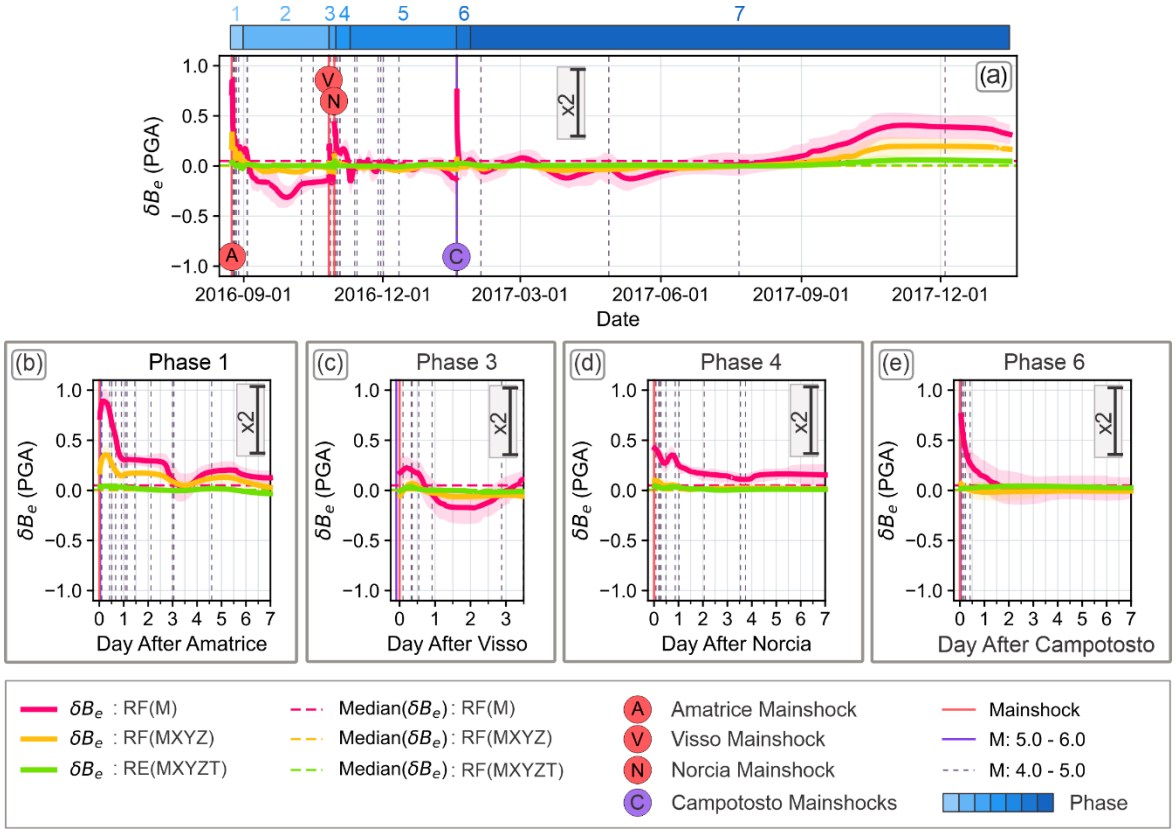

Figure 3.6. Comparison of the temporal evolution of $\delta B_e(PGA)$ obtained from RF(***M***), RF(***MXYZ***), and RF(***MXYZT***) for **(a)** the entire seismic sequence, **(b)** Phase 1: the first week following the Amatrice mainshock, **(c)** Phase 3: the four days after the Visso mainshock, **(d)**

Phase 4: the first week following the Norcia mainshock, **(e)** Phase 6: the first week post the three Campotosto mainshocks. The pink, orange, and green curves represent $\delta B_e(PGA)$ derived from RF(***M***), RF(***MXYZ***), and RF(***MXYZT***), respectively. The blue color bar indicates the period corresponding to each phase. Horizontal dashed lines and shaded areas in matching colors illustrate the median values and ±1 standard deviation of $\delta B_e(PGA)$, $\Delta\sigma_N$, depth, and $Q_{0,e}$, respectively. Circles labelled A, V, N, and C denote the occurrence times of the Amatrice, Visso, Norcia, and Campotosto mainshocks, respectively. The vertical red, purple, and dashed grey lines demonstrate the occurrence times of the mainshocks, events with ***M***5.0-6.0, and events with ***M***4.0-5.0, respectively. The scale line labeled "x2" represents two units on a linear scale.

3.3.5. Cluster Analysis

Although model RF(***MXYZ***) reveals the transient changes of $\delta B_e(PGA)$, it presents relative variations across the entire sequence. For example, during Phase 1, which exhibits the most pronounced transient changes (Figure 3.6b), the seismicity is distributed along a 40 km fault strike and spans the full depth range. Consequently, the magnitude of transient changes may vary spatially along both strike and depth, potentially masking localized effects. We select small clusters of events at different positions relative to the mainshocks to isolate better and understand the transient behavior of $\delta B_e(PGA)$, $\Delta\sigma_N$, and $Q_{0,e}$. Because the events within a cluster are confined to a narrow spatial band, variability due to changes in X, Y, and Z is minimized. In this setting, $\delta B_e(PGA)$ derived from model RF(***M***) is expected to closely match that from model RF(***MXYZT***) (black curves in Figure 3.7), thereby providing a straightforward means to verify the robustness of our GMMs. Moreover, because spatial variability in $\Delta\sigma_N$ and $Q_{0,e}$ cannot be effectively removed by regression due to overfitting, this cluster-based approach provides an alternative for gaining insight into the transient behavior of these parameters. We analyze three clusters whose locations are shown in Figures 3.3 and A3.1:

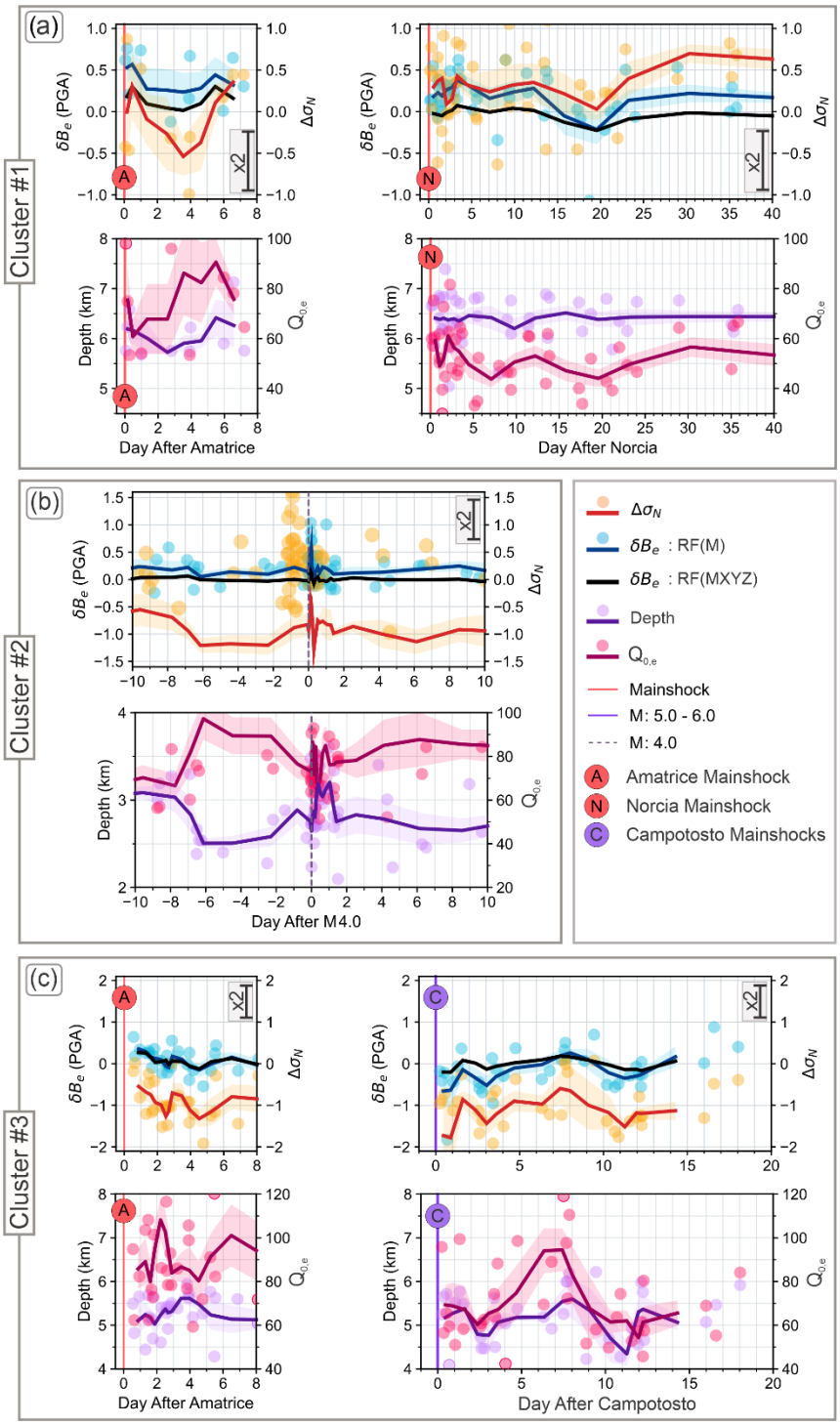

Figure 3.7. Transient changes of $\delta B_e(PGA)$, $\Delta\sigma_N$, and $Q_{0,e}$ for the selected clusters: **(a)** Cluster #1; left panel: the period following the Amatrice mainshock, right panel: the period following the Norcia mainshock, **(b)** Cluster #2; a 20-days window before and after a ***M***4.0 event occurred on 2016-11-27T21:41:15 UTC, **(c)** Cluster #3; left panel: the period following the Amatrice mainshock, right panel: the period after the Campotosto mainshocks. The blue,

orange, purple, and magenta curves represent $\delta B_e(PGA)$ from RF(***M***), $\Delta\sigma_N$, depth, and $Q_{0,e}$, respectively. The black curve shows $\delta B_e(PGA)$ obtained from RF(***MXYZ***). Shaded areas in matching colors illustrate ±1 standard deviation of $\delta B_e(PGA)$, $\Delta\sigma_N$, depth, and $Q_{0,e}$. The scale line labeled "x2" represents two units on a linear scale. Circles labelled A, V, N, and C denote the occurrence times of the Amatrice, Visso, Norcia, and Campotosto mainshocks, respectively. The vertical red, purple, and dashed grey lines demonstrate the occurrence times of the mainshocks, the Campotosto events, and an event with ***M***4.0, respectively.

- **Cluster #1 (C1):** This ~3 km–wide cluster lies between the Amatrice and Norcia hypocenters, close to the main slip patches of both events, suggesting potential influence from both ruptures. Depth variations within the cluster are minimal (Figure 3.7a), whereas $\delta B_e(PGA)$, $\Delta\sigma_N$, and $Q_{0,e}$ exhibit clear transient changes. Following the Amatrice mainshock, $\Delta\sigma_N$ shows strong variability (a 35% increase within the first day, followed by a 110% drop and a 140% increase), approximately three times larger than the variations in $\delta B_e(PGA)$, which are damped by strong $Q_{0,e}$ changes (an 18% decrease within the first day followed by a 50% increase). Parameter variations are more pronounced and persist longer after the Amatrice event (~7 days) than after the Norcia event (~4 days), despite the cluster being closer to the Norcia hypocenter. Although this contrast may partly reflect limited data availability after Amatrice, similar $\delta B_e(PGA)$ patterns are observed throughout the sequence using model RF(***MXYZ***) (Figures 3.6b and 3.6d). The denser dataset following the Norcia mainshock further indicates that parameter variations persist from days 5 to 40, albeit with more stable behavior than in the immediate post-event period.
- **Cluster #2 (C2):** This cluster, with a 3 km dimension, includes the aftershocks surrounding a ***M***4.0 event that occurred on 2016-11-27T21:41:15 UTC. C2 is located about 15 km north of the Visso Mainshock, within the shallow crustal section at depths between 2 and 4.5 km. As shown in Figure 3.7b, all examined parameters exhibit significant variations, especially sharp increases and decreases of $\Delta\sigma_N$ and $\delta B_e(PGA)$ within less than one day after the ***M***4.0 event.

The cluster is probably sufficiently distant in both space and time from the mainshocks to avoid significant influence from them. It is therefore noteworthy that a moderate ***M***4.0 event can still induce clear and rapid changes in parameter behavior.

- **Cluster #3 (C3):** This cluster, approximately 5 km in diameter, is located within the LFS segment, south of the Amatrice slip patch and near the Campotosto mainshocks. Given its position, it is likely influenced by both events. As illustrated in Figure 3.7c, a minor limitation of this cluster is the absence of aftershocks during the first day following the mainshocks. Following the Amatrice event, a short drop (1 day) of about 100% in $\Delta\sigma_N$ is observed, together with a sharp increase in $Q_{0,e}$, resulting in a 35% drop in $\delta B_e(PGA)$ within the first two days. Following the Campotosto events, $\Delta\sigma_N$ increases by 150% during the first two days and then exhibits smaller fluctuations, displaying a similar trend to $\delta B_e(PGA)$. A notable variation in $Q_{0,e}$, marked by a 60% increase followed by a 40% decrease between days 4 and 10, appears to have little impact on the overall relationship between $\Delta\sigma_N$ and $\delta B_e(PGA)$.

3.4. Discussion

Our results indicate that high-frequency ground-motion observed during the seismic sequence exhibits strong temporal variability, especially within a few days following the mainshocks. This variability is not solely driven by changes in stress-drop but results from a combination of stress-drop and quality-factor variations. In the following, we discuss the relationship between $\delta B_e(PGA)$, $\Delta\sigma_N$, $Q_{0,e}$, their depth dependence, and potential physical interpretations underlying the observed temporal variabilities.

3.4.1. Relationship Between $\Delta\sigma_N$ and $\delta B_e(PGA)$

Assuming a Brune's source model and using the theory of random vibrations, PGA should be proportional to $\Delta\sigma^a$ with $a \approx 0.8$ (e.g., Cotton et al., 2013; Causse &

Song, 2015), implying that the correlation between $\delta B_e(PGA)$ and $\Delta\sigma$ equals 1. Analyses of the relationship between stress-drop and PGA effectively reveal a high correlation (Oth et al., 2011; Trugman & Shearer, 2018). As shown in Figure 3.5, the temporal evolution of the cross-correlation between $\Delta\sigma_N$ and $\delta B_e(PGA)$ across the three catalogs exhibits a consistent pattern, with overall high values but sharp decreases lasting for several days following each mainshock, coinciding with the largest variations in $Q_{0,e}$. The overall level of correlation depends on the methodology adopted to compute stress-drop. The average correlation is 0.96 using stress-drop values from B24, which assumes constant $Q(f)$, while it drops to 0.78 and 0.59 using our study and K21, respectively, allowing for a time-dependent quality-factor. To further understand the origin of the observed relationship between $\Delta\sigma_N$ and $\delta B_e(PGA)$, we design two ground-motion simulation models. We use the Point Source Stochastic simulation method (Boore, 1983, 2003) to simulate the entire catalog based on the estimated source and path parameters. This method combines a theoretical amplitude spectrum (typically from Brune's source model) with random phases to generate time series whose durations depend on the earthquake size and distance from the source. In the first model (SIM1), we incorporate event-specific stress-drop values from our newly developed catalog while assuming a constant $Q(f)$ equal to its mean value for all events. In the second model (SIM2), we account for the variability in both stress-drop and $Q(f)$ as observed in our catalog. For both simulation models, we assume a generic rock site condition for all stations as the site response. We then estimate $\delta B_e(PGA)$ using the regression model RF($\boldsymbol{M}$) (Figure 3.8). The comparison between the two simulation models highlights that incorporating a variable $Q(f)$ factor affects both the level and temporal pattern of $\delta B_e(PGA)$. Note that the simulation sets do not fully reproduce the observed $\delta B_e(PGA)$ values, particularly during the early days of Phase 1 and Phase 6, which could be attributed to errors in $Q(f)$, $\Delta\sigma$, or the use of a generic rock site condition for all stations in the simulation.

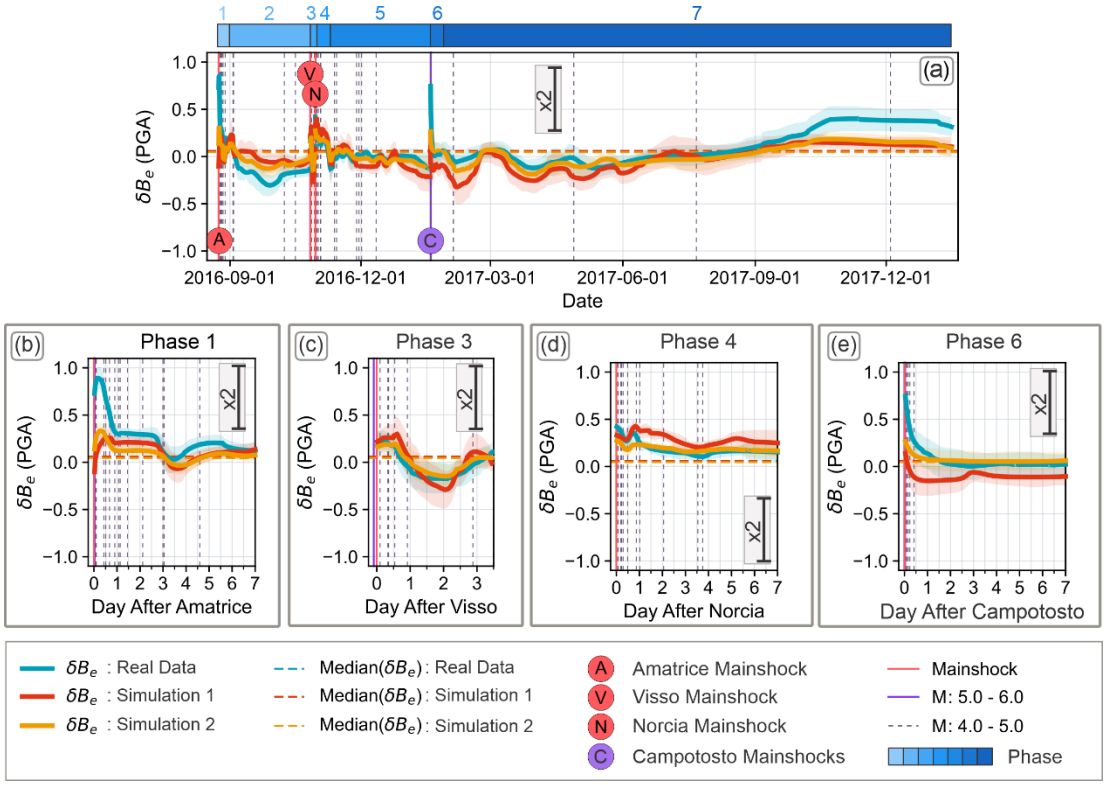

Figure 3.8. Comparison of the temporal evolution of $\delta B_e(PGA)$ obtained from RF(***M***) for real data (blue curve), simulation 1 (SIM1) (red curve), and simulation 2 (SIM2) (orange curve) for: **(a)** the entire seismic sequence, **(b)** Phase 1: the first week following the Amatrice mainshock, **(c)** Phase 3: the four days after the Visso mainshock, **(d)** Phase 4: the first week following the Norcia mainshock, **(e)** Phase 6: the first week post the three Campotosto mainshocks. The blue color bar indicates the period corresponding to each phase. Horizontal dashed lines and shaded areas in matching colors illustrate the median values and ±1 standard deviation of $\delta B_e(PGA)$, $\Delta\sigma_N$, depth, and $Q_{0,e}$, respectively. Circles labelled A, V, N, and C denote the occurrence times of the Amatrice, Visso, Norcia, and Campotosto mainshocks, respectively. The vertical red, purple, and dashed grey lines demonstrate the occurrence times of the mainshocks, events with ***M***5.0-6.0, and events with ***M***4.0-5.0, respectively. The scale line labeled "x2" represents two units on a linear scale.

We also compute the temporal evolution of cross-correlations between $\Delta\sigma_N$ and the simulated sets of $\delta B_e(PGA)s$ from SIM1 and SIM2, as well as between real and simulated $\delta B_e(PGA)s$ (Figure A3.8 in Appendix 3). The cross-correlation between $\Delta\sigma_N$

and $\delta B_e(PGA)$ from SIM1 (with a constant $Q(f)$) is 0.97 and shows no significant drops throughout the sequence (Figure A3.8a). In contrast, the cross-correlation between $\Delta\sigma_N$ and $\delta B_e(PGA)$ from SIM2 (with $Q(f)$ variation) closely matches that of the real data, both in terms of average level (0.84 and 0.78) and temporal pattern. These results confirm that the analysis of $\delta B_e(PGA)$ during a seismic sequence represents a good indicator of the stress-drop variability only when attenuation remains relatively stable. Additionally, the $\delta B_e(PGA)$ values derived from the real and SIM2 data yield a high correlation of 0.9 (Figure A3.8c), with drops following the mainshocks. This high correlation indicates that SIM2 better captures the real data compared to SIM1, which shows a correlation of 0.79. The observed drops following the mainshocks likely result from uncertainties in moment magnitude, stress-drop, and/or quality-factor. In particular, as previously discussed, any error in $Q(f)$ leads to deviations in moment magnitude and stress-drop during the fitting process (Figure 3.1). Error in $\boldsymbol{M}$ influences $\delta B_e(PGA)$ during the regression process and subsequently affects the stress-drop, because the stress-drop is proportional to $\boldsymbol{M}/f_c^3$ (Brune, 1970). Since stress-drop also depends on shear-wave velocity, an additional explanation for the observed drop of correlation between the $\delta B_e(PGA)$ of real and SIM2 could be associated with changes in shear-wave velocity following each mainshock, potentially caused by fault-zone cracking or variations in pore pressure. Several studies (e.g., Schaff & Beroza, 2004; Soldati et al., 2015, 2019) have documented post-mainshock changes in seismic velocity in the source region. For example, (Soldati et al., 2019) reported maximum changes of about 0.08% during the 2016-2017 Central Italy sequence. But since this represents a relatively minor change, it is not expected to cause significant errors in moment magnitude or stress-drop estimates.

3.4.2. Depth Dependency of $\Delta\sigma_N$ and δB_e

The relationship between stress-drop and depth remains a topic of debate. While some studies have reported depth-dependent variations in stress-drop (Hardebeck & Aron, 2009; Huang et al., 2017; Annemarie S. Baltay et al., 2019; Trugman, 2020), others have not observed such trends (Shearer et al., 2006; Allmann & Shearer, 2007;

Abercrombie et al., 2021). Our results indicate a significant increase in $\Delta\sigma_N$ estimates with depth, evidenced by a cross-correlation of 0.63. However, this increase does not follow a strictly linear trend throughout the entire depth range (Figure A3.9a in Appendix 3). Specifically, $\Delta\sigma_N$ increases linearly up to a depth of 6 km and then tends to remain relatively constant at deeper sections. Therefore, it diverges from the common assumption that stress-drop represents a fraction of the effective normal stress imposed by overburden pressure (Scholz, 2019; Huang et al., 2017). The observed depth dependency could be attributed to different factors, including variations of shear-wave velocity with depth, changes in pore fluid pressure, or systematic biases introduced by not fully correcting for attenuation effects in the spectral fitting process (e.g., Allmann & Shearer, 2007; Hardebeck & Aron, 2009; Trugman, 2020; Abercrombie et al., 2021; Abercrombie & Baltay, 2025), as discussed subsequently. The increase in stress-drop with depth may be associated with the increase in shear-wave velocity with depth (Allmann & Shearer, 2007; Vallée, 2013). Assuming an oversimplified velocity model may introduce bias into the stress-drop in the upper crust. To mitigate this, we utilize a 3D velocity model that accounts for lateral and depth variations, thereby reducing the potential for artificial depth dependency in stress-drop estimates. However, Huang et al. (2017) mentioned that the increase in shear-wave velocity with depth alone cannot explain the stress-drop increase, which also involves other processes. Additionally, mainshock-induced fluid diffusion may increase pore pressure in the shallow crust, reducing effective normal stress and consequently lowering stress-drop (e.g., Lengliné et al., 2014; Brown & Ge, 2018; Convertito et al., 2020; Fonzetti et al., 2024), which is investigated in Section 3.4.3. Finally, stress-drop derived from single-spectrum fitting can be biased by the trade-offs between stress-drop and depth-dependency of attenuation term (Abercrombie et al., 2021). If $Q(f)$ increases with depth, the waves radiated from deeper events experience smaller attenuation than shallower events. Therefore, a simplified $Q(f)$ model without accounting for plausible depth variations could introduce the depth-dependency of stress-drop as an artifact. The "effective Q" factor used in this study represents a path-averaged measure of attenuation across the

recording stations. As such, it may yield similar $Q(f)$ values for two events at different depths, thereby masking true depth-dependent variations in attenuation. Moreover, variations in station distribution could further influence this measurement. If deeper and shallower events are predominantly recorded by different subsets of stations, the associated seismic waves will sample different portions of the crust. As a result, any observed differences in "effective Q" may reflect differences in ray paths and station locations rather than intrinsic attenuation variations with source depth.

Using the same event dataset, our study, K21, and B24 yield cross-correlations of 0.63, 0.41, and 0.60 between $\Delta\sigma_N$ and depth, respectively (Figures A3.9b and A3.9c). Notably, B24 employs a simplified attenuation model that does not account for differences in wave propagation paths between deep and shallow events, as it is only dependent on distance and frequency. To further investigate this, we examine the depth dependence of stress-drop estimates from K21, derived using both the Empirical Green's Function (EGF) and Cluster-Event methods. These techniques are generally considered more robust in mitigating attenuation effects (e.g., Sonley & Abercrombie, 2006; Ko et al., 2012; Abercrombie et al., 2021). As illustrated in Figures A3.9d and A3.9e, stress-drop estimates obtained from the EGF and Cluster-Event methods show no significant depth dependence (cross-correlation of 0.13 and 0.18, respectively), in contrast to the clear depth trend observed in results from single-spectrum fitting approaches. This discrepancy suggests that the apparent depth dependence in the latter partly stems from inadequate attenuation modeling and subsequent inaccuracies in spectral correction.

Past studies have shown that deeper earthquakes generate larger high-frequency ground-motions (e.g., McGarr, 1984; Abercrombie et al., 2021). $\delta B_e(PGA)$ derived from RF($\boldsymbol{M}$) exhibits depth-dependent behavior that varies across the three catalogs. For our catalog (Figure A3.9f), $\delta B_e(PGA)$ shows a shallow (< 3 km) depth dependence with moderate correlation (0.43), which is weaker than that observed for $\Delta\sigma_N$. In contrast, the K21 catalog (Figure A3.9g) displays a strong depth correlation for $\delta B_e(PGA)$ (0.67) but a weaker correlation for $\Delta\sigma_N$, whereas the B24 (Figure A3.9h)

exhibits comparable correlations for both parameters. Overall, these contrasts highlight the combined effects of stress-drop and attenuation on $\delta B_e(PGA)$. Because $\boldsymbol{M}$ is the only input parameter that varies among the three catalogs, the observed discrepancies likely stem from uncertainties in $\boldsymbol{M}$. Since $\boldsymbol{M}$ is estimated from the low-frequency spectral plateau and depends on both attenuation and shear-wave velocity ($\boldsymbol{M} \propto \beta^{-3}$), comparison with B24 indicates that low-frequency attenuation differences dominate, given that both catalogs use the same 3D shear-wave velocity model.

3.4.3. Spatial and Temporal Evolution of Stress-Drop, Attenuation, and Ground-motion

3.4.3.1. Migration of Seismicity

Our results indicate that the migration of seismicity plays a key role in the observed temporal evolution of ground-motion during the seismic sequence, as both source properties and propagation effects are spatially variable. Notably, for a given magnitude and distance, shallow seismicity is generally associated with lower stress-drop and hence lower high-frequency ground-motion (Section 3.4.2). Therefore, understanding the processes that control earthquake depths is important. Figure 3.9 presents a schematic illustration of the temporal evolution of seismicity. Following the Amatrice mainshock, seismicity migrates toward the shallower sections of the crust (pink arrows in Figure 3.9a), while activity in the deeper sections remains limited (see Figures 3.3a and 3.3b). This upward migration may be governed by the so-called "fault-valve" effect (e.g., Sibson, 1992, 2020; Matsumoto et al., 2021), where over-pressured fluids are trapped at depth due to the presence of a barrier that prevents their upward movement (Figure 3.9b). The occurrence of a mainshock can damage or rupture this barrier, allowing the trapped fluid to escape into the shallower sections and surrounding host rocks (Figure 3.9c). A 3D poroelastic model by Convertito et al. (2020) for the 2016-2017 Central Italy sequence supports this interpretation. Similarly, Miller et al. (2004) suggested that the aftershocks of the 1997 Colfiorito earthquake in Central Italy were likely triggered by upward

migration of over-pressured fluids released through the mainshock-damaged fault zone. After the Amatrice event, the Visso mainshock occurred in the shallower section of the region, likely within an over-pressured fluid zone (Tung & Masterlark, 2018). Following the Visso event, seismicity propagates within the shallow crust and extends deeper toward the Norcia hypocenter (Figure 3.3c and blue arrows in Figure 3.9a). After the Norcia mainshock, seismicity primarily occurs at greater depths and migrates northward and southward mainly along the LFS segment, which hosted the Campotosto mainshocks (Figure 3.8d and 3.8e, and orange arrows in Figure 3.14a). Additionally, the existing thrust systems (black lines in Figure 3.9b) may play a crucial role by trapping fluids and seismicity in the shallower sections, while also creating pathways in the deeper zones that facilitate the migration of fluids and seismicity along the normal fault system (e.g., Chiaraluce et al., 2017; Michele et al., 2020; Barchi et al., 2021).

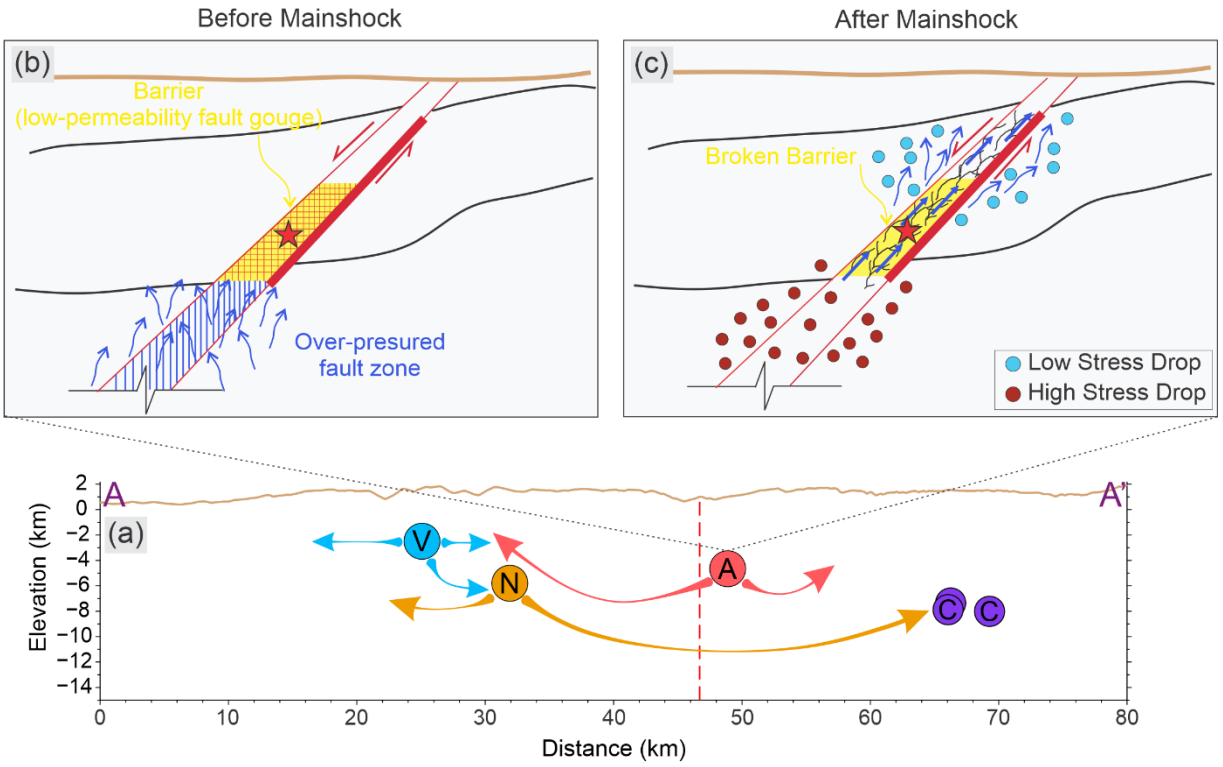

Figure 3.9. Schematic illustration of the spatial and temporal migration of seismicity during the 2016–2017 Central Italy sequence. **(a)** Cross-sectional view (along cross-section A–A′ in Figure A3.1) showing the locations of the mainshocks and the direction of seismicity migration following each event: pink arrows for the Amatrice, blue arrows for the Visso, and orange arrows for the Norcia mainshocks. The circles labelled A, V, N, and C mark the epicenters of Amatrice, Visso, Norcia, and Campotosto mainshocks, respectively. The red vertical dashed line separates events along the strike of the VBFS (0 – 47 km from A) and the LFS (47–80 km from A), **(b)** Conceptual model of the fault-valve mechanism before the Amatrice mainshock. The blue zone indicates an overpressured fault segment, and the yellow zone represents a sealing barrier, **(c)** the post-Amatrice rupture phase. The thick red line marks the coseismic rupture of the Amatrice mainshock. The yellow zone shows the breached barrier, and the blue arrows indicate upward fluid migration. Red and blue circles represent areas of high and low stress-drop, respectively. The red star symbol marks the Amatrice hypocenter. Black lines denote thrust faults.

Furthermore, both $\delta B_e(PGA)$ and $\Delta\sigma_N$ vary spatially along the fault strike and with depth (Figures A3.4 and A3.5 in Appendix 3). Earthquakes in the VBFS consistently exhibit higher $\Delta\sigma_N$ than those in the LFS at comparable depths. This difference can primarily be attributed to variations in geological properties, with the Mount-Sibilini-Thrust (*MST*) Fault acting as a boundary separating the two fault systems (Chiaraluce et al., 2017; Barchi et al., 2021). The lower $\Delta\sigma_N$ observed in the LFS may result from a lower coefficient of friction due to low-strength materials or from elevated pore pressure, which reduces the effective normal stress. Additionally, high stress-drop values have been associated with fault complexity (e.g., Goebel et al., 2015; Chu et al., 2021). The more complex fault structure in the VBFS may contribute to its higher $\Delta\sigma_N$, as this region features multiple synthetic and antithetic normal faults overprinting thrust faults at both the surface and depth (Kemna et al., 2021). Despite these differences, $\delta B_e(PGA)$ for both VBFS and LFS yields similar values, suggesting that the lower stress-drop values in the LFS result in high ground-motions, which could be due to lower attenuation along this segment. Gabrielli et al. (2023) demonstrated that wave scattering, as a proxy for attenuation, is lower in the LFS than in the VBFS during the sequence. The lower $\Delta\sigma_N$ and $\delta B_e(PGA)$ observed at shallow depths could be attributed to a combination of several factors, including the presence of mechanically weak materials, a reduction in effective normal stress due to elevated pore fluid pressure, and increased attenuation resulting from seismic waves propagating through sediments and softer geological structures.

3.4.3.2. Temporal Variability of $\Delta\sigma_N$, $\delta B_e(PGA)$, and $Q_{0,e}$

As shown in Figure 3.4, $\Delta\sigma_N$, $\delta B_e(PGA)$, and $Q_{0,e}$ exhibit temporal variations throughout the sequence, with changes occurring primarily during the phases following each mainshock. Notably, after the Amatrice mainshock (Phase 1), the median values of $\Delta\sigma_N$ and $\delta B_e(PGA)$ increase significantly for approximately half a day. A short increase of the same amplitude is also observed using model RF(***MXYZ***) (Figure 3.6b) and from the cluster analysis (Cluster C1, Figure 3.7a), suggesting that it is associated with transient, local changes. Note that the number of aftershocks

recorded immediately after the mainshock in our database is unfortunately too small to quantify this increase fully. These high values are observed in the regions adjacent to the maximum slip patches (Figures A3.5), possibly reflecting stress release in areas of high frictional strength that did not rupture during the mainshocks (e.g., Hardebeck & Aron, 2009; Adrien Oth & Kaiser, 2014; Moyer et al., 2018; Yamada et al., 2021; Folesky & Kummerow, 2025). This initial increase may also be influenced by the above-explained "fault-valve" effect (Figures 9b and 9c). Seismicity within the first half day primarily occurs below a depth of ~8 km, coinciding with the lower depth of the Amatrice surface rupture. The region located below this limit may experience dehydration, thereby leading to reduced effective normal stress, larger fault strength, and larger stress-drop (e.g., Noir et al., 1997; Di Toro et al., 2011; De Gori et al., 2023; Fonzetti et al., 2024).

Following the early post-mainshock period of the Amatrice earthquake, the median values of $\Delta\sigma_N$, $\delta B_e(PGA)$, and $Q_{0,e}$ decline to below-average levels. This decrease is observed for both RF(***M***) and RF(***MXYZ***), but with a smaller magnitude for the latter, indicating that ~40% of the reduction is associated with transient, local changes (Figure 3.6b). The trend observed for RF(***MXYZ***) is also consistent with the above-mentioned "fault-valve" effect, with seismicity and fluid migrating toward shallower depth (<~8 km), accompanied by a reduction of fault strength and stress-drop (Figures 3.3a and 3.9c). Another hypothesis is a reduction in fault strength due to extensive damage or fracturing along and near the mainshock fault planes (Allmann & Shearer, 2007; Shaw et al., 2015; Trugman & Shearer, 2017; Baltay et al., 2019). Interestingly, a short-lived increase and decrease of $\Delta\sigma_N$ and $\delta B_e(PGA)$, as reported above following the Amatrice mainshock, is also observed following a ***M***4.0 event located at a depth of 4 km, north of the Visso rupture (Cluster C2, Figure 3.7b). This suggests that the above-described process can also be activated following moderate events. The amplitude of changes is larger than after Amatrice, possibly due to the shallower depth.

Bindi et al. (2018) and Kemna et al. (2021) also observed an overall decrease in stress-drop followed by a gradual increase in the average following the different mainshocks, which they associated with the damage created by the mainshocks and a healing phase. Bindi et al. (2018) observed a similar trend for $\delta B_e(PGA)$, using a regression model based on $\boldsymbol{M}$ and R only, as presented in Figure 3.4. We argue this behaviour may simply arise from the spatial variability of $\Delta\sigma_N$ and $\delta B_e(PGA)$, as discussed in Section 3.4.3.1. Analyses using model RF($\boldsymbol{MXYZ}$) and clustering, therefore, provide a complementary approach to investigate the origin of the temporal changes. Cluster C1 exhibits notable changes during the period following the Amatrice mainshock, in contrast to the relatively stable behavior observed after the Norcia event, despite C1 being located very close to the Norcia hypocenter. This suggests that the portion of the fault ruptured during the first mainshock may not have fully healed, thereby limiting the reactivation of fluid or damage-related processes, and thus showing weaker transient changes in the later phase. Note that the limited number of events (2,503) in this study restricts the ability to define more spatially refined clusters for further analysis. The $\delta B_e(PGA)$ values estimated from RF($\boldsymbol{MXYZ}$) further support this interpretation: they show clear temporal variability in Phase 1 (following the Amatrice event), but no variability in Phase 4 (following the Norcia event). Finally, we note that model RF($\boldsymbol{MXYZ}$) indicates stable $\delta B_e(PGA)$ values during Phase 2, and hence does not reveal any recovery phase after the Amatrice event (Figure 3.6a). Further investigations are necessary to understand whether this indicates an absence of the recovery phase or is due to the resolution limit of our analysis.

3.4.3.3. Impact of Potential Changes of Shallow Subsurface on $\delta B_e(PGA)$

Several studies (Bonilla et al., 2019; Vassallo et al., 2022; Esfahani et al., 2024; Miroslav Hallo et al., 2025) have shown that surface geological conditions beneath recording stations can undergo temporal changes following a mainshock. For instance, Vassallo et al. (2022) reported that the closest station to the mainshocks experienced a sudden drop of 7%-10% in the dominant frequency during the 2016-

2017 Central Italy sequence, with a gradual recovery over several months to years. However, it remains unclear whether such variations have a significant impact on ground-motions that could bias our results and interpretations of observed $\delta B_e(PGA)$. To investigate this, we perform two tests. First, we exclude stations located within 10 km of each mainshock from our catalog. The remaining set of stations is expected to be only poorly affected by such a non-linear effect. Given that this effect is time-dependent, we apply model RF(***MXYZ***) to compute $\delta B_e(PGA)$, which accounts for temporal variability while minimizing the influence of spatial heterogeneity in the aftershock distribution. As shown in Figure A3.10 in Appendix 3, the temporal variation of $\delta B_e(PGA)$ for this test dataset closely matches that of the full catalog, indicating a negligible impact of site response variations on ground-motion estimates. In the second test, we use the Point Source Stochastic method to simulate virtual earthquakes with varying magnitudes at a station located 10 km from the sources, with a characterized site response. We then introduce a 15% downward shift in the dominant site frequency, without altering amplification, and rerun the simulations. The resulting changes in *PGA* range from 1% to 3%, suggesting a minimal effect of dominant frequency shifts on peak ground-motion levels.

3.5. Conclusion

To investigate the origin of the temporal variability in high-frequency ground-motion during the 2016–2017 central Italy seismic sequence, we analyzed a catalog of 2,503 earthquakes containing moment magnitude (***M***), stress-drop ($\Delta\sigma$), event-specific frequency-dependent quality-factor ($Q_e(f)$) as a proxy for attenuation and path effects, and between-event residuals of PGA ($\delta B_e(PGA)$), as computed in Chapter 2. $\delta B_e(PGA)$ was computed as the residual relative to non-parametric models (Random Forest), which incorporate magnitude, distance, and possibly event location and origin time as input parameters (models RF(***M***), RF(***MXYZ***), and RF(***MXYZT***)). The main conclusions are as follows:

- The $Q_{0,e}$ values exhibit significant changes during the first few days following the four mainshocks, strongly influencing $\Delta\sigma$ and $\boldsymbol{M}$ estimates. This highlights the need to account for the spatial variability of attenuation in spectral-based estimates of stress-drop in seismic sequences.
- The $\delta B_e(PGA)$ values derived using model RF($\boldsymbol{M}$) significantly vary during the first few days following the four mainshocks, particularly after the Amatrice and Campotosto earthquakes, with drops exceeding 100%. These variations are driven by variation in $\Delta\sigma$ but are also significantly affected by variability in $Q_{0,e}$. The average correlation between $\delta B_e(PGA)$ and $\Delta\sigma_N$ is 0.78. It generally exceeds 0.85 over the sequence, except during the first few days following the mainshocks, due to the strong temporal variability of $Q_{0,e}$. As a result, $\delta B_e(PGA)$ is not necessarily a good indicator of stress-drop and frictional fault properties in the first days following mainshocks.
- Since earthquake locations vary significantly throughout the sequence, and $\delta B_e(PGA)$ values are spatial variables, $\delta B_e(PGA)$ values obtained using RF($\boldsymbol{M}$) also vary over time. Notably, seismicity generally migrates towards shallower depths following the mainshocks, and shallower earthquakes typically exhibit lower $\delta B_e(PGA)$ values, resulting in an overall decrease in $\delta B_e(PGA)$ over time. These decreases do not necessarily reflect local temporal changes of the medium or source properties. Therefore, GMMs based on only magnitude and distance should be used cautiously when interpreting the temporal variability in ground-motion.
- Among the most notable temporal changes of the $\delta B_e(PGA)$ values, we observe a ~25% short-lived increase followed by a ~100% drop within three days following the Amatrice event. Using model RF($\boldsymbol{MXYZ}$) and cluster analysis, we show that ~40 - 50% of these changes stem from local, transient changes in medium and source properties. We attribute these to changes in fault strength, likely induced by fluid-driven and/or damage-driven processes. Such transient changes are observed after the Amatrice earthquake but not after the other mainshocks. This suggests that these processes could not be reactivated

following the other mainshocks, possibly due to incomplete fault healing. However, similar changes are observed following an ***M***4.0 shallow earthquake located north of the Visso mainshocks, indicating that such processes can also occur after moderate earthquakes.

- These findings emphasize the importance of accounting for the temporal variability of path-propagation effects and of using GMMs that incorporate earthquake location to analyze the spatio-temporal variability of ground-motion. Our results may also provide valuable constraints for seismic hazard and risk analysis by improving predictions of aftershock ground-motions during earthquake sequences.

Data and Resources

The catalog released by Kemna et al. (2021) is available for download at: https://zenodo.org/records/5196236 (last accessed March 2026). The catalog published by Bindi et al. (2020) is accessible at: https://zenodo.org/records/13313095 (last accessed March 2026). Random Forest regressions are performed using the publicly available scikit-learn Python programming package (Pedregosa et al., 2011). Several figures were plotted using GMT 6.6.0 (Wessel et al., 2019), available at: https://www.pygmt.org/v0.16.0/ (last accessed March 2025). Some figures were also generated using Matplotlib 3.10.0 (Hunter, 2007) available at: https://matplotlib.org/ (last accessed March 2025).

Acknowledgments

This study benefited from funding from Ministère de la Transition Ecologique et de la Cohésion des Territoires, through Convention DGPR-Univ. Gustave Eiffel 2024. We would like to thank Dino Bindi for providing detailed information about the attenuation model they used in their study. We also thank Editor XXXX and XXXX reviewers for their valuable comments, which helped improve the quality of the manuscript.

Conflict of Interest

The authors declare there are no conflicts of interest for this manuscript.

Appendix 3

Text A3.1. Comparison of Moment Magnitude and Stress-Drop from the Three Catalogs

In Figure A3.2, we compare the moment magnitude and stress-drop estimates from this study to those of Kemna et al. (2021) (K21) and Bindi et al. (2024). K21 estimated source parameters by adopting shear-wave velocity from a 1D velocity structure model and frequency-independent Q values, allowing Q to vary to account for potential spatial and temporal variations during the spectral fitting process. In contrast, B24 used a 3D shear-wave velocity model and a simplified nonparametric attenuation model, which depends only on hypocentral distance and frequency. B24 study, extending from Central to Southern Italy, assumes constant attenuation parameters for the Amatrice-Norcia area. This approach implies that ground-motion attenuation at a given distance is similar for two events with different locations and occurrence times; hence, it does not capture the spatial and temporal variability of attenuation in the sequence. Compared with these approaches, our study employs a methodology that integrates a 3D shear-wave velocity model (similar to B24) with a frequency-dependent Q model, and allows for spatial and temporal variability of attenuation. However, it is important to note that our Q estimates represent the effective, average attenuation between an event and a station network and are not expected to capture fine spatial variations of attenuation.

A comparison of moment magnitude estimates reveals that our $\boldsymbol{M}$ values have a mean slightly higher than those reported by K21 (3.0 and 2.87, respectively, Figure A3.2a). This discrepancy may be attributed to differences in adopted shear-wave velocity models and the fundamental distinction between using frequency-independent versus frequency-dependent attenuation models. Notably, several studies (Pisconti et al., 2015; Akinci et al., 2022; Castro et al., 2021) showed that the Q factor in Central Italy is strongly frequency-dependent. Furthermore, Supino et al.

(2019) noted that when source scaling parameters are inverted using a frequency-independent Q within an attenuation model with frequency-dependent Q, the estimated quality factor may not represent a true average value. The influence of the attenuation model on magnitude bias becomes even more apparent when comparing our $\boldsymbol{M}$ estimates to $\boldsymbol{M}$(B24). Despite using the same 3D shear-wave velocity model, B24 reports systematically lower $\boldsymbol{M}$ values, with a mean of 2.61. This suggests that the simplified attenuation model employed by B24 may underestimate $\boldsymbol{M}$ relative to our study and K21 (Figures A3.2b and A3.2c).

As illustrated in Figure A3.2d, our stress-drop estimates ($\Delta\sigma$) are systematically lower (median: 0.37 MPa) than those reported by K21, $\Delta\sigma$(K21) (median: 2.61 MPa). Because our moment magnitudes ($\boldsymbol{M}$) are consistently larger than $\boldsymbol{M}$(K21), this discrepancy likely reflects an overestimation of the corner frequency in K21 relative to our study. Based on the result of our tests (Figure 3.1a), such overestimation of f_c can occur when the attenuation (expressed as the inverse of the Q factor) is lower than the assumed value. This suggests that the average attenuation model used by K21 during the fitting process is lower than the average attenuation represented in our model. On the other hand, $\Delta\sigma$(B24) estimates (median of 0.076 MPa) are notably lower than our estimates and those of K21 (Figures A3.2e and A3.2f). Given the identical shear-wave velocity model, discrepancies in stress-drop values are more likely driven by differences in the assumed attenuation model. It is plausible that the averaged attenuation employed by B24 is stronger than that used in our study (similar to the synthetic test depicted in Figure 3.1b). Despite these variations, our $\Delta\sigma$ estimates exhibit a stronger correlation with those of B24 (0.83) than with K21 (0.62). This suggests that although absolute stress-drop values differ across studies due to modeling assumptions, the relative trends in our estimates are more consistent with B24 than with K21.

Text A3.2. Comparison of the Standard Deviation of δB_e for FAS and PGA from the Three Catalogs

Figure A3.3 compares the standard deviation of $\delta B_e(\tau)$ for PGA and FAS derived from the GMMs based on the three catalogs. In model RF(***M***), τ from our catalog consistently remains higher than τ(K21) across the entire frequency range, but converges with τ(B24) at frequencies above 6 Hz. τ(B24) is significantly lower than those from the other two catalogs at frequencies below 2 Hz. Since ground motions at low frequencies are primarily influenced by moment magnitude and attenuation (e.g., Boore & Atkinson, 2008; Campbell & Bozorgnia, 2008), this discrepancy may arise from the simplified attenuation model used by B24 to estimate source parameters. This model does not account for potential spatial and temporal variability, which may instead be absorbed into the moment magnitude and reflected in the between-event residuals during the regression process. In contrast to τ(B24), the standard deviations from our catalog and K21 exhibit similar trends, likely due to the incorporation of spatiotemporal variations in the Q factor during the fitting process. Differences in standard deviation values may be attributed to variations in the definition of the Q factor (frequency-dependent vs frequency-independent) and to the adopted shear-wave velocity models. Despite the dramatic decrease in τ achieved by model RF(***MXYZ***), a frequency dependency is still observed across the three catalogs, with this effect being more pronounced for B24. Finally, model RF(***MXYZT***) yields similar standard deviation values across the three catalogs without showing a frequency-dependent trend. The standard deviation of PGA follows a similar pattern to that observed across the full frequency range. In model RF(***M***), τ from our catalog (0.49) is consistent with that of B24 (0.5) and slightly larger than that of K21 (0.41). As expected, models RF(***MXYZ***) and RF(***MXYZT***) substantially reduce the standard deviation, yielding similar values across the three catalogs of approximately 0.15 and 0.08, respectively.

Text A3.3. Smoothing

We begin by dividing the dataset into four subsets corresponding to different periods: from the Amatrice to Visso mainshocks, from Visso to Norcia, from Norcia to Campotosto, and after the Campotosto mainshocks. For each subset, we compute the median values over 29, 10, 58, and 27 moving windows of consecutive earthquakes, respectively. The window lengths vary from 0.2% to 5% of the total number of events within each subset. This consistent range of window lengths ensures a comparable level of smoothing across subsets. Shorter window lengths (0.2%) reduce the degree of smoothing, allowing for finer resolution, particularly useful for interpreting changes immediately following mainshocks. Finally, we average the medians from all windows within each subset to produce a single smoothed curve that captures the temporal behavior of the data in that period.

Text A3.4. Comparison of Temporal Variability of $\delta B_e(PGA)$ and $\Delta\sigma_N$ for the Three Catalogs

As shown in Figure A3.7, for the K21 catalog, $\delta B_e(PGA)$ and $\Delta\sigma_N$ exhibit a similar relationship to our results, particularly during the early stages of the phases following the mainshocks, likely because both models employ spatial and temporal variable Q models. In contrast to our model, a notable and rapid drop in $\delta B_e(PGA)$ and $\Delta\sigma_N$ is not observed during the 1.5 days following the Campotosto mainshocks in Phase 6, when the LFS segment predominantly hosts the seismicity (Figure 3.3f). K21 used a 1D shear-wave velocity model for both VBFS and LFS segments during the fitting process; however, the 3D velocity model by Menichelli et al. (2023) used in our study indicates that the velocity in the LFS segments is significantly higher than that suggested by the 1D model. Therefore, the discrepancies between the two models in this phase may stem from differences in velocity models and the use of frequency-independent versus frequency-dependent Q models. Contrary to our model, B24 (Figure A3.7) does not reveal any noticeable difference between $\delta B_e(PGA)$ and $\Delta\sigma_N$ during the early period of Phase 1 following the Amatrice mainshock. This could be

attributed to the simplified attenuation model employed by B24, which may not capture the rapid drop in $Q_{0,e}$ immediately after the Amatrice event. For the remaining phases, the results from B24 and our model differ only slightly. A direct comparison of $\delta B_e(PGA)$ and $\Delta\sigma_N$ from the three catalogs is presented in Figure A3.7. A high degree of similarity in both the pattern and values of $\delta B_e(PGA)$ is observed across all phases for the three catalogs, except at the onset of Phase 1 and Phase 6, where our model yields noticeably higher values. As shown in Figures 3.3a and 3.3f, seismicity during these phases is primarily concentrated along the LFS segment. In this region, the attenuation characteristics (Figures A3.6a and A3.6f) and shear-wave velocity structure deviate significantly from the median observed across the entire sequence, which our model captures through incorporating a spatiotemporally variable Q and a spatial variable 3D velocity model. This leads to discrepancies in $\boldsymbol{M}$ and $\delta B_e(PGA)$ estimates over the different catalogs.

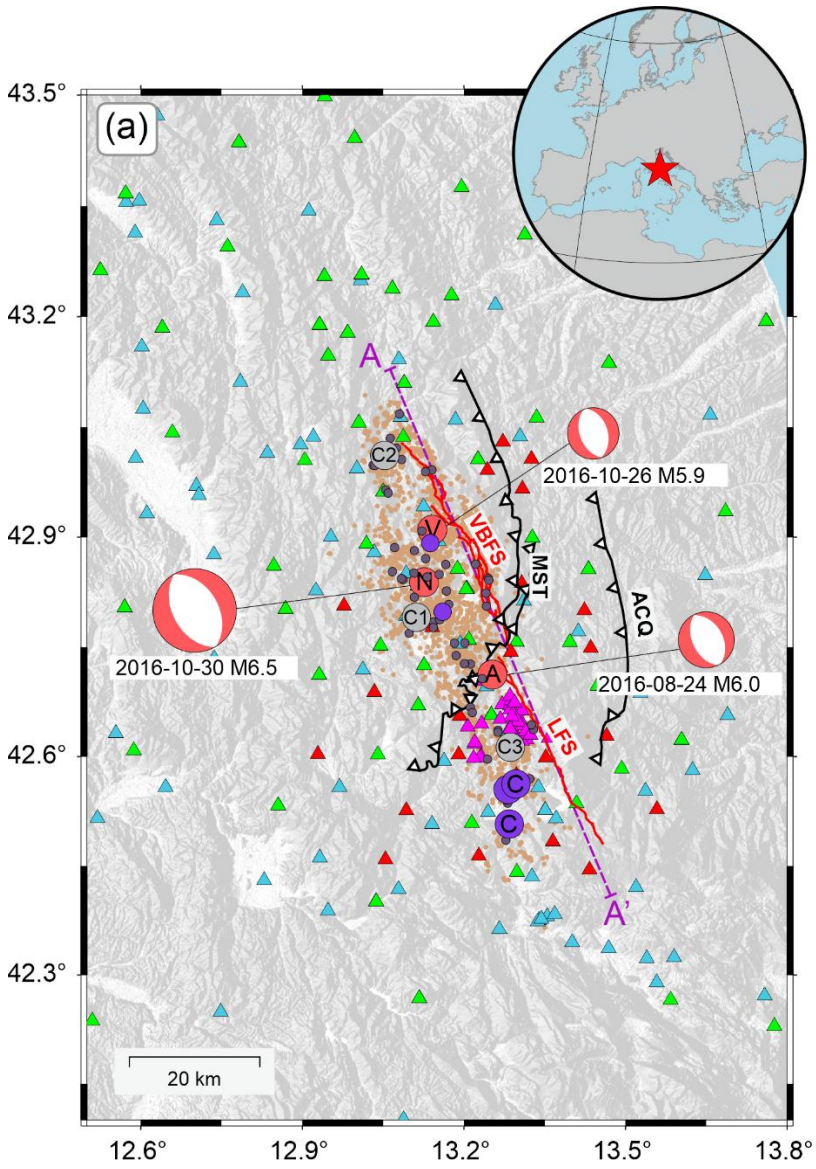

Figure A3.1. Map of the epicentral area of the 2016-2017 Central Italy seismic sequence. The red lines represent the two causative Normal faults of the Vettore-Bove (VBFS) and the Laga (LFS) regions. The black barbed lines indicate the thrust fronts of the Mount-Sibilini-Thrust (MST) and the Acquasanta Thrust (ACQ). The red circles labelled A, V, N, and C mark the epicenters of Amatrice, Visso, Norcia, and Campotosto mainshocks, respectively. The grey circles labelled C1, C2, and C3 depict the location of the clusters presented in Section 3.5 in the paper. The purple, dark grey, and brown circles denote the epicenters of events with $\boldsymbol{M}$5-6, $\boldsymbol{M}$4-5, and $\boldsymbol{M} < 4$, respectively. The triangles represent the locations of the recording stations, color-coded according to the network to which each station belongs.

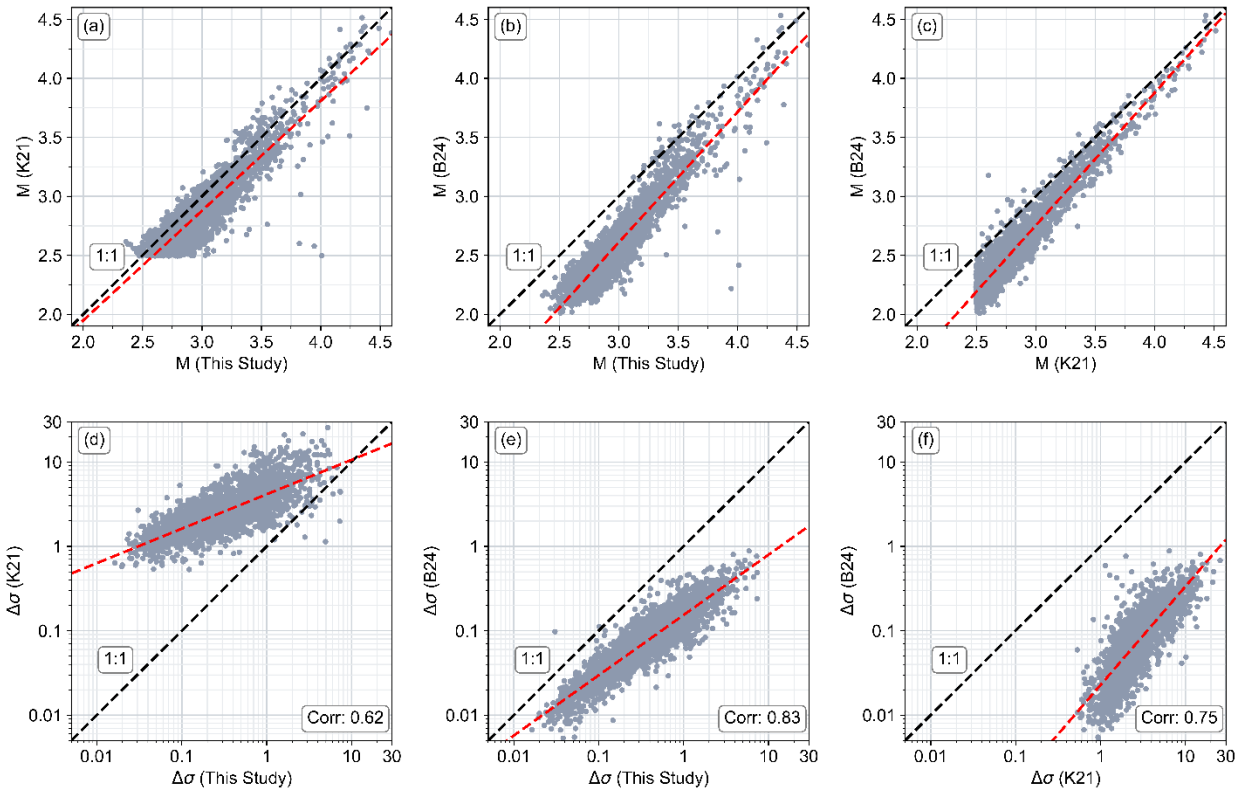

Figure A3.2. Comparison of moment magnitude and stress-drop across the three catalogs. **(a)** M from this study versus K21, **(b)** ***M*** from this study versus B24, **(c)** ***M*** from K21 versus B24, **(d)** $\Delta\sigma$ from this study versus K21, **(e)** $\Delta\sigma$ from this study versus B24, **(f)** $\Delta\sigma$ from K21 versus B24. The black dashed line depicts the 1:1 reference line, indicating perfect agreement, while the red dashed line represents the best-fitted line for each dataset, respectively.

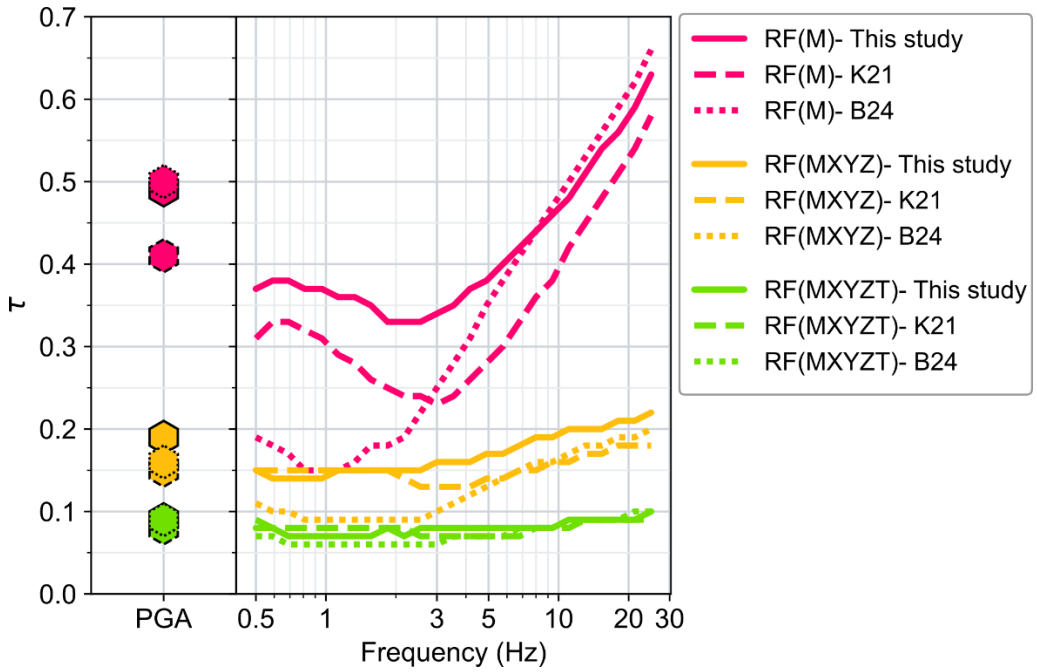

Figure A3.3. Comparison of the standard deviation of δBe for PGA and FAS computed using the defined Random Forest GMMs across the three catalogs. Solid, dashed, and dotted pink curves represent the τ values derived from RF(M) for this study, K21, and B24 catalogs, respectively. Solid, dashed, and dotted orange curves represent the τ values obtained from RF(***MXYZ***) for this study, K21, and B24 catalogs, respectively. Solid, dashed, and dotted green curves represent the τ values from RF(***MXYZT***) for this study, K21, and B24 catalogs, respectively.

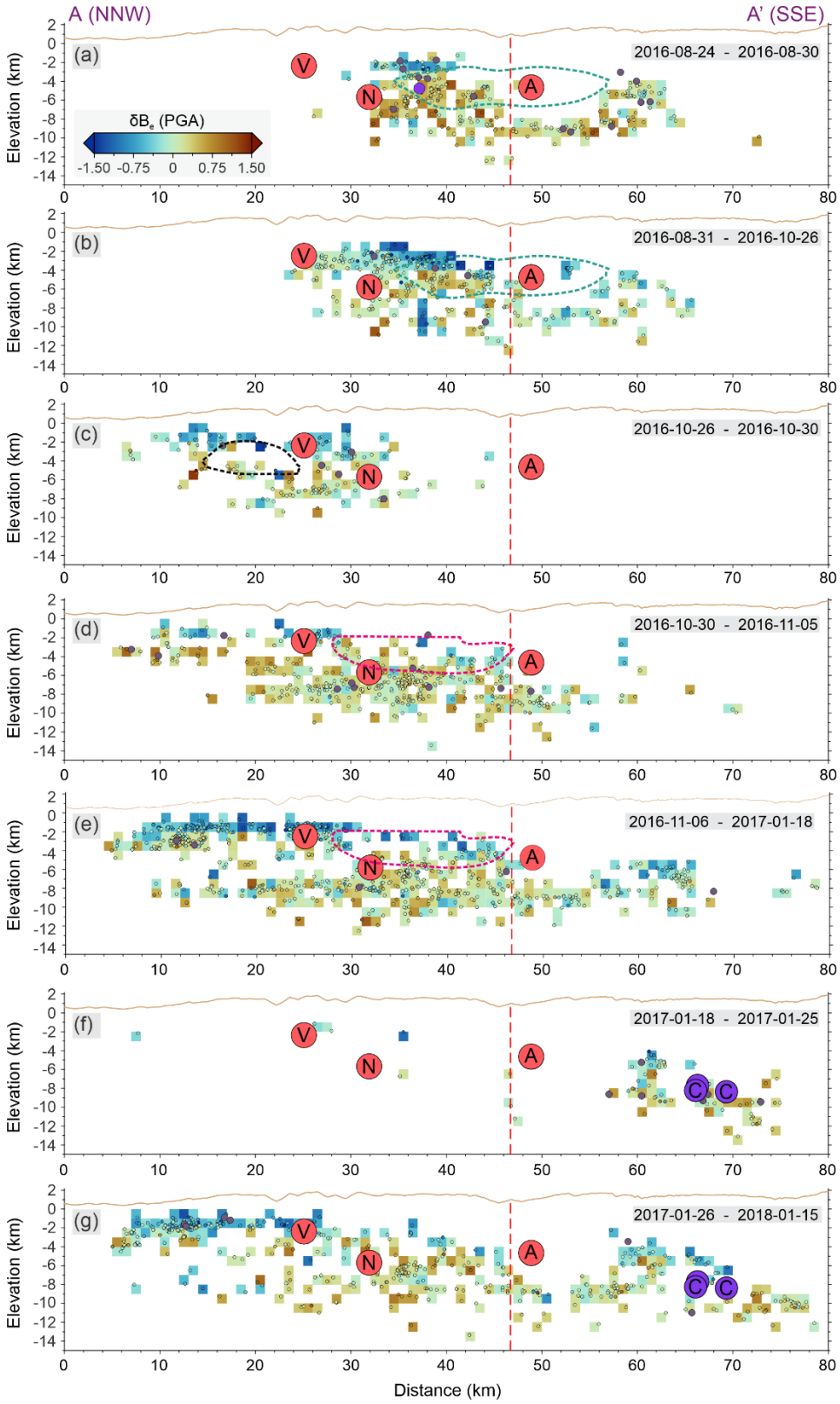

Figure A3.4. Same as Figure A3.3, but for the spatial distribution of $\delta B_e(PGA)$ based on our catalog.

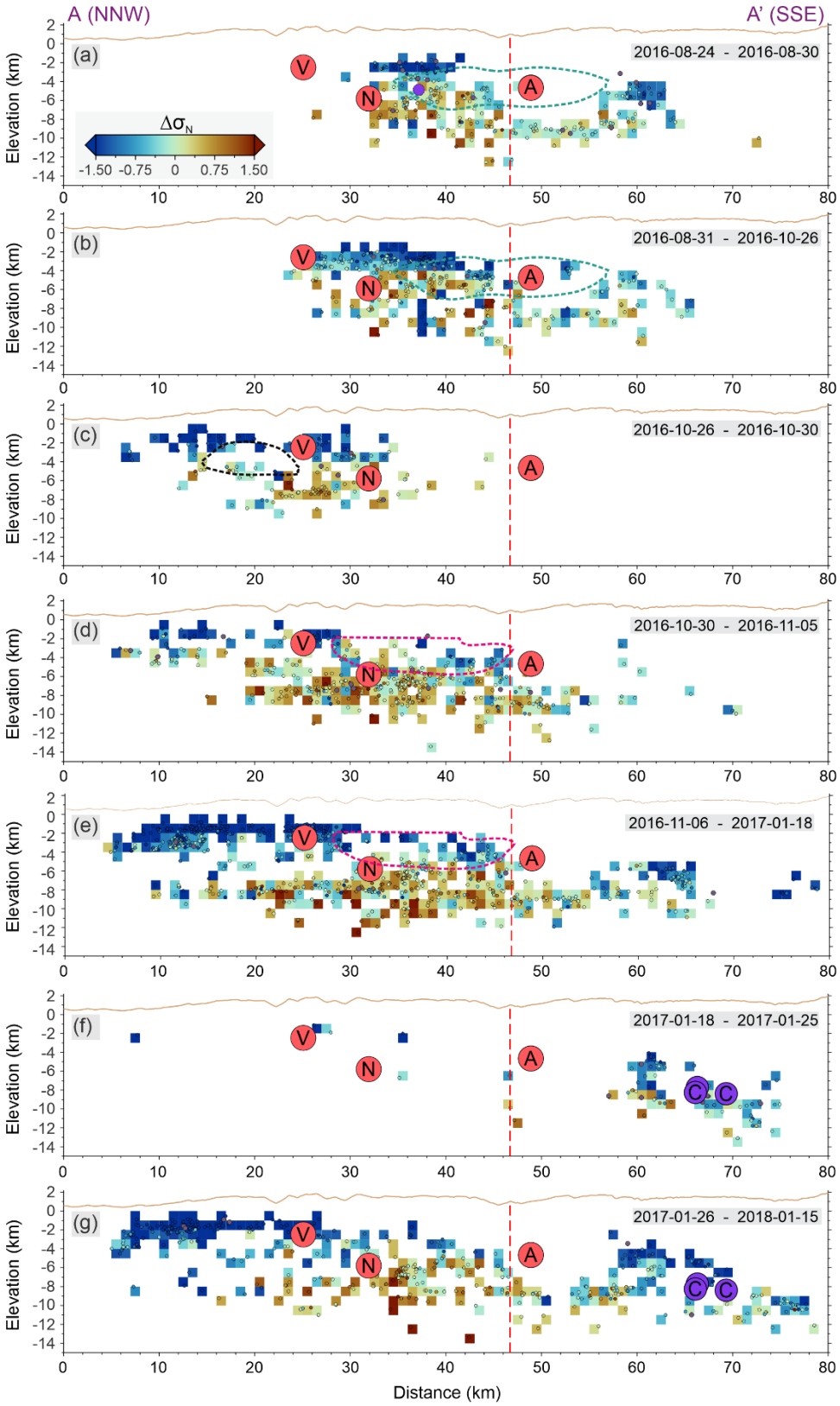

Figure A3.5. Same as Figure A3.3, but for the spatial distribution of $\Delta\sigma_N$ based on our catalog.

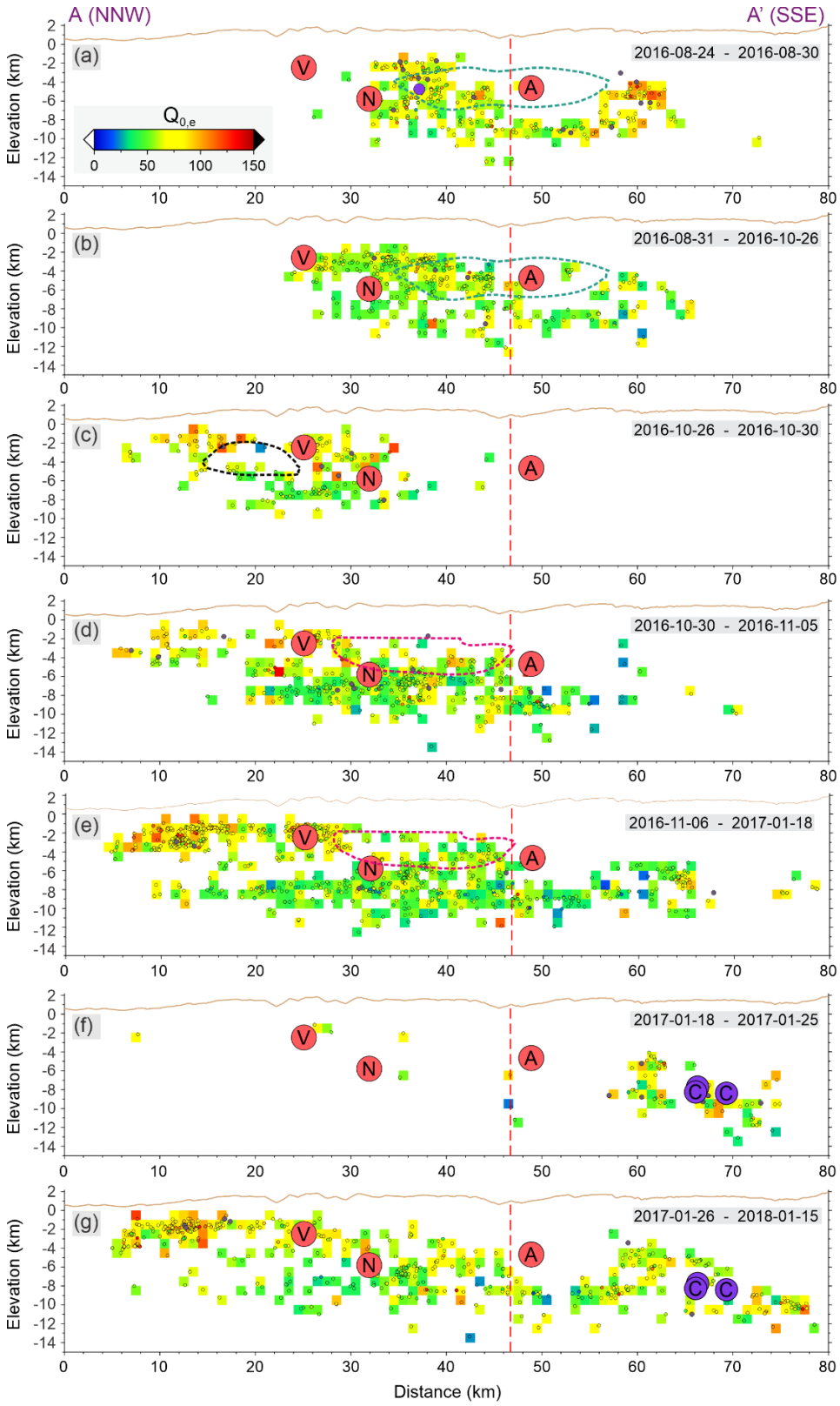

Figure A3.6. Same as Figure A3.3, but for the spatial distribution of $Q_{0,e}$ based on our catalog.

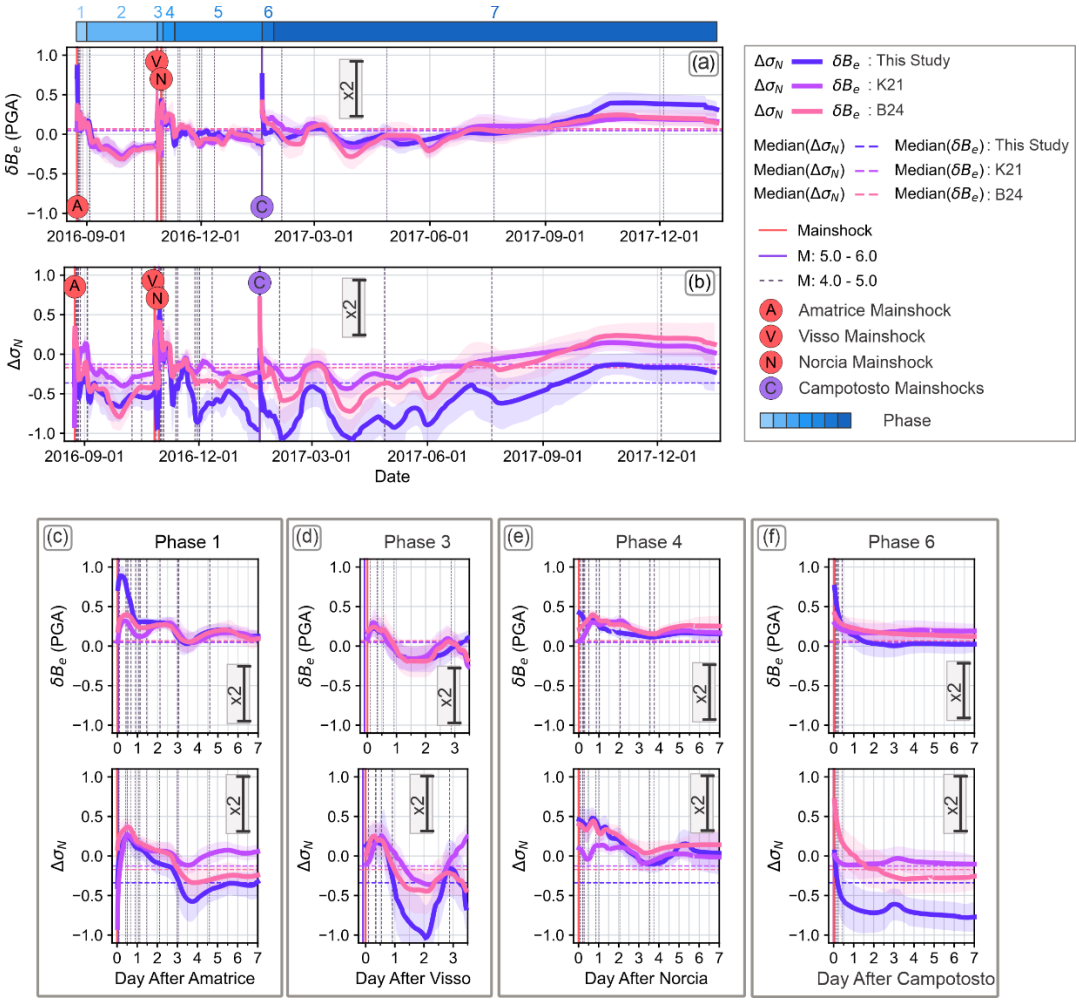

Figure A3.7. Temporal evolution of between-event residuals and normalized stress-drop derived from three earthquake catalogs. Comparison of the temporal evolution of **(a)** $\delta B_e(PGA)$ obtained from the three catalogs for the entire sequence, **(b)** $\Delta\sigma_N$ from the three catalogs for the entire sequence. Comparison of the temporal evolution of $\delta B_e(PGA)$ and $\Delta\sigma_N$ based on the three catalogs for **(c)** Phase 1: the first week following the Amatrice mainshock, **(d)** Phase 3: the four days after the Visso mainshock, **(e)** Phase 4: the first week following the Norcia mainshock, **(f)** Phase 6: the first week post the three Campotosto mainshocks. The blue color bar indicates the period corresponding to each phase. Horizontal dashed lines and shaded areas in matching colors illustrate the median values and ±1 standard deviation of $\delta B_e(PGA)$ and $\Delta\sigma_N$, respectively. Circles labelled A, V, N, and C denote the occurrence times of the Amatrice, Visso, Norcia, and Campotosto mainshocks, respectively. The vertical red, purple, and dashed grey lines demonstrate the occurrence times of the mainshocks, events with ***M***5.0-6.0, and events with ***M***4.0-5.0, respectively.

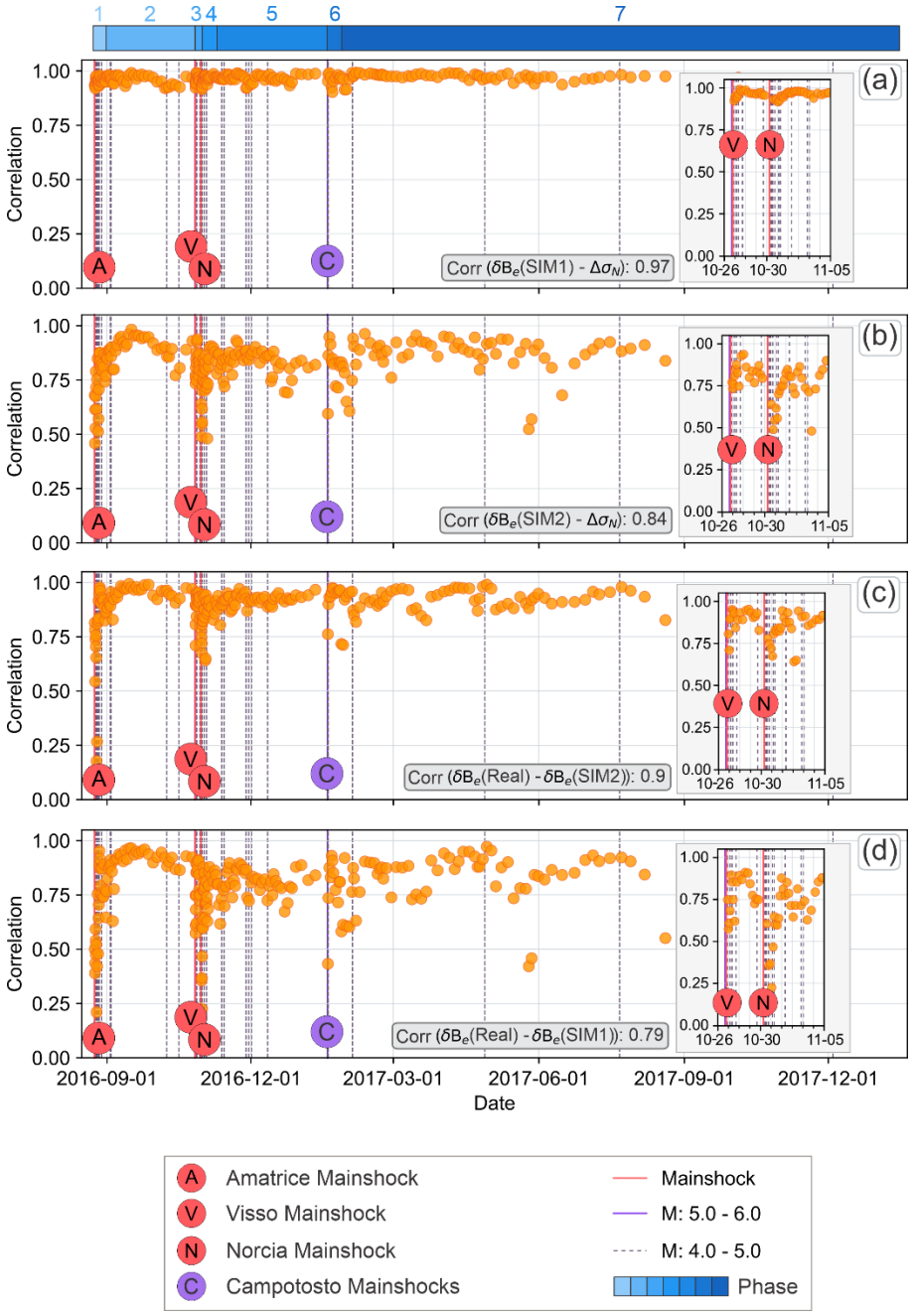

Figure A3.8. Temporal evolution of cross-correlations between between-event residuals and stress-drop derived from simulations and real data. Temporal evolution of **(a)** cross-correlation between $\delta B_e(PGA)$ from SIM1 and $\Delta\sigma_N$ from this study, **(b)** cross-correlation between $\delta B_e(PGA)$ from SIM2 and $\Delta\sigma_N$ from this study, **(c)** cross-correlation between $\delta B_e(PGA)$ from real data and $\delta B_e(PGA)$ from SIM2, **(d)** cross-correlation between $\delta B_e(PGA)$ from real data and $\delta B_e(PGA)$ from SIM1. The inset in each subplot provides a zoomed-in view for the period from 2016-10-26 to 2016-11-05 (Phases 3 and 4). The blue color bar indicates

the period corresponding to each phase. Circles labelled A, V, N, and C denote the occurrence times of the Amatrice, Visso, Norcia, and Campotosto mainshocks, respectively. The vertical red, purple, and dashed grey lines demonstrate the occurrence times of the mainshocks, events with ***M***5.0-6.0, and events with ***M***4.0-5.0, respectively.

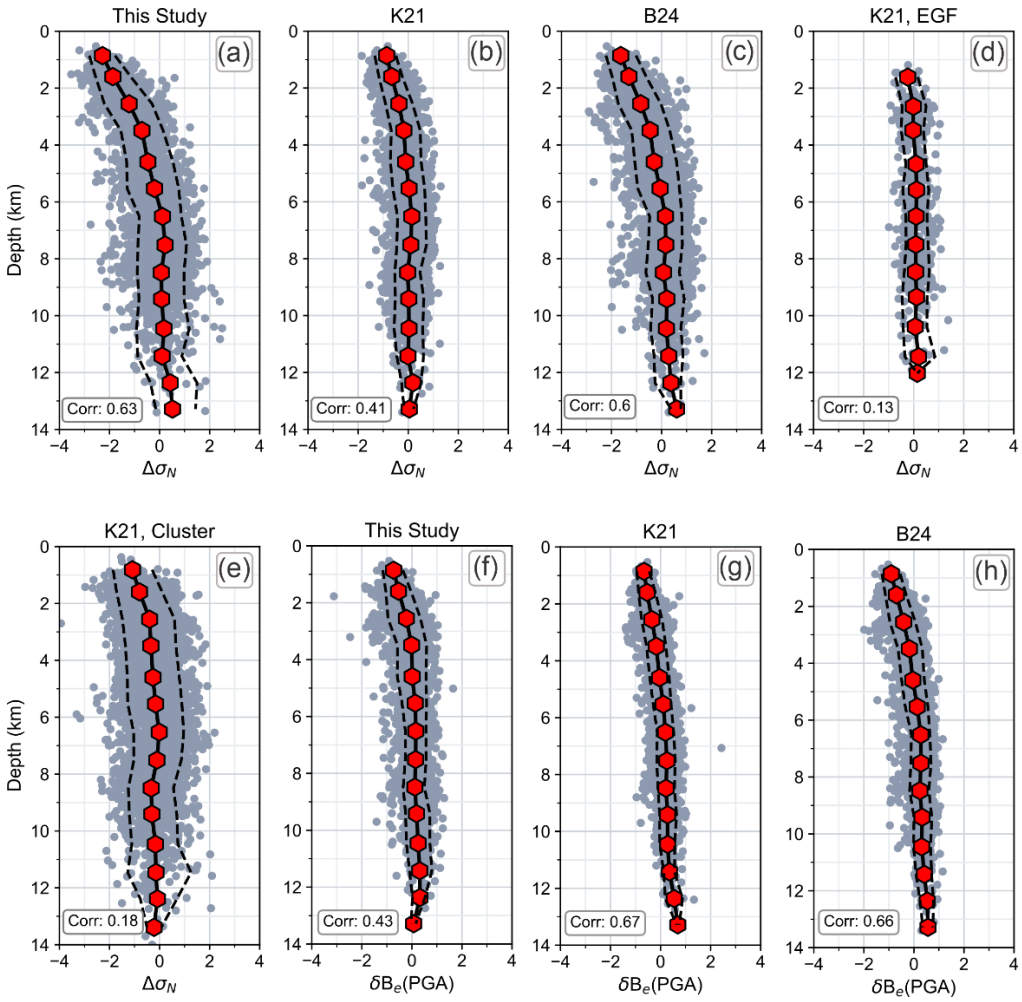

Figure A3.9. Depth dependency of normalized stress-drop and PGA between-event residuals. **(a)** $\Delta\sigma_N$ computed in this study, **(b)** $\Delta\sigma_N$ from K21 using the single-spectrum fitting method, **(c)** $\Delta\sigma_N$ from B24, **(d)** $\Delta\sigma_N$ from K21 using the Empirical Green's Function (EGF) method, **(e)** $\Delta\sigma_N$ from K21 using the cluster-event method, **(f)** $\delta B_e(PGA)$ computed using moment magnitude from our catalog, **(g)** $\delta B_e(PGA)$ computed using moment magnitude from the K21 catalog, **(h)** $\delta B_e(PGA)$ computed using moment magnitude from the B24 catalog. Red hexagons represent the median $\Delta\sigma_N$ or $\delta B_e(PGA)$ within 1 km depth. Dashed lines indicate the 10th and 90th percentiles.

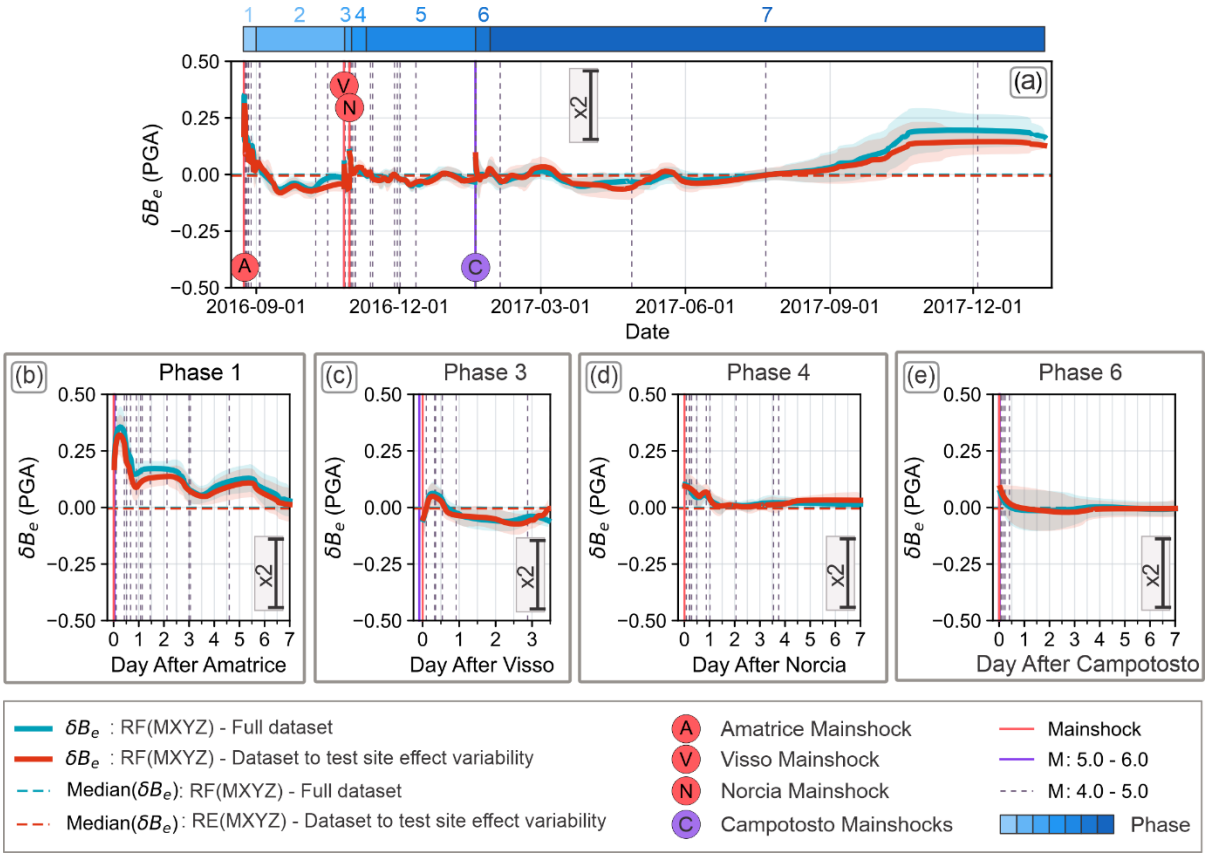

Figure A3.10. Comparison of the temporal evolution of $\delta B_e(PGA)$ obtained from model RF(***MXYZ***) for the full dataset and the dataset to test site effect variability for **(a)** the entire seismic sequence, **(b)** Phase 1: the first week following the Amatrice mainshock, **(c)** Phase 3: the four days after the Visso mainshock, **(d)** Phase 4: the first week following the Norcia mainshock, **(e)** Phase 6: the first week post the three Campotosto mainshocks. The blue color bar indicates the period corresponding to each phase. Horizontal dashed lines and shaded areas in matching colors illustrate the median values and ±1 standard deviation of $\delta B_e(PGA)$ obtained from the two models. Circles labelled A, V, N, and C denote the occurrence times of the Amatrice, Visso, Norcia, and Campotosto mainshocks, respectively. The vertical red, purple, and dashed grey lines demonstrate the occurrence times of the mainshocks, events with ***M***5.0-6.0, and events with ***M***4.0-5.0, respectively.

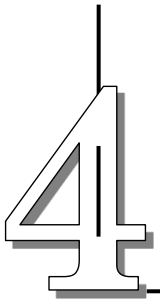

Kinematic Source Rupture Modeling of the 2016 Norcia Earthquake

This chapter discusses the developed Bayesian kinematic source inversion framework based on the Parallel Tempering Markov Chain Monte Carlo sampler. First, the methodology and the rupture parameterizations are described. The reliability of the approach is then evaluated through the recovery of a benchmark rupture model. Finally, the framework is applied to retrieve the rupture process of the Norcia mainshock (***M***6.5), the largest event of the 2016-2017 Central Italy seismic sequence. The resulting model is subsequently compared with a previously published source model.

4.1. Introduction

Earthquake ground-motions are generated by ruptures on faults. During an earthquake, rupture propagates along a fault, producing slip that varies both spatially and temporally with variation in rate and direction. This complex behavior reflects the heterogeneous nature of faulting and strongly influences the characteristics of the generated ground-motions. Understanding earthquake source physics is crucial for predicting future strong ground motions, which is a key factor in improving modern seismic hazard assessments and reducing earthquake risk. Since direct observations of the rupture process are unavailable, we rely on seismic

recordings at Earth's surface. These observations are used to infer rupture characteristics and extract information about the underlying source process. In this context, waveform inversions (e.g., Olson & Apsel, 1982; Hartzell & Heaton, 1983; Graves & Wald, 2001; Sekiguchi & Iwata, 2002; Zhou et al., 2004) play an important role in resolving the spatiotemporal evolution of the rupture process on faults.

There are different approaches to infer the rupture process during earthquakes using waveform inversion, which differ mainly in the selected parametrization of the source model. The first approach is linear (e.g., Olson & Apsel, 1982; Hartzell & Heaton, 1983), where the slip history on a fault is estimated by solving a linear relationship between observed waveforms and a discretized set of source parameters, typically slip rates on predefined subfaults. While this approach is computationally efficient and often provides stable solutions, it suffers from several limitations. In particular, the problem is inherently ill-posed and underdetermined (Gallovič & Ampuero, 2015), requiring strong regularization or smoothing constraints that can bias the resulting slip distribution and obscure small-scale features. Linear inversions generally assume that Green's functions are perfectly known, neglecting modelling uncertainty arising from imperfect velocity models. As a result, discrepancies between observations and synthetics are attributed to the source model, leading to biased slip distributions. This is especially the case when wave propagation is complex and the velocity structure poorly constrained (e.g., sedimentary basins, poorly instrumented areas, etc).

Another approach is nonlinear fault slip inversion, in which the rupture process is described through a spatiotemporal parameterization of the slip rate function. This parameterization reduces the number of unknowns and naturally stabilizes the problem by enforcing smooth and physically realistic rupture behavior (e.g., Archuleta, 1984; Bouchon et al., 2002; Liu & Archuleta, 2004; Monelli et al., 2009; Minson et al., 2013). However, the resulting inverse problem is strongly nonlinear and computationally demanding, and is typically addressed using Monte Carlo methods. Within this framework, a Bayesian formulation is particularly

well-suited, as it allows prior information to be incorporated explicitly and provides a rigorous treatment of uncertainty in both the data and the forward model (e.g., Sambridge & Mosegaard, 2002; Tarantola & Valette, 1981). In particular, modeling errors, such as uncertainty in Green's functions, can be explicitly incorporated through the likelihood function, rather than being implicitly absorbed into the source model. Rather than yielding a single optimal solution, the Bayesian approach explores the posterior distribution of acceptable models, thereby capturing non-uniqueness, parameter trade-offs, and the impact of modeling uncertainty on the inferred rupture process (e.g., Minson et al., 2013, 2014).

In nonlinear source inversion, the posterior distribution of the model parameters is typically high-dimensional, strongly correlated, and often multimodal, so that standard single-chain Markov Chain Monte Carlo (MCMC) methods may fail to adequately explore the model space, for instance, by leading to solutions associated with local minima (Geyer, 1991). This can lead to poor mixing and biased estimates of the posterior distribution. Parallel tempering Markov Chain Monte Carlo (PTMCMC) can help solve this limitation by evolving multiple chains at different temperatures and allowing exchanges between them (Earl & Deem, 2005; Sambridge, 2014), enabling high-temperature chains to explore the parameter space more broadly and escape local minima, while the low-temperature chains sample the target posterior. This approach has been shown to significantly improve convergence and exploration efficiency in complex geophysical inverse problems (e.g., Sambridge, 2014; Hallo & Gallovič, 2020).

In this Chapter, we focus on the 30 October 2016 Norcia earthquake, the largest mainshock of the 2016-2017 Central Italy seismic sequence (Figure 4.1), to retrieve its source rupture model. The central Apennines in Italy have experienced several major seismic sequences in recent decades, reflecting the activation of multiple segments within a complex normal-fault system, including the 1980 Irpinia earthquake (Bernard & Zollo, 1989; Pantosti & Valensise, 1990), the 1997 Umbria-Marche sequence (Chiaraluce et al., 2003), and the 2009 L'Aquila earthquake

(Valoroso et al., 2013). Earthquake ruptures in this region are characterized by strongly heterogeneous slip distributions on the causative faults, resulting from the combined effects of fault geometry and spatial variations in frictional properties (Scognamiglio et al., 2018). To retrieve a reliable source rupture model, we compute numerical Green's Functions using a 1D velocity model tailored to the target region. Furthermore, rather than relying on classical optimization techniques to perform the inversion, we adopt a Bayesian inference framework and sample the posterior distribution using a PTMCMC algorithm.

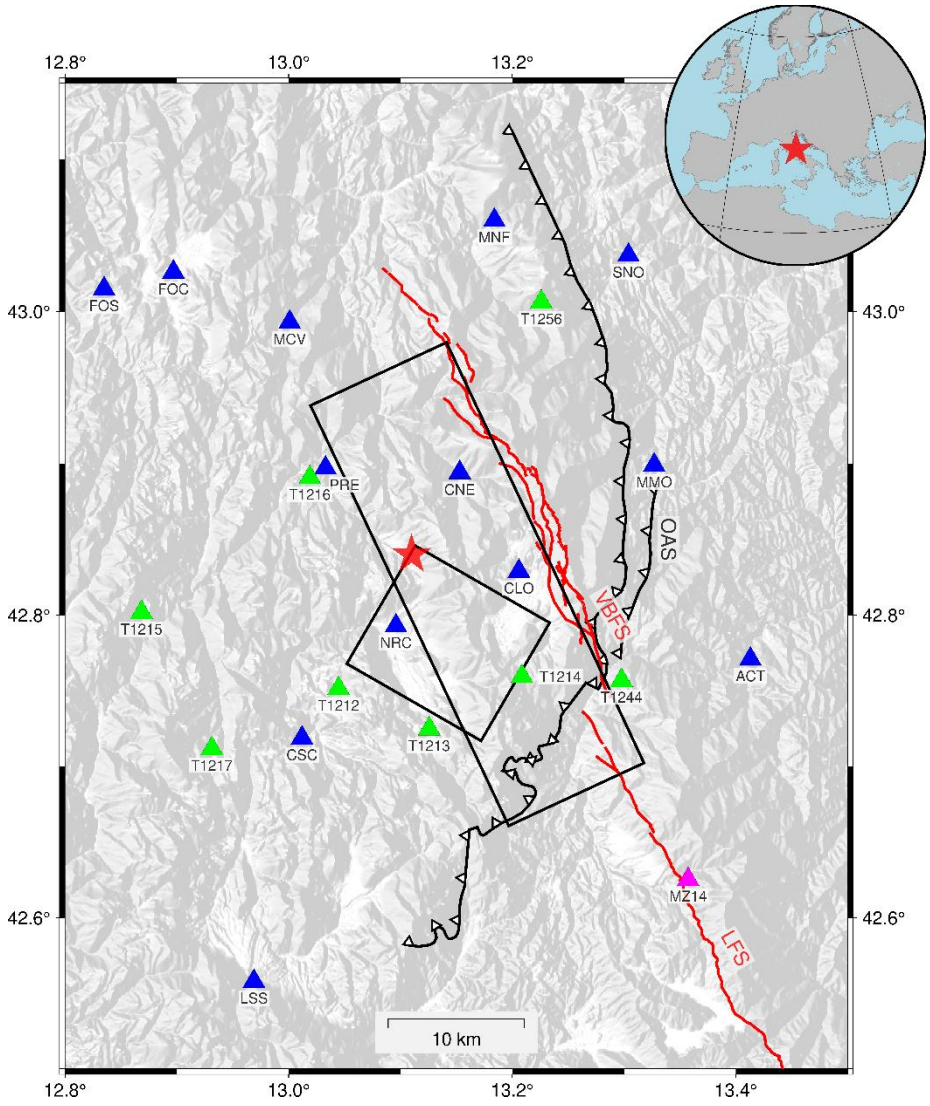

Figure 4.1. Map of the epicentral area showing the distribution strong-motion stations and the geometry of fault planes used in the inversion. The two black rectangles outline the fault planes used in the inversion models. The red star marks the epicenter of the Norcia mainshock. Green, blue, and pink triangles represent stations from the Italian Strong Motion Network (RAN), the Italian National Seismic Network (INSN), and the CentroMz network, respectively. Red lines denote the two normal fault systems of the Vettore-Bove Fault System (VBFS) and the Laga Fault System (LFS), while black barbed lines indicate the thrust fronts of the Mount Sibillini Thrust.

4.2. Strong Motion Waveforms Processing and Fault Geometry

To constrain the rupture model of the 2016 Norcia mainshock, we analyze waveforms recorded at 22 three-component strong motion stations located within 40 km of the epicenter (Figure 4.1). These stations belong to the Italian Strong Motion Network (RAN), the Italian National Seismic Network (INSN), and the 2016 Central Italy Seismic Sequency Network (CentroMZ). The recorded acceleration waveforms are processed by removing instrumental corrections, applying a 4th-order Butterworth bandpass filter in the range of 0.02-0.5 Hz, and using zero-phase filtering. Furthermore, a Cosine taper with a length of 5 percent of the signal length is applied to both sides of the signals. Finally, the filtered accelerograms are integrated to derive velocity waveforms and resampled to 10 samples per second.

Scognamiglio et al. (2018) proposed a two-segment fault system: the primary segment corresponds to the Vittore-Bove Fault System, striking N155°, dipping 47° toward the southwest, with a length of 34 km and a width of 16 km; the secondary segment strikes N210°, dips 36° toward the northwest, and has a length of 10 km and a width of 14 km. The shallow top edges of the primary and secondary segments are buried 0 km and 1.8 km below the modeled free surface, respectively. As a primary analysis, we only consider the main fault plane (N155°) in our inversion model.

4.3. Kinematic Source Inversion Methodology

4.3.1. Bayesian Inversion

The core of source inversion lies in solving the forward problem, which defines the relationship between model parameters and the observed data. To explicitly account for uncertainties, we formulate the problem in a Bayesian inference framework (e.g., Minson et al., 2013; Duputel et al., 2014; Razafindrakoto & Mai, 2014; Hallo & Gallovič, 2016). Unlike classic optimization methods, which aim to produce a single "best-fit" model, Bayesian inference yields a set of solutions that fit the data within an acceptable level of fit, conditioned on the data uncertainty. This

set of solutions is expressed through the posterior probability distribution of the model parameters, which characterizes the range of plausible solutions and their associated likelihoods:

$$p(\boldsymbol{m}|\boldsymbol{d}) = \frac{p(\boldsymbol{d}|\boldsymbol{m})p(\boldsymbol{m})}{p(\boldsymbol{d})}, \tag{4.1}$$

where $\boldsymbol{d}$ and $\boldsymbol{m}$ represent the data and model parameters, respectively. $p(\boldsymbol{d}|\boldsymbol{m})$ is the likelihood function, which defines a statistical model for the difference between the observed data and modeled data generated by the forward model with parameters $\boldsymbol{m}$. $p(\boldsymbol{m})$ is the prior distribution, representing our prior knowledge or assumptions about the possible model parameters. $p(\boldsymbol{d})$ is the marginal likelihood, which is not necessary and is often impossible to compute.

The form of the likelihood function depends on the characteristics of the measurement noise and on the modeling error. The measurement noise in the observed data is assumed to follow a Gaussian distribution. Accordingly, the likelihood function is defined as:

$$p(\boldsymbol{d}|\boldsymbol{m}) = c.exp\left(-\frac{\|\boldsymbol{d} - g(\boldsymbol{m})\|_2^2}{2\sigma^2}\right), \tag{4.2}$$

where c is a constant, g denotes the forward model used to generate synthetic seismograms from the rupture parameters $\boldsymbol{m}$, σ^2 includes the modeling error, and $||\ ||_2^2$ represents the squared L_2 norm of the residual.

We use the Markov Chain Monte Carlo (MCMC) algorithm to explore the model space and draw samples from the posterior Probability Density Function (PDF) through a random walk process (e.g., Robert & Casella, 2004; J. S. Liu, 2004). During the walk, a new sample $\boldsymbol{m}_{i+1}$ at iteration $i+1$ depends only on the previous sample $\boldsymbol{m}_i$. Following the Metropolis-Hastings algorithm (Metropolis et al., 1953), a sample $\boldsymbol{m}_{i+1}$ is accepted only if the likelihood ratio yields a probability larger than a random number drawn from the uniform interval [0,1]:

$$P = \frac{p(\boldsymbol{d}|\boldsymbol{m_{i+1}})}{p(\boldsymbol{d}|\boldsymbol{m_i})} = min\left(1, c.exp\left(\frac{\|\boldsymbol{d} - g(\boldsymbol{m_i})\|_2^2 - \|\boldsymbol{d} - g(\boldsymbol{m_{i+1}})\|_2^2}{2\sigma^2}\right)\right), \quad (4.3)$$

An important point regarding the error term is that the likelihood function is highly sensitive to the choice of σ^2. If the selected σ^2 is underestimated, the posterior distribution becomes overly narrow, leading to overfitting of the data and underestimation of the uncertainties on the inverted parameters. Conversely, if σ^2 is overestimated, the posterior distribution becomes excessively broad, resulting in underfitting of the data. In finite-fault earthquake source modeling, such errors may be associated with poorly constrained source geometry (e.g., Ragon et al., 2018, 2019), inaccuracies in the elastic velocity structure used to compute Green's functions (e.g., Minson et al., 2013; Duputel et al., 2014; Hallo & Gallovič, 2020), and simplifications in the model parameterization. In this study, we use the definition of Variance Reduction (VR) to compute σ^2. We simply assume that the square of the L_2 norm of the residual obtained from the variance reduction is equal to σ^2:

$$\sigma^2 = \|\boldsymbol{d} - g(\boldsymbol{m})\|_2^2 = (1 - VR_e).\|\boldsymbol{d}\|_2^2, \quad (4.4)$$

here, $VR_e \in (0, 1)$ is the expected variance reduction that we seek to recover from the best inverted model fit to the observed data, where 1 indicates the best fit.

Although the method proposed by Hallo & Gallovič (2016) provides a robust framework for estimating σ, Razafindrakoto & Mai (2014) proposed an alternative empirical likelihood to simplify the problem. To avoid the explicit estimation of σ, they replaced Eq. 4.2 by:

$$p(\boldsymbol{d}|\boldsymbol{m}) = c.exp(-\phi(\boldsymbol{m})), \quad (4.5)$$

where $\phi(\boldsymbol{m})$ is defined as:

$$\phi(\boldsymbol{m}) = \frac{S(\boldsymbol{m}) - S(\boldsymbol{m_{best}})}{S(\boldsymbol{m_{best}})} \times 100, \quad (4.6)$$

here, $S(\boldsymbol{m})$ denotes the value of the cost function measuring the misfit between synthetic and observed data, and $S(\boldsymbol{m_{best}})$ represents the expected misfit of the best-

fitting model. In this study, we consider two cost functions: variance reduction and the metric proposed by Liu & Archuleta (2004) (LA). For the variance reduction approach, $S(\boldsymbol{m_{best}}) = 1 - VR_e$, in which $VR_e \in (0, 1)$ is the expected variance reduction. For the LA metric, $S(\boldsymbol{m_{best}}) = LA_e$, where $LA_e \in (0, 1)$. Unlike VR, in the LA formulation, 0 represents the best fit between synthetic and observed data.

4.3.2. Parallel Tempering

In the earthquake source inversion problem, the likelihood function, which quantifies the misfit between data and model predictions, is typically highly complex and often multimodal, exhibiting multiple local minima in the posterior distribution. This arises from the nonlinear nature of the inverse problem, where the relationship between the data and model is sufficiently complex that the classical optimization methods may become trapped in secondary local minima. Similarly, probabilistic sampling methods can become inefficient in exploring the parameter space and may converge slowly toward the high posterior probability density (Sambridge, 2014). To address these challenges, we employ an improved Parallel Tempering MCMC (PTMCMC) algorithm (Falcioni & Deem, 1999). PTMCMC runs multiple Markov Chains in parallel, with each chain sampling from a tempered version of the posterior distribution:

$$p_i(\boldsymbol{m}|\boldsymbol{d}) = p(\boldsymbol{d}|\boldsymbol{m})^{1/T_i} p(\boldsymbol{m}), \tag{4.7}$$

where T_i, the so-called "Temperature", is a scaling factor that controls the smoothness of the posterior PDF in the *i-th* chain. The temperatures are distributed within the interval [1, T_{max}], commonly referred to as the temperature ladder. The chain with T_1 = 1 (the cold chain) samples the true posterior PDF, and its samples are considered solutions of the source inversion problem. However, it may become trapped in local minima because the posterior PDF can be very rough. In contrast, at higher-temperature chains (T_i > 1, hot chains), the posterior PDF becomes flatter; therefore, the sampler can more easily escape the local minima, explore other regions of

parameter space faster due to a higher acceptance rate, and ultimately locate the true global minima.

Periodically, Parallel Tempering attempts to swap the information between chains (for example, between the cold and hot chains), because the hot chains may discover promising regions in the posterior PDF that the cold chain could not reach. When a swap occurs, the cold chain can then explore these new regions more carefully. This swap is performed through a Metropolis-Hastings swap step, and whether the swap is accepted depends on the swap acceptance probability (Sambridge, 2014):

$$\alpha(i,j) = min\left(1, \left[\frac{p(\boldsymbol{d}|\boldsymbol{m_j})}{p(\boldsymbol{d}|\boldsymbol{m_i})}\right]^{\frac{1}{T_i}} \left[\frac{p(\boldsymbol{d}|\boldsymbol{m_i})}{p(\boldsymbol{d}|\boldsymbol{m_j})}\right]^{\frac{1}{T_j}}\right), \tag{4.8}$$

If $\alpha(i,j)$ is greater than a random number drawn from the interval [0,1], the swap is accepted.

The selection of the T_{max} and the temperature ladder is a critical component of the PTMCMC algorithm, as it governs the balance between local exploration and global mixing across chains. In practice, temperatures are commonly distributed geometrically, such that adjacent chains maintain sufficient overlap. The number of chains is typically tuned to achieve an acceptable rate for swap proposals between neighboring chains in the range of approximately 0.2-0.4, which promotes efficient inter-chain communication (Earl & Deem, 2005). The choice of T_{max} should ensure that the highest-temperature chain sufficiently flattens the posterior distribution, enabling it to cross the barriers and explore distinct modes, while avoiding excessively large values that may lead to inefficient sampling of regions dominated by the prior (Sambridge, 2014). Choosing a high unnecessary T_{max} requires a denser temperature ladder to maintain sufficient overlap between adjacent chains, thereby increasing the number of chains and the overall computation cost. A practical diagnostic for assessing whether T_{max} is adequate is to examine the standard deviation of the untampered log-likelihood across temperatures, $T_i . \log\left(p_i(d|m)\right)$. The standard deviation should increase progressively with temperature, indicating that

higher-temperature chains explore a broader range of the likelihood. If the variability at the highest temperature remains comparable to that of lower temperatures, this suggests that T_{max} is insufficient. Importantly, the optimal ladder configuration depends on the dimensionality and complexity of the target distribution, with higher-dimensional or strongly correlated problems generally requiring a finer temperature discretization. Table A4.1 in Appendix 4 provides a brief guideline for tuning the temperature ladder.

4.3.3. Random Walk to Draw Samples from PDF

We employ a component-wise random walk proposal, where at each iteration, a single parameter $\theta_i \in m$ is selected and perturbed. The proposed value is generated using a Gaussian random walk of the form $\theta'_i = \theta_i + \epsilon$, with $\epsilon \sim \mathcal{N}(0, \psi_i^2)$. The proposal standard deviation is defined as $\psi_i = s_i . \beta^{-1/2}$, where $\boldsymbol{s_i}$ is the parameter step size and β is the inverse temperature of the chain, allowing larger exploratory steps at higher temperatures. Following Hallo & Gallovič (2020) and to enforce bounded uniform priors, we apply a first-order reflective boundary condition, whereby any proposed value falling outside the prescribed parameter bounds is mirrored back into the admissible interval.

The use of a component-wise update offers several advantages for high-dimensional and heterogeneous inverse problems. In particular, block Metropolis updates are known to suffer from a rapidly decreasing acceptance rate as dimensionality increases, which can significantly reduce sampling efficiency (Roberts et al., 1997; Roberts & Rosenthal, 2001). In contrast, component-wise proposals restrict the perturbation to a one-dimensional subspace, thereby avoiding this curse of dimensionality and leading to more stable acceptance behavior. For Gaussian random-walk proposals, the efficiency of the algorithm depends on the acceptance rate. In high-dimensional settings with full-block updates, the optimal acceptance rate approaches approximately 0.23 (Roberts et al., 1997), whereas for one-dimensional or component-wise updates, the optimal rate is higher, around 0.4. In

our implementation, the acceptance rate is primarily controlled by the proposal step size $\boldsymbol{s_i}$; therefore, we provide practical guidelines (Table A4.2 in Appendix 4) to assist in selecting step sizes that yield a reasonable acceptance rate.

Based on the above explanations, we develop a kinematic earthquake source inversion Python package, KiNvPtPy, built on top of the PTMCMCSampler package (Ellis & Van Haasteren, 2017), which uses MPI to handle communication among parallel MCMC chains.

4.3.4. Rupture Model Parametrization

Here, we describe the model parameters that characterize the spatiotemporal evolution of rupture propagation on fault planes, including hypocentral locations, slip distribution, rupture velocity (V_{rup}), rise-time, and slip rate function:

1. We first define the dimensions of the sub-faults based on the maximum target frequency (f_{max}) for which the data are inverted, where the sub-fault dimension must be smaller than $V_{rup}/2f_{max}$. Assuming an average V_{rup} of 2.5 km/s, we select sub-fault dimensions of 2×2 km² for the frequency band of 0.02-0.5 Hz.
2. We adopt a self-adapting grid approach (e.g., Causse et al., 2017; Hallo & Gallovič, 2020; Žilić et al., 2025), in which the slip values are not inverted on regular subfaults. Instead, the model inverts slip values at a limited number of control points, whose spatial locations are simultaneously treated as unknowns and inverted along with the slip. The number of control points provides direct control over the model complexity and allows us to adjust the level of parameterization required to fit the data. Once the locations of the control points and their associated slip values are inverted, the overall slip across the fault plane is interpolated at the center of each sub-fault using a biharmonic spline interpolation. Because biharmonic splines require boundary constraints, zero slip values must be imposed along the fault edges. To allow for potential shallow slip near the upper fault boundary, we append a 3 km virtual plane in the dip direction and along strike above the fault plane and

enforce zero slip along the top of the virtual plane (Figure 4.2a). In the case of multiple fault planes, such as the model proposed by Scognamiglio et al. (2018) for the Norcia earthquake, the treatment differs between segments. For the main fault segment, zero slip is enforced along both edges in the dip direction without introducing virtual planes, permitting the real mesh boundaries to remain fixed. For the secondary fault plane, however, a 3 km virtual plane is appended along the northeastern (left) edge to allow for non-zero slip, as this boundary is interpreted as the likely rupture-entry point connecting the two segments. Along the southwestern (right) edge, slip is constrained to zero.

3. We define two models for inverting rupture velocity. In the first model, rupture is assumed to propagate from the rupture initiation points at a constant rupture velocity. In the case of multiple fault planes, each fault plane is sampled independently, allowing different values of V_{rup} on each segment. The second model accounts for heterogeneous rupture propagation. Similar to the first approach, a mean V_{rup} is sampled for each fault plane. In addition, perturbations to rupture velocity are introduced. These perturbations are parameterized using control points, similar to the slip parameterization, with the exception that the perturbations are constrained not to take zero values in the fault plane edges by introducing virtual planes along all boundaries (Figure 4.2b). The perturbed rupture velocity is interpolated onto a dense grid using a biharmonic spline. The local rupture velocity is then obtained by adding the perturbation to the mean rupture velocity. Rupture times, which describe the rupture-front propagation from the hypocenter, are calculated using the eikonal finite-difference solver of Podvin & Lecomte (1991) on the dense grid network. Finally, the rupture velocity and the rupture time values for each defined subfault are obtained through bilinear interpolation.
4. The temporal evolution of the slip-rate function (SRF) is represented using a regularized Yoffe function (Tinti et al., 2005). The regularized Yoffe function is a non-negative function of unit area and is consistent with rupture dynamics (Bizzarri, 2012). The rise-time (T_{rise}) is a key parameter that controls the SRF

shape and is therefore included in the inversion. As with the rupture velocity parameterization, two models are considered for inverting the rise-time. The first model assumes a homogeneous rise-time ranging, sampled independently for each fault segment in the case of multiple fault planes. The second model accounts for heterogeneous rise-time distribution by introducing control points, similar to the rupture velocity parameterization. Rise-time values are constrained not to reach zero at the edges of the fault plane by introducing virtual planes along all boundaries (Figure 4.2c). Finally, the rise-time for each subfault is obtained via biharmonic spline interpolation.

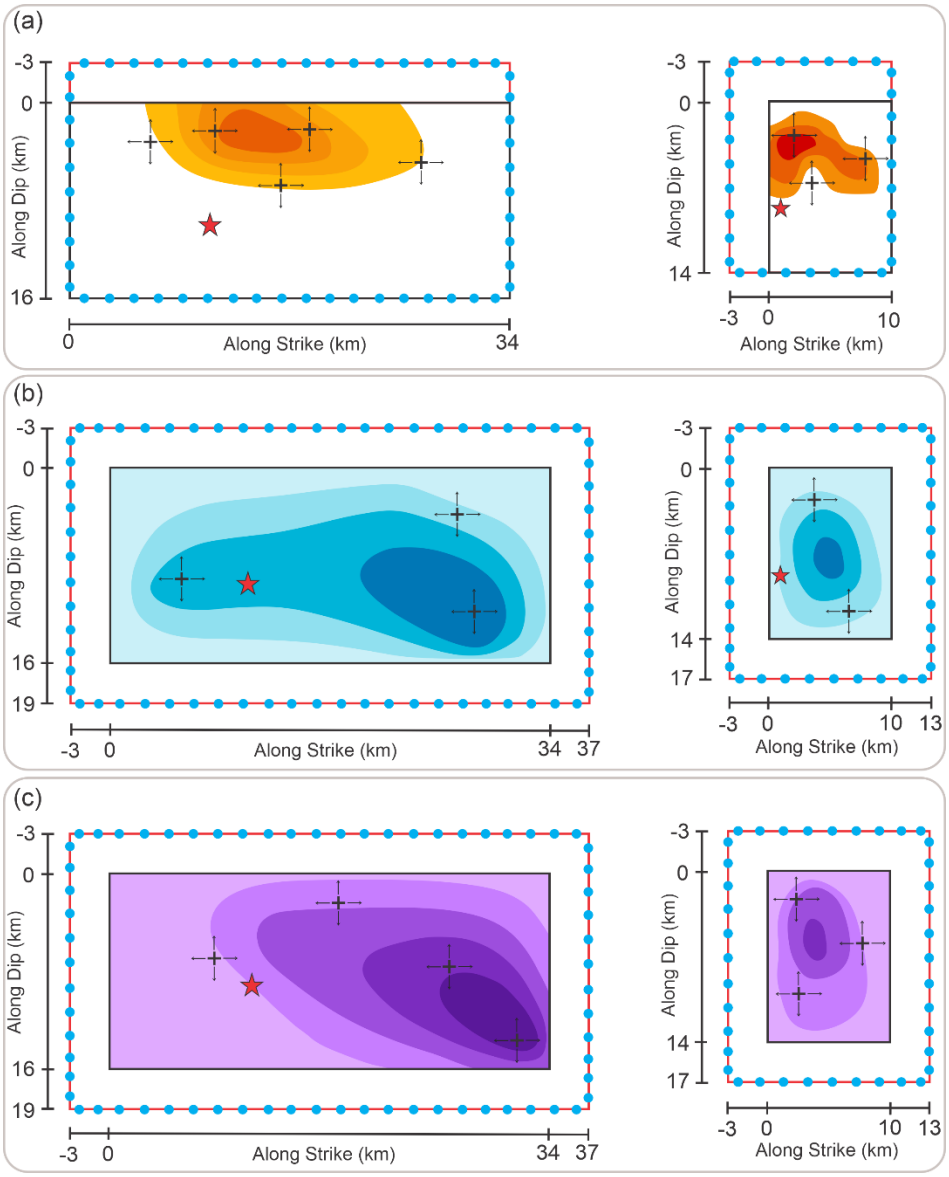

Figure 4.2. Schematic illustration of parameterizing space-time rupture evolution using control points. The rupture is parameterized in terms of **(a)** slip, **(b)** rupture velocity, and **(c)** rise time. The black rectangles represent the two fault planes used in the inversion models, while the red rectangles indicate the virtual planes added along the boundaries. The star marks the hypocenter location on each fault plane. The plus symbols denote the positions of the control points at each iteration. Blue dots along the edges represent auxiliary zero-value constraints, enforcing slip, rupture velocity, and rise time to approach zero at the boundaries.

4.4. Results

4.4.1. Inversion Synthetic Test

To evaluate the reliability of the developed inversion method, we apply it to the community inversion benchmark *Inv1* from the SIV project (Mai et al., 2016). The benchmark source model is based on a spontaneous dynamic rupture simulation for an 80° dipping strike-slip fault corresponding to an event with $\boldsymbol{M}$6.6 (seismic moment 1.06×10^{19} Nm). We slightly modify the fault plane dimensions to 35 km along strike and 18 km along dip (Figure 4.3a), and discretize the fault into 35 × 18 subfaults with a size of 1 × 1 km. The depth to the top of the fault plane is set to 2 km. The synthetic velocity waveforms from the SIV project are filtered in the frequency band of 0.05-0.5 Hz and then integrated to obtain displacement. The Green's function for each subfault is computed using the discrete wavenumber method (Bouchon, 1981), adopting the same 1D velocity model used in the *Inv1* model (Figure 4.3b). The rake angle is not inverted and is assumed constant, using the same value specified in the SIV project (180°). To compute the modelling error in Eq. 4.2, we use Eq. 4.4 with VR_e = 0.95, reflecting the noise-free nature of the dataset.

To identify the optimal rupture model, we perform the inversion using multiple configurations of rupture parameters. In all models, no constraints are imposed on the nucleation point, allowing it to be sampled over the entire fault plane. This approach tests the ability of the inversion to recover the true nucleation location. The half-duration of the triangular regularization parameter of the Yoffe function (τ_s) is fixed at 0.2 s. We explore different parameterizations by varying the number of control points for slip, rupture velocity perturbation, and rise time. In addition, we consider simplified models in which rupture velocity and rise time are assumed to be spatially uniform.

We run the developed nonlinear inversion in parallel on eight CPU cores, using eight Markov chains with a geometrically spaced temperature ladder $T \in [1, 15]$. The chain with T = 1 is the cold chain and samples the true posterior distribution. The

total number of iterations is set to 25,000, with a burn-in period of 2,000 iterations, requiring approximately 9 hours of computational time.

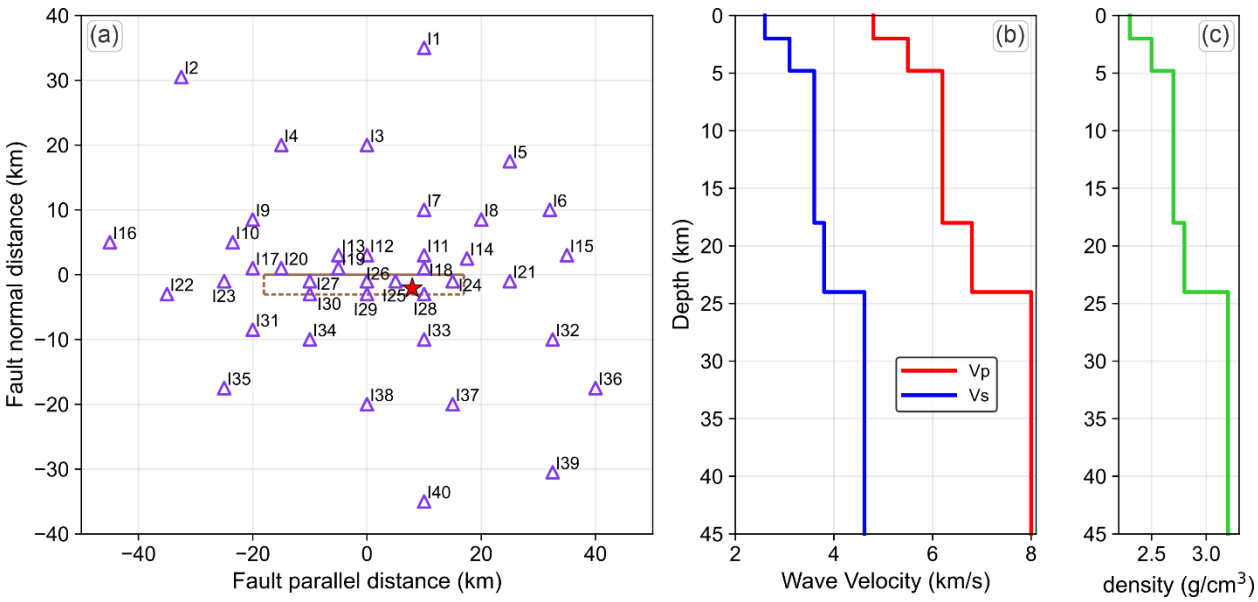

Figure 4.3. Configuration of the reference SIV model for the Inv1 benchmark. **(a)** Fault geometry (brown rectangle) and station locations (purple triangles), **(b)** P-wave and S-wave velocity model, **(c)** Density structure corresponding to each layer.

4.4.1.1 Inversion Results of the Synthetic Test

Our best-performing model shows that an optimal fit to the SIV rupture model can be achieved when we allow for perturbation of rupture velocity and rise-time variation. The best model only requires five, three, and three control points for slip, rupture velocity perturbation, and rise time, respectively. This results in a total model dimension of 36 parameters, which is significantly lower than that of conventional inversion approaches.

Figure 4.4 presents a comparison between the rupture model obtained in this study and the reference SIV model. For a consistent comparison, the original SIV slip model is projected onto a fault plane with dimensions matching those of our model. The spatial distribution of slip (Figure 4.4a) shows good agreement with the SIV model

(Figure 4.4b), with a cross-correlation of 0.89. Our model successfully resolves the location of the nucleation point in both the along-strike and depth directions, with both models indicating a nucleation depth of approximately 14 km. The location and extent of the high-slip patches are also well reproduced, with a maximum slip of 1.83 m in our model compared to 1.9 m in the SIV model. The estimated seismic moment corresponds to a moment magnitude of $\boldsymbol{M}$6.6 (seismic moment of 1.05×10^{19} Nm), matching the reference model. Figure 4.4c further compares the slip-rate functions of our model with those of the SIV model at six selected subfaults, whose locations are indicated by black stars in Figure 4.4b. The results show that our model reproduces the slip-rate functions at these subfaults with good agreement. In addition, both the rise time and rupture time are consistent with those of the reference model. This rupture model yields a strong fit to the synthetic waveforms, with a variance reduction of 93%, as shown in Figure 4.5.

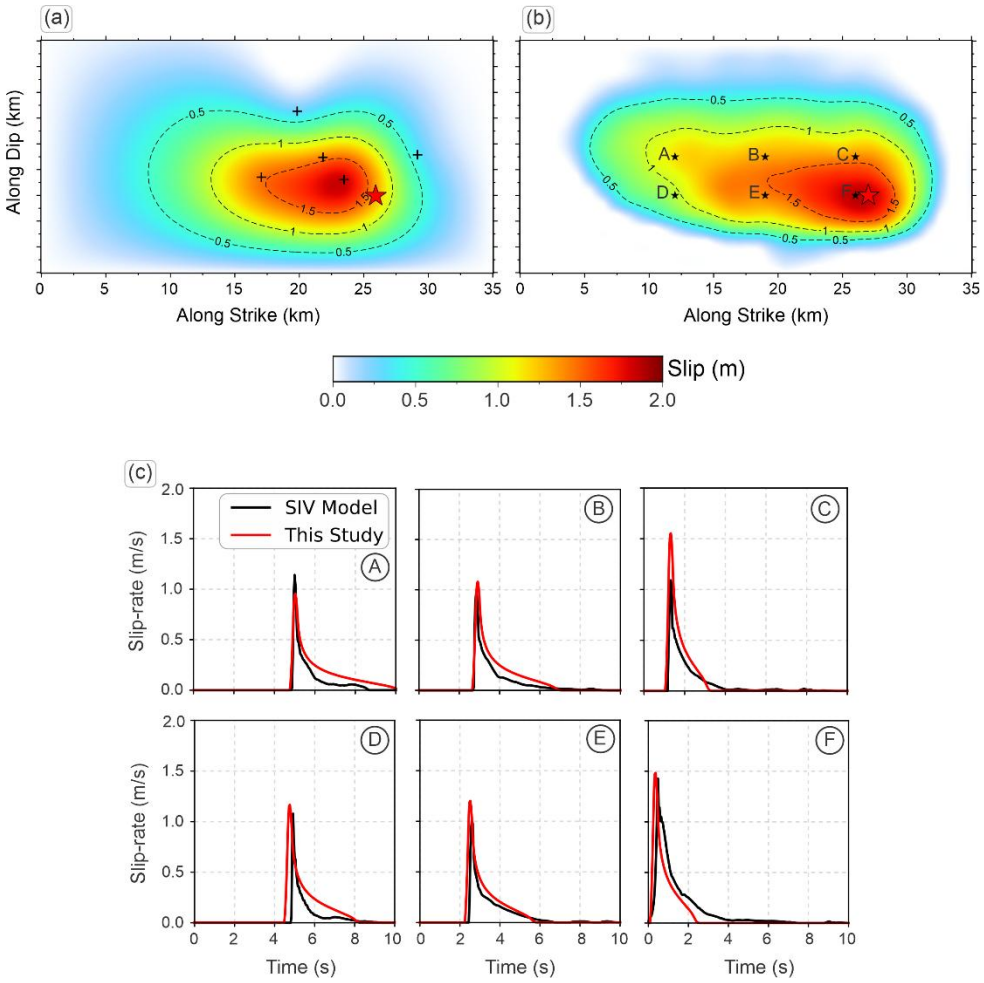

Figure 4.4. Comparison of the rupture model obtained in this study with the reference SIV model. **(a)** Slip distribution from our inversion model; black plus symbols indicate the locations of the slip control points. **(b)** Slip distribution of the reference SIV model. **(c)** Comparison of slip-rate functions at six selected subfaults (locations indicated by black stars in panel b). The hypocenter is shown by a red star.

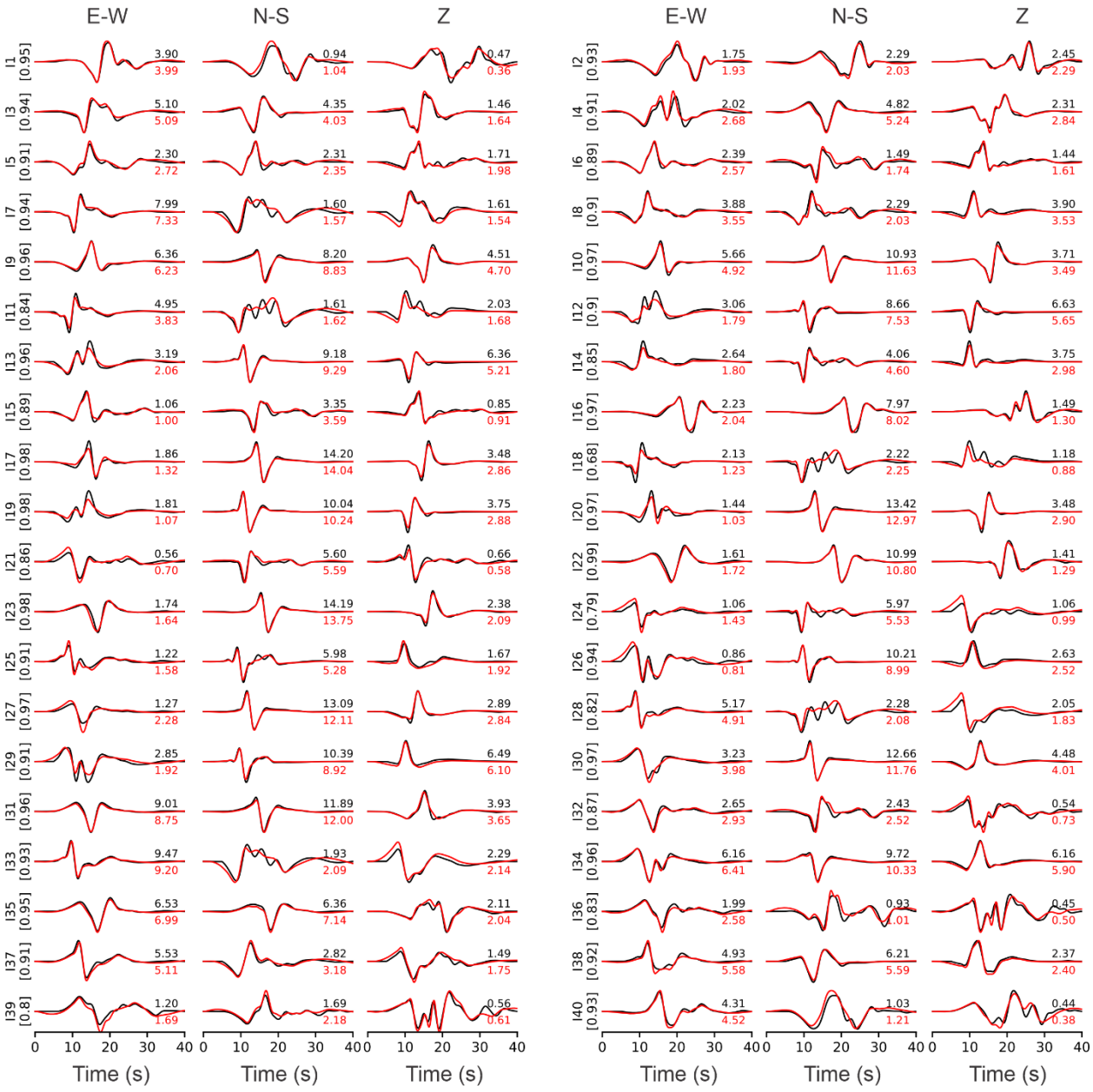

Figure 4.5. Comparison of displacement waveforms from the reference SIV model (black) and the synthetics (red) obtained from the rupture model of this study, filtered in the frequency band 0.05-0.5 Hz. The fit between the two is quantified by a variance reduction of 93%. The station name and corresponding variance reduction (values in parentheses) are shown on the left side of each waveform. The values on the right indicate the peak ground displacement (PGD) of the reference SIV model (black) and the synthetics (red), in cm.

4.4.2. Primary Results for Inversion of the Norica Mainshock

For the primary analysis, the single fault plane is discretized into 17 × 8 subfaults, each with dimensions of 2 × 2 km. For this model, the inversion solves for the location of the nucleation point, rupture velocity, rise-time, and slip, while the rake angle is fixed at 90°, corresponding to a pure normal faulting mechanism. It is noted that the rupture velocity and rise-time are assumed to be spatially homogeneous, and no variability of these parameters is considered. The Green's function for each subfault-station pair is computed using the discrete wavenumber method (Bouchon, 1981), adopting the velocity model proposed by Herrmann et al. (2011) for Central Italy. We adopt the same parallel tempering configuration as described for the SIV model inversion in Section 4.4.1. For this model, instead of using a Gaussian likelihood and L2 norm definition as the cost function (Eq. 4.2), we used the empirical form of likelihood (Eq. 4.5) and variance reduction as the cost function. Also, we set VR_e to be 0.75.

We test different numbers of control points for slip to identify the optimal rupture model for the Norcia mainshock. The best model is selected based on the highest variance reduction. Among the tested configurations, the model with eight control points yields the highest variance reduction of 61%. Therefore, the results presented in the following are based on this model. The spatial distribution of slip is shown in Figure 4.6a. The comparison between the observed and synthetic waveforms obtained from the best model is presented in Figure 4.7.

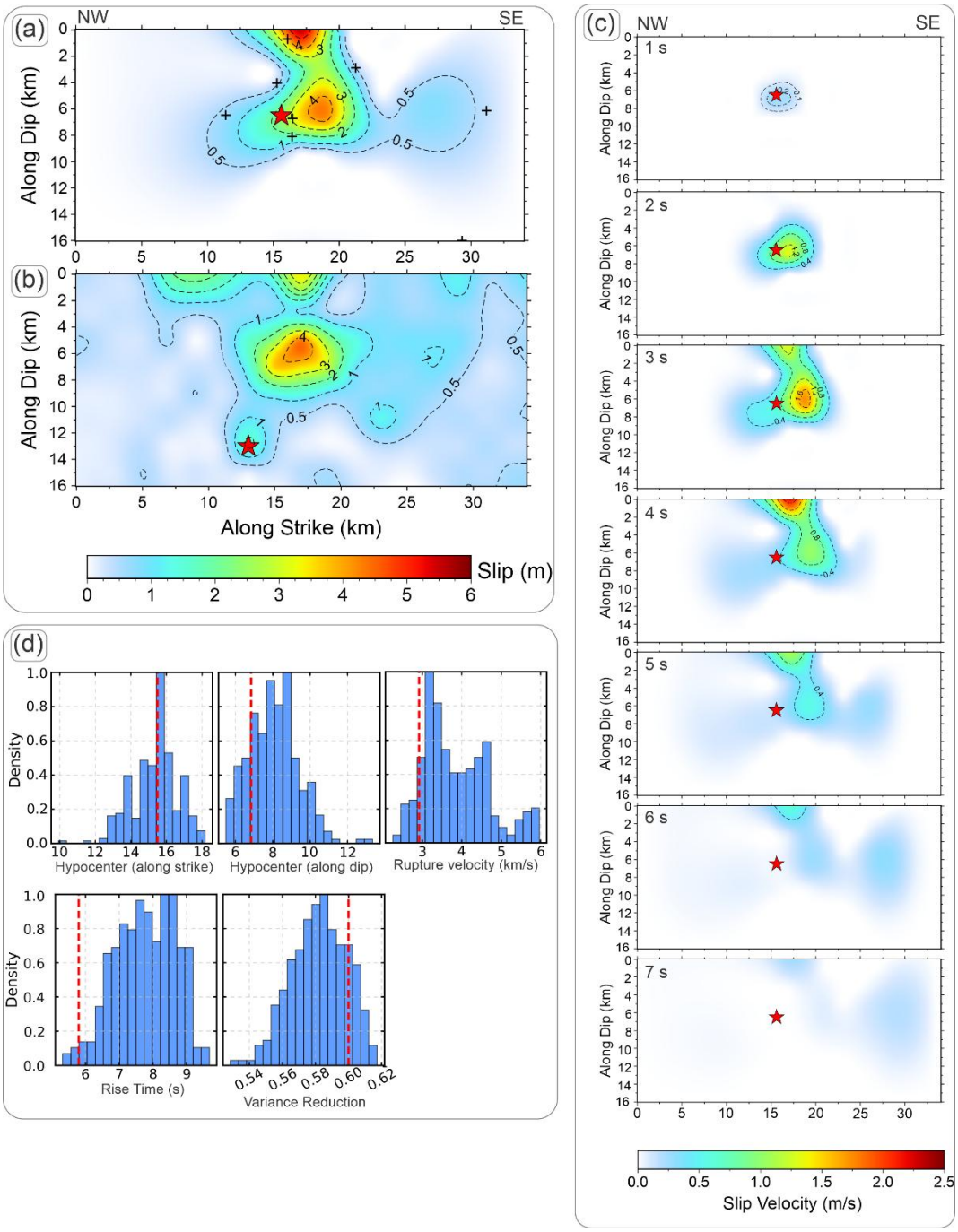

Figure 4.6. Results of the Kinematic source rupture inversion for the Norcia Mainshock. **(a)** Slip distribution obtained from this study, **(b)** slip distribution introduced by Scognamiglio et al. (2018), **(c)** posterior distribution of key model parameters.

The nucleation point is located at a depth of 5 km (approximately 7 km along dip). The rupture propagates at a constant velocity of about 3 km/s. The model yields

a relatively long rise time of 5.9 s, which is consistent with the long rise-time reported for the Norcia mainshock by Pizzi et al. (2017). The slip distribution is characterized by two main high-slip patches. The first patch is located near the hypocenter, spanning depths between 4 and 8 km along dip, with a maximum slip of approximately 4 m. The second patch is situated in the shallower portion of the fault plane, extending to the surface, where the maximum slip reaches about 5 m. The model yields a seismic moment of 5.4×10^{18} ($\boldsymbol{M}$ 6.42). The slip distribution is comparable with the slip model introduced by Scognamiglio et al. (2018) for a single fault plane based on inversion of strong-motion data, and performing inversion only with strong-motion data (Figure 4.6b). The temporal slip-rate function (Figure 4.6c) indicates that peak slip occurs at approximately 2 s and 3 s for the first and second slip patches, respectively. Figure 4.6d presents the marginal posterior distributions of the inferred parameters. To minimize the effect of autocorrelation between samples induced by the random walk, only every 80th sample is retained, resulting in 280 effectively uncorrelated samples. The marginal posterior distributions indicate that the hypocenter location is relatively well constrained, whereas rupture velocity and rise time exhibit broader distributions, reflecting parameter trade-offs and increased uncertainty. In contrast, the variance reduction displays a narrow distribution, indicating a consistently stable data fit across the posterior ensemble.

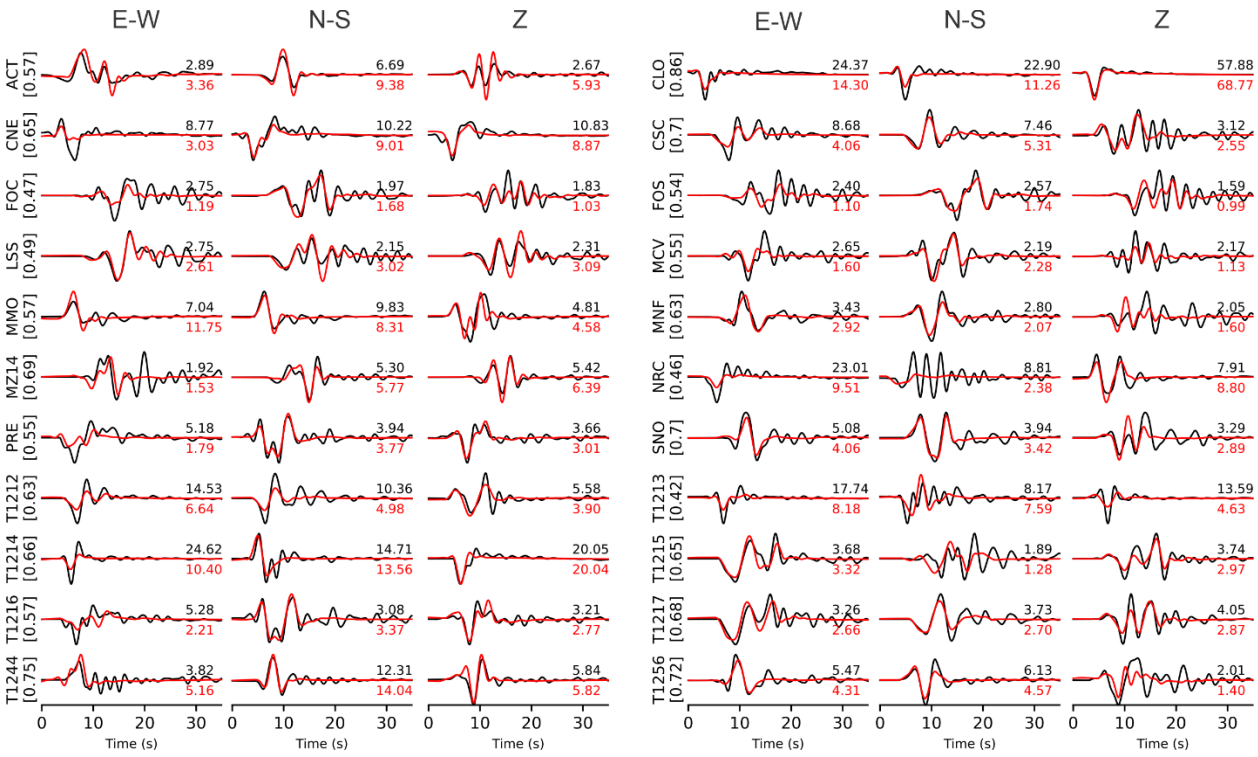

Figure 4.7. Comparison of velocity waveforms observed data (black) and the synthetics (red) obtained from the rupture model of this study, filtered in the frequency band 0.02-0.5 Hz. The fit between the two is quantified by a variance reduction of 61%. The station name and corresponding variance reduction (values in brackets) are shown on the left side of each waveform. The values on the right indicate the peak ground velocity (PGV) of the observed data (black) and the synthetics (red), in cm/s.

A direct comparison with the model of Scognamiglio et al. (2018) shows that the hypocenter in their model is located at a deeper section (9.52 km, 13 km along dip). In our approach, the hypocenter is not constrained to a predefined location; instead, its position is sampled over the entire fault plane during the inversion. Nevertheless, the hypocenter depth obtained in our model is consistent with independent estimates reported by Spallarossa et al. (2021) (6.2 km) and Pizzi et al. (2017) (6.4 km). The peak slip in their model is slightly lower, reaching 4.3 m compared to 5 m in our model. The rupture velocities in both models are comparable: 2.8 km/s in their model versus 2.97 km/s in ours. In addition, our estimated moment magnitude (M 6.42) is

slightly lower than their value of 6.5. This difference may be attributed to the presence of low-amplitude background slip in their model, which is less pronounced in our results. This behavior arises from our parameterization using control points combined with biharmonic interpolation, which produces a smoother slip distribution and tends to reduce background slip outside the main rupture areas. Overall, part of the discrepancy between the two models could be attributed to differences in rupture parameterization. For example, the rake angle is not inverted in our model, which may significantly affect the fit level, particularly for near-field observation. In addition, the two studies adopt different source time functions: Scognamiglio et al. (2018) use the boxcar function, whereas our model employs a regularized Yoffe function.

4.5. Conclusion and Discussion

This chapter presents a kinematic source inversion of the 2016 Norcia earthquake using a nonlinear Bayesian framework combined with Parallel Tempering Markov Chain Monte Carlo (PTMCMC). The primary objective is to improve the characterization of the spatiotemporal rupture process while explicitly accounting for uncertainties.

From a methodological perspective, the proposed inversion framework demonstrates several important advantages. First, the Bayesian formulation accounts for the model uncertainty by exploring the full posterior distribution of model parameters rather than relying on a single optimal solution. This is particularly relevant for earthquake source inversion, where non-uniqueness and parameter trade-offs are inherent. Second, the use of PTMCMC significantly enhances the exploration of the parameter space, overcoming limitations of conventional MCMC methods that may become trapped in local minima. The inter-chain exchanges ensure efficient sampling of complex, multimodal posterior distributions. Third, the adaptive parameterization based on control points provides a flexible representation of the rupture process. By reducing the number of free

parameters while maintaining physical plausibility, this approach mitigates overfitting and stabilizes the inversion.

The robustness of the methodology is confirmed through the synthetic benchmark test, where the inversion successfully recovers the main characteristics of the reference rupture model with high accuracy. The strong agreement in slip distribution, nucleation location, and slip-rate functions demonstrates the capability of the method to resolve complex rupture features with a relatively low-dimensional parameter space. The high variance reduction achieved in the synthetic test further validates the reliability of the forward modeling and inversion strategy.

Application to the 2016 Norcia earthquake provides meaningful insights into the rupture process. The inferred slip distribution reveals two high-slip patches, consistent with previous studies, with significant slip both near the hypocenter and in the shallow portion of the fault. The estimated rupture velocity is in agreement with independent studies, while the inversion suggests a relatively long rise-time. The inferred hypocenter depth aligns well with independent seismological estimates. Despite these consistencies, the overall variance reduction remains moderate compared to previous studies.

The differences between the present results and those of previous studies, particularly in terms of slip amplitude, rise-time, and overall fit quality, highlight the sensitivity of source inversion to model parameterization and underlying assumptions. The smoother slip distribution obtained in this study reflects the influence of the control-point parameterization and interpolation scheme, which tends to suppress small-scale variations and background slip. Similarly, fixing certain parameters, such as the rake angle, and assuming homogeneous rupture properties can restrict the model's ability to fully capture the complexity of the rupture process.

Future work should focus on extending the methodology to include multi-segment fault geometries, heterogeneous rupture velocity and rise-time distributions,

treating rake angle as an unknown parameter, and joint inversion of multiple data types.

Appendix 4

Table A4.1. A guideline for calibrating the swap acceptance rate

Acceptance Rate	Interpretation	Action
> 0.6	The ladder is too dense	Reduce the number of chains or increase T_{max}
0.4 – 0.6	Conservative ladder	Slightly reduce the number of chains or slightly increase T_{max}
0.15 – 0.4	Efficient regime	OK
0.1 – 0.15	Marginal communication	Consider more chains
< 0.1	Poor chain coupling	Increase the number of chains or reduce T_{max}

Table A4.2. A guideline for calibrating the proposal acceptance rate

Acceptance Rate	Interpretation	Action
> 0.5	Steps are too small, slow exploration	Increase step size
0.4 – 0.5	It is OK during the burn-in period, but the steps are small	Slightly increase the step size
0.2 – 0.4	Optimal regime	OK
0.1 – 0.20	Steps are optimal, but still a bit large	Slightly decrease the step size
< 0.1	The steps are too large	Decrease the step size

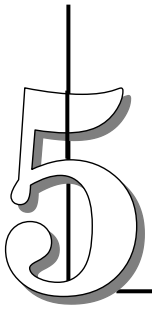

Improving Wave Propagation Models for Finite-Fault Inversion

This chapter builds on the dataset of small events introduced in Chapter 2 to compute Empirical Green's Functions (EGFs) using a clustering approach at near-field strong-motion stations associated with the Norcia mainshock. Source rupture model inversions are typically limited to frequencies below ~0.5 Hz due to the limited resolution of numerical Green's functions at higher frequencies. The use of EGFs offers the potential to extend the analysis to higher frequencies, thereby providing more detail on the rupture process. In this study, cluster-derived EGFs are compared with reference EGFs within the 0.3-1 Hz frequency band to evaluate the capability of the method to reproduce EGFs at the locations of the reference events. In addition, numerical Green's functions are compared with the reference EGFs at the same frequency band to assess the performance of the numerical model in simulating high-frequency waveforms.

5.1. Introduction

As discussed in Chapters 1 and 4, in source inversion, the retrieved rupture model is strongly influenced by the representation of wave propagation along the source–receiver path. This propagation is typically described using Green's functions, which must be evaluated over a frequency band suitable for resolving the rupture evolution. Consequently, uncertainties in the wave propagation model can lead to

significantly different solutions, thereby limiting the reliability of physical interpretations of the rupture process. Computing accurate theoretical Green's functions (e.g., Bouchon, 1981; Cotton & Coutant, 1997; Komatitsch & Vilotte, 1998; Maeda et al., 2017) requires detailed knowledge of the spatial distribution of P- and S-wave velocities and density within the target region (Aki & Richards, 2002). In practice, the propagation medium is often approximated by a 1D velocity model, which can adequately describe low-frequency seismic wave propagation in many settings. However, such simplifications may be insufficient in regions where 3D effects are significant, such as sedimentary basins, strong lateral heterogeneities, and complex topography, which can substantially perturb seismic-wave amplitudes and phases (e.g., Hartzell, 1989; Graves & Wald, 2001; Gallovič et al., 2015; Maufroy et al., 2015). Despite their improved physical realism, the use of a 3D velocity model in computing Green's functions (Graves, 1996; Moczo et al., 1999; Chaljub et al., 2007) remains challenging. Constructing reliable 3D velocity and density models requires dense and high-quality seismic and geophysical observations, which are often unavailable, particularly in regions with sparse instrumentation. In addition, 3D wave propagation modeling is computationally demanding, especially for broadband frequencies and large spatial areas, making it impractical for applications that require repeated forward simulations, such as iterative waveform inversion. In general, uncertainties in 1D or 3D structural models are difficult to quantify and may introduce strong trade-offs between source and path effects, potentially biasing inferred source parameters (e.g., Graves & Wald, 2001; Liu & Archuleta, 2004; Razafindrakoto & Mai, 2014; Hallo & Gallovič, 2016; Spudich et al., 2019). For example, Spudich et al. (2019) investigated the impact of Green's function uncertainty by quantifying the associated variance, defined as discrepancies between observed aftershock recordings and synthetic waveforms computed with an imperfect velocity model at two near-field stations within the L'Aquila sedimentary basin. They incorporated this uncertainty into source rupture modeling, demonstrating that errors in Green's functions significantly influence the variability of synthetic ground motions, and consequently, the inferred source rupture characteristics.

Assuming a linear response of medium, the Empirical Green's Function (EGF) method (e.g., Hartzell, 1978; Irikura, 1983; Hough, 1997) uses the waveforms of small earthquakes occurring in the vicinity of the target mainshock source and sharing similar focal mechanisms. Because EGFs inherently include path and site effects, this approach does not require an explicit velocity model. The EGF method has been widely applied to source inversions for earthquakes spanning a broad range of magnitudes (Ide, 2001; Dreger et al., 2007; Okuda & Ide, 2018; Causse et al., 2017; Ide et al., 2011; Uchide & Song, 2018; Wu et al., 2021; Shibata & Aso, 2025; Žilić et al., 2025). Compared to theoretical Green's functions, EGFs more accurately capture high-frequency propagation effects, thereby extending the frequency band over which waveform inversion can be performed (e.g., Kakehi & Irikura, 1996; Nakahara et al., 1998; Pulido et al., 2008; Satoh, 2023). Although EGFs can better capture the wave propagation effects, several limitations restrict their applicability and must be carefully considered when they are used in source inversion. Because Green's functions are defined as the impulse response of the medium to a point-source dislocation with unit seismic moment, EGF waveforms must be deconvolved to remove source effects, including seismic moment and corner frequency, typically under the assumption of Brune's source model (Brune, 1970). Estimating the corner frequency, particularly for small events, is highly challenging and subject to substantial uncertainty (e.g., Abercrombie, 2021; Abercrombie & Baltay, 2025), which can propagate into the derived EGFs through the deconvolution process. Furthermore, in regions of large coseismic slip during a mainshock, stress is commonly reduced to near-dynamic levels, making repeated slip on the same fault patches unlikely (Day et al., 1998; Johnson & Nadeau, 2002; Toda et al., 2012). As a result, the number and spatial distribution of suitable EGFs may be limited, potentially preventing accurate reconstruction of mainshock rupture details.

The central Apennines in Italy exhibit pronounced lateral and vertical heterogeneity in crustal structure, which strongly affects seismic wave propagation and complicates the construction of reliable Green's functions. High-resolution

tomographic studies (e.g., Alesssandrini et al., 2001; Menichelli et al., 2023) reveal significant P- and S-wave velocity variations in the upper crust that correlate with constraining lithologies such as rigid carbonate platforms and ductile evaporitic horizons. These variations reflect the complex fold-and-thrust belt architecture and its subsequent overprinting by extensional faulting and sedimentary basins, features that laterally homogeneous models may not adequately represent. Such heterogeneity produces complex wave propagation effects as seismic waves traverse regions with strong contrasts in seismic velocities, sediment basins, and folded carbonate sequences. Consequently, the use of a simple 1D velocity model to compute Green's functions may fail to reproduce the observed waveforms, underscoring the need for 3D velocity models or empirical Green's functions to achieve more accurate waveform modeling.

In this chapter, we use the dataset compiled in Chapter 2 to compute empirical Green's functions (EGFs) for the near-field strong-motion stations that recorded the ***M***6.5 Norcia mainshock (Figure 5.1). The objective is to improve the representation of wave propagation, thereby reducing biases in rupture imaging. To this end, we employ clusters of events with similar waveforms to assign appropriate EGFs to each subfault of the assumed fault plane of the Norcia mainshock. The analysis in this chapter is restricted to the main fault plane of the fault geometry model proposed by Scognamiglio et al., (2018). This fault is represented as a single planar surface with a strike of N155°, a dip of 47° toward the southwest, a length of 34 km, and a width of 16 km (Figure 5.1). Finally, we compare the EGFs and the theoretical Green's functions computed using a 1D velocity model with a set of reference EGFs.

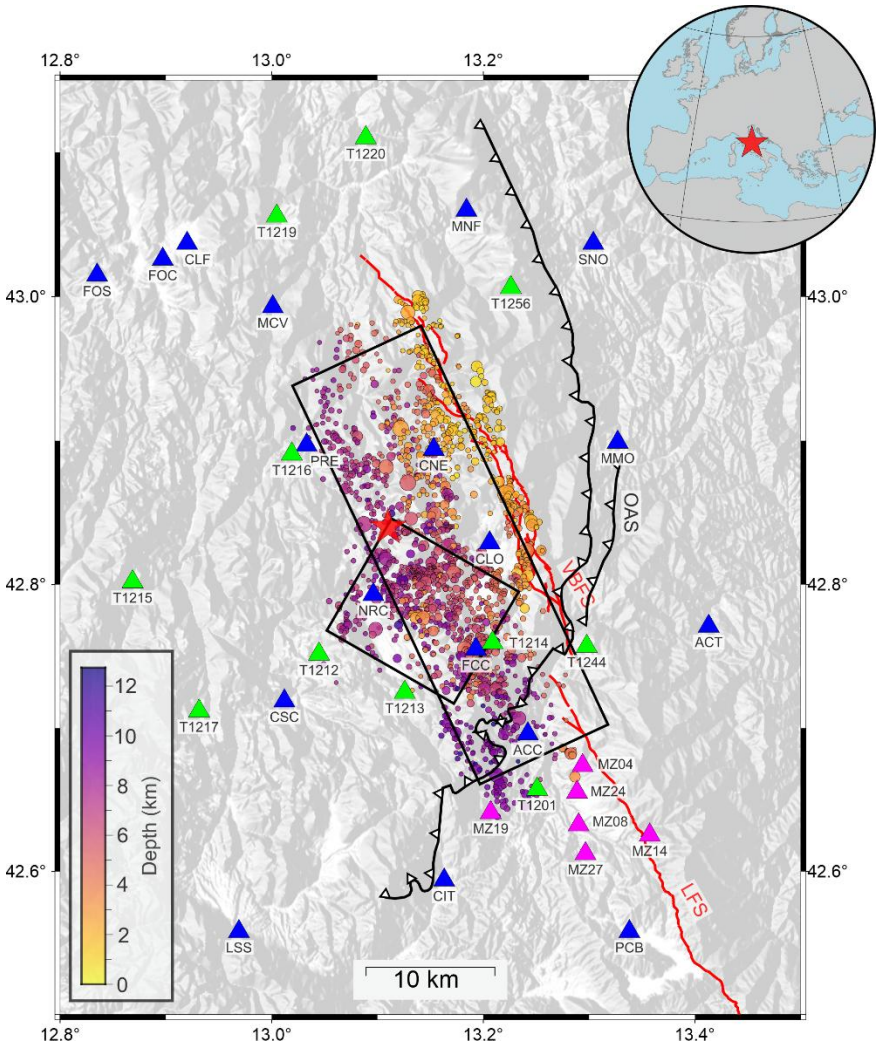

Figure 5.1. Map of the epicentral area showing the distribution of small events and near-field strong motion stations. The two black rectangles outline the fault planes used in the inversion models. The red star marks the epicenter of the Norcia mainshock. Circles colored by depth indicate the epicenters of the small events used to compute empirical Green's functions (EGFs). Green, blue, and pink triangles represent stations from the Italian Strong Motion Network (RAN), the Italian National Seismic Network (INSN), and the CentroMz network, respectively. Red lines denote the two normal fault systems of the Vettore–Bove Fault System (VBFS) and the Laga Fault System (LFS), while black barbed lines indicate the thrust fronts of the Mount Sibillini Thrust.

5.2. Waveforms Processing

For EGFs analysis, we select foreshock and aftershock events (hereafter referred to as small events) occurring between 2016-08-24 and 2018-01-12, with moment magnitude (***M***) ranging from 2.5 to 4.5. To compute EGFs, the small events are projected onto predefined subfaults on the fault plane hosting the target rupture. To ensure that the path propagation characteristics of the selected events are approximately consistent with those from sub-faults, only small events located within 3 km of the fault plane are selected (Figure 5.1). This selection may also help identify small events with focal mechanisms similar to the mainshock. Following these criteria, we process the acceleration waveforms for 960 small events recorded at the same stations that recorded the mainshock. To discard poor-quality waveforms, we apply the following strict criteria to process them:

- All waveforms are visually inspected, and those with poor-quality features are discarded. Poor-quality records include signals indistinguishable from background noise, records lacking clear P- and S-wave arrivals, and waveforms containing spikes, etc.
- Waveforms containing multiple overlapping small events with a short time lag within the time window are excluded. When time lags are long enough to distinguish arrivals, signals are manually trimmed to isolate the waveform corresponding to the target event.
- For the remaining waveforms, the Signal-to-Noise (SNR) is computed over 10 logarithmically spaced frequencies between 0.3 and 1.0 Hz. Waveforms are admitted into the EGFs computation if the SNR calculated within the target frequency band exceeds the threshold value of 3.

Finally, the accepted small-event waveforms are processed by removing instrumental corrections, applying a 4th-order Butterworth bandpass filter in the ranges of 0.3–1.0 Hz, and using zero-phase filtering. Furthermore, a Cosine taper with a length of 5 percent of the signal length is applied to both sides of the signals.

Finally, the filtered accelerograms are integrated to obtain velocity waveforms and resampled to 10 samples per second.

5.3. Methodology

This study employs two different approaches to compute Green's functions for each sub-fault at the selected stations. The first method, referred to as 1DGFs, is a numerical approach based on the discrete wavenumber method (Bouchon, 1981), implemented using the Axitra code (Cotton & Coutant, 1997) together with a 1D velocity model for central Italy proposed by Herrmann et al. (2011). The assumption of a 1D-velocity model is extensively used in source inversion studies and is thus considered here for comparison purposes. The second approach uses a modified Empirical Green's functions (Figure 5.2) method introduced by Causse et al. (2017), in which clusters of small events are used to compute EGFs. This approach is referred to as CEGFs. We classify the stations into two groups (Table A5.1 in Appendix 5): stations with sufficient recordings of small events to enable clustering, designated as Group 1 (G1), and stations with limited recordings of small events, for which clustering cannot be applied, designated as Group 2 (G2). The main steps required to compute EGFs are summarized as follows:

1. To remove source effects, all the waveforms are deconvolved using the Brune (1970) source model and the corresponding seismic moment and corner frequency for each event. Because the corner frequencies of the selected events are generally above 1 Hz, the source spectra within the analyzed frequency band can be considered approximately flat. Therefore, removing source effects primarily requires scaling the waveforms by the seismic moment. We use the seismic moment estimates from Chapter 2, which account for the spatial and temporal variability in source characteristics.
2. P- and S-wave arrival times for all sub-faults and small events are computed at the selected stations using the 1D velocity model proposed by Herrmann et al., (2011).

3. For G1 stations, an unsupervised hierarchical clustering analysis is performed using the "cluster.hierarchy" module from SciPy (Virtanen et al., 2020) to classify waveforms recorded from small-magnitude events. Clustering is based on pairwise similarity measures (e.g., correlation-based distances), enabling the identification of groups of waveforms with similar waveforms at each station. The waveform window includes only P- and S-wave phases, with the end of the S-wave window estimated empirically as $2(t_s - t_p) + 3$, where t_p and t_s are P- and S-wave arrival times, respectively. The three-component waveforms of each event are concatenated to form a single composite signal. For each pair of events, the composite waveforms are shifted in time relative to one another to maximize their cross-correlation. The resulting maximum correlation coefficient is used as a measure of similarity, and event pairs with values exceeding 0.7 are classified as similar and assigned to the same cluster. The events located more than 3 km from the cluster centroid are subsequently excluded. Each cluster is then paired with one or a few sub-faults if the distance between its centroid and the center of the sub-faults is less than 4 km (see Section 5.4.2 for details). To account for the S-wave geometrical spreading, the waveform amplitudes within each cluster are scaled by $d_{hypo}/d_{i,j}$, where d_{hypo} is the hypocentral distance between the events within the cluster and the station, and $\boldsymbol{d_{i,j}}$ is the hypocentral distance between the sub-fault and the station. If no cluster exists within 4 km of a given sub-fault, the nearest single event is selected as the EGF, which is processed in the same manner as the G2 station described in step 5.
4. After grouping small events in clusters, a "master event" is selected within each cluster, defined as the event with the highest average cross-correlation with all other events in the cluster. All events are then aligned with respect to the master event by maximizing cross-correlation and trimmed at a time corresponding to the P-wave arrival time of the master event. Then the trimmed waveforms are averaged to obtain the CEGFs, representing the approximated Green's function. This averaging reduces potential uncertainties

arising from imperfect source deconvolution, uncertainties in aftershock locations, and variability in aftershock focal mechanisms. Finally, the averaged CEGF is time-shifted according to the P-wave arrival time at the target station for each subfault to ensure correct wave arrival times.

5. For G2 stations, the nearest single event to each sub-fault is selected to compute the EGF. The waveform amplitude is then scaled to account for the S-wave geometrical spreading in the same manner as described in step 3. Because each waveform is already trimmed within a window starting at the P-wave onset, the waveform is subsequently time-shifted based on the P-wave arrival time of the corresponding subfault at the target station.

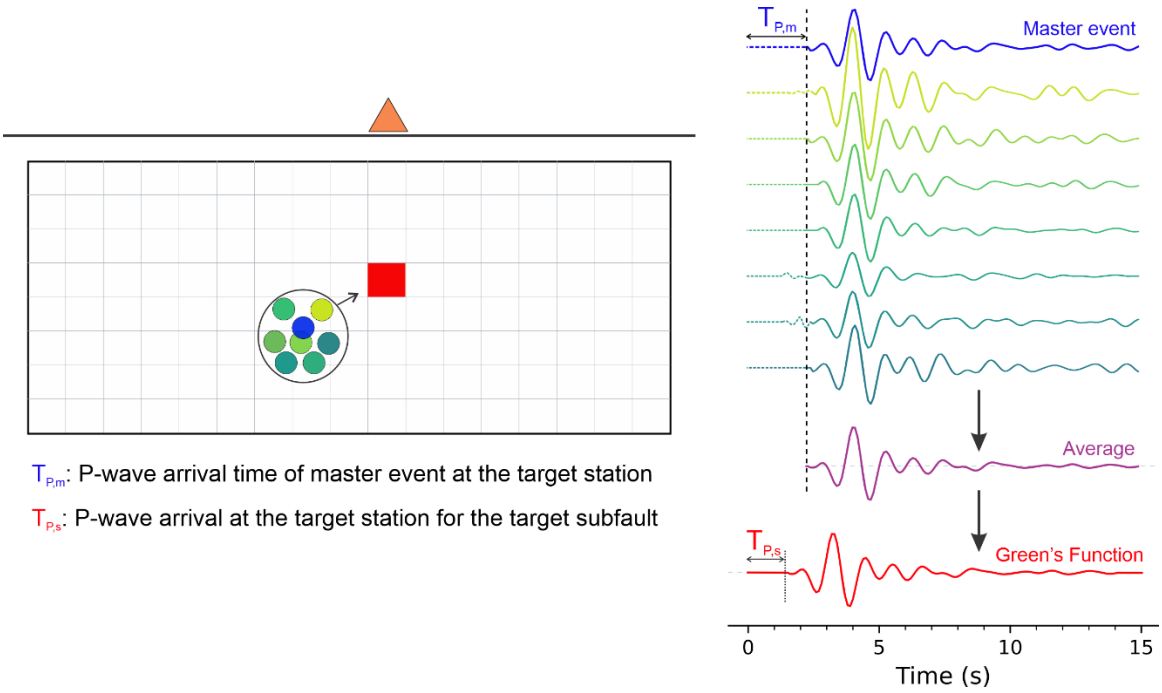

Figure 5.2. Schematic illustration of the CEGFs methodology used to compute Green's functions. **(a)** The fault plane is discretized into smaller subfaults for which EGFs are computed. The target subfault is shown in red, and the surrounding events within the circle represent the cluster used to compute the EGF at the station indicated by the orange triangle. **(b)** Waveforms of events within the cluster are aligned relative to the master event (blue waveform). The purple waveform represents the averaged waveform, and the red waveform shows the time-shifted average, which corresponds to the final EGF for the target subfault at the target station.

Since it is recommended to select the small events with a similar focal mechanism to that of the mainshock, we refine our catalog using available focal mechanism solutions, prioritizing those from INGV Time-Domain Moment Tensor (TDMT, Scognamiglio et al. (2006)), the Moment Tensor Solution for Italy (Herrmann et al., 2011), and a Deep Learning-based focal mechanism solution by Meier et al. (2025). For the latter, we retain only the solutions of quality A and B, which show strong consistency with the first two datasets for events in common. As a result, 68%

of the small events in our catalog are associated with a known focal mechanism. The remaining 32% lack focal mechanism solutions; however, they are retained in the catalog and included in the EGF computation.

5.4. Results

Here, we present the results of several tests designed to assess the reliability of the computed Green's functions using both the CEGF and the 1DGF approaches. All results are based on the frequency range 0.3–1 Hz, and the analysis focuses exclusively on Green's functions computed for the assumed fault plane of the Norcia mainshock.

5.4.1. Waveforms Similarity and Focal Mechanisms

Because the number of small events with focal mechanisms similar to that of the mainshock is limited, we decide to include all available events without explicitly accounting for their focal mechanisms. To assess the relevance of this choice, we examine whether the hierarchical clustering method described above implicitly groups events with similar focal mechanisms, or whether it primarily reflects waveform similarity regardless of differences in focal mechanisms. To that end, we compute the simplified Kagan angle (Kagan, 2007) for each small event with respect to the main fault plane mechanism. The Kagan angle ranges from 0º to 90º, where 0º indicates identical mechanisms and 90º indicates maximally different mechanisms with reference. We select 13 clusters containing at least seven events with available Kagan angle estimates and plot the focal mechanism (beach-ball diagram) of each event, along with their corresponding Kagan angles, as shown in Figure 5.3a. Most clusters exhibit a wide range of Kagan angles, indicating substantial variability in focal mechanisms. Events with higher Kagan angles still predominantly show normal faulting mechanisms, but with some moderate-to-strong strike-slip components. The 2016-2017 central Italy sequence ruptured several secondary and antithetic normal faults (Chiaraluce et al., 2017; Improta et al., 2019; Michele et al., 2020), whose focal mechanism may differ from that of the main fault plane. For example, the secondary

fault plane adopted by Scognamiglio et al., (2018) exhibits a normal faulting mechanism with a significant strike-slip component. Therefore, events with high Kagan angle may be associated with the rupture of these secondary or antithetic fault structures. In our case, the clustering is performed independently for events recorded at each station, rather than jointly across multiple stations. While this approach ensures consistency in path and site effects for a given station, it may limit the ability to resolve well source-related differences. In contrast, clustering based on recordings from a broader network of stations with good azimuthal coverage may better capture source-related information and provide a more robust discrimination of source mechanisms. However, in our case, the number of events recorded across a sufficiently wide range of stations with adequate azimuthal coverage is limited, which prevents the application of such a multi-station clustering approach.

To further assess whether events with different mechanisms can exhibit similar waveforms, we plot the waveforms of 16 events from Cluster 7 in Figure 5.3b. Despite the large range of Kagan angles within this cluster, the waveforms are highly similar, with an average cross-correlation coefficient of 0.83 between events. Therefore, Waveform similarity does not necessarily imply identical focal mechanisms. These results indicate that, at the frequency range 0.3–1 Hz and for the stations considered, the computed EGFs show only a weak dependence on focal mechanism. This suggests that accurate focal mechanism information is not a primary requirement in the construction of EGFs.

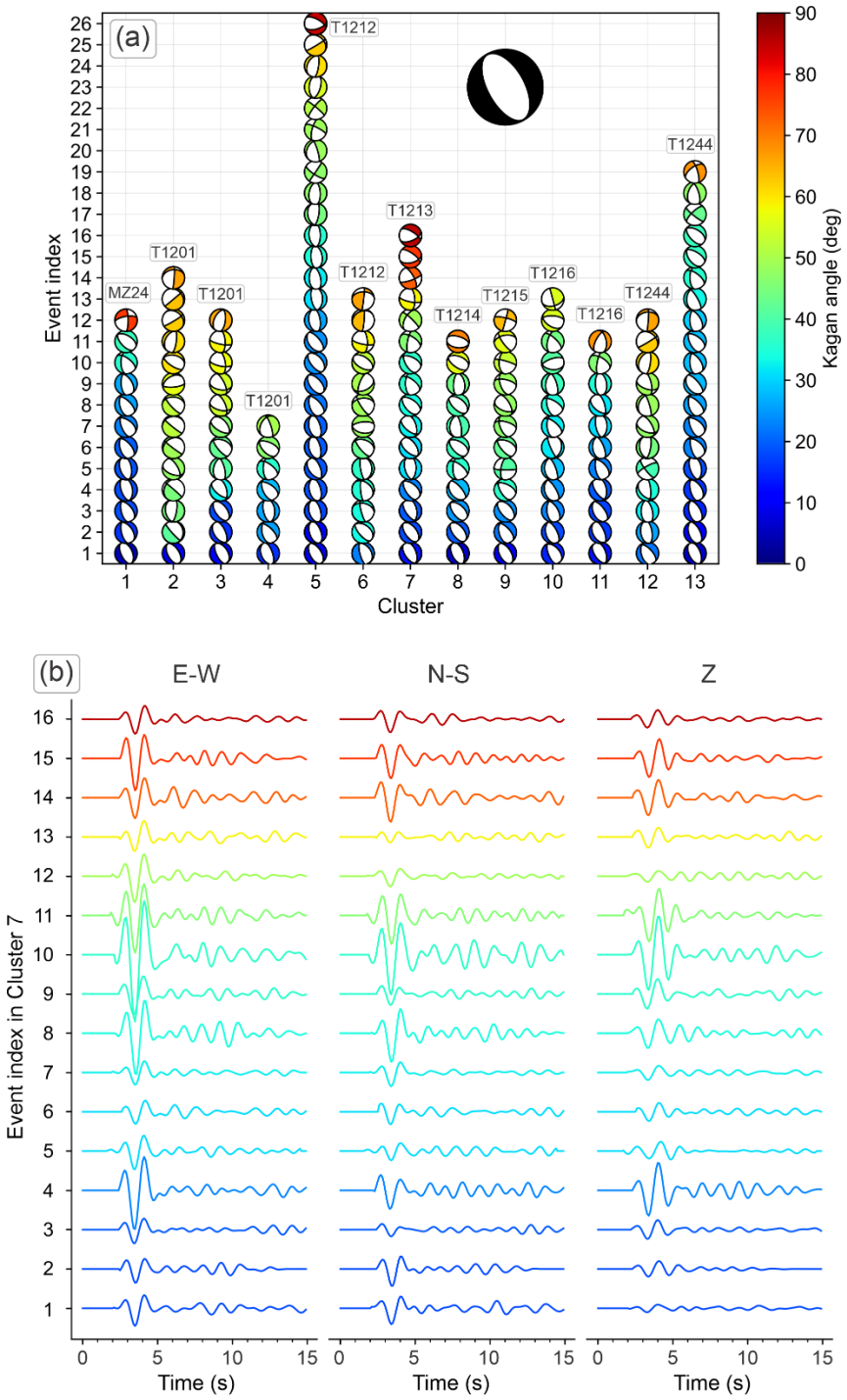

Figure 5.3. Focal mechanism and waveform similarity of events within clusters. (a) Variability of Kagan angles for small events within the 13 selected clusters. The label above each group of beach-ball diagrams indicates the corresponding station code. **(b)** Aligned waveforms of events within Cluster 7. Each waveform is colored according to the Kagan angle of its corresponding event.

5.4.2. Comparison of Computed Green's Functions with Reference EGFs

5.4.2.1. Comparison Between the CEGF Approach and Reference EGFs

To assess the reliability of the Green's functions obtained from the CEGF approach, we compare them with seven reference EGFs at stations T1214 and T1215. The reference EGFs correspond to small deconvolved events located within 250 m from the fault plane exhibiting focal mechanisms with Kagan angles less than 25° relative to the main fault plane. The locations of the reference events and the stations are shown in Figure 5.4a. The distances between each station and the subfaults corresponding to the reference EGFs are summarized in the table presented in Figure 5.4b.

First, we compare the reference EGFs with those obtained from the CEGF approach at the subfaults corresponding to each reference EGF (Figure 5.4c). To quantify their similarity, we use the cross-correlation coefficient (shown in blue at the top right of each waveform). In addition, to assess amplitude consistency, we compute the peak amplitude ratio between the CEGFs and the reference EGFs (shown in green at the bottom right of each waveform). It is noted that the cross-correlation is computed from the onset of the P-wave to the end of the S-wave. Overall, the C EGFs show strong agreement with the reference EGFs, exhibiting high correlation coefficients and, in most cases, comparable peak amplitudes. However, in a few examples, such as case 4 at station T1215 and cases 4 and 5 at station T1214, the CEGFs exhibit significantly lower amplitudes than the corresponding reference EGFs. Similar discrepancies are observed only occasionally at other stations and for different reference EGFs. Hereafter, we discuss the possible origins of these amplitude differences:

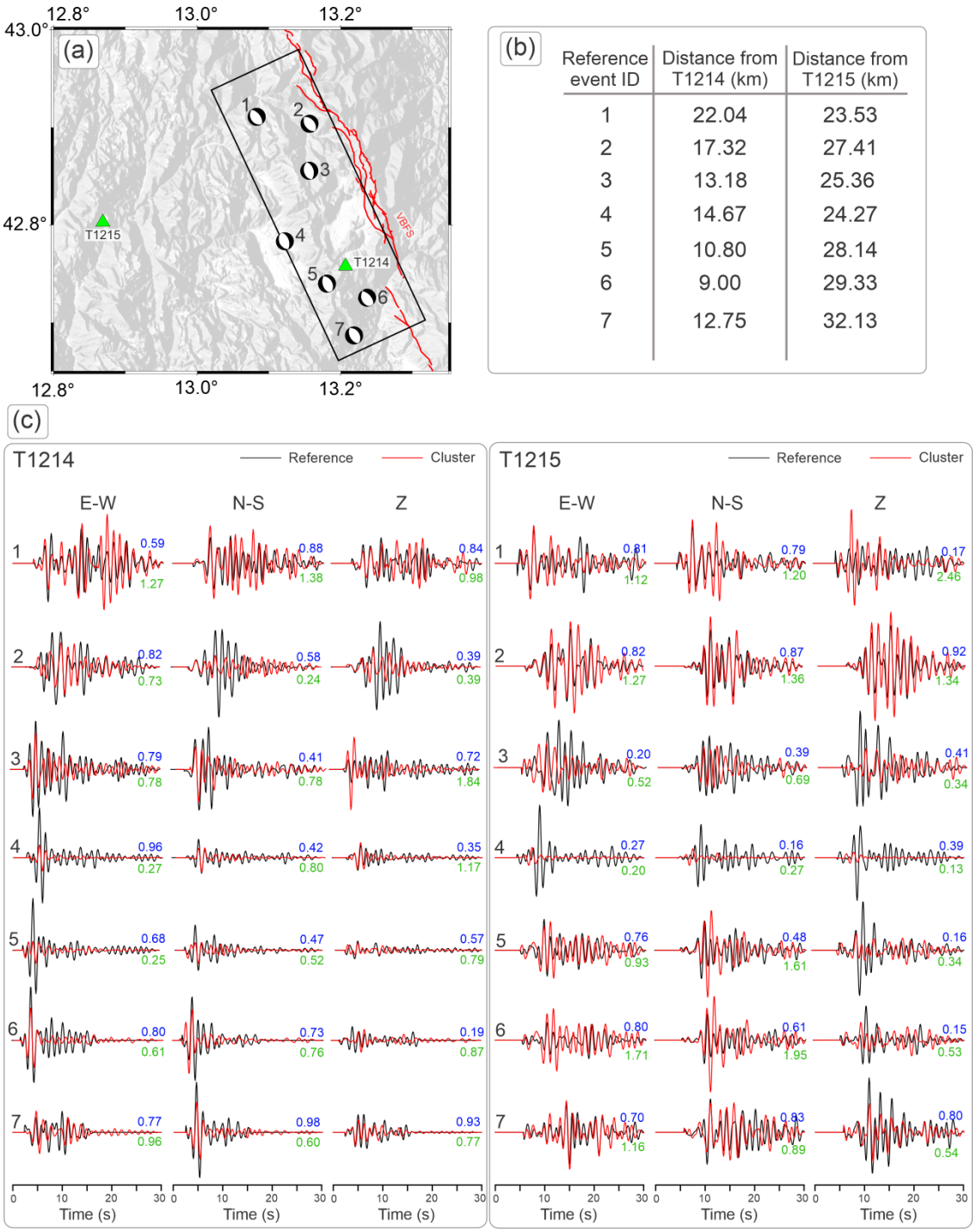

Reference event ID	Distance from T1214 (km)	Distance from T1215 (km)
1	22.04	23.53
2	17.32	27.41
3	13.18	25.36
4	14.67	24.27
5	10.80	28.14
6	9.00	29.33
7	12.75	32.13

Figure 5.4. Comparison of CEGFs with reference EGFs for seven cases at two stations. **(a)** Map showing the locations of the seven reference events and the two stations (T1214 and T1215) relative to the main fault plane (black rectangle). **(b)** Table summarizing the distances between each reference event and the stations. **(c)** Comparison between the CEGFs (red) and the reference EGFs (black) at stations T1214 (left panel) and T1215 (right panel).

The blue and green numbers show the cross-correlation between the two waveforms and the peak amplitude ratio between the CEGFs and the reference EGFs, respectively.

One possible explanation for the larger amplitudes observed in the reference EGFs is the influence of directivity effects in the reference events. In contrast, potential directivity effects among events within each cluster are likely suppressed through waveform averaging. The directivity effects are well-documented for small-to-moderate earthquakes in Central Italy (e.g., Cultrera et al., 2009; Colavitti et al., 2022, 2026). Colavitti et al. (2022) showed that these effects are more pronounced along the strike of the main normal fault system (VBFS). However, for case 4 at station T1215, the larger amplitude of the reference EGF is unlikely to be explained by directivity, as the station is located in the fault-normal direction relative to the fault system.

An alternative explanation may involve nonlinear site response effects. Such effects typically require specific conditions, including soft soil properties and high levels of peak ground acceleration (PGA). Under these conditions, events occurring at the same location but at different times (e.g., before and shortly after the mainshock) may generate different amplitudes. To support this, several studies (Bonilla et al., 2019; Vassallo et al., 2022; Esfahani et al., 2024; Miroslav Hallo et al., 2025) have shown that surface geological conditions beneath recording stations can undergo temporal changes following a mainshock. In the case of station T1215, however, this explanation is also unlikely. The station is classified as site class A (hard rock), and the generated PGA by the mainshock is relatively low (87 cm/s^2), suggesting that nonlinear site effects are not expected to be significant. In contrast, the recorded PGA at Station T1214 with a site class B (rock) is 592 cm/s^2. Nevertheless, events within the clusters at this station do not exhibit substantial variability in amplitude relative to the mean values observed before and after the Norcia earthquake. Furthermore, the horizontal-to-vertical spectral ratio (HVSR) provided by the Italian Accelerometric Archive (Itaca) shows a peak frequency of 4 Hz. According to Vassallo

et al. (2022), the peak frequency of a site following a strong shaking event typically shifts by only about 7% to 10% toward a lower frequency. Therefore, significant changes in site response are unlikely within the frequency range of our interest, where the HVSR remains relatively flat and close to unity.

To further investigate, we compute the variability of the peak ratio (ratio between the amplitude of each EGF within the cluster and the amplitude of the averaged EGF) for all stations with sufficient recordings to perform clustering (Table A5.1) with site classes of A (hard rock), B (rock), and C (soil). As illustrated in Figure 5.5a, the standard deviation shows no clear dependence on site class or on the recorded PGA from the mainshock. Figure 5.5b presents the EGFs within a cluster for station T1214 (site class B). No systematic difference is observed between events occurring before and after the Norcia mainshock (2016-10-30T06:40:18). If nonlinear site effects were significant, EGFs from pre-mainshock events would be expected to show larger amplitudes compared to those from early post-mainshock events. A more robust assessment would ideally involve stations with softer site conditions. In this context, station MZ24 (site class C), which recorded a PGA of approximately 1000 cm/s^2, would be particularly suitable. However, the available dataset for this station does not include sufficient recordings before the Norcia event to enable a meaningful comparison.

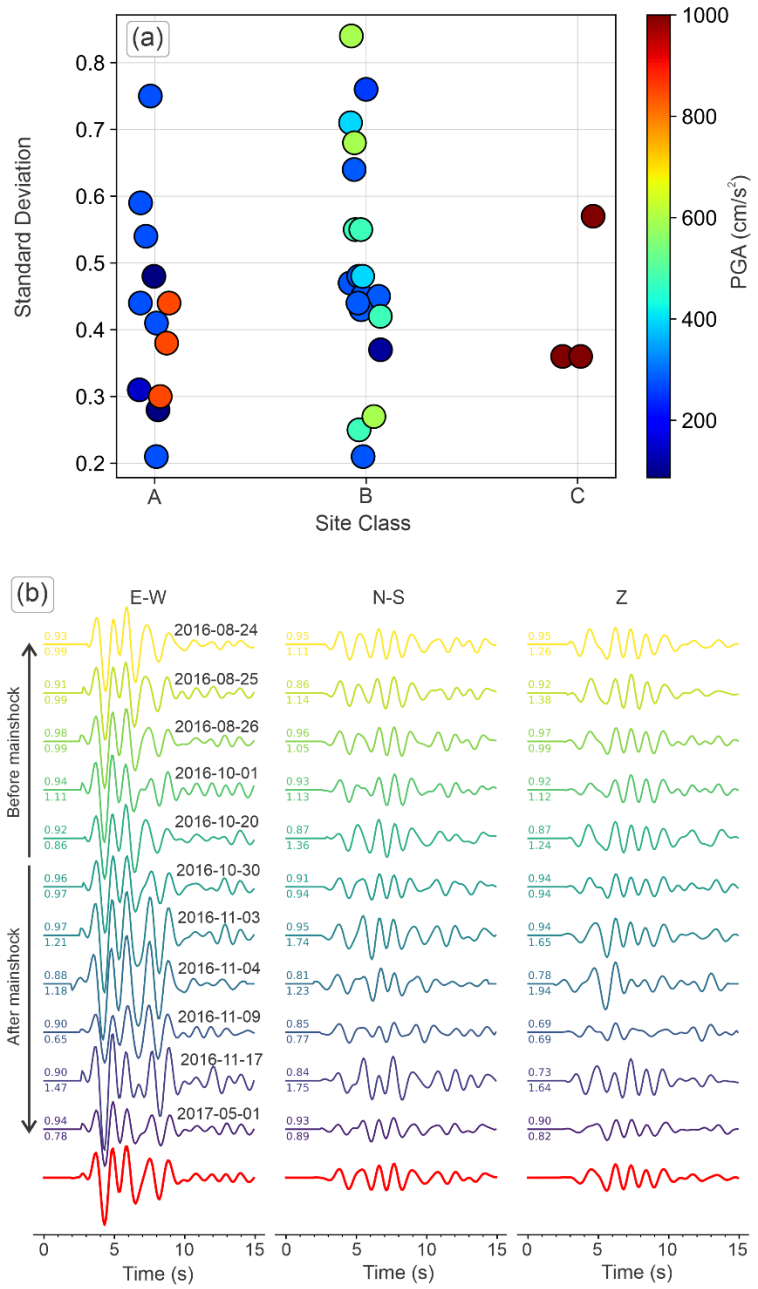

Figure 5.5. Investigation of potential nonlinear site effects beneath the stations. **(a)** Standard deviation of the peak amplitude ratio, defined as the ratio between the amplitude of each EGF within a cluster and that of the averaged EGF, for all clusters at stations with site classes A, B, and C. Each circle is colored according to the PGA recorded during the Norcia mainshock at the corresponding station. **(b)** Waveforms of events within a cluster recorded at station T1214 (site class B). Events occurring before and after the Norcia mainshock (2016-10-30T06:40:18) are indicated by arrows on the left side of the plot. The red waveform represents the averaged EGF.

A third possible explanation is the uncertainty in estimating the source parameters required for deconvolution, such as seismic moment and corner frequency. Because the waveform amplitude is scaled by the seismic moment during deconvolution, uncertainties in seismic moment estimation are likely to contribute to the observed amplitude differences. To further investigate this possibility, we compare the moment magnitudes reported by the two independent studies of Kemna et al. (2021) (hereafter referred to as K21) and Bindi et al. (2024) (hereafter referred to as B24) with those of our estimates for the reference events and the events within the clusters (see Chapter 2). For reference events 4 and 5, the reported moment magnitudes are [3.62, 3.49, 3.33] and [2.73, 2.78, 2.46], respectively. The mean moment magnitudes of the events within the corresponding clusters are [3.27, 2.95, 2.86] and [3.27, 3.13, 2.90], respectively, where the three values in each bracket correspond to the estimates from the three studies. The inter-study variability is approximately 0.15 for the reference events and 0.2 for the clustered events, indicating maximum discrepancies in seismic moment estimates with a factor of ~2. Therefore, uncertainties in seismic moment are unlikely to fully explain the observed amplitude differences. Moreover, any residual uncertainty in individual events is expected to be reduced in the CEGFs, as it represents the average of multiple EGFs within each cluster.

5.4.2.2. Comparison Between the 1DGF approach and Reference EGFs

Here, we compare the reference EGFs with those obtained from the numerical method (1DGF), computed using the 1D velocity model in the frequency range 0.3-1.0 Hz, at the corresponding subfault to each reference EGF (Figure 5.6). As in the previous comparison, we use cross-correlation and peak ratio to quantify the agreement between the two Green's function approaches. Overall, the cross-correlation values are high, indicating strong waveform similarity between the 1DGF approach and the reference EGFs. However, the amplitudes predicted by 1DGFs are systematically higher than those of the reference EGFs.

One possible explanation for this discrepancy is the limitation of the adopted 1D velocity model in accurately representing wave propagation in the study region. In addition, even within the considered frequency band, wave propagation can be influenced by small-scale 3D heterogeneities and local site effects (Aki & Richards, 2002), which are not captured by a 1D model. As a result, the theoretical Green's functions may not fully reproduce the observed amplitudes.

Moreover, although uncertainties in seismic moment of the reference events could, in principle, introduce amplitude differences, this explanation is unlikely here. The observed discrepancies are consistent across all stations and reference events, suggesting a systematic bias rather than event-specific uncertainties. Therefore, the amplitude differences are more plausibly attributed to limitations in the velocity model and its inability to fully capture the complexity of wave propagation in the region.

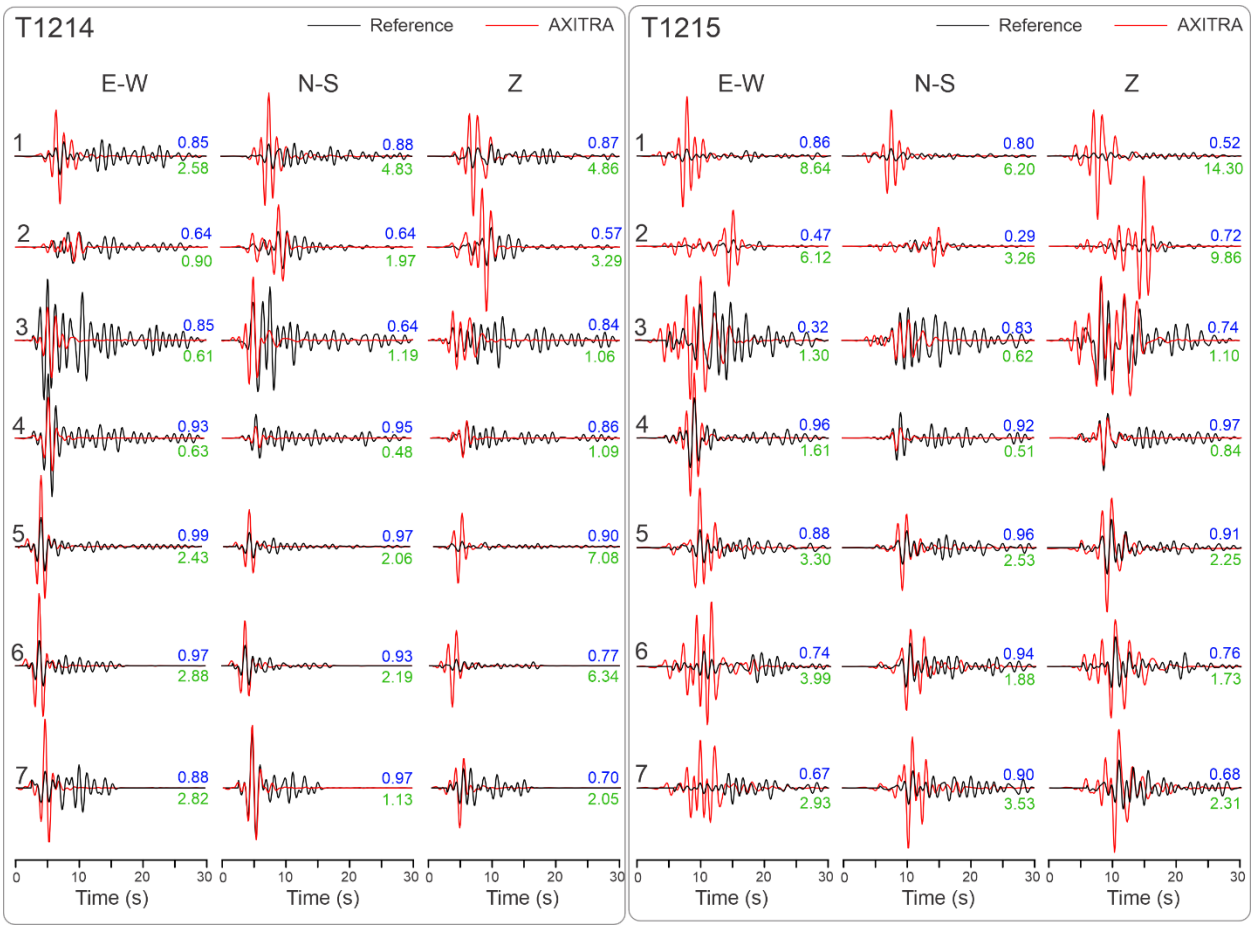

Figure 5.6. Comparison of Green's functions obtained from 1DGF (red) with the reference EGFs (black) for the seven cases shown in Figure 5.5a, at stations T1214 (left panel) and T1215 (right panel). The blue and green numbers show the cross-correlation between the two waveforms and the peak amplitude ratio between the 1DGFs and the reference EGFs, respectively.

To further compare the CEGF and 1DGF approaches to the reference EGFs, we consider all stations with available clusters and all reference events. The results are summarized in Figure 5.7.

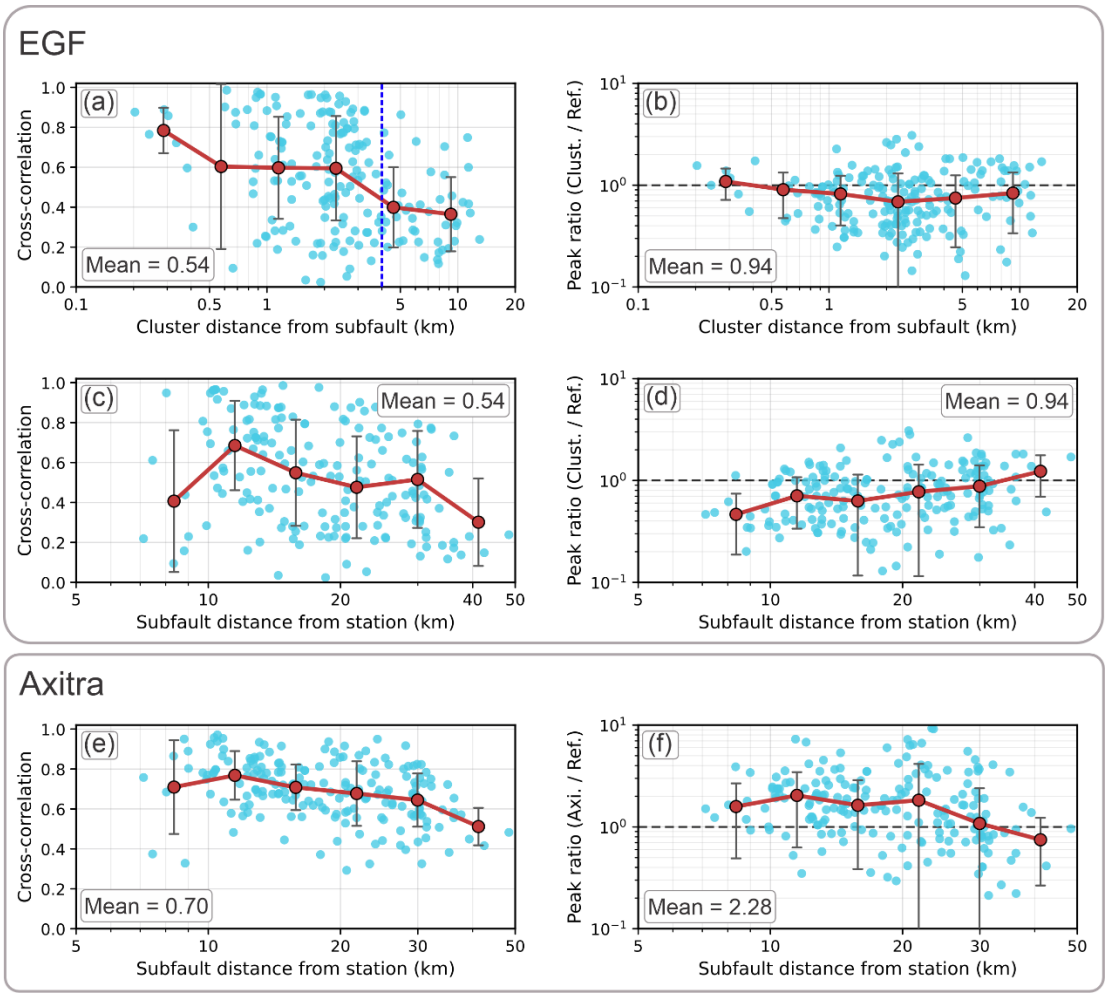

Figure 5.7. Comparison of cross-correlation and peak ratio of C EGFs, Green's functions obtained from 1DGF, and reference EGFs across all possible reference events and stations. **(a)** Cross-correlation between CEGFs and reference EGFs as a function of cluster-subfault distance. The vertical blue dashed line marks the selected threshold distance between cluster and subfault, **(b)** peak ratio of the C EGFs to the reference EGFs as a function of cluster-subfault distance, **(c)** same as (a) but as a function of subfault-station distance, **(d)** same as (b) but as a function of subfault-station distance, **(e)** cross-correlation between Green's functions obtained from 1DGF and the reference EGFs as a function of subfault-station distance, (f) peak ratio of the Green's functions obtained from 1DGFs to the reference EGFs as a function of subfault-station distance. Orange lines with circles represent binned averages, and black vertical lines indicate the corresponding standard deviations within each bin. Each blue circle shows the mean value of the three components.

Figures 5.7a and 5.7b present the cross-correlation and peak amplitude ratio between the CEGF approach and the reference EGFs as a function of the distance between the cluster centroid and the subfault hosting each reference EGF. The cross-correlation, with an overall mean value of 0.54, decreases gradually with increasing distance from the subfault. Based on this trend, we restrict the selection to clusters located within 4 km of the subfaults, corresponding to cross-correlation values greater than 0.4. Only these clusters are considered for computing the final set of Green's functions. For the remaining subfaults, the nearest single event is selected. The peak amplitude ratio yields values close to 1, with an overall mean of 0.94, indicating that, the amplitudes of the CEGFs are generally consistent with those of the reference EGFs. Figures 5.7c and 5.7d show the same metrics as a function of the distance between the subfaults and the stations. The cross-correlation decreases with increasing subfault-station distance. The peak amplitude ratio indicates that the amplitudes of the CEGFs are slightly lower than those of the reference EGFs for subfaults located within 10 km of the stations, while for larger distances the ratio remains close to 1.

Figures 5.7e and 5.7f present the cross-correlation and peak amplitude ratio between the 1DGFs and the reference EGFs as a function of the distance between the subfaults and the stations. The cross-correlation between the 1DGFs and the reference EGFs is relatively high, with a mean of 0.7, and is generally higher than that obtained for the CEGFs. As expected, the cross-correlation decreases gradually with increasing subfault-station distance. However, the peak amplitude ratio, with a mean value of 2.28, is significantly higher than that of the CEGFs, particularly for subfault-station distances shorter than 30 km, indicating a systematic overestimation of amplitudes by the 1DGFs.

5.4.3. Impact of Uncertainty in Source Parameters on Deconvolved EGFs

To further investigate the effect of uncertainty in seismic moment on the obtained EGF, we compare the deconvolved waveforms of two selected events using

seismic moment estimates obtained from Chapter 2, as well as from K21 and B24. These events have corner frequencies larger than 1Hz, so that the deconvolution process depends only on seismic moment. Figure 5.8 shows the comparison between the obtained EGFs, while Table 5.1 summarizes the characteristics of the two events used in the comparison. As expected, differences in seismic moment significantly affect the amplitude of the EGFs. For example, the comparison between EGFs computed using the seismic moment estimates from this study and those from B24 (Figure 5.8b, lower panel) highlights substantial amplitude differences. As discussed in Chapter 2 and shown in Figure A2.2, the B24 catalog systematically underestimates moment magnitude relative to this study and K21; consequently, EGFs derived from B24 exhibit higher amplitudes. The mean seismic moments across all events for this study, K21, and B24 are 4.85e14, 4.21e14, and 3.46e14 Nm, respectively. While the values from this study and K21 are comparable, both differ from those of B24. As discussed in Chapter 2, these differences primarily arise from the assumption in B24 of a time-independent quality factor. This highlights the importance of accounting for the temporal variability of medium properties when estimating source parameters of small events within a seismic sequence, and consequently for the robust application of EGFs.

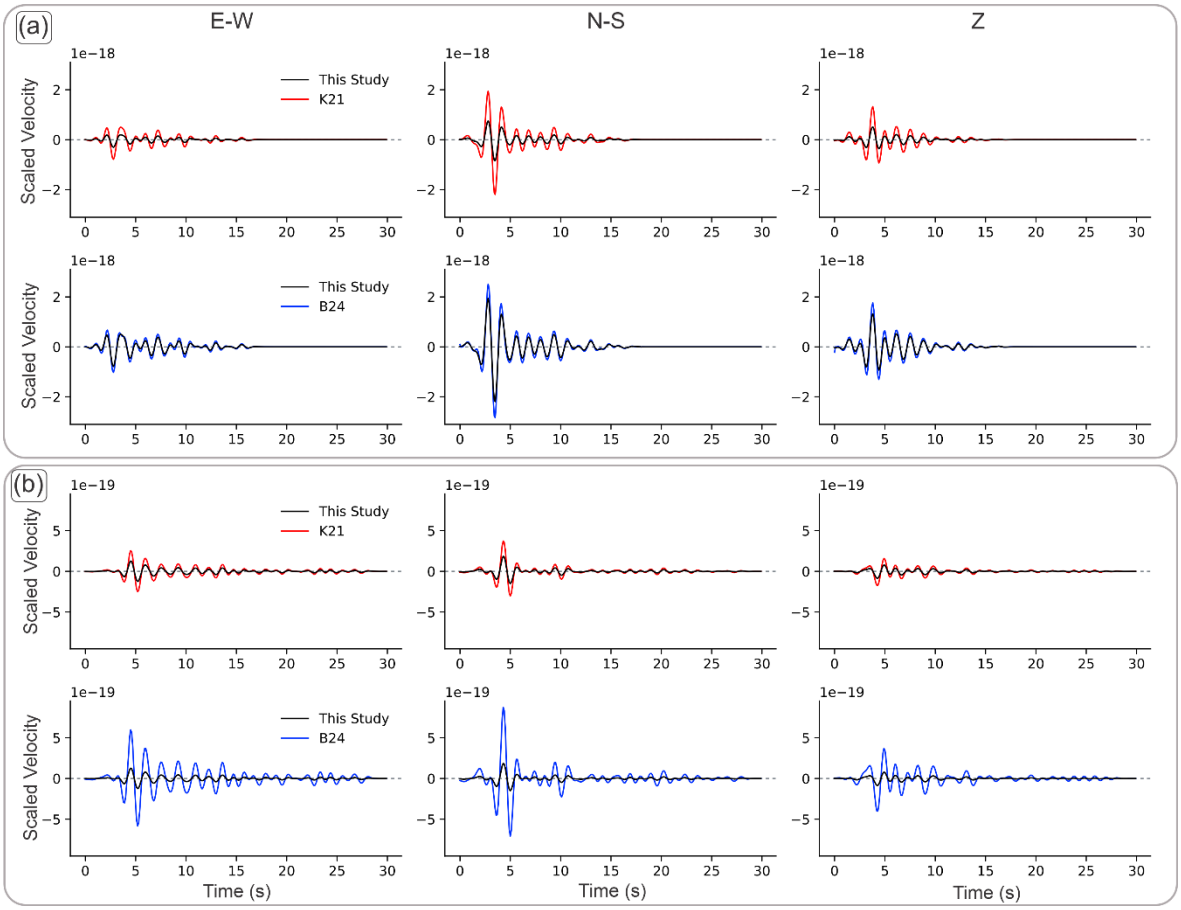

Figure 5.8. Comparison of cluster-derived EGFs (CEGFs) deconvolved using seismic moment estimates from this study (black), K21 (red), and B24 (blue). **(a)** Comparison for Event 1; **(b)** comparison for Event 2. The corresponding seismic parameters for each event are summarized in Table 5.1.

Table 5.1. Comparison of seismic moment, moment magnitude, and corner frequency of the two selected events across the three datasets.

Seismic Parameters	Event 1 (Figure 5.8a)	Event 2 (Figure 5.8b)	Dataset
Seismic Moment (Nm)	3.35e14	1.43e15	This Study
	8.65e14	7.10e14	K21
	4e14	3.03e14	B24
Moment Magnitude	3.65	4.06	This Study
	3.92	3.86	K21
	3.66	3.59	B24
Corner Frequency (Hz)	1.84	2.67	This Study
	2.28	3.27	K21
	1.06	2.18	B24

5.5. Conclusion and Discussion

This chapter evaluates the performance of the proposed method for computing Empirical Green's Functions by grouping events with similar waveforms into clusters (CEGFs). Within each cluster, the waveforms are aligned to maximize cross-correlation and then averaged to obtain the final EGF. In the context of a finite-fault model, each EGF is assigned to the nearest subfault. To assess the reliability of the CEGFs, we compare them with reference events that have focal mechanisms similar to that of the Norcia mainshock and are located close to the defined fault plane.

One of the main findings is that the waveform similarity does not necessarily imply similarity in focal mechanisms. The clustering analysis shows that events with a wide range of Kagan angles can still produce highly correlated waveforms within the selected frequency band (0.3-1.0 Hz). This indicates that, at these frequencies, waveform similarity is primarily controlled by propagation effects and source-receiver geometry rather than detailed source radiation patterns. The use of

clustering for EGF computation may imply that the resulting EGFs may average over heterogeneous source mechanisms, potentially smoothing source-related variability.

The comparison with reference EGFs reveals that CEGFs generally reproduce waveform shapes and amplitude well, with peak amplitude ratios close to unity and acceptable cross-correlation levels. However, the observed decrease in cross-correlation with increasing cluster-subfault distance highlights the importance of spatial proximity when assigning EGFs. The adopted 4 km threshold represents a reasonable trade-off between data availability and the similarity of waveforms between CEGFs and the references. However, it also introduces spatial limitations in regions with sparse seismicity. The intermediate cross-correlation values between the CEGFs and the reference EGFs may be attributed to time stretching and/or compression of the CEGFs. For example, in the E-W and N-S components of case 5 at station T1215 (Figure 5.4c), the two waveforms show good agreement for durations shorter than 12 seconds. Beyond this point, however, the CEGF appears to be stretched over a time window of approximately 5 seconds, while largely keeping its overall shape and amplitude. Such time distortions may occur multiple times within a single waveform, leading to a decrease in the overall cross-correlation. In the CEGF approach, the averaged waveforms are simply time-shifted to the positions of the corresponding subfaults, without applying any correction to their waveform shape. However, changes in source location can alter propagation effects and rupture characteristics, which are reflected in the waveform shape. The absence of such corrections may therefore contribute to the observed mismatches between the CEGFs and reference EGFs.

In contrast to the CEGFs, the numerical Green's functions (1DGFs) computed using a 1D velocity model systematically overestimate amplitude, despite showing relatively high waveforms cross-correlation with respect to the reference EGFs. This systematic bias may reflect the inability of the 1D model to capture the possible strong lateral heterogeneity and geological complexity in the region. Also, this discrepancy may be attributed to uncertainties in seismic moment estimations, which

directly affect amplitude scaling and may introduce biases in the comparison between theoretical and empirical Green's functions.

Overall, these results show that both the CEGFs and the 1DGFs have strengths and limitations. Empirical methods naturally include path and site effects, while numerical methods rely on a physical model of wave propagation. However, the numerical Green's functions computed using a 1D velocity model may not be reliable at higher frequencies, especially in regions with strong structural heterogeneity. On the other hand, using more realistic 3D velocity models can improve accuracy, but they are computationally expensive and often impractical for iterative source inversion. Given the uncertainties associated with both approaches, it is not possible to definitively determine which method better captures path propagation effects. Instead, using both methods in source inversion may provide more reliable results and help better understand the trade-offs between source and Green's functions.

Appendix 5

Table A5.1. List of stations used in computing the Empirical Green's Functions

Station Name	Number of Recordings	Group
ACC	19	G2
ACT	18	G2
CIT	14	G2
CLF	16	G2
CLO	11	G2
CNE	10	G2
CSC	16	G2
FCC	11	G2
FOC	23	G2
FOS	17	G2
LSS	22	G2
MCV	18	G2
MMO	15	G2
MNF	22	G2
MZ04	104	G1
MZ08	200	G1
MZ14	112	G1
MZ19	170	G1
MZ24	245	G1
MZ27	170	G1
NRC	23	G2
PCB	17	G2
PRE	16	G2
SNO	18	G2
T1201	325	G1
T1212	425	G1
T1213	271	G1
T1214	601	G1
T1215	227	G1
T1216	311	G1
T1217	122	G1
T1219	157	G1
T1220	193	G1
T1244	361	G1
T1256	174	G1

Conclusion

Despite significant advances in seismic hazard assessment and earthquake engineering, a major challenge remains in accurately characterizing and predicting ground-motion variability during seismic sequences. Ground Motion Models (GMMs), which form the backbone of Probabilistic Seismic Hazard Assessment (PSHA), typically rely on simplified assumptions and are primarily calibrated using datasets dominated by mainshock recordings, without explicitly accounting for the strong spatial and temporal variability associated with aftershocks. This variability, controlled by the complexity of source and path effects, can significantly influence ground-motion estimates, particularly in near-field regions. To further understand the physical processes controlling ground-motion variability, it is essential to investigate the earthquake source itself. Source modeling provides a framework to characterize the rupture process, including the spatial and temporal evolution of slip and rupture velocity, which directly influence the generated ground-motion. Reliable source models are particularly important in near-field regions, where rupture complexity plays an important role. However, the accuracy of source inversion strongly depends on the quality of the Green's Functions used to represent wave propagation. In this context, Empirical Green's Functions (EGFs) offer a practical alternative, as they naturally incorporate path and site effects without relying on simplified velocity models. Therefore, developing reliable methods to compute EGFs is a key step toward improving source modeling and, ultimately, toward better understanding the origin of ground-motion variability.

In this thesis, these challenges are investigated using a large dataset from the 2016-2017 Central Italy seismic sequence. The main findings are summarized in the following:

First, we investigated the behavior of parametric and non-parametric ground-motion models with the aim of improving the understanding of spatial and temporal

variability in ground motion. The results highlight fundamental limitations of parametric GMMs, particularly their reliance on linear functional forms in magnitude and distance, which may not adequately represent complex earthquake processes in hazard-relevant scenarios. In contrast, non-parametric Random Forest mixed-effects models demonstrate a strong ability to capture nonlinear dependencies in the data, leading to a significant reduction in ground-motion variability. This reduction is primarily associated with the ability of these models to account for stress-drop and quality factor variabilities through their dependence on hypocentral location. Our findings show that the influence of these properties is strongly frequency-dependent and decreases with increasing distance, challenging common assumptions in current parametric formulations. While non-parametric models are not directly applicable to PSHA due to their limited extrapolation capability, they provide valuable insight into underlying earthquake physics that can inform the development of improved parametric models.

Second, we investigated the origin of temporal variability in high-frequency ground-motion during the sequence. The results show that both stress-drop and event-specific quality factor exhibit strong temporal variations, particularly in the first days following the mainshocks, significantly influencing ground-motion estimates. These variations complicate the interpretation of between-event residuals, which cannot be considered as reliable proxies for stress-drop immediately after mainshocks because it absorbs the variability in stress-drop and quality factor. We further demonstrate that part of the observed temporal variability in ground-motion is linked to spatial changes in seismicity, such as migration toward shallower depths, rather than to intrinsic transient changes in stress-drop or medium properties. However, a significant part of the short-term variations (for ~40-50%) following the Amatrice earthquake can be attributed to transient, localized changes in the medium and stress-drop, likely associated with fluid and/or damage-related processes. not observed after mainshocks.

Third, we developed a Bayesian kinematic source inversion framework based on a Parallel Tempering Markov Chain Monte Carlo (PTMCMC) sampler. Instead of discretizing the fault into a dense grid of subfaults, we adopted a control-point representation, in which a limited number of points constrain the spatial and temporal evolution of the rupture. This approach significantly reduces the model dimensionality while preserving the ability to capture the key features of the rupture process. The framework successfully reproduces the rupture complexity of a benchmark model derived from a dynamic rupture simulation. It was then applied to the Norcia mainshock, the largest event of the 2016-2017 Central Italy seismic sequence. The resulting slip distribution is generally consistent with that obtained by Scognamiglio et al. (2018) for a single fault-plane geometry. However, the model shows a lower waveform fit, with a variance reduction of 0.61 compared to their results. This difference may be attributed to the fact that rake angle is not inverted in our framework and is assumed to be constant over the fault plane.

Finally, we evaluated a clustering-based approach for computing Empirical Green's Functions (CEGFs), in which events with similar waveforms are grouped into clusters and averaged to obtain EGFs in the frequency band 0.3-1.0 Hz. One important outcome of this clustering is that, although the grouped waveforms are highly similar, the corresponding events may exhibit different focal mechanisms. The comparison between cluster-derived EGFs and reference EGFs shows that waveform shapes and amplitudes are generally fairly well reproduced, while also highlighting the importance of spatial proximity when assigning EGFs to subfaults. In contrast, the comparison between numerical Green's functions computed using a 1D velocity model and the reference EGFs shows that, although waveform similarity is relatively well captured, amplitudes are systematically overestimated, reflecting limitations in representing structural heterogeneity. In addition, uncertainties in seismic moment estimation during the deconvolution process may affect amplitude scaling and contribute to the observed discrepancies.

Perspectives

In the following, the main perspectives and possible extensions of this thesis are presented:

1. Toward Next-Generation GMPEs: Embedding Spatial and Temporal Variability

The developed non-parametric models show that spatial and temporal variability in ground motion can be effectively captured. However, a major limitation of non-parametric models is that they cannot be directly applied in probabilistic seismic hazard analysis (PSHA), because they are unable to extrapolate beyond the range of data used for training. For this reason, it may be valuable for GMPE developers to incorporate X, Y, Z, and T into parametric GMPMs. Doing so could help reduce ground-motion variability and improve applications in seismic hazard and risk assessment.

2. Toward 4D Fault-Zone Imaging: Linking Stress-Drop to Rupture and Healing Processes

The limited number of events analyzed in this study prevents the robust application of non-parametric GMMs to predict stress-drop as a function of magnitude (M), spatial location (X, Y), depth (Z), and time (T), primarily due to overfitting. Extending this approach to larger earthquake catalogs, such as those compiled by Kemna et al. (2021) and Bindi et al. (2024) for the 2016-2017 Central Italy sequence, or Trugman and Shearer (2018) for the 2019 Ridgecrest sequence, would provide sufficient data density to exploit the full potential of non-parametric methods. With an adequately large dataset, such models could resolve spatial and temporal variations in stress drop in four dimensions (X, Y, Z, T), enabling the creation of a 4D map of fault-zone properties. This, in turn, could offer new insights into the structure and evolution of damage zones, including their relationship to rupture processes and post-mainshock healing.

3. Residual-Based Analysis of Frequency-Dependent Radiation in Small Earthquakes

The left-over residual (Section 2.3.3) can be used to investigate the frequency-dependent radiation pattern of individual small events. The results can then be compared with previous studies that have examined the directivity of small earthquakes in central Italy using both empirical and theoretical approaches.

4. Toward High-Frequency Earthquake Source Imaging: From Empirical Green's Functions to Envelope-Based Inversion

Empirical Green's Functions are useful for imaging the source rupture process of earthquakes at higher frequencies, which reveals more detail about the rupture. In this thesis, we developed an approach to compute EGFs using a large dataset in the frequency range of 0.3 to 1 Hz. These EGFs can be used in earthquake source inversion to image the rupture process within this frequency range.

It may be possible to image the earthquake source rupture process up to frequencies of about 10 Hz or even higher. However, at high frequencies, seismic waveforms exhibit rapid phase variations, making them highly sensitive to small timing errors; even slight mismatches can lead to large discrepancies between observed and synthetic signals. To mitigate this, one can invert the envelope of the seismograms instead of the full waveforms, as the envelope smooths out these rapid phase variations and captures the energy of the signal while being largely insensitive to phase errors. This approach reduces the impact of timing uncertainties and makes the inversion more stable.

5. Toward the Application of Machine Learning for Empirical Green's Function Interpolation

In the case of a large and high-quality dataset, machine learning (ML) techniques can be applied to interpolate EGFs directly on subfaults. The model can be trained using a suitable number of deconvolved small events distributed around the fault plane. This model can be applied to both waveforms in lower frequency

ranges (< 1 Hz) and to the envelope of seismograms at higher frequency ranges. One advantage of machine learning models is that they can both time-shift and modify the shape of waveforms, whereas in our clustering approach, the EGFs are only time-shifted without changing the waveform shape. As a preliminary test, we applied an ML model to reproduce the EGFs of some reference events by training the model using our dataset. Some of the initial results are promising, as illustrated in Figure P1; however, further development and validation are required before this approach can be fully implemented.

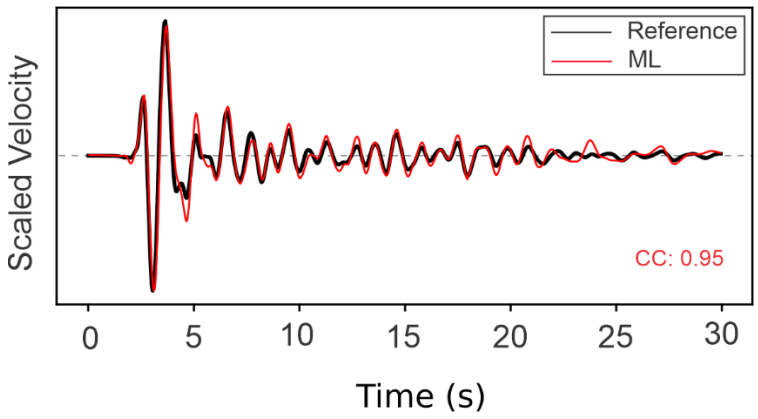

Figure P1. Reproducing the EGF of a reference event (black) using an ML technique (red).

6. Toward Improving the KiNPtPy Code: Practical Extensions and Future Enhancements

The following strategies can be implemented to improve the developed kinematic inversion code (KiNPtPy):

1. The code does not account for the inversion of rake angle and peak time of the Yoffe function for modeling the source time function. Therefore, adding these two parameters to the inversion process may allow for more realistic waveform inversion.

2. In addition to inverting waveforms, the code can be extended to invert Apparent Source Time Functions (ASTFs) extracted using empirical Green's functions, providing complementary constraints on rupture duration, directivity, and rupture velocity.

3. The code can be further improved by enabling the joint inversion of strong-motion and GPS data.

Bibliography

Abercrombie, R. E. (1995). Earthquake source scaling relationships from −1 to 5 M_L using seismograms recorded at 2.5-km depth. *Journal of Geophysical Research: Solid Earth*, *100*(B12), 24015–24036. https://doi.org/10.1029/95JB02397

Abercrombie, R. E. (2021). Resolution and uncertainties in estimates of earthquake stress drop and energy release. *Philosophical Transactions of the Royal Society A: Mathematical, Physical and Engineering Sciences*, *379*(2196), 20200131. https://doi.org/10.1098/rsta.2020.0131

Abercrombie, R. E., & Baltay, A. S. (2025). Magnitude, Depth, and Methodological Variations of Spectral Stress Drop Within the SCEC/USGS Community Stress Drop Validation Study Using the 2019 Ridgecrest Earthquake Sequence. *Bulletin of the Seismological Society of America*, *115*(6), 2741–2768. https://doi.org/10.1785/0120250056

Abercrombie, R. E., Bannister, S., Ristau, J., & Doser, D. (2017). Variability of earthquake stress drop in a subduction setting, the Hikurangi Margin, New Zealand. *Geophysical Journal International*, *208*(1), 306–320. https://doi.org/10.1093/gji/ggw393

Abercrombie, R. E., Trugman, D. T., Shearer, P. M., Chen, X., Zhang, J., Pennington, C. N., et al. (2021). Does Earthquake Stress Drop Increase With Depth in the Crust? *Journal of Geophysical Research: Solid Earth*, *126*(10), e2021JB022314. https://doi.org/10.1029/2021JB022314

Abrahamson, N., Gregor, N., & Addo, K. (2016). BC Hydro Ground Motion Prediction Equations for Subduction Earthquakes. *Earthquake Spectra*, *32*(1), 23–44. https://doi.org/10.1193/051712EQS188MR

Abrahamson, N. A., Silva, W. J., & Kamai, R. (2014). Summary of the ASK14 Ground Motion Relation for Active Crustal Regions. *Earthquake Spectra*, *30*(3), 1025–1055. https://doi.org/10.1193/070913EQS198M

Aguirre, J., & Irikura, K. (1997). Nonlinearity, liquefaction, and velocity variation of soft soil layers in Port Island, Kobe, during the Hyogo-ken Nanbu earthquake. *Bulletin of the Seismological Society of America*, *87*(5), 1244–1258. https://doi.org/10.1785/BSSA0870051244

Aki, K. (1966, July 25). Generation and Propagation of G Waves from the Niigata Earthquake of June 16, 1964. : Part 2. Estimation of earthquake moment, released energy, and stress-strain drop from the G wave spectrum. **東京大学地震研究所**. https://doi.org/10.15083/0000033586

Aki, K. (1967). Scaling law of seismic spectrum. *Journal of Geophysical Research (1896-1977)*, *72*(4), 1217–1231. https://doi.org/10.1029/JZ072i004p01217

Aki, K. (1980). Attenuation of shear-waves in the lithosphere for frequencies from 0.05 to 25 Hz. *Physics of the Earth and Planetary Interiors*, *21*(1), 50–60. https://doi.org/10.1016/0031-9201(80)90019-9

Aki, K., & Chouet, B. (1975). Origin of coda waves: Source, attenuation, and scattering effects. *Journal of Geophysical Research*, *80*(23), 3322–3342. https://doi.org/10.1029/JB080i023p03322

Aki, K., & Richards, P. G. (2002). *Quantitative seismology* (2nd ed). Sausalito, Calif: University Science Books.

Akinci, A., Munafò, I., & Malagnini, L. (2022). S-Wave Attenuation Variation and its Impact on Ground Motion Amplitudes During 2016–2017 Central Italy Earthquake Sequence. *Frontiers in Earth Science*, *10*, 903955. https://doi.org/10.3389/feart.2022.903955

Al Atik, L. A., Abrahamson, N., Bommer, J. J., Scherbaum, F., Cotton, F., & Kuehn, N. (2010). The Variability of Ground-Motion Prediction Models and Its Components. *Seismological Research Letters*, *81*(5), 794–801. https://doi.org/10.1785/gssrl.81.5.794

Alesssandrini, B., Filippi, L., & Borgia, A. (2001). Upper-crust tomographic structure of the Central Apennines, Italy, from local earthquakes. *Tectonophysics*, *339*(3–4), 479–494. https://doi.org/10.1016/S0040-1951(01)00140-8

Alidadi, N., & Pezeshk, S. (2024). Ground-Motion Model for Small-to-Moderate Potentially Induced Earthquakes Using an Ensemble Machine Learning Approach for CENA. *Bulletin of the Seismological Society of America*, *114*(4), 2202–2215. https://doi.org/10.1785/0120230242

Allmann, B. P., & Shearer, P. M. (2007). Spatial and temporal stress drop variations in small earthquakes near Parkfield, California. *Journal of Geophysical Research: Solid Earth*, *112*(B4), 2006JB004395. https://doi.org/10.1029/2006JB004395

Allmann, B. P., & Shearer, P. M. (2009). Global variations of stress drop for moderate to large earthquakes. *Journal of Geophysical Research: Solid Earth*, *114*(B1), 2008JB005821. https://doi.org/10.1029/2008JB005821

Anderson, J. G., & Brune, J. N. (1999). Probabilistic Seismic Hazard Analysis without the Ergodic Assumption. *Seismological Research Letters*, *70*(1), 19–28. https://doi.org/10.1785/gssrl.70.1.19

Andrews, D. J. (2005). Rupture dynamics with energy loss outside the slip zone. *Journal of Geophysical Research: Solid Earth*, *110*(B1), 2004JB003191. https://doi.org/10.1029/2004JB003191

Archuleta, R. J. (1984). A faulting model for the 1979 Imperial Valley earthquake. *Journal of Geophysical Research: Solid Earth*, *89*(B6), 4559–4585. https://doi.org/10.1029/JB089iB06p04559

Atkinson, G. M., & Boore, D. M. (2006). Earthquake Ground-Motion Prediction Equations for Eastern North America. *Bulletin of the Seismological Society of America*, *96*(6), 2181–2205. https://doi.org/10.1785/0120050245

Atkinson, Gail M. (1990). A Comparison of Eastern North American ground Motion Observations with Theoretical Predictions. *Seismological Research Letters*, *61*(3–4), 171–180. https://doi.org/10.1785/gssrl.61.3-4.171

Atkinson, Gail M., & Silva, W. (1997). An empirical study of earthquake source spectra for California earthquakes. *Bulletin of the Seismological Society of America*, *87*(1), 97–113. https://doi.org/10.1785/BSSA0870010097

Baltay, A. S., & Hanks, T. C. (2014). Understanding the Magnitude Dependence of PGA and PGV in NGA-West 2 Data. *Bulletin of the Seismological Society of America*, *104*(6), 2851–2865. https://doi.org/10.1785/0120130283

Baltay, Annemarie S., Hanks, T. C., & Beroza, G. C. (2013). Stable Stress-Drop Measurements and their Variability: Implications for Ground-Motion Prediction. *Bulletin of the Seismological Society of America*, *103*(1), 211–222. https://doi.org/10.1785/0120120161

Baltay, Annemarie S., Hanks, T. C., & Abrahamson, N. A. (2019). Earthquake Stress Drop and Arias Intensity. *Journal of Geophysical Research: Solid Earth*, *124*(4), 3838–3852. https://doi.org/10.1029/2018JB016753

Barchi, M. R., Carboni, F., Michele, M., Ercoli, M., Giorgetti, C., Porreca, M., et al. (2021). The influence of subsurface geology on the distribution of earthquakes during the 2016-–2017 Central Italy seismic sequence. *Tectonophysics*, *807*, 228797. https://doi.org/10.1016/j.tecto.2021.228797

Bates, D., Mächler, M., Bolker, B., & Walker, S. (2015). Fitting Linear Mixed-Effects Models Using lme4. *Journal of Statistical Software*, *67*(1). https://doi.org/10.18637/jss.v067.i01

Bayless, J., & Abrahamson, N. A. (2019). Summary of the BA18 Ground-Motion Model for Fourier Amplitude Spectra for Crustal Earthquakes in California. *Bulletin of the Seismological Society of America*, *109*(5), 2088–2105. https://doi.org/10.1785/0120190077

Ben-Zion, Y., & Sammis, C. G. (2003). Characterization of Fault Zones. *Pure and Applied Geophysics*, *160*(3), 677–715. https://doi.org/10.1007/PL00012554

Beresnev, I. A., & Atkinson, G. M. (1997). Modeling finite-fault radiation from the ωn spectrum. *Bulletin of the Seismological Society of America*, *87*(1), 67–84. https://doi.org/10.1785/BSSA0870010067

Bernard, P., & Zollo, A. (1989). The Irpinia (Italy) 1980 earthquake: Detailed analysis of a complex normal faulting. *Journal of Geophysical Research: Solid Earth*, *94*(B2), 1631–1647. https://doi.org/10.1029/JB094iB02p01631

Bindi, D., & Kotha, S. R. (2020). Spectral decomposition of the Engineering Strong Motion (ESM) flat file: regional attenuation, source scaling and Arias stress drop. *Bulletin of Earthquake Engineering*, *18*(6), 2581–2606. https://doi.org/10.1007/s10518-020-00796-1

Bindi, D., Parolai, S., Grosser, H., Milkereit, C., & Durukal, E. (2007). Empirical ground-motion prediction equations for northwestern Turkey using the aftershocks of the 1999 Kocaeli earthquake. *Geophysical Research Letters*, *34*(8). https://doi.org/10.1029/2007GL029222

Bindi, D., Kotha, S.-R., Weatherill, G., Lanzano, G., Luzi, L., & Cotton, F. (2019). The pan-European engineering strong motion (ESM) flatfile: consistency check via residual analysis. *Bulletin of Earthquake Engineering*, *17*(2), 583–602. https://doi.org/10.1007/s10518-018-0466-x

Bindi, Dino, Cotton, F., Spallarossa, D., Picozzi, M., & Rivalta, E. (2018). Temporal Variability of Ground Shaking and Stress Drop in Central Italy: A Hint for

Fault Healing? *Bulletin of the Seismological Society of America*, *108*(4), 1853–1863. https://doi.org/10.1785/0120180078

Bindi, Dino, Spallarossa, D., Picozzi, M., & Morasca, P. (2020). Reliability of Source Parameters for Small Events in Central Italy: Insights from Spectral Decomposition Analysis Applied to Both Synthetic and Real Data. *Bulletin of the Seismological Society of America*, *110*(6), 3139–3157. https://doi.org/10.1785/0120200126

Bindi, Dino, Spallarossa, D., Picozzi, M., & Tarchini, G. (2024). Scaling and Depth Variability of Source Parameters in Central and Southern Italy Using Regional Attenuation Models. *Bulletin of the Seismological Society of America*, *115*(3), 983–999. https://doi.org/10.1785/0120240144

Bindi, Dino, Oth, A., Parolai, S., Picozzi, M., & Spallarossa, D. (2025). Interevent Variability in Ground-Motion Prediction Models: The Role of the Source Parameter Selection. *Bulletin of the Seismological Society of America*, *115*(6), 2857–2866. https://doi.org/10.1785/0120250098

Bishop, C. M. (2006). *Pattern recognition and machine learning*. New York: Springer.

Bizzarri, A. (2012). Analytical representation of the fault slip velocity from spontaneous dynamic earthquake models. *Journal of Geophysical Research: Solid Earth*, *117*(B6). https://doi.org/10.1029/2011JB009097

Boatwright, J., & Boore, D. M. (1982). Analysis of the ground accelerations radiated by the 1980 Livermore Valley earthquakes for directivity and dynamic source

characteristics. *Bulletin of the Seismological Society of America*, *72*(6A), 1843–1865. https://doi.org/10.1785/BSSA07206A1843

Boatwright, J., & Cocco, M. (1996). Frictional constraints on crustal faulting. *Journal of Geophysical Research: Solid Earth*, *101*(B6), 13895–13909. https://doi.org/10.1029/96JB00405

Bommer, J. J., & Abrahamson, N. A. (2006). Why Do Modern Probabilistic Seismic-Hazard Analyses Often Lead to Increased Hazard Estimates? *Bulletin of the Seismological Society of America*, *96*(6), 1967–1977. https://doi.org/10.1785/0120060043

Bonilla, L. F., Guéguen, P., & Ben-Zion, Y. (2019). Monitoring Coseismic Temporal Changes of Shallow Material during Strong Ground Motion with Interferometry and Autocorrelation. *Bulletin of the Seismological Society of America*, *109*(1), 187–198. https://doi.org/10.1785/0120180092

Boore, D. M. (2003). Simulation of Ground Motion Using the Stochastic Method. *Pure and Applied Geophysics*, *160*(3), 635–676. https://doi.org/10.1007/PL00012553

Boore, D. M., Skarlatoudis, A. A., Margaris, B. N., Papazachos, C. B., & Ventouzi, C. (2009). Along-Arc and Back-Arc Attenuation, Site Response, and Source Spectrum for the Intermediate-Depth 8 January 2006 M 6.7 Kythera, Greece, Earthquake. *Bulletin of the Seismological Society of America*, *99*(4), 2410–2434. https://doi.org/10.1785/0120080229

Boore, David M. (1983). Stochastic simulation of high-frequency ground motions based on seismological models of the radiated spectra. *Bulletin of the*

Seismological Society of America, *73*(6A), 1865–1894. https://doi.org/10.1785/BSSA07306A1865

Boore, David M., & Atkinson, G. M. (1987). Stochastic prediction of ground motion and spectral response parameters at hard-rock sites in eastern North America. *Bulletin of the Seismological Society of America*, *77*(2), 440–467. https://doi.org/10.1785/BSSA0770020440

Boore, David M., & Atkinson, G. M. (1989). Spectral scaling of the 1985 to 1988 Nahanni, Northwest Territories, earthquakes. *Bulletin of the Seismological Society of America*, *79*(6), 1736–1761. https://doi.org/10.1785/BSSA0790061736

Boore, David M., & Atkinson, G. M. (2008). Ground-Motion Prediction Equations for the Average Horizontal Component of PGA, PGV, and 5%-Damped PSA at Spectral Periods between 0.01 *s* and 10.0 *s*. *Earthquake Spectra*, *24*(1), 99–138. https://doi.org/10.1193/1.2830434

Boore, David M., Stewart, J. P., Seyhan, E., & Atkinson, G. M. (2014). NGA-West2 Equations for Predicting PGA, PGV, and 5% Damped PSA for Shallow Crustal Earthquakes. *Earthquake Spectra*, *30*(3), 1057–1085. https://doi.org/10.1193/070113EQS184M

Bouchon, M. (1981a). A simple method to calculate Green's functions for elastic layered media. *Bulletin of the Seismological Society of America*, *71*(4), 959–971. https://doi.org/10.1785/BSSA0710040959

Bouchon, M. (1981b). A simple method to calculate Green's functions for elastic layered media. *Bulletin of the Seismological Society of America*, *71*(4), 959–971. https://doi.org/10.1785/BSSA0710040959

Bouchon, M., Toksöz, M. N., Karabulut, H., Bouin, M.-P., Dietrich, M., Aktar, M., & Edie, M. (2002). Space and Time Evolution of Rupture and Faulting during the 1999 İzmit (Turkey) Earthquake. *Bulletin of the Seismological Society of America*, *92*(1), 256–266. https://doi.org/10.1785/0120000845

Breiman, L. (2001). Random Forests. *Machine Learning*, *45*(1), 5–32. https://doi.org/10.1023/A:1010933404324

Brown, M. R. M., & Ge, S. (2018). Distinguishing Fluid Flow Path from Pore Pressure Diffusion for Induced Seismicity. *Bulletin of the Seismological Society of America*, *108*(6), 3684–3686. https://doi.org/10.1785/0120180149

Brune, J. N. (1970). Tectonic stress and the spectra of seismic shear waves from earthquakes. *Journal of Geophysical Research*, *75*(26), 4997–5009. https://doi.org/10.1029/JB075i026p04997

Brunelli, G., Lanzano, G., Sgobba, S., & Luzi, L. (2023). Spatial variability of non-ergodic GMM residuals related to source and path effects in Italy. *Bull. Geoph. Ocean*, *64*, 417–432.

Calderoni, G., & Abercrombie, R. E. (2023). Investigating Spectral Estimates of Stress Drop for Small to Moderate Earthquakes With Heterogeneous Slip Distribution: Examples From the 2016–2017 Amatrice Earthquake Sequence.

Journal of Geophysical Research: Solid Earth, *128*(6), e2022JB025022. https://doi.org/10.1029/2022JB025022

Campbell, K. W., & Bozorgnia, Y. (2008). NGA Ground Motion Model for the Geometric Mean Horizontal Component of PGA, PGV, PGD and 5% Damped Linear Elastic Response Spectra for Periods Ranging from 0.01 to 10 s. *Earthquake Spectra*, *24*(1), 139–171. https://doi.org/10.1193/1.2857546

Campbell, K. W., & Bozorgnia, Y. (2014). NGA-West2 Ground Motion Model for the Average Horizontal Components of PGA, PGV, and 5% Damped Linear Acceleration Response Spectra. *Earthquake Spectra*, *30*(3), 1087–1115. https://doi.org/10.1193/062913EQS175M

Campbell, K. W., & Bozorgnia, Y. (2025). Empirical ground-motion models for horizontal Fourier amplitude spectra from fixed-effects and mixed-effects analyses of the NGA-West2 database. *Earthquake Spectra*, *41*(2), 1119–1150. https://doi.org/10.1177/87552930241312708

Caramenti, L., Menafoglio, A., Sgobba, S., & Lanzano, G. (2022). Multi-source geographically weighted regression for regionalized ground-motion models. *Spatial Statistics*, *47*, 100610. https://doi.org/10.1016/j.spasta.2022.100610

Castro, R. R., Franceschina, G., Pacor, F., Bindi, D., & Luzi, L. (2006). Analysis of the Frequency Dependence of the S-Wave Radiation Pattern from Local Earthquakes in Central Italy. *Bulletin of the Seismological Society of America*, *96*(2), 415–426. https://doi.org/10.1785/0120050066

Castro, R. R., Pacor, F., & Spallarossa, D. (2021). Depth-Dependent Shear-Wave Attenuation in Central Apennines, Italy. *Pure and Applied Geophysics*, *178*(6), 2059–2075. https://doi.org/10.1007/s00024-021-02744-9

Causse, M., & Song, S. G. (2015). Are stress drop and rupture velocity of earthquakes independent? Insight from observed ground motion variability. *Geophysical Research Letters*, *42*(18), 7383–7389. https://doi.org/10.1002/2015GL064793

Causse, M., Cultrera, G., Moreau, L., Herrero, A., Schiappapietra, E., & Courboulex, F. (2017). Bayesian rupture imaging in a complex medium: The 29 May 2012 Emilia, Northern Italy, earthquake. *Geophysical Research Letters*, *44*(15), 7783–7792. https://doi.org/10.1002/2017GL074698

Causse, M., Cornou, C., Maufroy, E., Grasso, J.-R., Baillet, L., & El Haber, E. (2021). Exceptional ground motion during the shallow Mw 4.9 2019 Le Teil earthquake, France. *Communications Earth & Environment*, *2*(1), 14. https://doi.org/10.1038/s43247-020-00089-0

Chaljub, E., Komatitsch, D., Vilotte, J.-P., Capdeville, Y., Valette, B., & Festa, G. (2007). Spectral-element analysis in seismology. In *Advances in Geophysics* (Vol. 48, pp. 365–419). Elsevier. https://doi.org/10.1016/S0065-2687(06)48007-9

Chen, X., & Shearer, P. M. (2011). Comprehensive analysis of earthquake source spectra and swarms in the Salton Trough, California. *Journal of Geophysical Research*, *116*(B9), B09309. https://doi.org/10.1029/2011JB008263

Chen, Xiaowei, & Shearer, P. M. (2013). California foreshock sequences suggest aseismic triggering process. *Geophysical Research Letters*, *40*(11), 2602–2607. https://doi.org/10.1002/grl.50444

Chiaraluce, L., Ellsworth, W. L., Chiarabba, C., & Cocco, M. (2003). Imaging the complexity of an active normal fault system: The 1997 Colfiorito (central Italy) case study. *Journal of Geophysical Research: Solid Earth*, *108*(B6), 2002JB002166. https://doi.org/10.1029/2002JB002166

Chiaraluce, L., Di Stefano, R., Tinti, E., Scognamiglio, L., Michele, M., Casarotti, E., et al. (2017). The 2016 Central Italy Seismic Sequence: A First Look at the Mainshocks, Aftershocks, and Source Models. *Seismological Research Letters*, *88*(3), 757–771. https://doi.org/10.1785/0220160221

Chiou, B., Darragh, R., Gregor, N., & Silva, W. (2008). NGA Project Strong-Motion Database. *Earthquake Spectra*, *24*(1), 23–44. https://doi.org/10.1193/1.2894831

Chu, S. X., Tsai, V. C., Trugman, D. T., & Hirth, G. (2021). Fault Interactions Enhance High-Frequency Earthquake Radiation. *Geophysical Research Letters*, *48*(20), e2021GL095271. https://doi.org/10.1029/2021GL095271

Colavitti, L., Lanzano, G., Sgobba, S., Pacor, F., & Gallovič, F. (2022). Empirical Evidence of Frequency-Dependent Directivity Effects From Small-To-Moderate Normal Fault Earthquakes in Central Italy. *Journal of Geophysical Research: Solid Earth*, *127*(6), e2021JB023498. https://doi.org/10.1029/2021JB023498

Colavitti, L., Lanzano, G., Sgobba, S., & Pacor, F. (2026). Empirical Modeling of Source Directivity Effects into a Ground-Motion Model for Central Italy. *Bulletin of the Seismological Society of America*. https://doi.org/10.1785/0120250200

Convertito, V., De Matteis, R., Improta, L., & Pino, N. A. (2020). Fluid-Triggered Aftershocks in an Anisotropic Hydraulic Conductivity Geological Complex: The Case of the 2016 Amatrice Sequence, Italy. *Frontiers in Earth Science*, *8*, 541323. https://doi.org/10.3389/feart.2020.541323

Cornell, C. A. (1968). Engineering seismic risk analysis. *Bulletin of the Seismological Society of America*, *58*(5), 1583–1606. https://doi.org/10.1785/BSSA0580051583

Cotton, F., & Campillo, M. (1995). Frequency domain inversion of strong motions: Application to the 1992 Landers earthquake. *Journal of Geophysical Research: Solid Earth*, *100*(B3), 3961–3975. https://doi.org/10.1029/94JB02121

Cotton, F., Archuleta, R., & Causse, M. (2013). What is Sigma of the Stress Drop? *Seismological Research Letters*, *84*(1), 42–48. https://doi.org/10.1785/0220120087

Cotton, Fabrice, & Coutant, O. (1997). Dynamic stress variations due to shear faults in a plane-layered medium. *Geophysical Journal International*, *128*(3), 676–688. https://doi.org/10.1111/j.1365-246X.1997.tb05328.x

Cultrera, G., Pacor, F., Franceschina, G., Emolo, A., & Cocco, M. (2009). Directivity effects for moderate-magnitude earthquakes (Mw 5.6–6.0) during the 1997

Umbria–Marche sequence, central Italy. *Tectonophysics*, *476*(1), 110–120. https://doi.org/10.1016/j.tecto.2008.09.022

Dawood, H. M., & Rodriguez-Marek, A. (2013). A Method for Including Path Effects in Ground-Motion Prediction Equations: An Example Using the Mw 9.0 Tohoku Earthquake Aftershocks. *Bulletin of the Seismological Society of America*, *103*(2B), 1360–1372. https://doi.org/10.1785/0120120125

Day, S. M., Yu, G., & Wald, D. J. (1998). Dynamic stress changes during earthquake rupture. *Bulletin of the Seismological Society of America*, *88*(2), 512–522. https://doi.org/10.1785/BSSA0880020512

De Gori, P., Michele, M., Chiaraluce, L., & Chiarabba, C. (2023). Fault Rheology Control on Rupture Propagation and Aftershocks Distribution during the 2016–2017 Central Italy Earthquakes. *Seismological Research Letters*, *94*(6), 2642–2654. https://doi.org/10.1785/0220220284

Di Luccio, F., Ventura, G., Di Giovambattista, R., Piscini, A., & Cinti, F. R. (2010). Normal faults and thrusts reactivated by deep fluids: The 6 April 2009 M_w 6.3 L'Aquila earthquake, central Italy. *Journal of Geophysical Research: Solid Earth*, *115*(B6), 2009JB007190. https://doi.org/10.1029/2009JB007190

Di Toro, G., Han, R., Hirose, T., De Paola, N., Nielsen, S., Mizoguchi, K., et al. (2011). Fault lubrication during earthquakes. *Nature*, *471*(7339), 494–498. https://doi.org/10.1038/nature09838

Dreger, D., Nadeau, R. M., & Chung, A. (2007). Repeating earthquake finite source models: Strong asperities revealed on the San Andreas Fault. *Geophysical*

Research Letters, *34*(23), 2007GL031353. https://doi.org/10.1029/2007GL031353

Drouet, S., Chevrot, S., Cotton, F., & Souriau, A. (2008). Simultaneous Inversion of Source Spectra, Attenuation Parameters, and Site Responses: Application to the Data of the French Accelerometric Network. *Bulletin of the Seismological Society of America*, *98*(1), 198–219. https://doi.org/10.1785/0120060215

Duputel, Z., Agram, P. S., Simons, M., Minson, S. E., & Beck, J. L. (2014). Accounting for prediction uncertainty when inferring subsurface fault slip. *Geophysical Journal International*, *197*(1), 464–482. https://doi.org/10.1093/gji/ggt517

Earl, D. J., & Deem, M. W. (2005). Parallel Tempering: Theory, Applications, and New Perspectives. *Physical Chemistry Chemical Physics*, *7*(23), 3910. https://doi.org/10.1039/B509983H

Ellis, J., & Van Haasteren, R. (2017, October 26). jellis18/PTMCMCSampler: Official Release (Version 1.0.0). Zenodo. https://doi.org/10.5281/ZENODO.1037579

Esfahani, R., Cotton, F., & Bonilla, L. F. (2024). Temporal variations of the ' *in-situ* ' nonlinear behaviour of shallow sediments during the 2016 Kumamoto Earthquake sequence. *Geophysical Journal International*, *238*(3), 1626–1637. https://doi.org/10.1093/gji/ggae222

Eshelby, J. D. (1957). The determination of the elastic field of an ellipsoidal inclusion, and related problems. *Proceedings of the Royal Society of London. Series A. Mathematical and Physical Sciences*, *241*(1226), 376–396. https://doi.org/10.1098/rspa.1957.0133

Falcioni, M., & Deem, M. W. (1998). A Biased Monte Carlo Scheme for Zeolite Structure Solution (Version 2). https://doi.org/10.48550/ARXIV.COND-MAT/9809085

Falcioni, M., & Deem, M. W. (1999). A biased Monte Carlo scheme for zeolite structure solution. *The Journal of Chemical Physics*, *110*(3), 1754–1766. https://doi.org/10.1063/1.477812

Fernandez-Delgado, M., Cernadas, E., Baro, S., & Amorim, D. (2014). Do we need hundreds of classifiers to solve real world classification problems? *J. Mach. Learn. Res*, *15*, 3133–3181.

Folesky, J., & Kummerow, J. (2025). Time-Dependent Stress Drop Variations After Large Earthquakes Along the North Chilean Megathrust. *Bulletin of the Seismological Society of America*, *115*(3), 1051–1061. https://doi.org/10.1785/0120240121

Fonzetti, R., Valoroso, L., De Gori, P., & Chiarabba, C. (2024). Localization of Deformation on Faults Driven by Fluids During the L'Aquila 2009 Earthquake. *Journal of Geophysical Research: Solid Earth*, *129*(8), e2024JB029075. https://doi.org/10.1029/2024JB029075

Fukushima, Y. (1996). Scaling relations for strong ground motion prediction models with *M* 2 terms. *Bulletin of the Seismological Society of America*, *86*(2), 329–336. https://doi.org/10.1785/BSSA0860020329

Gabrielli, S., Akinci, A., Ventura, G., Napolitano, F., Del Pezzo, E., & De Siena, L. (2022). Fast Changes in Seismic Attenuation of the Upper Crust due to

Fracturing and Fluid Migration: The 2016–2017 Central Italy Seismic Sequence. *Frontiers in Earth Science*, *10*, 909698. https://doi.org/10.3389/feart.2022.909698

Gabrielli, S., Akinci, A., De Siena, L., Del Pezzo, E., Buttinelli, M., Maesano, F. E., & Maffucci, R. (2023). Scattering Attenuation Images of the Control of Thrusts and Fluid Overpressure on the 2016–2017 Central Italy Seismic Sequence. *Geophysical Research Letters*, *50*(8), e2023GL103132. https://doi.org/10.1029/2023GL103132

Gabrielli, S., Akinci, A., & Del Pezzo, E. (2025). Temporal and spatial variability of S-wave and coda attenuation in the Central Apennines, Italy. *Frontiers in Earth Science*, *12*, 1487797. https://doi.org/10.3389/feart.2024.1487797

Gallovič, F., & Ampuero, J.-P. (2015). A New Strategy to Compare Inverted Rupture Models Exploiting the Eigenstructure of the Inverse Problem. *Seismological Research Letters*, *86*(6), 1679–1689. https://doi.org/10.1785/0220150096

Gallovič, František, Imperatori, W., & Mai, P. M. (2015). Effects of three-dimensional crustal structure and smoothing constraint on earthquake slip inversions: Case study of the *Mw* 6.3 2009 L'Aquila earthquake. *Journal of Geophysical Research: Solid Earth*, *120*(1), 428–449. https://doi.org/10.1002/2014JB011650

Geyer, C. J. (1991). Markov Chain Monte Carlo Maximum Likelihood. Retrieved from https://hdl.handle.net/11299/58440

Geyer, C. J., & Thompson, E. A. (1995). Annealing Markov Chain Monte Carlo with Applications to Ancestral Inference. *Journal of the American Statistical*

Association, *90*(431), 909–920. https://doi.org/10.1080/01621459.1995.10476590

Ghofrani, H., & Atkinson, G. M. (2011). Forearc versus Backarc Attenuation of Earthquake Ground Motion. *Bulletin of the Seismological Society of America*, *101*(6), 3032–3045. https://doi.org/10.1785/0120110067

Goebel, T. H. W., Hauksson, E., Shearer, P. M., & Ampuero, J. P. (2015). Stress-drop heterogeneity within tectonically complex regions: a case study of San Gorgonio Pass, southern California. *Geophysical Journal International*, *202*(1), 514–528. https://doi.org/10.1093/gji/ggv160

Goertz-Allmann, B. P., Goertz, A., & Wiemer, S. (2011). Stress drop variations of induced earthquakes at the Basel geothermal site. *Geophysical Research Letters*, *38*(9), 2011GL047498. https://doi.org/10.1029/2011GL047498

Goulet, C. A., Abrahamson, N. A., Somerville, P. G., & Wooddell, K. E. (2015). The SCEC Broadband Platform Validation Exercise: Methodology for Code Validation in the Context of Seismic-Hazard Analyses. *Seismological Research Letters*, *86*(1), 17–26. https://doi.org/10.1785/0220140104

Graves, R. W. (1996). Simulating seismic wave propagation in 3D elastic media using staggered-grid finite differences. *Bulletin of the Seismological Society of America*, *86*(4), 1091–1106. https://doi.org/10.1785/BSSA0860041091

Graves, R. W., & Wald, D. J. (2001a). Resolution analysis of finite fault source inversion using one- and three-dimensional Green's functions: 1. Strong

motions. *Journal of Geophysical Research: Solid Earth*, *106*(B5), 8745–8766. https://doi.org/10.1029/2000JB900436

Graves, R. W., & Wald, D. J. (2001b). Resolution analysis of finite fault source inversion using one- and three-dimensional Green's functions: 1. Strong motions. *Journal of Geophysical Research: Solid Earth*, *106*(B5), 8745–8766. https://doi.org/10.1029/2000JB900436

Gregor, N., Abrahamson, N. A., Atkinson, G. M., Boore, D. M., Bozorgnia, Y., Campbell, K. W., et al. (2014). Comparison of NGA-West2 GMPEs. *Earthquake Spectra*, *30*(3), 1179–1197. https://doi.org/10.1193/070113EQS186M

Hallo, M, & Gallovič, F. (2016a). Fast and cheap approximation of Green function uncertainty for waveform-based earthquake source inversions. *Geophysical Journal International*, *207*(2), 1012–1029. https://doi.org/10.1093/gji/ggw320

Hallo, M, & Gallovič, F. (2016b). Fast and cheap approximation of Green function uncertainty for waveform-based earthquake source inversions. *Geophysical Journal International*, *207*(2), 1012–1029. https://doi.org/10.1093/gji/ggw320

Hallo, M., & Gallovič, F. (2020). Bayesian Self-Adapting Fault Slip Inversion With Green's Functions Uncertainty and Application on the 2016 M_w 7.1 Kumamoto Earthquake. *Journal of Geophysical Research: Solid Earth*, *125*(3), e2019JB018703. https://doi.org/10.1029/2019JB018703

Hallo, Miroslav, Asano, K., & Iwata, T. (2025). Softening and Recovery of Near-Surface Layers During the 2024 M7.6 Noto Earthquake. *Journal of*

Geophysical Research: Solid Earth, *130*(4), e2024JB029961. https://doi.org/10.1029/2024JB029961

Hanks, T. C., & Kanamori, H. (1979). A moment magnitude scale. *Journal of Geophysical Research: Solid Earth*, *84*(B5), 2348–2350. https://doi.org/10.1029/JB084iB05p02348

Hanks, T. C., & McGuire, R. K. (1981). The character of high-frequency strong ground motion. *Bulletin of the Seismological Society of America*, *71*(6), 2071–2095. https://doi.org/10.1785/BSSA0710062071

Hardebeck, J. L., & Aron, A. (2009). Earthquake Stress Drops and Inferred Fault Strength on the Hayward Fault, East San Francisco Bay, California. *Bulletin of the Seismological Society of America*, *99*(3), 1801–1814. https://doi.org/10.1785/0120080242

Hartzell, S. (1989). Comparison of seismic waveform inversion results for the rupture history of a finite fault: Application to the 1986 North Palm Springs, California, earthquake. *Journal of Geophysical Research: Solid Earth*, *94*(B6), 7515–7534. https://doi.org/10.1029/JB094iB06p07515

Hartzell, S. H. (1978). Earthquake aftershocks as Green's functions. *Geophysical Research Letters*, *5*(1), 1–4. https://doi.org/10.1029/GL005i001p00001

Hartzell, S. H., & Heaton, T. H. (1983a). Inversion of strong ground motion and teleseismic waveform data for the fault rupture history of the 1979 Imperial Valley, California, earthquake. *Bulletin of the Seismological Society of America*, *73*(6A), 1553–1583. https://doi.org/10.1785/BSSA07306A1553

Hartzell, S. H., & Heaton, T. H. (1983b). Inversion of strong ground motion and teleseismic waveform data for the fault rupture history of the 1979 Imperial Valley, California, earthquake. *Bulletin of the Seismological Society of America*, *73*(6A), 1553–1583. https://doi.org/10.1785/BSSA07306A1553

Haskell, N. A. (1964). Total energy and energy spectral density of elastic wave radiation from propagating faults. *Bulletin of the Seismological Society of America*, *54*(6A), 1811–1841. https://doi.org/10.1785/BSSA05406A1811

Hastie, T., Tibshirani, R., & Friedman, J. (2009). *The Elements of Statistical Learning*. New York, NY: Springer New York. https://doi.org/10.1007/978-0-387-84858-7

Herrmann, R. B., Malagnini, L., & Munafo, I. (2011). Regional Moment Tensors of the 2009 L'Aquila Earthquake Sequence. *Bulletin of the Seismological Society of America*, *101*(3), 975–993. https://doi.org/10.1785/0120100184

Herrmann, Robert B., Malagnini, L., & Munafò, I. (2011). Regional Moment Tensors of the 2009 L'Aquila Earthquake Sequence. *Bulletin of the Seismological Society of America*, *101*(3), 975–993. https://doi.org/10.1785/0120100184

Hough, S. E. (1997). Empirical Green's function analysis: Taking the next step. *Journal of Geophysical Research: Solid Earth*, *102*(B3), 5369–5384. https://doi.org/10.1029/96JB03488

Huang, Y., Ellsworth, W. L., & Beroza, G. C. (2017). Stress drops of induced and tectonic earthquakes in the central United States are indistinguishable. *Science Advances*, *3*(8), e1700772. https://doi.org/10.1126/sciadv.1700772

Huber, P. J. (1964). Robust Estimation of a Location Parameter. *The Annals of Mathematical Statistics*, *35*(1), 73–101. https://doi.org/10.1214/aoms/1177703732

Hunter, J. D. (2007). Matplotlib: A 2D Graphics Environment. *Computing in Science & Engineering*, *9*(3), 90–95. https://doi.org/10.1109/MCSE.2007.55

Ide, S. (2001). Complex source processes and the interaction of moderate earthquakes during the earthquake swarm in the Hida-Mountains, Japan, 1998. *Tectonophysics*, *334*(1), 35–54. https://doi.org/10.1016/S0040-1951(01)00027-0

Ide, S., Baltay, A., & Beroza, G. C. (2011). Shallow Dynamic Overshoot and Energetic Deep Rupture in the 2011 M_w 9.0 Tohoku-Oki Earthquake. *Science*, *332*(6036), 1426–1429. https://doi.org/10.1126/science.1207020

Iervolino, I., Chioccarelli, E., & Suzuki, A. (2020). Seismic damage accumulation in multiple mainshock–aftershock sequences. *Earthquake Engineering & Structural Dynamics*, *49*(10), 1007–1027. https://doi.org/10.1002/eqe.3275

Improta, L., Latorre, D., Margheriti, L., Nardi, A., Marchetti, A., Lombardi, A. M., et al. (2019). Multi-segment rupture of the 2016 Amatrice-Visso-Norcia seismic sequence (central Italy) constrained by the first high-quality catalog of Early Aftershocks. *Scientific Reports*, *9*(1), 6921. https://doi.org/10.1038/s41598-019-43393-2

Irikura, K. (1983). Semi-Empirical Estimation of Strong Ground Motions During Large Earthquakes. *Bulletin of the Disaster Prevention Research Institute*. Retrieved from https://www.semanticscholar.org/paper/Semi-Empirical-

Estimation-of-Strong-Ground-Motions-Irikura/81c8b08b0966eb5d5f070dc20d9b7c7f38141e95

Johnson, K. M. (2006). Frictional Properties on the San Andreas Fault near Parkfield, California, Inferred from Models of Afterslip following the 2004 Earthquake. *Bulletin of the Seismological Society of America*, *96*(4B), S321–S338. https://doi.org/10.1785/0120050808

Johnson, L. R., & Nadeau, R. M. (2002). Asperity Model of an Earthquake: Static Problem. *Bulletin of the Seismological Society of America*, *92*(2), 672–686. https://doi.org/10.1785/0120000282

Kagan, Y. Y. (2007). Simplified algorithms for calculating double-couple rotation. *Geophysical Journal International*, *171*(1), 411–418. https://doi.org/10.1111/j.1365-246X.2007.03538.x

Kakehi, Y., & Irikura, K. (1996). Estimation of high-frequency wave radiation areas on the fault plane by the envelope inversion of acceleration seismograms. *Geophysical Journal International*, *125*(3), 892–900. https://doi.org/10.1111/j.1365-246X.1996.tb06032.x

Kanamori, H. (1977). The energy release in great earthquakes. *Journal of Geophysical Research*, *82*(20), 2981–2987. https://doi.org/10.1029/JB082i020p02981

Kanamori, H., & Anderson, D. L. (1975). Theoretical basis of some empirical relations in seismology. *Bulletin of the Seismological Society of America*, *65*(5), 1073–1095. https://doi.org/10.1785/BSSA0650051073

Kanamori, H., Mori, J., Hauksson, E., Heaton, T. H., Hutton, L. K., & Jones, L. M. (1993). Determination of earthquake energy release and ML using TERRAscope. *Bulletin of the Seismological Society of America*, *83*(2), 330–346. https://doi.org/10.1785/BSSA0830020330

Kaneko, Y., Avouac, J.-P., & Lapusta, N. (2010). Towards inferring earthquake patterns from geodetic observations of interseismic coupling. *Nature Geoscience*, *3*(5), 363–369. https://doi.org/10.1038/ngeo843

Kausel, E. (2006). *Fundamental Solutions in Elastodynamics: A Compendium* (1st ed.). Cambridge University Press. https://doi.org/10.1017/CBO9780511546112

Kemna, K. B., Verdecchia, A., & Harrington, R. M. (2021). Spatio-Temporal Evolution of Earthquake Static Stress Drop Values in the 2016–2017 Central Italy Seismic Sequence. *Journal of Geophysical Research: Solid Earth*, *126*(11), e2021JB022566. https://doi.org/10.1029/2021JB022566

Kennett, B. L. N., & Kerry, N. J. (1979). Seismic waves in a stratified half space. *Geophysical Journal International*, *57*(3), 557–583. https://doi.org/10.1111/j.1365-246X.1979.tb06779.x

Khosravikia, F., & Clayton, P. (2021). Machine learning in ground motion prediction. *Computers & Geosciences*, *148*, 104700. https://doi.org/10.1016/j.cageo.2021.104700

Kirkpatrick, S., Gelatt, C. D., & Vecchi, M. P. (1983). Optimization by Simulated Annealing. *Science*, *220*(4598), 671–680. https://doi.org/10.1126/science.220.4598.671

Ko, Y., Kuo, B., & Hung, S. (2012). Robust determination of earthquake source parameters and mantle attenuation. *Journal of Geophysical Research: Solid Earth*, *117*(B4), 2011JB008759. https://doi.org/10.1029/2011JB008759

Komatitsch, D., & Vilotte, J.-P. (1998a). The spectral element method: An efficient tool to simulate the seismic response of 2D and 3D geological structures. *Bulletin of the Seismological Society of America*, *88*(2), 368–392. https://doi.org/10.1785/BSSA0880020368

Komatitsch, D., & Vilotte, J.-P. (1998b). The spectral element method: An efficient tool to simulate the seismic response of 2D and 3D geological structures. *Bulletin of the Seismological Society of America*, *88*(2), 368–392. https://doi.org/10.1785/BSSA0880020368

Konno, K., & Ohmachi, T. (1998). Ground-motion characteristics estimated from spectral ratio between horizontal and vertical components of microtremor. *Bulletin of the Seismological Society of America*, *88*(1), 228–241. https://doi.org/10.1785/BSSA0880010228

Kotha, S. R., Cotton, F., & Bindi, D. (2018). A new approach to site classification: Mixed-effects Ground Motion Prediction Equation with spectral clustering of site amplification functions. *Soil Dynamics and Earthquake Engineering*, *110*, 318–329. https://doi.org/10.1016/j.soildyn.2018.01.051

Kotha, S. R., Cotton, F., & Bindi, D. (2019). Empirical Models of Shear-Wave Radiation Pattern Derived from Large Datasets of Ground-Shaking

Observations. *Scientific Reports*, *9*(1), 981. https://doi.org/10.1038/s41598-018-37524-4

Kotha, S. R., Weatherill, G., Bindi, D., & Cotton, F. (2020). A regionally-adaptable ground-motion model for shallow crustal earthquakes in Europe. *Bulletin of Earthquake Engineering*, *18*(9), 4091–4125. https://doi.org/10.1007/s10518-020-00869-1

Kotha, S. R., Bindi, D., & Cotton, F. (2022). A regionally adaptable ground-motion model for fourier amplitude spectra of shallow crustal earthquakes in Europe. *Bulletin of Earthquake Engineering*, *20*(2), 711–740. https://doi.org/10.1007/s10518-021-01255-1

Kuehn, N. M., & Scherbaum, F. (2015). Ground-motion prediction model building: a multilevel approach. *Bulletin of Earthquake Engineering*, *13*(9), 2481–2491. https://doi.org/10.1007/s10518-015-9732-3

Kuehn, Nicolas M, Bozorgnia, Y., Campbell, K. W., & Gregor, N. (2023). A regionalized partially nonergodic ground-motion model for subduction earthquakes using the NGA-Sub database. *Earthquake Spectra*, *39*(3), 1625–1657. https://doi.org/10.1177/87552930231180906

Landwehr, N., Kuehn, N. M., Scheffer, T., & Abrahamson, N. (2016). A Nonergodic Ground-Motion Model for California with Spatially Varying Coefficients. *Bulletin of the Seismological Society of America*, *106*(6), 2574–2583. https://doi.org/10.1785/0120160118

Lanzano, G., Sgobba, S., Luzi, L., Puglia, R., Pacor, F., Felicetta, C., et al. (2019). The pan-European Engineering Strong Motion (ESM) flatfile: compilation criteria and data statistics. *Bulletin of Earthquake Engineering*, *17*(2), 561–582. https://doi.org/10.1007/s10518-018-0480-z

Lavecchia, G., Castaldo, R., De Nardis, R., De Novellis, V., Ferrarini, F., Pepe, S., et al. (2016). Ground deformation and source geometry of the 24 August 2016 Amatrice earthquake (Central Italy) investigated through analytical and numerical modeling of DInSAR measurements and structural-geological data. *Geophysical Research Letters*, *43*(24). https://doi.org/10.1002/2016GL071723

Lavrentiadis, G., & Abrahamson, N. A. (2023). A non-ergodic spectral acceleration ground motion model for California developed with random vibration theory. *Bulletin of Earthquake Engineering*, *21*(11), 5265–5291. https://doi.org/10.1007/s10518-023-01689-9

Lengliné, O., Lamourette, L., Vivin, L., Cuenot, N., & Schmittbuhl, J. (2014). Fluid-induced earthquakes with variable stress drop. *Journal of Geophysical Research: Solid Earth*, *119*(12), 8900–8913. https://doi.org/10.1002/2014JB011282

Lin, P.-S., Chiou, B., Abrahamson, N., Walling, M., Lee, C.-T., & Cheng, C.-T. (2011). Repeatable Source, Site, and Path Effects on the Standard Deviation for Empirical Ground-Motion Prediction Models. *Bulletin of the Seismological Society of America*, *101*(5), 2281–2295. https://doi.org/10.1785/0120090312

Lin, Y.-Y., Ma, K.-F., Kanamori, H., Song, T.-R. A., Lapusta, N., & Tsai, V. C. (2016). Evidence for non-self-similarity of microearthquakes recorded at a Taiwan borehole seismometer array. *Geophysical Journal International*, *206*(2), 757–773. https://doi.org/10.1093/gji/ggw172

Liu, J. S. (2004). *Monte Carlo Strategies in Scientific Computing*. New York, NY: Springer New York. https://doi.org/10.1007/978-0-387-76371-2

Liu, P., & Archuleta, R. J. (2004). A new nonlinear finite fault inversion with three-dimensional Green's functions: Application to the 1989 Loma Prieta, California, earthquake. *Journal of Geophysical Research: Solid Earth*, *109*(B2), 2003JB002625. https://doi.org/10.1029/2003JB002625

Louppe, G. (2014). *Understanding Random Forests: From theory to practice*. University of Liege, Belgium.

Loviknes, K., Kotha, S. R., Cotton, F., & Schorlemmer, D. (2021). Testing Nonlinear Amplification Factors of Ground-Motion Models. *Bulletin of the Seismological Society of America*, *111*(4), 2121–2137. https://doi.org/10.1785/0120200386

Maeda, T., Takemura, S., & Furumura, T. (2017). OpenSWPC: an open-source integrated parallel simulation code for modeling seismic wave propagation in 3D heterogeneous viscoelastic media. *Earth, Planets and Space*, *69*(1), 102. https://doi.org/10.1186/s40623-017-0687-2

Mai, P. M., Schorlemmer, D., Page, M., Ampuero, J., Asano, K., Causse, M., et al. (2016). The Earthquake-Source Inversion Validation (SIV) Project.

Seismological Research Letters, *87*(3), 690–708. https://doi.org/10.1785/0220150231

Malagnini, L., Akinci, A., Mayeda, K., Munafo', I., Herrmann, R. B., & Mercuri, A. (2011). Characterization of earthquake-induced ground motion from the L'Aquila seismic sequence of 2009, Italy: Earthquake-induced GM in the Apennines. *Geophysical Journal International*, *184*(1), 325–337. https://doi.org/10.1111/j.1365-246X.2010.04837.x

Malagnini, L., Munafo', I., Cocco, M., Nielsen, S., Mayeda, K., & Boschi, E. (2014). Gradual Fault Weakening with Seismic Slip: Inferences from the Seismic Sequences of L'Aquila, 2009, and Northridge, 1994. *Pure and Applied Geophysics*, *171*(10), 2709–2730. https://doi.org/10.1007/s00024-013-0752-0

Malagnini, L., Parsons, T., Munafò, I., Mancini, S., Segou, M., & Geist, E. L. (2022). Crustal permeability changes inferred from seismic attenuation: Impacts on multi-mainshock sequences. *Frontiers in Earth Science*, *10*, 963689. https://doi.org/10.3389/feart.2022.963689

Marinari, E., & Parisi, G. (1992). Simulated Tempering: A New Monte Carlo Scheme. *Europhysics Letters (EPL)*, *19*(6), 451–458. https://doi.org/10.1209/0295-5075/19/6/002

Marone, C. (1998). The effect of loading rate on static friction and the rate of fault healing during the earthquake cycle. *Nature*, *391*(6662), 69–72. https://doi.org/10.1038/34157

Massey Jr., F. J. (1951). The Kolmogorov-Smirnov Test for Goodness of Fit. *Journal of the American Statistical Association*, *46*(253), 68–78. https://doi.org/10.1080/01621459.1951.10500769

Matsumoto, Y., Yoshida, K., Matsuzawa, T., & Hasegawa, A. (2021). Fault-Valve Behavior Estimated From Intensive Foreshocks and Aftershocks of the 2017 M 5.3 Kagoshima Bay Earthquake Sequence, Kyushu, Southern Japan. *Journal of Geophysical Research: Solid Earth*, *126*(5), e2020JB020278. https://doi.org/10.1029/2020JB020278

Maufroy, E., Chaljub, E., Hollender, F., Kristek, J., Moczo, P., Klin, P., et al. (2015). Earthquake Ground Motion in the Mygdonian Basin, Greece: The E2VP Verification and Validation of 3D Numerical Simulation up to 4 Hz. *Bulletin of the Seismological Society of America*, *105*(3), 1398–1418. https://doi.org/10.1785/0120140228

Mayeda, K., & Walter, W. R. (1996). Moment, energy, stress drop, and source spectra of western United States earthquakes from regional coda envelopes. *Journal of Geophysical Research: Solid Earth*, *101*(B5), 11195–11208. https://doi.org/10.1029/96JB00112

McGarr, A. (1984). Scaling of ground motion parameters, state of stress, and focal depth. *Journal of Geophysical Research: Solid Earth*, *89*(B8), 6969–6979. https://doi.org/10.1029/JB089iB08p06969

McGuire, R. K. (2004). *Seismic hazard and risk analysis*. Oakland, Calif: Earthquake Engineering Research Institute.

McGuire, R. K. (2008). Probabilistic seismic hazard analysis: Early history. *Earthquake Engineering & Structural Dynamics*, *37*(3), 329–338. https://doi.org/10.1002/eqe.765

McGuire, R. K., & Hanks, T. C. (1980). RMS accelerations and spectral amplitudes of strong ground motion during the San Fernando, California earthquake. *Bulletin of the Seismological Society of America*, *70*(5), 1907–1919. https://doi.org/10.1785/BSSA0700051907

Meier, M., Lanza, F., Martínez-Garzón, P., & Chiaraluce, L. (2025). Insights into Extensional Tectonics from a Large Deep Learning Focal Mechanism Catalog. *Bulletin of the Seismological Society of America*, *115*(6), 2690–2704. https://doi.org/10.1785/0120250103

Menichelli, I., De Gori, P., Lucente, F. P., Improta, L., & Chiarabba, C. (2023). Lithosphere Structure, Processes, and Physical State of the Alpine-Apennine System. *Journal of Geophysical Research: Solid Earth*, *128*(4), e2023JB026411. https://doi.org/10.1029/2023JB026411

Metropolis, N., & Ulam, S. (1949). The Monte Carlo Method. *Journal of the American Statistical Association*, *44*(247), 335–341. https://doi.org/10.1080/01621459.1949.10483310

Metropolis, N., Rosenbluth, A. W., Rosenbluth, M. N., Teller, A. H., & Teller, E. (1953). Equation of State Calculations by Fast Computing Machines. *The Journal of Chemical Physics*, *21*(6), 1087–1092. https://doi.org/10.1063/1.1699114

Michele, M., Chiaraluce, L., Di Stefano, R., & Waldhauser, F. (2020). Fine-Scale Structure of the 2016–2017 Central Italy Seismic Sequence From Data Recorded at the Italian National Network. *Journal of Geophysical Research: Solid Earth*, *125*(4), e2019JB018440. https://doi.org/10.1029/2019JB018440

Miller, S. A., Collettini, C., Chiaraluce, L., Cocco, M., Barchi, M., & Kaus, B. J. P. (2004). Aftershocks driven by a high-pressure CO2 source at depth. *Nature*, *427*(6976), 724–727. https://doi.org/10.1038/nature02251

Minson, S. (2010). *A Bayesian approach to earthquake source studies*. California Institute of Technology.

Minson, S. E., Simons, M., & Beck, J. L. (2013). Bayesian inversion for finite fault earthquake source models I—theory and algorithm. *Geophysical Journal International*, *194*(3), 1701–1726. https://doi.org/10.1093/gji/ggt180

Minson, S. E., Simons, M., Beck, J. L., Ortega, F., Jiang, J., Owen, S. E., et al. (2014). Bayesian inversion for finite fault earthquake source models – II: the 2011 great Tohoku-oki, Japan earthquake. *Geophysical Journal International*, *198*(2), 922–940. https://doi.org/10.1093/gji/ggu170

Moczo, P., Lucká, M., Kristek, J., & Kristeková, M. (1999). 3D Displacement finite differences and a combined memory optimization. *Bulletin of the Seismological Society of America*, *89*(1), 69–79. https://doi.org/10.1785/BSSA0890010069

Monelli, D., Mai, P. M., Jónsson, S., & Giardini, D. (2009). Bayesian imaging of the 2000 Western Tottori (Japan) earthquake through fitting of strong motion and

GPS data. *Geophysical Journal International*, *176*(1), 135–150. https://doi.org/10.1111/j.1365-246X.2008.03943.x

Moyer, P. A., Boettcher, M. S., McGuire, J. J., & Collins, J. A. (2018). Spatial and Temporal Variations in Earthquake Stress Drop on Gofar Transform Fault, East Pacific Rise: Implications for Fault Strength. *Journal of Geophysical Research: Solid Earth*, *123*(9), 7722–7740. https://doi.org/10.1029/2018JB015942

Muller, G. (1985). The reflectivity method: a tutorial. *Journal of Geophysics*, *58*(1), 153–174.

Nakahara, H., Nishimura, T., Sato, H., & Ohtake, M. (1998). Seismogram envelope inversion for the spatial distribution of high-frequency energy radiation from the earthquake fault: Application to the 1994 far east off Sanriku earthquake, Japan. *Journal of Geophysical Research: Solid Earth*, *103*(B1), 855–867. https://doi.org/10.1029/97JB02676

Nielsen, S., & Madariaga, R. (2003). On the Self-Healing Fracture Mode. *Bulletin of the Seismological Society of America*, *93*(6), 2375–2388. https://doi.org/10.1785/0120020090

Noir, J., Jacques, E., Békri, S., Adler, P. M., Tapponnier, P., & King, G. C. P. (1997). Fluid flow triggered migration of events in the 1989 Dobi Earthquake sequence of central Afar. *Geophysical Research Letters*, *24*(18), 2335–2338. https://doi.org/10.1029/97GL02182

Okuda, T., & Ide, S. (2018). Streak and hierarchical structures of the Tohoku–Hokkaido subduction zone plate boundary. *Earth, Planets and Space*, *70*(1), 132. https://doi.org/10.1186/s40623-018-0903-8

Olson, A. H., & Apsel, R. J. (1982a). Finite faults and inverse theory with applications to the 1979 Imperial Valley earthquake. *Bulletin of the Seismological Society of America*, *72*(6A), 1969–2001. https://doi.org/10.1785/BSSA07206A1969

Olson, A. H., & Apsel, R. J. (1982b). Finite faults and inverse theory with applications to the 1979 Imperial Valley earthquake. *Bulletin of the Seismological Society of America*, *72*(6A), 1969–2001. https://doi.org/10.1785/BSSA07206A1969

Oth, A., Bindi, D., Parolai, S., & Di Giacomo, D. (2011). Spectral Analysis of K-NET and KiK-net Data in Japan, Part II: On Attenuation Characteristics, Source Spectra, and Site Response of Borehole and Surface Stations. *Bulletin of the Seismological Society of America*, *101*(2), 667–687. https://doi.org/10.1785/0120100135

Oth, Adrien. (2013). On the characteristics of earthquake stress release variations in Japan. *Earth and Planetary Science Letters*, *377–378*, 132–141. https://doi.org/10.1016/j.epsl.2013.06.037

Oth, Adrien, & Kaiser, A. E. (2014). Stress Release and Source Scaling of the 2010–2011 Canterbury, New Zealand Earthquake Sequence from Spectral Inversion of Ground Motion Data. *Pure and Applied Geophysics*, *171*(10), 2767–2782. https://doi.org/10.1007/s00024-013-0751-1

Oth, Adrien, Miyake, H., & Bindi, D. (2017). On the relation of earthquake stress drop and ground motion variability. *Journal of Geophysical Research: Solid Earth*, *122*(7), 5474–5492. https://doi.org/10.1002/2017JB014026

Pacor, F., Gallovič, F., Puglia, R., Luzi, L., & D'Amico, M. (2016). Diminishing high-frequency directivity due to a source effect: Empirical evidence from small earthquakes in the Abruzzo region, Italy. *Geophysical Research Letters*, *43*(10), 5000–5008. https://doi.org/10.1002/2016GL068546

Pacor, F., Spallarossa, D., Oth, A., Luzi, L., Puglia, R., Cantore, L., et al. (2016). Spectral models for ground motion prediction in the L'Aquila region (central Italy): evidence for stress-drop dependence on magnitude and depth. *Geophysical Journal International*, *204*(2), 697–718. https://doi.org/10.1093/gji/ggv448

Pacor, Francesca, Felicetta, C., Lanzano, G., Sgobba, S., Puglia, R., D'Amico, M., et al. (2018). NESS1: A Worldwide Collection of Strong-Motion Data to Investigate Near-Source Effects. *Seismological Research Letters*, *89*(6), 2299–2313. https://doi.org/10.1785/0220180149

Pantosti, D., & Valensise, G. (1990). Faulting mechanism and complexity of the November 23, 1980, Campania-Lucania Earthquake, inferred from surface observations. *Journal of Geophysical Research: Solid Earth*, *95*(B10), 15319–15341. https://doi.org/10.1029/JB095iB10p15319

Pedregosa, F., Varoquaux, G., Gramfort, A., Michel, V., Thirion, B., Grisel, O., et al. (2011). Scikit-learn: Machine Learning in Python. *Journal of Machine Learning Research*, *12*(85), 2825–2830.

Piatanesi, A., Tinti, E., Cocco, M., & Fukuyama, E. (2004). The dependence of traction evolution on the earthquake source time function adopted in kinematic rupture models. *Geophysical Research Letters*, *31*(4). https://doi.org/10.1029/2003GL019225

Picozzi, M., Spallarossa, D., Iaccarino, A. G., & Bindi, D. (2024). Event-specific ground motion anomalies highlight the preparatory phase of earthquakes during the 2016–2017 Italian seismicity. *Communications Earth & Environment*, *5*(1), 289. https://doi.org/10.1038/s43247-024-01455-y

Pisconti, A., Del Pezzo, E., Bianco, F., & De Lorenzo, S. (2015). Seismic Q estimates in Umbria Marche (Central Italy): hints for the retrieval of a new attenuation law for seismic risk. *Geophysical Journal International*, *201*(3), 1370–1382. https://doi.org/10.1093/gji/ggv055

Pizzi, A., Di Domenica, A., Gallovič, F., Luzi, L., & Puglia, R. (2017). Fault Segmentation as Constraint to the Occurrence of the Main Shocks of the 2016 Central Italy Seismic Sequence. *Tectonics*, *36*(11), 2370–2387. https://doi.org/10.1002/2017TC004652

Podvin, P., & Lecomte, I. (1991). Finite difference computation of traveltimes in very contrasted velocity models: a massively parallel approach and its associated

tools. *Geophysical Journal International*, *105*(1), 271–284. https://doi.org/10.1111/j.1365-246X.1991.tb03461.x

Prieto, G. A., Shearer, P. M., Vernon, F. L., & Kilb, D. (2004). Earthquake source scaling and self-similarity estimation from stacking *P* and *S* spectra. *Journal of Geophysical Research: Solid Earth*, *109*(B8), 2004JB003084. https://doi.org/10.1029/2004JB003084

Pulido, N., Aoi, S., & Fujiwara, H. (2008). Rupture process of the 2007 Notohanto earthquake by using an isochrones back-projection method and K-NET/KiK-net data. *Earth, Planets and Space*, *60*(10), 1035–1040. https://doi.org/10.1186/BF03352865

Ragon, T., Sladen, A., & Simons, M. (2018). Accounting for uncertain fault geometry in earthquake source inversions – I: theory and simplified application. *Geophysical Journal International*, *214*(2), 1174–1190. https://doi.org/10.1093/gji/ggy187

Ragon, T., Sladen, A., & Simons, M. (2019). Accounting for uncertain fault geometry in earthquake source inversions – II: application to the Mw 6.2 Amatrice earthquake, central Italy. *Geophysical Journal International*, *218*(1), 689–707. https://doi.org/10.1093/gji/ggz180

Razafindrakoto, H. N. T., & Mai, P. M. (2014). Uncertainty in Earthquake Source Imaging Due to Variations in Source Time Function and Earth Structure. *Bulletin of the Seismological Society of America*, *104*(2), 855–874. https://doi.org/10.1785/0120130195

Razafindrakoto, Hoby N. T., & Mai, P. M. (2014). Uncertainty in Earthquake Source Imaging Due to Variations in Source Time Function and Earth Structure. *Bulletin of the Seismological Society of America*, *104*(2), 855–874. https://doi.org/10.1785/0120130195

Rice, J. R., Sammis, C. G., & Parsons, R. (2005). Off-Fault Secondary Failure Induced by a Dynamic Slip Pulse. *Bulletin of the Seismological Society of America*, *95*(1), 109–134. https://doi.org/10.1785/0120030166

Robert, C. P., & Casella, G. (2004). *Monte Carlo Statistical Methods*. New York, NY: Springer New York. https://doi.org/10.1007/978-1-4757-4145-2

Roberts, G. O., Gelman, A., & Gilks, W. R. (1997). Weak convergence and optimal scaling of random walk Metropolis algorithms. *The Annals of Applied Probability*, *7*(1), 110–120. https://doi.org/10.1214/aoap/1034625254

Roberts, Gareth O., & Rosenthal, J. S. (2001). Optimal scaling for various Metropolis-Hastings algorithms. *Statistical Science*, *16*(4), 351–367. https://doi.org/10.1214/ss/1015346320

Sahakian, V., Baltay, A., Hanks, T., Buehler, J., Vernon, F., Kilb, D., & Abrahamson, N. (2018). Decomposing Leftovers: Event, Path, and Site Residuals for a Small-Magnitude Anza Region GMPE. *Bulletin of the Seismological Society of America*, *108*(5A), 2478–2492. https://doi.org/10.1785/0120170376

Sahakian, V. J., Baltay, A., Hanks, T. C., Buehler, J., Vernon, F. L., Kilb, D., & Abrahamson, N. A. (2019). Ground Motion Residuals, Path Effects, and Crustal Properties: A Pilot Study in Southern California. *Journal of*

Geophysical Research: Solid Earth, *124*(6), 5738–5753. https://doi.org/10.1029/2018JB016796

Sambridge, M. (2014). A Parallel Tempering algorithm for probabilistic sampling and multimodal optimization. *Geophysical Journal International*, *196*(1), 357–374. https://doi.org/10.1093/gji/ggt342

Sambridge, M., & Mosegaard, K. (2002). Monte Carlo Methods in Geophysical Inverse Problems. *Reviews of Geophysics*, *40*(3), 3-1-3–29. https://doi.org/10.1029/2000RG000089

Sato, T., & Hirasawa, T. (1973). Body wave spectra from propagating shear cracks. *Journal of Physics of the Earth*, *21*(4), 415–431. https://doi.org/10.4294/jpe1952.21.415

Satoh, T. (2023). Broadband Source Model of the 2023 Mw 7.8 Türkiye Earthquake from Strong-Motion Records by Isochrone Backprojection and Empirical Green's Function Method. *Seismological Research Letters*, *95*(2A), 584–595. https://doi.org/10.1785/0220230268

Schaff, D. P., & Beroza, G. C. (2004). Coseismic and postseismic velocity changes measured by repeating earthquakes. *Journal of Geophysical Research: Solid Earth*, *109*(B10), 2004JB003011. https://doi.org/10.1029/2004JB003011

Scholz, C. H. (2019). *The Mechanics of Earthquakes and Faulting* (3rd ed.). Cambridge: Cambridge University Press. https://doi.org/10.1017/9781316681473

Scognamiglio, L., Tinti, E., & Quintiliani, M. (2006). Time Domain Moment Tensor (TDMT) [Data set] [Data set]. Data set. https://doi.org/https://doi.org/10.13127/TDMT

Scognamiglio, L., Tinti, E., Casarotti, E., Pucci, S., Villani, F., Cocco, M., et al. (2018a). Complex Fault Geometry and Rupture Dynamics of the M_W 6.5, 30 October 2016, Central Italy Earthquake. *Journal of Geophysical Research: Solid Earth*, *123*(4), 2943–2964. https://doi.org/10.1002/2018JB015603

Scognamiglio, L., Tinti, E., Casarotti, E., Pucci, S., Villani, F., Cocco, M., et al. (2018b). Complex Fault Geometry and Rupture Dynamics of the M_W 6.5, 30 October 2016, Central Italy Earthquake. *Journal of Geophysical Research: Solid Earth*, *123*(4), 2943–2964. https://doi.org/10.1002/2018JB015603

Segou, M., McCloskey, J., Baptie, B., & Hawthorn, D. (2016). Armatrice Sequence International [SEED data]. International Federation of Digital Seismograph Networks. https://doi.org/10.7914/SN/YR_2016

Sekiguchi, H., & Iwata, T. (2002). Rupture Process of the 1999 Kocaeli, Turkey, Earthquake Estimated from Strong-Motion Waveforms. *Bulletin of the Seismological Society of America*, *92*(1), 300–311. https://doi.org/10.1785/0120000811

Shaw, B. E., Richards-Dinger, K., & Dieterich, J. H. (2015). Deterministic model of earthquake clustering shows reduced stress drops for nearby aftershocks. *Geophysical Research Letters*, *42*(21), 9231–9238. https://doi.org/10.1002/2015GL066082

Shearer, P. M., Prieto, G. A., & Hauksson, E. (2006). Comprehensive analysis of earthquake source spectra in southern California. *Journal of Geophysical Research: Solid Earth*, *111*(B6), 2005JB003979. https://doi.org/10.1029/2005JB003979

Shearer, P. M., Abercrombie, R. E., Trugman, D. T., & Wang, W. (2019). Comparing EGF Methods for Estimating Corner Frequency and Stress Drop From *P* Wave Spectra. *Journal of Geophysical Research: Solid Earth*, *124*(4), 3966–3986. https://doi.org/10.1029/2018JB016957

Shibata, R., & Aso, N. (2025). Kinematic Source Modeling Using Radiation-Corrected Empirical Green's Functions in Waveform Inversion. *Bulletin of the Seismological Society of America*, *115*(3), 1212–1232. https://doi.org/10.1785/0120240077

Sibson, R. H. (1992). Implications of fault-valve behaviour for rupture nucleation and recurrence. *Tectonophysics*, *211*(1–4), 283–293. https://doi.org/10.1016/0040-1951(92)90065-E

Sibson, R. H. (2020). Preparation zones for large crustal earthquakes consequent on fault-valve action. *Earth, Planets and Space*, *72*(1), 31. https://doi.org/10.1186/s40623-020-01153-x

Soldati, G., Zaccarelli, L., Faenza, L., & Michelini, A. (2015). Monitoring of crustal seismic velocity variations in the L'Aquila fault zone inferred from noise cross-correlation. *Geophysical Journal International*, *202*(1), 604–611. https://doi.org/10.1093/gji/ggv172

Soldati, G., Zaccarelli, L., & Faenza, L. (2019). Spatio-temporal seismic velocity variations associated to the 2016–2017 central Italy seismic sequence from noise cross-correlation. *Geophysical Journal International*, *219*(3), 2165–2173. https://doi.org/10.1093/gji/ggz429

Sonley, E., & Abercrombie, R. E. (2006). Effects of methods of attenuation correction on source parameter determination. In R. Abercrombie, A. McGarr, H. Kanamori, & G. Di Toro (Eds.), *Geophysical Monograph Series* (Vol. 170, pp. 91–97). Washington, D. C.: American Geophysical Union. https://doi.org/10.1029/170GM11

Spallarossa, D., Cattaneo, M., Scafidi, D., Michele, M., Chiaraluce, L., Segou, M., & Main, I. (2021). An automatically generated high-resolution earthquake catalogue for the 2016–2017 Central Italy seismic sequence, including P and S phase arrival times. *Geophysical Journal International*, *225*(1), 555–571. https://doi.org/10.1093/gji/ggaa604

Spudich, P., Cirella, A., Scognamiglio, L., & Tinti, E. (2019). Variability in synthetic earthquake ground motions caused by source variability and errors in wave propagation models. *Geophysical Journal International*, *219*(1), 346–372. https://doi.org/10.1093/gji/ggz275

Steacy, S., Gomberg, J., & Cocco, M. (2005). Introduction to special section: Stress transfer, earthquake triggering, and time-dependent seismic hazard. *Journal of Geophysical Research: Solid Earth*, *110*(B5), 2005JB003692. https://doi.org/10.1029/2005JB003692

Strasser, F. O., Abrahamson, N. A., & Bommer, J. J. (2009). Sigma: Issues, Insights, and Challenges. *Seismological Research Letters*, *80*(1), 40–56. https://doi.org/10.1785/gssrl.80.1.40

Sumy, D. F., Neighbors, C. J., Cochran, E. S., & Keranen, K. M. (2017). Low stress drops observed for aftershocks of the 2011 M_w 5.7 Prague, Oklahoma, earthquake. *Journal of Geophysical Research: Solid Earth*, *122*(5), 3813–3834. https://doi.org/10.1002/2016JB013153

Supino, M., Festa, G., & Zollo, A. (2019). A probabilistic method for the estimation of earthquake source parameters from spectral inversion: application to the 2016–2017 Central Italy seismic sequence. *Geophysical Journal International*, *218*(2), 988–1007. https://doi.org/10.1093/gji/ggz206

Tarantola, A., & Valette, B. (1981). Inverse problems = Quest for information. *Journal of Geophysics*, *50*(1), 159–170.

Tarantola, Albert. (2005). *Inverse Problem Theory and Methods for Model Parameter Estimation*. SIAM.

Tinti, E., Fukuyama, E., Piatanesi, A., & Cocco, M. (2005). A Kinematic Source-Time Function Compatible with Earthquake Dynamics. *Bulletin of the Seismological Society of America*, *95*(4), 1211–1223. https://doi.org/10.1785/0120040177

Toda, S., Stein, R. S., Beroza, G. C., & Marsan, D. (2012). Aftershocks halted by static stress shadows. *Nature Geoscience*, *5*(6), 410–413. https://doi.org/10.1038/ngeo1465

Trifunac, M. D. (1976). Preliminary empirical model for scaling Fourier Amplitude Spectra of strong ground acceleration in terms of earthquake magnitude, source-to-station distance, and recording site conditions. *Bulletin of the Seismological Society of America*, *66*(4), 1343–1373. https://doi.org/10.1785/BSSA0660041343

Trugman, D. T. (2020). Stress-Drop and Source Scaling of the 2019 Ridgecrest, California, Earthquake Sequence. *Bulletin of the Seismological Society of America*, *110*(4), 1859–1871. https://doi.org/10.1785/0120200009

Trugman, D. T., & Shearer, P. M. (2017). Application of an improved spectral decomposition method to examine earthquake source scaling in Southern California. *Journal of Geophysical Research: Solid Earth*, *122*(4), 2890–2910. https://doi.org/10.1002/2017JB013971

Trugman, D. T., & Shearer, P. M. (2018). Strong Correlation between Stress Drop and Peak Ground Acceleration for Recent M 1–4 Earthquakes in the San Francisco Bay Area. *Bulletin of the Seismological Society of America*, *108*(2), 929–945. https://doi.org/10.1785/0120170245

Trugman, D. T., Chu, S. X., & Tsai, V. C. (2021). Earthquake Source Complexity Controls the Frequency Dependence of Near-Source Radiation Patterns. *Geophysical Research Letters*, *48*(17), e2021GL095022. https://doi.org/10.1029/2021GL095022

Tung, S., & Masterlark, T. (2018). Delayed Poroelastic Triggering of the 2016 October Visso Earthquake by the August Amatrice Earthquake, Italy. *Geophysical Research Letters*, *45*(5), 2221–2229. https://doi.org/10.1002/2017GL076453

Uchide, T., & Song, S. G. (2018). Fault Rupture Model of the 2016 Gyeongju, South Korea, Earthquake and Its Implication for the Underground Fault System. *Geophysical Research Letters*, *45*(5), 2257–2264. https://doi.org/10.1002/2017GL076960

Vallée, M. (2013). Source time function properties indicate a strain drop independent of earthquake depth and magnitude. *Nature Communications*, *4*(1), 2606. https://doi.org/10.1038/ncomms3606

Valoroso, L., Chiaraluce, L., Piccinini, D., Di Stefano, R., Schaff, D., & Waldhauser, F. (2013). Radiography of a normal fault system by 64,000 high-precision earthquake locations: The 2009 L'Aquila (central Italy) case study. *Journal of Geophysical Research: Solid Earth*, *118*(3), 1156–1176. https://doi.org/10.1002/jgrb.50130

Vassallo, M., Cultrera, G., Di Giulio, G., Cara, F., & Milana, G. (2022). Peak Frequency Changes From HV Spectral Ratios in Central Italy: Effects of Strong Motions and Seasonality Over 12 Years of Observations. *Journal of Geophysical Research: Solid Earth*, *127*(5), e2021JB023848. https://doi.org/10.1029/2021JB023848

Vidale, J. E., & Li, Y.-G. (2003). Damage to the shallow Landers fault from the nearby Hector Mine earthquake. *Nature*, *421*(6922), 524–526. https://doi.org/10.1038/nature01354

Virtanen, P., Gommers, R., Oliphant, T. E., Haberland, M., Reddy, T., Cournapeau, D., et al. (2020). SciPy 1.0: fundamental algorithms for scientific computing in Python. *Nature Methods*, *17*(3), 261–272. https://doi.org/10.1038/s41592-019-0686-2

Waldhauser, F. (2000). A Double-Difference Earthquake Location Algorithm: Method and Application to the Northern Hayward Fault, California. *Bulletin of the Seismological Society of America*, *90*(6), 1353–1368. https://doi.org/10.1785/0120000006

Weatherill, G., Kotha, S. R., & Cotton, F. (2020). A regionally-adaptable "scaled backbone" ground motion logic tree for shallow seismicity in Europe: application to the 2020 European seismic hazard model. *Bulletin of Earthquake Engineering*, *18*(11), 5087–5117. https://doi.org/10.1007/s10518-020-00899-9

Wessel, P., Luis, J. F., Uieda, L., Scharroo, R., Wobbe, F., Smith, W. H. F., & Tian, D. (2019). The Generic Mapping Tools Version 6. *Geochemistry, Geophysics, Geosystems*, *20*(11), 5556–5564. https://doi.org/10.1029/2019GC008515

Wu, S.-L., Nozu, A., & Nagasaka, Y. (2021). Rupture Process of the Mainshock of the 2019 Ridgecrest Earthquake Sequence from Waveform Inversion with

Empirical Green's Functions. *Bulletin of the Seismological Society of America*, *111*(2), 1014–1031. https://doi.org/10.1785/0120200266

Yamada, T., Duan, M., & Kawahara, J. (2021). Spatio-temporal characteristics of frictional properties on the subducting Pacific Plate off the east of Tohoku district, Japan estimated from stress drops of small earthquakes. *Earth, Planets and Space*, *73*(1), 18. https://doi.org/10.1186/s40623-020-01326-8

Yenier, E., & Atkinson, G. M. (2015). Regionally Adjustable Generic Ground-Motion Prediction Equation Based on Equivalent Point-Source Simulations: Application to Central and Eastern North America. *Bulletin of the Seismological Society of America*, *105*(4), 1989–2009. https://doi.org/10.1785/0120140332

Yoshida, K., Saito, T., Urata, Y., Asano, Y., & Hasegawa, A. (2017). Temporal Changes in Stress Drop, Frictional Strength, and Earthquake Size Distribution in the 2011 Yamagata-Fukushima, NE Japan, Earthquake Swarm, Caused by Fluid Migration. *Journal of Geophysical Research: Solid Earth*, *122*(12). https://doi.org/10.1002/2017JB014334

Youngs, R. R., Chiou, S.-J., Silva, W. J., & Humphrey, J. R. (1997). Strong Ground Motion Attenuation Relationships for Subduction Zone Earthquakes. *Seismological Research Letters*, *68*(1), 58–73. https://doi.org/10.1785/gssrl.68.1.58

Zhang, J., Chen, X., & Abercrombie, R. E. (2022). Spatiotemporal Variability of Earthquake Source Parameters at Parkfield, California, and Their

Relationship With the 2004 M6 Earthquake. *Journal of Geophysical Research: Solid Earth*, *127*(6), e2021JB022851. https://doi.org/10.1029/2021JB022851

Zhou, S., Irikura, K., & Chen, X. (2004). Analysis of the reliability and resolution of the earthquake source history inferred from waveforms, taking the Chi-Chi earthquake as an example. *Geophysical Journal International*, *157*(3), 1217–1232. https://doi.org/10.1111/j.1365-246X.2004.02247.x

Zhu, L., & Rivera, L. A. (2002). A note on the dynamic and static displacements from a point source in multilayered media. *Geophysical Journal International*, *148*(3), 619–627. https://doi.org/10.1046/j.1365-246X.2002.01610.x

Žilić, I., Causse, M., Vallée, M., & Markušić, S. (2025). High Stress Drop and Slow Rupture During the 2020 M_W 6.4 Intraplate Petrinja Earthquake, Croatia. *Journal of Geophysical Research: Solid Earth*, *130*(1), e2024JB029107. https://doi.org/10.1029/2024JB029107